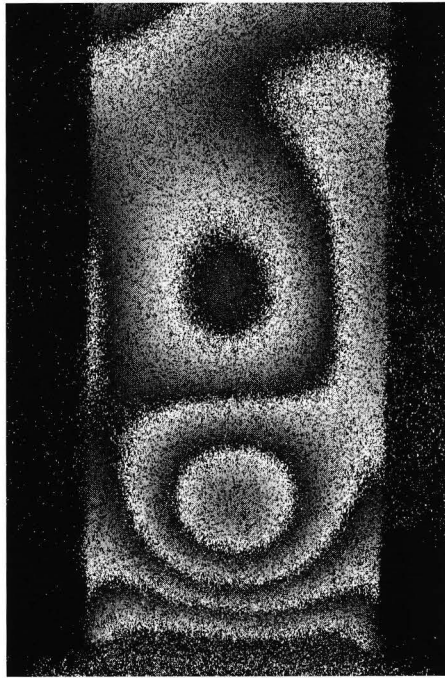


Cross-sectional stability of aluminium extrusions

Prediction of the actual local buckling behaviour



Jeroen Mennink

ISBN 90-386-1546-9

Copyright 2002 by J. Mennink

Printed in The Netherlands

Stellingen

Behorende bij het proefschrift

Cross-sectional stability of aluminium extrusions

door J. Mennink

1. De huidige beschrijving van plooi, die ook in de normen wordt toegepast, geeft slechts een praktische en meestal conservatieve oplossing voor het tot nu toe moeizaam te beschrijven fenomeen doorsnede-stabiliteit.
 2. Ondanks de complexiteit van aluminium extrusieprofielen is het mogelijk een eenduidige en algemeen toepasbare toetsingsregel voor doorsnede-stabiliteit te formuleren.
 3. Voor de bepaling van de doorsnede-capaciteit is het te allen tijde geoorloofd een profieldoorsnede te schematiseren met weglating van geometrische elementen.
 4. In de huidige regelgeving wordt de interactie tussen plooi en knik beschreven op basis van (plaat-)sterkte, terwijl deze juist afhankelijk is van stijfheid.
 5. Aluminium is drie maal minder stijf dan staal; dit betekent echter niet dat de elasticiteitsmodulus van aluminium gelijk is aan 70 kN/mm^2 .
 6. Nieuwe en nauwkeuriger rekenregels zijn vaak zo complex dat het gebruik ervan tot minder betrouwbare resultaten leidt.
 7. Een simulatie is ook een proef.
 8. De wetenschap is uit het niets ontstaan en tracht de betekenis van het niets terug te vinden.
 9. Praktische oplossingen voor complexe problemen zijn vaak verbazingwekkend eenvoudig.
 10. Aluminium is vergelijkbaar met een goed huwelijk: onder druk zal het niet breken maar plooiën.
 11. De computer is het beste dat papier ooit is overkomen.
 12. Gezien de uitkomsten van “tien-voor-taal” van de afgelopen jaren, zullen Vlaamse stellingen ongetwijfelt beter zijn dan Nederlandse.
-

Propositions

With respect to the Ph.D. thesis

Cross-sectional stability of aluminium extrusions

by J. Mennink

1. The current description of local buckling, also applied in codes, is merely a practical and in most cases conservative solution for the complex phenomenon of cross-sectional stability.
 2. Despite the complexity of aluminium extrusions, it is possible to formulate clear and generally applicable design rules for cross-sectional stability.
 3. In the determination of the cross-sectional capacity it is always allowed to schematise the cross-section with the omission of geometrical elements.
 4. Current design rules with respect to the interaction of local and flexural buckling are described as a function of (plate) strength, though this relation is essentially based on stiffness.
 5. Though the stiffness of aluminium is only one third of that of steel, this does not imply that the modulus of elasticity of aluminium is equal to 70 kN/mm².
 6. The complexity of new and more accurate design rules is often such, that application in practice results in less reliable results.
 7. A simulation is a test.
 8. Science originated from nothingness and attempts to retrieve the meaning of nothing.
 9. Practical solutions for complex problems are often amazingly simple.
 10. Aluminium is like a good marriage; under pressure it buckles, but it will not break.
 11. The personal computer is the best thing that could happen to paper.
 12. Considering the outcome of the Dutch-Flemish language quiz “tien-voor-taal” of recent years, one must conclude that Flemish statements are undoubtedly better than Dutch ones.
-

Cross-sectional stability of aluminium extrusions

Prediction of the actual local buckling behaviour

Proefschrift

ter verkrijging van de graad van doctor aan de Technische Universiteit Eindhoven,
op gezag van de Rector Magnificus, prof.dr. R.A. van Santen, voor een commissie
aangewezen door het College voor Promoties in het openbaar te verdedigen op
maandag 23 december 2002 om 16.00 uur

door

Jeroen Mennink

geboren te Sumve (Tanzania)

Dit proefschrift is goedgekeurd door de promotoren:

prof.ir. F. Soetens

en

prof.ir. H.H. Snijder

De samenstelling van de promotiecommissie:

prof. ir. J. Westra	TU Eindhoven (Voorzitter)
prof. ir. F. Soetens	TU Eindhoven / TNO Bouw
prof. ir. H.H. Snijder	TU Eindhoven
prof. dr. ir. J.D. Janssen	TU Eindhoven
prof. ir. F.S.K. Bijlaard	TU Delft
prof. dr. F.M. Mazzolani	University of Naples, Italy
prof. dr. T. Peköz	Cornell University, USA
ir. B.W.E.M. van Hove	TNO Bouw / TU Eindhoven
dr. ir. I.J.J. van Straalen	TNO Bouw

Acknowledgements

After six years of study and research, experimenting, number crunching, and writing the work is done. A strange period that consists of important changes in both professional and personal life. A period that shapes your mind to cope with large and “important” tasks and allows a very thorough investigation of one tiny bit of reality, a major aspect of your own field of research. It defines borders and scopes the relation with the people around you. This thesis is thus only a very small part of a six-year adventure.

The support and financing of both the Technical University of Eindhoven and my current employer TNO Building and Construction research are greatly appreciated. The combination of fundamental research at Eindhoven with more target-related research at TNO proved to be an excellent combination.

The first person to thank is Frans Soetens, promoter and friend. Without him I would not have started, but certainly not finished this research. Secondly, my permanent mentors Dianne van Hove, Bert Snijder, IJsbrand van Straalen en Frans Bijlaard. I will never forget the endless lists of corrections and questions. These resulted, more often than not, in heated discussions that shaped a thorough foundation for my brain waves. Furthermore, my colleagues at both Eindhoven and TNO I thank for their support and interest, especially my roommate Johan Maljaars. In addition, I would like to thank my students who executed the experiments: Paul Brouwer, Robert Peters and Jop Schillemans, as well as Eric Wijen of the lab who made things happen.

Only bad times let you know your friends. Barbara and I highly appreciated your help and support. Specifically I'd like to mention our “wedding staff”, Carlo Kuiper and Ingrid Bonnet, as well as my friend Marcel Bosch who made most of the figures in this thesis. However, there is no place like home. I really appreciate the support and warmth of my family (in law), which has grown substantially over the past six years. Finally, my thoughts are for Barbara, for bearing my temper, comforting my disappointments and for keeping things running while I was at work. This thesis is as much her credit as it is mine.

Summary

Aluminium extrusions applied in daily practice are often thin-walled with complex cross-sectional shapes. These shapes are based on a variety of demands that are in general non-structural. As a result, several types of instability may occur, including overall and cross-sectional instability modes as well as mode interactions. Research on overall buckling is usually based on simple and symmetrical cross-sections, whereas cross-sectional instability is simplified to buckling of individual plates. It is therefore highly unlikely that these design rules provide an accurate description of the actual buckling behaviour of arbitrary cross-sections. As predicted failure modes not necessarily agree with actual ones, the outcome of the results may be overly conservative but could be unsafe as well.

In order to investigate the actual cross-sectional stability behaviour of aluminium extrusions, a large experimental program is executed at Eindhoven University of Technology. This program consists of aluminium extrusions under uniform axial compression. Test specimens with rectangular hollows (SHS), U-sections (US), as well as very complex cross-sectional shapes (CS) have been tested. A detailed investigation is made into the influence of the test set-up, initial imperfections, as well as the material characteristic. This results in a large set of test data on the actual buckling behaviour of aluminium extrusions, including local, distortional, flexural and flexural-torsional buckling, as well as mode interaction.

To support the findings of the experiments, a numerical program using the finite element (FE) method is executed. Most experiments are simulated using the actual geometry, material, and imperfections. Comparison of the experimental and numerical results shows that an accurate prediction is achieved. Furthermore, the FE-analyses allow a detailed investigation of specific aspects like the bifurcation load, the influence of imperfections and materials, the test set-up, and mode interaction.

The FE-results enable the development of a new and general prediction model for the local buckling behaviour of aluminium extrusions. Based on the actual local buckling behaviour of cross-sections, it is derived for uniformly compressed aluminium extrusions with arbitrary cross-sections consisting of flat plates. As such, it allows an accurate and conservative prediction of the strength and stiffness of a large range of commercial extrusions. The promising results of this model may result in design rules that enable more economical designs and are able to include distortional buckling and mode interaction. This combination of experimental, numerical (FE), and analytical work results in a thorough investigation on the actual local buckling behaviour of aluminium extrusions with arbitrary and complex cross-sections.

Table of Contents

<i>Acknowledgements</i>	<i>vi</i>
<i>Summary</i>	<i>vii</i>
<i>Table of Contents</i>	<i>ix</i>
<i>List of symbols</i>	<i>xiii</i>
I Introduction and thesis outline	I
<i>Chapter abstract</i>	<i>1</i>
<i>1.1 Aluminium extrusions in structural applications</i>	<i>3</i>
<i>1.2 Buckling of axially compressed aluminium extrusions</i>	<i>4</i>
<i>1.3 Problem statement, research goal and limitations</i>	<i>6</i>
<i>1.4 Research approach and thesis outline</i>	<i>8</i>
2 State of the art – stability behaviour	11
<i>Chapter abstract</i>	<i>11</i>
<i>2.1 Theory of elastic stability - Bifurcation buckling</i>	<i>13</i>
2.1.1 Definitions	13
2.1.2 Initially perfect systems	14
2.1.3 Initially imperfect systems	16
<i>2.2 Centrally loaded columns – Column buckling</i>	<i>18</i>
2.2.1 General description	18
2.2.2 Column buckling - Inelastic materials	21
2.2.3 Column buckling - Imperfections	22
2.2.4 Column buckling - Design practice	25
<i>2.3 Uniformly compressed plates – Plate buckling</i>	<i>28</i>
2.3.1 General description	28
2.3.2 Plate buckling – Determination of the critical stress	29
2.3.3 Plate buckling - Post-buckling and ultimate strength	33
2.3.4 Plate buckling - Effective width approach	36
<i>2.4 Cross-sectional instability – Local and distortional buckling</i>	<i>38</i>
2.4.1 General description	38
2.4.2 Local buckling	38
2.4.3 Distortional buckling	40
2.4.4 Numerical investigation	42
<i>2.5 Interaction of buckling modes</i>	<i>43</i>
2.5.1 General description	43
2.5.2 Interaction between local and overall buckling	43
2.5.3 Interaction between local and distortional buckling	44
<i>2.6 Evaluation of the existing literature on stability</i>	<i>45</i>

3	Experimental investigation on cross-sectional stability of aluminium extrusions	47
	<i>Chapter abstract</i>	47
3.1	<i>Summary of existing experimental work</i>	49
3.1.1	General	49
3.1.2	Salerno (SHS, RHS, US)	49
3.1.3	Helsinki (RHS, CS)	50
3.2	<i>Executed tests – Eindhoven program</i>	51
3.2.1	Test series	51
3.2.2	Dimensions and geometrical properties	54
3.3	<i>Test set-up</i>	56
3.3.1	Methods of testing	56
3.3.2	Test set-up Eindhoven experimental program	58
3.3.3	Test equipment	59
3.4	<i>Imperfection measurements</i>	60
3.4.1	Imperfection measurements on rectangular hollow and U-sections	60
3.4.2	Imperfection measurements on complex cross-sections	61
3.4.3	Determination of the imperfection amplitude	62
3.4.4	Results imperfection measurements	64
3.5	<i>Material characteristics</i>	65
3.5.1	Test set-up tensile tests	65
3.5.2	Determination of tensile test results	66
3.5.3	Remarks	69
3.6	<i>Results compression tests</i>	69
3.6.1	Deformation patterns and failure modes	69
3.6.2	Axial strength	72
3.6.3	Axial stiffness	74
3.7	<i>Observations with respect to experimental research on stability</i>	75
4	Numerical research	77
	<i>Chapter abstract</i>	77
4.1	<i>Executed FE-analyses</i>	79
4.1.1	General	79
4.1.2	Applied imperfections	79
4.1.3	Applied material characteristic	80
4.2	<i>Set-up finite element model</i>	81
4.2.1	Mesh	81
4.2.2	General calculation procedure	83

4.3	<i>Parameter analyses</i>	85
4.3.1	General	85
4.3.2	Experimental input	85
4.3.3	Mesh density	86
4.4	<i>Results FE-analyses</i>	87
4.4.1	Deformation patterns and failure modes	87
4.4.2	Axial strength	89
4.4.3	Axial stiffness	92
4.4.4	Determination of the characteristic FE-results	93
4.5	<i>Comparison of experimental and FE-results</i>	93
4.5.1	Overview of results	93
4.5.2	Comparison of bifurcation and failure loads	96
4.5.3	Observations	98
5	Investigation of plate buckling and local buckling of cross-sections	
	- Development of a general prediction model	99
	<i>Chapter abstract</i>	<i>99</i>
5.1	<i>General</i>	<i>101</i>
5.2	<i>Elastic plate buckling</i>	<i>103</i>
5.2.1	Elastic buckling of simply supported plates	103
5.2.2	Elastic buckling of clamped plates	107
5.2.3	Elastic buckling of outstands	108
5.2.4	Evaluation of elastic plate buckling	109
	<i>Summarising procedure for elastic plate buckling</i>	<i>112</i>
5.3	<i>Inelastic plate buckling</i>	<i>113</i>
5.3.1	Material characteristic	113
5.3.2	Theory	114
5.3.3	Actual behaviour	117
5.3.4	Evaluation of inelastic plate buckling	119
	<i>Summarising procedure for inelastic plate buckling</i>	<i>121</i>
5.4	<i>Elastic local buckling of cross-sections</i>	<i>122</i>
5.4.1	Square hollow sections (SHS)	122
5.4.2	Rectangular hollow sections (RHS)	123
5.4.3	I-sections (IS)	126
5.4.4	Theory – Local buckling modes	130
5.4.5	Evaluation of elastic local buckling of cross-sections	134
	<i>Summarising procedure for elastic local buckling of cross-sections</i>	<i>139</i>

5.5	<i>Inelastic local buckling of cross-sections</i>	141
5.5.1	Rectangular hollow sections (RHS)	141
5.5.2	I-sections (IS)	143
5.5.3	Inelastic local buckling of actual cross-sections	145
	<i>Summarising procedure for inelastic local buckling of cross-sections</i>	147
6	Validation of the developed prediction model	151
	<i>Chapter abstract</i>	151
6.1	<i>Determination of representative experiments</i>	153
6.2	<i>Comparison of the prediction model with test results</i>	156
6.3	<i>Development of design rules</i>	160
7	Conclusions and recommendations	161
7.1	<i>Conclusions</i>	161
7.2	<i>Recommendations for further research</i>	163
	<i>Literature</i>	165
	Appendix A - Results of the Salerno and Helsinki experiments	175
A.1	Geometry of the Salerno program	175
A.2	Test results of the Salerno program	177
A.3	Geometry and test results of the Helsinki program	179
	Appendix B - Results of the Eindhoven program	181
B.1	Cross-sectional properties RHS and US specimen	181
B.2	Cross-sectional properties CS specimen	182
B.3	Experimental results	188
B.4	Numerical results	190
B.5	Results prediction model	192
	Appendix C - Comparison of experimental, numerical and predicted results	195
	<i>Samenvatting</i>	209
	<i>Curriculum Vitae</i>	211

List of symbols and abbreviations

A	cross-sectional area	mm^2
D	plate stiffness parameter	N/mm^2
E	modulus of elasticity	N/mm^2
E_c	modulus of elasticity measured from compression tests	N/mm^2
E^*	tangential stiffness	N/mm^2
E_{th}^*	theoretical tangential post-buckling stiffness at initial buckling	N/mm^2
E_{pm}^*	predicted tangential post-buckling stiffness	N/mm^2
E_T	tangential stiffness of the inelastic material characteristic	N/mm^2
I_{11}, I_{22}	second moment of inertia around the principal, respectively secondary axis	mm^4
I_{xx}, I_{yy}	second moment of inertia around the x-, respectively y-axis	mm^4
I_T	torsional rigidity	mm^4
L	axial length of the specimen	mm
L_{cr}	critical buckling length	mm
N	reaction force / axial resistance	N
N_{cr}	critical axial load at initial buckling	N
$N_{cr,E}$	critical load of the Euler column	N
$N_{cr,T}$	critical tangent-modulus load	N
N_d	axial design strength	N
N_{pm}	predicted axial resistance	N
N_r	reduced modulus load	N
N_u	ultimate or failure load	N
N_t	axial load at which tensile stresses occur at the supports	N
$N_{0.2}$	axial squash load ($= f_{0.2} \cdot A$)	N
b	plate width	mm
b_{eff}	effective plate width	mm
e_0	amplitude of the initial imperfections	mm
$e_{0,ov}$	amplitude of the initial overall imperfections	mm
$e_{0,loc}$	amplitude of the initial local imperfections	mm
$f_{0.1}$	0.1% proof strength of the material characteristic	N/mm^2
$f_{0.2}$	0.2% proof strength of the material characteristic	N/mm^2
f_p	proportional limit of the material characteristic	N/mm^2

f_y	yield stress of bi-linear materials	N/mm ²
k_{cr}	plate buckling coefficient	-
n	Ramberg-Osgood strain-hardening parameter	-
n_{cr}	number of buckling half-waves	-
p	lateral distributed load on plates	N/mm ²
t	plate thickness	mm
u	axial shortening of the specimen	mm
v	in-plane plate deformations	mm
w	out-of-plane deflections	mm
w_0	initial out-of-plane deflections	mm
w_{rel}	relative out-of-plane deflections	-
$w_{0,rel}$	relative initial out-of-plane deflections	-
χ_T	inelastic buckling coefficient	-
$\Delta\sigma$	load eccentricity	N/mm ²
ε	axial strain	-
ε_{av}	average axial strain	-
$\underline{\varepsilon}_{av}$	non-dimensionalised axial strain with respect to initial buckling ($=\varepsilon_{av}/\varepsilon_{cr}$)	-
$\underline{\varepsilon}_{av,2}$	non-dimensionalised axial strain with respect to secondary buckling ($=\varepsilon_{av}/\varepsilon_{cr,2}$)	-
ε_{cr}	elastic critical strain at initial buckling ($=\sigma_{cr}/E$)	-
ε_p	elastic strain according to the proportional limit of the material	-
$\varepsilon_{cr,2}$	elastic critical strain at secondary buckling ($=\sigma_{cr,2}/E$)	-
$\varepsilon_{cr,T}$	inelastic critical strain at initial buckling	-
η	plasticity reduction factor	-
φ	plate slenderness parameter	-
ν	Poisson's ratio	-
$\bar{\lambda}$	relative slenderness	-
ρ_u	non-dimensionalised ultimate load	-
σ	axial stress	N/mm ²
σ_{av}	average axial stress	N/mm ²
$\underline{\sigma}_{av}$	non-dimensionalised axial stress at initial buckling ($=\sigma_{av}/\sigma_{cr}$)	-
$\underline{\sigma}_{av,2}$	non-dimensionalised axial stress at secondary buckling ($=\sigma_{av}/\sigma_{cr,2}$)	-
σ_{cr}	elastic critical stress at initial buckling	N/mm ²

$\sigma_{cr,T}$	inelastic critical axial stress at initial buckling	N/mm ²
$\sigma_{cr,2}$	elastic critical stress at secondary buckling	N/mm ²
$\sigma_{cr,2,T}$	inelastic critical stress at secondary buckling	N/mm ²
σ_{max}	maximum axial stress at the unloaded plate edges	N/mm ²
σ_p	elastic stress according to the proportional limit of the material	N/mm ²
σ_{pb}	predicted average axial stress with respect to post-buckling	N/mm ²
σ_{pm}	predicted average axial stress	N/mm ²
σ_u	maximum value of the average axial stress	N/mm ²

CS	complex cross-section
FE	finite element
FS	finite strip
HAZ	heat-affected zone
IS	I-section
RHS	rectangular hollow cross-sections
SHS	square hollow cross-sections
US	U-section
TUE	Eindhoven University of Technology

pg	plate group
pl	plate
pm	prediction model
mat	typical material characteristic
sec	section
T	inelasticity

I Introduction and thesis outline

Chapter abstract

This chapter outlines the background, scope and research approach used within this research. Focusing on cross-sectional instability of aluminium extrusions, it shows that the current design rules are based on simple cross-sections that are by no means representative for the very complex cross-sectional shapes applied in daily practice. This urges the investigation of the actual behaviour of those cross-sections and the subsequent development of a general prediction model.

1.1 Aluminium extrusions in structural applications

Aluminium extrusions are widely used in structural applications and transportation, including load-bearing structures, roof claddings, helicopter platforms, bridges, and greenhouses, as well as trucks, trains, ships and aeroplanes. The choice for aluminium is in almost all situations derived from its flexibility, as both material and shape can be designed to match the requirements of each specific situation. Summarised:

- The weight of the structure itself is often the main load in case of large spans (roof structures, bridges). Because of its low unit mass, application of aluminium reduces weight that subsequently leads to a vast reduction of material. Weight decrease may also be used to increase the allowable live load, which is the key aspect in transportation as well as bridge renovation. Additional advantages are the reduction of operating, assembly, and transportation costs.
- The extrusion manufacturing process provides an almost infinite range of possible cross-sectional shapes, as shown in Figure 1-1. Limitations to the size and shape of the cross-section are mainly based on the capacity of the extrusion press and the complexity, and thus the cost, of the extrusion dies. The designer can thus freely add additional functions to the extrusion, like stiffeners and weld backings, or to accommodate connections.
- When exposed to air, aluminium immediately forms a tight oxide-layer. Thus, most alloys are not susceptible to ongoing corrosion, even in extreme environments. For example, aluminium has been used successfully on offshore platforms for decades without the use of protective layers.

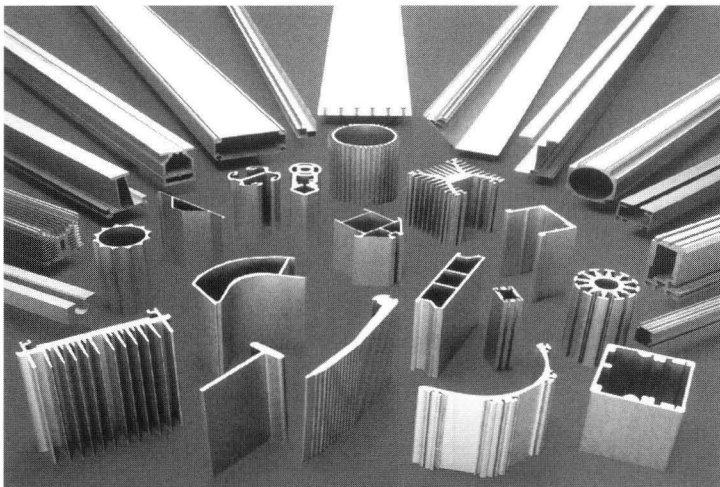


Figure 1-1 Examples of complex aluminium extrusions

These positive aspects show a very useful material. However, each material also has its inherent restrictions.

- The modulus of elasticity ($E = 70000 \text{ N/mm}^2$) of aluminium is only one third of that of steel. Thus, more material is necessary to fulfil comfort requirements based on structural stiffness. In addition, the so-called critical (Euler) stresses reduce linearly with the modulus of elasticity, making aluminium cross-sections more susceptible to instability (buckling).
- Temperature increases may substantially reduce the material strength and nullify heat-treatments. Welding results in a substantial reduction of the strength of both the weld itself as well as that of the material in the heat affected zone (HAZ). The design of the weld and the choice of weld material is thus a decisive design criterion. Furthermore, special provisions have to be taken with respect to fire resistance.
- Finally, the costs per kilogram of aluminium are higher than those of steel are. Optimisation, i.e. minimising of cross-sectional area or inclusion of additional functions, is thus an important part of the design process.

Though these negative aspects seem rather demanding, in most cases taking optimal advantage of the freedom of cross-sectional shape can compensate them. For example: extruded stiffeners can prevent stability problems, optimisation can minimise the cross-sectional area, while welds can be relocated to less stressed areas. Thus, optimisation is an important part of the design process. In practice, it often results in thin-walled extrusions with complex cross-sectional shapes.

1.2 Buckling of axially compressed aluminium extrusions

The previous section explained that practical extrusions are often thin-walled with complex cross-sectional shapes. Combined with the moderate value of E it must be concluded that the load-bearing capacity of an extrusion is often determined by instability (buckling) phenomena. In general, a distinction can be made between overall- and cross-sectional instability, though interaction may occur.

An important buckling mode is that of individual plate elements. This phenomenon is referred to as plate buckling:

- *Plate buckling* describes the buckling behaviour of compressed individual plates. With respect to this thesis, the term is used only with respect to the behaviour of long flat rectangular plates that are loaded axially into uniform compression. Various edge constraints may be considered, though they should be constant over the specimen length and load-independent.

With respect to the buckling behaviour of axially compressed aluminium extrusions, the following definitions are used to describe overall instability:

- *Flexural or column buckling* represents the situation wherein a perfect elastic axially loaded column deflects sideways at the critical load, while the shape of the cross-section remains unaltered.
- Comparably, *torsional buckling* represents the case where instability occurs due to rotation of the column around its shear centre.
- *Flexural-torsional buckling* results in both axial deflections and rotations. This mode occurs when the centre of load application does not coincide with the shear centre.

Finally, cross-sectional instability refers to buckling patterns that result in a deformation of the cross-section. Cross-sections susceptible to this type of instability often consist of slender plates that are connected at nodes. Two examples are presented in Figure 1-2. The upper figures present the undeformed cross-sections, while the lower figures include the deformed cross-sections. It can be seen that while some connecting nodes remain in place, others translate. As this may cause a significantly different behaviour, a distinction is made between local and distortional buckling:

- *Local buckling* refers to buckling patterns of the cross-section where each connecting node remains essentially in place. The distinction with plate buckling is made while though the supporting effect of the connecting plates may resemble specific edge restraints it is not load-independent.
- *Distortional buckling* refers to buckling patterns of the cross-section where at least one connecting node translates.

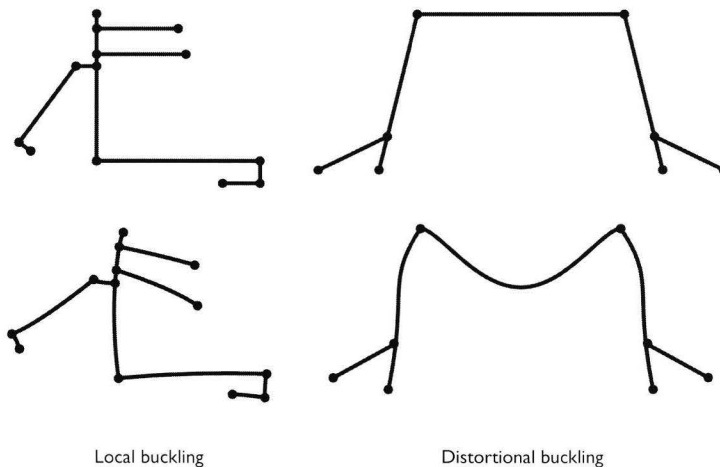


Figure 1-2 Cross-section instability – Local and distortional buckling

Though plate buckling and overall stability is relatively well accounted for in design codes, it will be shown that cross-sectional instability is not. Design rules for local buckling of cross-sections (see Chapter 2) are based on the theoretical solutions of the plate-buckling problem, empirically fitted to tests. This approach has proven itself for most traditional cross-sectional shapes like rectangular hollows, I-sections, U-sections, and hat-sections. However, as shown in Chapter 5, they do not represent the actual behaviour as they neglect plate interactions. As such it is unknown if they provide conservative, let alone accurate, results for arbitrary cross-sectional shapes.

Design rules for distortional buckling are limited to a few specific cases. For example, Eurocode 9 (CEN 1999) provides design rules only for flanges with edge stiffeners and webs with one or two intermediate stiffeners. Though steel design codes like Eurocode 3 (CEN 1993) provide design rules for some additional geometries, these rules tend to become very complicated and time-consuming with an increasing complexity of the cross-sectional shape.

In addition to the individual modes, interaction between local and overall buckling is hardly investigated, but rather drastically incorporated (see section 2.5.2). Again, research is limited to traditional cross-sections. Thus, it can be concluded that the existing design rules for instability are limited with respect to cross-sectional instability; only a very limited range of cross-sections is covered and only with a limited accuracy. The contrast with the complexity of cross-sections used in practice is manifest. Without validated and conservative design rules, daily practice might lead to disturbingly inaccurate and even unsafe results.

1.3 Problem statement, research goal and limitations

Section 1.1 concluded that aluminium extrusions often consist of thin-walled, complex cross-sectional shapes. Section 1.2 demonstrated that existing design rules for cross-sectional instability are mainly limited to local buckling of relatively simple cross-sections, while validated on even fewer sections. This results the following problem statement:

The actual cross-sectional instability behaviour (local and distortional buckling) of aluminium extrusions with arbitrary cross-sectional shapes is unknown. Application of the current design rules may therefore be inefficient (overly conservative) or even unsafe.

This statement is further elaborated into three sub-statements:

- Insight into cross-sectional instability is generally limited to a prediction of initial buckling. The actual post-buckling behaviour of cross-sections is in most cases unknown.
- Design rules for cross-sectional instability are validated on the local buckling capacity of traditional cross-sections. However, the actual behaviour of complex cross-sections is unknown, as no general model exists for distortional buckling. Calculated design loads might result overly conservative or even unsafe results
- Design rules regarding interaction between cross-sectional and overall instability are again based on the modelled local buckling behaviour of traditional cross-sections. As this behaviour is modelled inaccurately and neglects distortional buckling, questions arise about the accuracy of these interaction formulae.

Making a distinction between insight, design practice, and future development results the following research goals:

- To obtain insight into the actual cross-sectional instability behaviour of thin-walled aluminium extrusions with complex cross-sectional shapes. Though focusing on local buckling, interaction with distortional and overall buckling is addressed briefly.
- To develop a general prediction model for the actual load-bearing capacity of aluminium extrusions due to local buckling of the cross-section, validated for a wide range of cross-sectional shapes.
- To open the possibilities to incorporate interaction of distortional and overall buckling into the newly developed, or existing prediction models.

In addition, some research limitations have been set. Uniform compressed aluminium extrusions of 6000-alloys are studied using cross-sections mainly consisting of plate elements. The influence of stress-gradients due to bending, and the shift of both the gravity and shear centre is not accounted for; neither is that of residual strains. A cross-section consisting of plate elements will be reduced to its heart lines with thickness properties. The influence of additional elements, like angle radii and small extensions, is not taken into account. Thus, the resulting prediction model is comparable with existing models for cross-sectional instability, for example like those used in Eurocode 9 (CEN 1999), or the Specifications for aluminium structures, (AA 1994).

1.4 Research approach and thesis outline

To obtain the presented research goals, the research approach of Figure I-3 is followed. Subsequent to the first two chapters, consisting of introduction and literature survey, the thesis outline roughly follows the research approach; the respective chapter numbers are included in the figure.

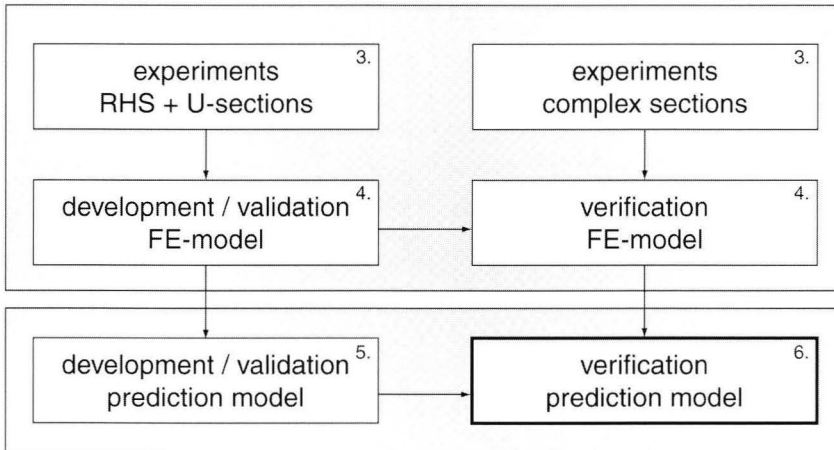


Figure I-3 Research approach PhD-thesis

The experimental data consist of data obtained from literature as well as a substantial experimental program executed within the scope of this thesis. Uniformly compressed columns have been investigated with three types of cross-sections:

- Rectangular hollows (RHS); in order to validate the experimental set-up as well as to obtain insight in, and data on, the actual local buckling behaviour of cross-sections containing internal plates (“webs”).
- U-sections (US); relatively simple cross-sections to verify the local buckling behaviour of and design rules for outstands (“flanges”) and the influence of their supporting webs.
- Complex sections (CS); these tests are executed to extend existing test data with the local buckling behaviour of a wide range of cross-sections, as well as to include distortional buckling. These tests give insight in the behaviour and specific buckling problems of complex cross-sections, including interaction between plates of various types and dimensions.

To obtain detailed information about the actual instability behaviour of cross-sections, the finite element (FE) method has been used to simulate the experiments. Once validated, the FE-model has been used to execute a parameter analysis on specific buckling aspects like shape, plate slenderness, and material influences. A distinction is made between the development/validation of the FE-model and its verification. Development and validation occurred on the RHS and US experiments and includes some fine-tuning of, for example, loading conditions, load step size, and mesh-fineness. From a hypothetical point of view, the suitability of the FE-model is therefore only validated for the regarded range of experiments. While the experiments cover a wide range of RHS and U-sections, such a view is of no practical consequence. It is impossible to fully cover the entire range of arbitrary cross-sectional shapes. Therefore, the accuracy and validity of the (unaltered) FE-model was determined from a comparison of its results with those of the experiments on complex sections. It is assumed that thus, application of the FE-model is verified for arbitrary cross-sections.

The development of the prediction model for local buckling is based on the results of a parameter study executed with the FE-model. As will be presented, the observed behaviour shows a remarkable coincidence with plate buckling specifics; thus obtaining an almost analytical background. The prediction model is developed with respect to the FE-results of analyses on RHS and I-sections and verified to the experimental results.

2 State of the art – stability behaviour

Chapter abstract

This chapter aims at a thorough description of existing literature related to the stability behaviour of unwelded aluminium extrusions. It describes results, insights and validity ranges of theories and design approaches. Though the focus of the thesis is on cross-sectional instability, this chapter discusses as well: the general theory of instability, column buckling, plate buckling, and mode interaction. Thus, it provides an overview of the available existing knowledge, outlining the basis for a general understanding of the actual cross-sectional instability behaviour of complex aluminium extrusions.

2.1 Theory of elastic stability - Bifurcation buckling

2.1.1 Definitions

It is assumed that the concept of elastic stability and terms like critical stress and bifurcation buckling are familiar to the reader. Nevertheless, to obtain a clear insight into the theory of elastic stability, sections 2.1.2 and 2.1.3 present several simple illustrative examples that are largely based upon the book by Galambos (1998). This section starts with providing some definitions with respect to elastic stability, freely based on some well-known references like: Timoshenko and Gere (1960), Allen and Bulson (1980), Mazzolani (1985), Galambos (1998), and Yu (2000).

- *Bifurcation buckling, bifurcation of equilibrium, or merely buckling* occurs when a perfect member, subjected to an increasing compressive load, initially deforms in one mode and then, at a load referred to as the critical load, suddenly deflects into a different deformation pattern. Axially compressed columns, plates, and cylindrical shells experience this type of instability. The associated modes have been explained in section 1.2.
- The *critical or buckling load* of a compression member represents the moment of bifurcation. However, obtained from the linear elastic analysis of an idealized perfect member, it does not necessarily coincide with the failure load of an actual member.
- The *maximum or failure load* represents the load at which collapse of a real, inelastic and imperfect, member occurs. To determine the failure load it is necessary to consider the entire non-linear load-deflection curve of the actual member, including actual imperfections, residual stresses, and (inelastic) material characteristics.
- In specific cases, failure may occur at loads beyond initial buckling. This phenomenon is referred to as *post-buckling strength*. Notably, failure of axially compressed plates may occur at loads up to four times as large as the critical load because of post-buckling capacity.

2.1.2 Initially perfect systems

A general understanding of bifurcation buckling, including the elastic critical load and post-buckling behaviour, can be obtained by considering the simple model in Figure 2-1. The model consists of two rigid bars that are hinged to each other and to the supports, and are restrained laterally by a non-linear elastic spring. Similar models are commonly used in literature, for example: Hoff (1966) and Galambos (1998).

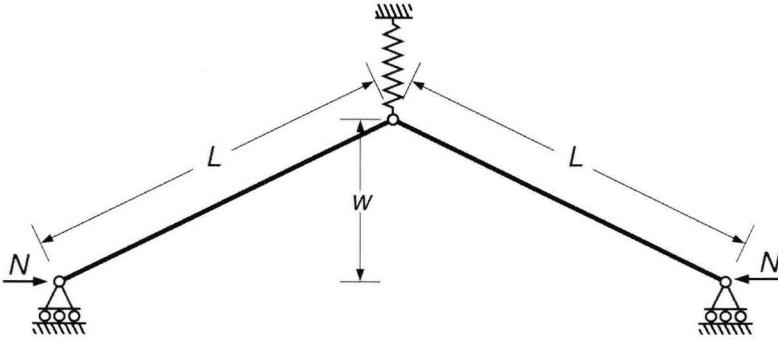


Figure 2-1 Explanation of Initially perfect systems

Obviously, the forces N are in balance as long as there is no deflection w . The deflection is presented by its non-dimensional equivalent w_{rel} according to:

$$w_{rel} = \frac{w}{L} \quad \text{eq. 2-1}$$

Once deflections occur, the non-linear spring results in a reaction force V . Note that the used presentation of the spring characteristics is merely to illustrate the possible buckling behaviour of structures.

$$V = c_1 w_{rel} + c_2 w_{rel}^2 + c_3 w_{rel}^3 \quad \text{eq. 2-2}$$

Equilibrium in a deflected configuration requires that:

$$N w = \frac{V}{2} \sqrt{L^2 - w^2} \quad \text{eq. 2-3}$$

Substitution of V and w_{rel} results in:

$$N w_{rel} = \frac{1}{2} (c_1 w_{rel} + c_2 w_{rel}^2 + c_3 w_{rel}^3) \sqrt{1 - w_{rel}^2} \quad \text{eq. 2-4}$$

This equation reduces for infinitely small values of w_{rel} to the critical load N_{cr} :

$$N_{cr} = c_1 / 2 \quad \text{eq. 2-5}$$

Based on the work of Koiter (1945), it has been demonstrated that the essential characteristics of the post-buckling behaviour of a member are determined at the initial stages of buckling. Thus, w_{rel} is assumed small but finite, reducing equation 2-4 to:

$$N w_{rel} = \frac{1}{2} (c_1 w_{rel} + c_2 w_{rel}^2 + c_3 w_{rel}^3) \quad \text{eq. 2-6}$$

Substitution of N_{cr} and simplification results in:

$$N = N_{cr} (1 + C_2 w_{rel} + C_3 w_{rel}^2) \quad \text{eq. 2-7}$$

where

$$C_2 = c_2 / c_1 \quad \text{and} \quad C_3 = c_3 / c_1 \quad \text{eq. 2-8}$$

The corresponding load-deflection curves are presented in Figure 2-2. This type of behaviour is referred to as bifurcation buckling. The figures show that no deflections occur until N_{cr} is reached, at which they occur suddenly.

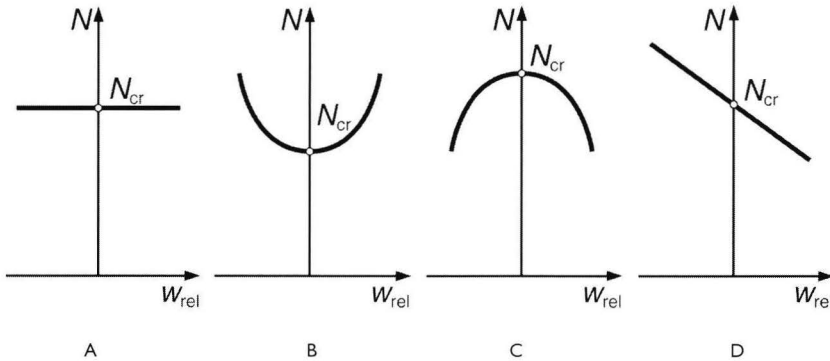


Figure 2-2 *Buckling curves of initially perfect systems:*
A - Neutral equilibrium, B - Stable symmetric buckling,
C - Unstable symmetric buckling, and D - Asymmetric buckling

Four different types of buckling have been specified:

- Figure 2-2A presents the most simple case of *neutral equilibrium* that occurs when $C_2 = C_3 = 0$. As long as N is less than N_{cr} , no deflections w_{rel} occur. However, w_{rel} becomes undefined once N_{cr} is reached. A common example is the initial buckling behaviour of axially compressed columns.

- Two modes are possible for structures behaving in a symmetrical manner ($C_2 = 0$); that is, the buckling characteristics are the same regardless of whether the deflection is positive or negative. A positive value of C_3 results in curve B, a negative value in curve C. These types are called *stable*, respectively *unstable symmetric buckling*. Structures that exhibit a stable behaviour are generally considered as safe, for example the behaviour of uniformly compressed plates. Unstable behaviour may result in the sudden failure of a structure. The most notorious example of such behaviour is that of an axially compressed cylindrical shell.
- It is also possible that structures are susceptible to *asymmetric buckling* ($C_2 \neq 0$), for $C_3 = 0$ this is presented by curve D. The structure is either stable or unstable, depending on the direction of the deflection. Examples of such structures can be found in frame analysis (e.g. Galambos 1998) or the lateral-torsional buckling behaviour of U-sections.

An understanding of these four equilibrium types is essential in the determination of design methods based on safety concepts.

2.1.3 Initially imperfect systems

Analysis of an initially perfect system results the critical load, the post-buckling curve, and thus the type of equilibrium. However, initial imperfections and load eccentricities that are present in all actual structures can result in a substantial deviation from the perfect curves of Figure 2-2.

If the model of the previous section has an initial imperfection $w_{0,rel}$ ($= w_0/L$), equation 2-4 takes the following form:

$$N(w_{rel} + w_{0,rel}) = \frac{1}{2}(c_1 w_{rel} - c_2 w_{rel}^2 + c_3 w_{rel}^3) \quad \text{eq. 2-9}$$

Which, using C_2 and C_3 according to equation 2-8, can subsequently be rewritten as:

$$N = \frac{N_{cr}(w_{rel} - C_2 w_{rel}^2 + C_3 w_{rel}^3)}{w_{rel} + w_{0,rel}} \quad \text{eq. 2-10}$$

The dashed lines in Figure 2-3 represent the resulting elastic load deflection curves. The results of the perfect model, as presented in Figure 2-2, are presented as well.

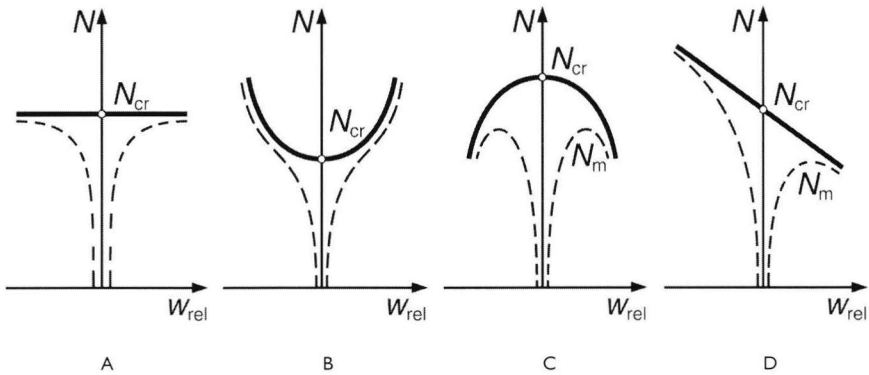


Figure 2-3 Buckling curves of initially perfect (full lines) and imperfect (dashed) systems: A - Neutral equilibrium, B - Stable symmetric buckling, C - Unstable symmetric buckling, and D - Asymmetric buckling

Evidently, small imperfections have no significant influence on the behaviour of systems with stable (and neutral) post-buckling curves. These members can resist increasing loads without failure taking place. However, imperfections have a very marked effect on systems with unstable and asymmetric post-buckling curves. These systems may fail at a maximum load N_m that is well below the critical load N_{cr} . These structures are accordingly referred to as imperfection sensitive.

The actual post-buckling strength depends on two factors: the steepness of the post-buckling curves, and the magnitude of the critical load versus that of yield initiation. For example, axially compressed plates possess a relatively steep post-buckling curve and consequently exhibit sizable post-buckling strength. Failure loads three to four times as large as the critical load have been obtained (Gerard 1957). The post-buckling curve of axially compressed columns is extremely shallow. Thus, failure coincides, for symmetrical cross-sections, approximately with the minimum of the elastic critical load or else the cross-sectional capacity due to yielding.

In conclusion, it is evident that the behaviour of imperfect members can be predicted from the shape of the post-buckling curve for perfect systems. Members with stable post-buckling curves will fail at loads equal or higher than the critical load, whereas members with unstable post-buckling curves will fail at loads below the critical load. This is also the most widely used path to determine the actual buckling behaviour of structures: the design load of a structure is determined as a function of its critical load.

2.2 Centrally loaded columns – Column buckling

The strength of axially loaded columns is characterised by the maximum axial force that can be supported without excessive deflections. As presented, the column strength is determined by yielding, overall instability, or cross-sectional instability; note that interactions might occur. The strength of metallic columns has been studied extensively over the past centuries. For detailed information is referred: Timoshenko and Gere (1960), Allen and Bulson (1980), Mazzolani (1985), Galambos (1998), and Yu (2000). Though this thesis focuses on cross-sectional instability, this section presents a limited survey of column buckling of unwelded, extruded, aluminium columns.

2.2.1 General description

All theories and design criteria for column buckling are based on the original work by Euler, as described by e.g. Timoshenko and Gere (1961). The Euler column is a mathematically straight, prismatic, pin-ended, perfectly centrally loaded strut with linear elastic material behaviour. The well known *critical* or *Euler load* is described by:

$$N_{cr,E} = \frac{\pi^2 E I_{11}}{L^2} \quad \text{eq. 2-11}$$

Where E is de modulus of elasticity, I_{11} is the second moment of inertia of the cross-section around the principal axis and L is the column length.

As explained in section 2.1.3, the critical load can be used to predict the failure load of an Euler column. However, columns used in daily practice are not perfectly straight, are part of a frame with end restraints and loading, and include non-linear material characteristics as well as residual stresses. Obviously, the influence of each of these aspects has to be studied in order to determine the actual failure load.

If end conditions other than perfectly frictionless pins can be defined mathematically, the expression of the critical load may be more generally expressed by:

$$N_{cr} = \frac{\pi^2 E I_{11}}{L_{cr}^2} \quad \text{eq. 2-12}$$

Where L_{cr} is the *critical length*, defining that part of the deflected shape of the column between points of zero curvature. In other words, L_{cr} is the length of an equivalent pin-ended column. The general approach for column buckling is to determine the failure or design load as a function of this critical load.

Equation 2-12 for the critical column strength is valid as long as the material is still elastic when buckling occurs. Such columns are described as *slender* columns. As explained in section 2.1.3, a stable equilibrium configuration is possible at N_{cr} , even if lateral deflections w occur, see Figure 2-4A. The resulting load-deflection path O-A-B is visualised in Figure 2-4B. Even in the presence of an initial deflection, w_0 , the maximum load will approach the Euler load asymptotically (curve C), as long as the material remains elastic.

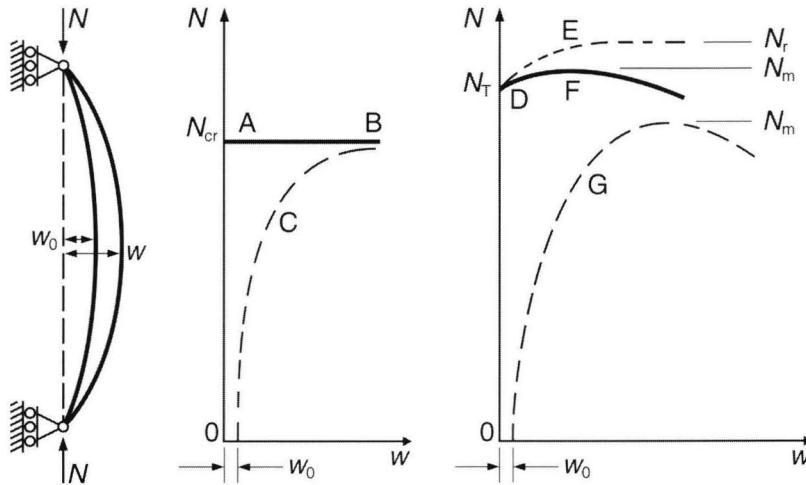


Figure 2-4 Behaviour of perfect (full lines) and imperfect (dashed) columns

For very short and compact columns, it is well known that the column may fail due to yielding. A lower bound for the column strength may be simply determined by $N = A f_p$. Where A is the cross-sectional area of the column and f_p is the proportional limit of the material characteristic. Note that for steel f_p equals the yield stress f_y , while for aluminium it may be substantially less than the 0.2% proof stress $f_{0.2}$, as will be explained in section 2.2.2. In order to determine the influence of yielding on initial buckling, the relative column slenderness $\bar{\lambda}$ is defined:

$$\bar{\lambda} = \sqrt{\frac{N_{cr,E}}{A f_y}} \quad (\text{for steel}) \quad \text{or} \quad \bar{\lambda} = \sqrt{\frac{N_{cr,E}}{A f_{0.2}}} \quad (\text{for aluminium}) \quad \text{eq. 2-13}$$

Many practical columns are in a range of slenderness where portions of the column are no longer elastic at buckling. As elasticity is one of the key assumptions underlying Euler column buckling, the theory is violated. Essentially, yielding reduces the stiffness of the column. This degradation of the stiffness may be the result of a non-linearity in the material itself (e.g., aluminium, which has a non-linear stress-strain curve), or it may be due to partial yielding of the cross-section at points of compressive residual stress (e.g. rolled steel shapes). The post-buckling behaviour of such a column is radically different from the elastic column. Shanley (1947) was the first to grasp this phenomenon successfully. Bifurcation buckling occurs at the critical tangent-modulus load, $N_{cr,T}$, described by equation 2-14 and point D in Figure 2-4. Where E_T is the tangent modulus of the non-linear stress-strain relation of the material, see Figure 2-5.

$$N_{cr,T} = \frac{\pi^2 E_T I_{11}}{L_{cr}^2} \quad \text{eq. 2-14}$$

Lateral deflections cause bending stresses that are only possible if the load increases. If there were no further changes in stiffness due to yielding ($E_T = E_{cr,T}$), the load would asymptotically approach a reduced-modulus load N_r (line E). Since increased loading beyond the tangent modulus load results in further yielding, stiffness continues to be reduced and the load-deflection curve achieves the ultimate or failure load N_u at point F, beyond which it falls off. Thus a perfect inelastic column will begin to deflect laterally when $N = N_{cr,T}$ and reach a maximum higher than $N_{cr,T}$ but less than N_r .

Geometric imperfections, in the form of unavoidable out-of-straightness of the column and/or eccentricity of the axial load, introduce bending from the onset of loading. Curve G of Figure 2-4 characterises the performance of such a column. Lateral deflection exists from the start of the load and the maximum load is reached when the moment capacity at the critical cross-section is equal to the external moment caused by the product of the load and the deflection. Though for some columns the maximum load is closely approximated by the tangent modulus load $N_{cr,T}$, for many types of columns the imperfections have to be included in the analysis to give a realistic maximum load.

2.2.2 Column buckling - Inelastic materials

Physical imperfections may cause a substantial deviation between the critical load and failure load. These imperfections arise as a natural property of the material, due to residual stresses, or due to local change in yield strength caused by welding.

The material characteristic of aluminium alloys is non-linear, and depends on the type of alloy and heat-treatment. Fortunately, research by Bernard et al. (1973) concluded that the value of the 0.2% proof strength $f_{0.2}$ does not vary significantly throughout of a profile. The simplest approach is a piecewise representation of the stress-strain relationship, by using a bi- or tri-linear curve. This approach has been allowed in different codes, for example the Eurocode 9 (CEN 1999). It is usually convenient to identify three separate regions, see Figure 2-5: (1) Elastic behaviour, (2) Inelastic behaviour, and (3) Strain-hardening behaviour. Different approaches, offering continuous models, are developed by: Sutter (1959), Baehre (1966) and Mazzolani (1972).

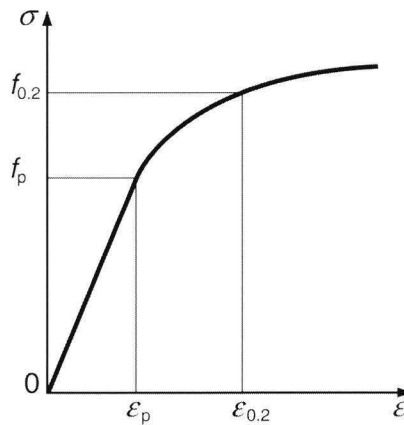


Figure 2-5 Representation of the material characteristic of aluminium alloys

However, because of its excellent agreement with tests, the currently generally applied approach is the Ramberg-Osgood law (1943). As described by Mazzolani (1985), The Ramberg-Osgood law was used to represent the stress-strain (σ - ε) relation in the following form:

$$\varepsilon = \frac{\sigma}{E} + 0.002 \left(\frac{\sigma}{f_{0.2}} \right)^n \quad \text{eq. 2-15}$$

The exponent n characterises the strain-hardening rate. For example, when n tends to infinity, the equation represents the behaviour of mild steel. When the Ramberg-Osgood law is used in specifications, the practical problem arises how to determine n . As the inelastic range is the most important part of the stress-strain relation, it is good

practice to fit the Ramberg-Osgood relation for the 0.1% proof stress $f_{0.1}$. The value of n can be obtained by substitution of $f_{0.1}$ into equation 2-15 for σ and its corresponding strain $\varepsilon_{0.1}$ ($=f_{0.1}/E + 0.001$) for ε . However, as $f_{0.1}$ is not specified in the codes, two approaches have been used. Steinhardt's suggestion (1971) that n is equal to the value of the yield strength in kN/cm^2 gives close agreement with test results. Mazzolani (1974) suggested an approach based on the ultimate strength and the elongation at rupture. The current version of the Eurocode 9 (CEN 1999) applies Steinhardt's suggestion.

Residual stresses in aluminium extrusions are small, because of the extrusion manufacturing process of aluminium and the subsequent straightening of the finished member by stretching. Note that substantial residual stresses may occur in cold-formed aluminium cross-sections. The fact that the influence of residual stresses on column strength of extruded aluminium members is insignificant has been confirmed by European studies (Mazzolani and Frey 1977).

For most alloys used in structural applications, welding-heat reduces the strength of the metal in a narrow zone around the weld. Thus, the capacity of columns of low and intermediate slenderness ratios $\bar{\lambda}$ is reduced. It also introduces (locally) residual stresses and causes initial curvatures of the column. The influence of welding is not investigated in this thesis. For more information, one is referred to literature like Mazzolani (1985) or Lai and Nethercot (1992).

2.2.3 Column buckling - Imperfections

Four major types of geometrical imperfections may occur: initial deflections and curvature, load eccentricities, eccentricities due to asymmetric cross-sections, and thickness deviations. Obviously, interaction between these types may occur, as well as interaction with the inelastic material behaviour.

Research analysing the strength of inelastic, initially curved columns either have made use of assumed values and shapes of the initial out-of-straightness, or have used actually measured data. The first approach is the most common, as available measurements on the amplitude and shape of column imperfections are scarce. The generally used approach is to apply a half-sine, Figure 2-4, over the length of the pin-ended column: Batteman and Johnston (1967), Bjorhovde and Tall (1971). Systematic measurements on steel columns have been performed by several researchers: Beer and Schultz (1970), Bjorhovde and Birkemoe (1979), Fukumoto et al. (1983), Essa and Kennedy (1993). However, only limited data is available for columns in actual (steel) structures: Tomonaga (1971), Lindner and Gietzelt (1984). The real shape of the imperfections may be very complicated, often consisting of simultaneous imperfections about both the principal axes of the cross-section.

Though commercial tolerances allow $L/500$ in some extruded aluminium members, $L/1000$ is rarely exceeded in reality (Mazzolani 1985). If two of such bars are connected to form the chord of a truss, the final out-of-straightness will be negligible in comparison to the inaccuracies in the assembly. Even in laboratory tests, the initial curvature of the bar as supplied has usually been less than the error in centring the specimen. Furthermore, the effect of edge supports can have a significant influence on the imperfection-sensitivity of the column. See for example the work by: Bernard et al. (1999), Gonçalves and Camotim (2001), and Dubina and Ungureanu (2002). Tests also indicate that the effect of load eccentricity was somewhat more pronounced than the effect of initial out-of-straightness, Hariri (1967). End moments, due to frame action or load eccentricities in joints, will thus in most cases dominate any moments due to initial curvature. Chapuis and Galambos (1982) studied the effect of end restraint on initially curved aluminium columns. They conclude that it is conservative to determine the design load of a column based on the effective critical length (eq. 2-12) and a column curve (see section 2.2.4) derived for pin-ended columns.

In inelastic analysis, the shape of the cross-section and thickness deviations may have a substantial influence, see Mazzolani (1985). The influence of the shape has been thoroughly studied numerically by Faella (1976), for double symmetrical aluminium extrusions. As presented in section 2.2.2, application of the tangent-modulus E_T results in a non-uniform stress distribution over the cross-section. As a result, the shape of the cross-section has an influence on the failure load of 5-6%, due to curvature of the column. The variation of the thickness with respect to the nominal dimensions in a profile can cause accidental eccentricities and shape asymmetries, which lead to a decrease in load-bearing capacity, see Bernard et al. (1973). Faella (1976) analysed this influence for square hollow sections, assuming a variation of plate thickness of 10%, which is the permitted tolerance for extruded profiles of small thickness as given by European manufacturers. He concluded that for double symmetric profiles the influence of thickness variation is more important than the shape of the cross-section. Note that both aspects result in even larger deviations when combined with the influence of inelastic material behaviour (see section 2.2.2).

The influence of the cross-sectional shape in combination with initial curvature is even more pronounced for asymmetrical shapes. This is illustrated by the computer-plotted curves on aluminium T-sections in Figure 2-6 by Hariri (1967). The deviation in failure load can be up to 18%, when comparing buckling to left or right. Apparently, the T-section shows the asymmetric equilibrium described in section 2.1.3. Thus, the buckling load of the imperfect column depends on the direction of the imperfection.

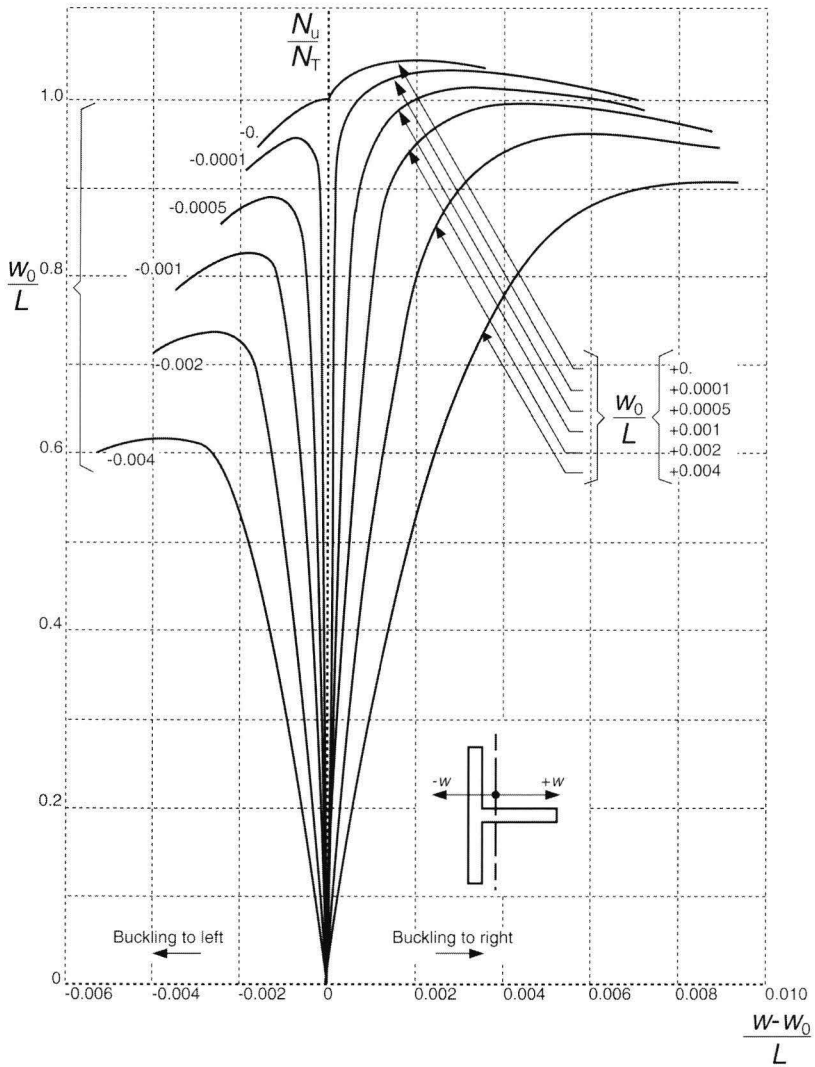


Figure 2-6 Theoretical behaviour of straight and initially curved aluminium alloy T-sections (Hariri 1967)

It can be concluded that the failure load of columns is highly influenced by interaction of the following aspects: non-linear material characteristics, initial imperfections, load eccentricities, edge restraints, the (a-) symmetrical cross-sectional shape, and thickness variations.

2.2.4 Column buckling - Design practice

Using a description of the influential parameters of the previous section, the failure load of columns can be determined numerically. Nevertheless, this is a very complicated process, involving numerical integration when physical and geometrical imperfections must be considered. Thus, this approach is not suitable for day-to-day work. Therefore, simplified column formulae are provided. These formulae involve parameters such as the yield strength, column length, and cross-sectional properties. Many design formulae have been used throughout history and are described in textbooks, like: Galambos (1998), Mazzolani (1985), CRCJ (1971), and Yu (2000).

There are essentially four basic ways, freely after Galambos (1998), by which column design formulae, curves, or charts have been developed:

1. *Empirical formulas based on the results of column tests*
 These formulae are applicable only to the material, the cross-section, and end constraints for which the tests were performed. The earliest column formulae from the 1840's were of this type. More recent papers have utilised computerised data banks that contain a large proportion of all column tests reported in the literature, for example Hall (1981) and Fukumoto et al. (1983).
2. *Formulas based on the yield limit state*
 These formulae define the strength of a column based on the elastic stress distribution of the axially loaded and slightly bended (due to initial imperfections) column. The design strength is reached when this elastic stress coincides with the yield stress. Such column formulae have a long history, also dating back to the middle of the nineteenth century, and they continue to enjoy popularity today (e.g. the British use of the Perry-Robertson formula (Trahair and Bradford 1988). Empirical factors can account for initial imperfections of geometry and loading, but the formulae do not consider the necessarily inelastic base of column strength.
3. *Formulas based on the tangent-modulus theory*
 These formulae take account for the bifurcation load, instead of the maximum strength of perfectly straight columns. If imperfections are such that they just reduce the maximum strength to the tangent modulus strength, these formulae have empirical justification. This approach has been used in the American codes up to 1996, as explained in Yu (2000).
4. *Formulas based on maximum strength*
 Modern trends in column design involve column formulae that are a numerical fit of curves obtained from maximum strength analysis of representative geometrically imperfect columns containing residual stresses. This resulted in the concept of multiple column curves (Mazzolani 1985). This concept is now the commonly used approach in Europe (e.g., Eurocode 3, Eurocode 9, NEN 6710 and NEN 6770).

This section presents the method originally proposed by ECCS committee 16 (1977), later ECCS-TC2, which subsequently progressed into the Eurocode 9 (CEN 1999). The approach is fully described by Mazzolani (1985). The buckling curves used for the Eurocode 9 are based upon the following assumptions:

- A sinusoidal shaped initial out-of-straightness, with an amplitude e_0 of $L/1000$, represents the geometrical imperfection.
- The influence of the shape of the cross-section and of its variations of thickness is smaller than 5 percent and can therefore be neglected if the profile is an open double-symmetric cross-section. It cannot be neglected if the profile is a box-section or an open asymmetric or single-symmetric section (T-, U-, ...). It has been calculated that the decrease of column strength due to an “eccentricity” of 10% is equal to 12 % in T-sections, 13 % in tubes, and 16 % in square box sections. The worst case is represented by the additive action of load eccentricity and asymmetry.
- The Ramberg-Osgood relation (eq. 2-15) can be conveniently used to describe the material characteristic, with values of $E = 70000 \text{ N/mm}^2$ and $n = f_{0.2}/10$.
- Buckling curves are used in a non-dimensionalised form as the elastic limits of commercially alloys vary substantially. Even though these curves depend substantially on n (and thus on $f_{0.2}$), experience has shown that these alloys can be divided into two classes. The first comprises those heat-treated alloys with high values of $f_{0.2}$ (from 200 to 300 N/mm^2), and the second non-heat-treated alloys having low values of $f_{0.2}$ (around 100 N/mm^2). Hence, two different buckling curves are determined.
- The influence of residual stresses and variations of the elastic limit along the cross-section is negligible for extruded members.
- Since experimental results were in close agreement with the numerical analysis, simulation computations can be systematically used to elaborate the basic data and then extrapolate them in order to use these results for all common cases.

The ECCS committee decided to determine three non-dimensional buckling curves, see Figure 2-7, to cover all of the extruded aluminium bars with a guaranteed elastic limit of at least 100 N/mm². For comparison, the steel design curves used in Eurocode 3 (CEN 1993) are presented as well. The buckling coefficient χ is obtained from the relative column slenderness $\bar{\lambda}$ (Equation 2-13). These curves were numerically computed using the following data:

- Curve a Minor axis bending of an I-section with $n = 20$;
- Curve b Tubular cross-section with an eccentricity of 10% and $n = 15$;
- Curve c Minor axis bending of a triangular box-section with an eccentricity equal to 10% and $n = 10$.

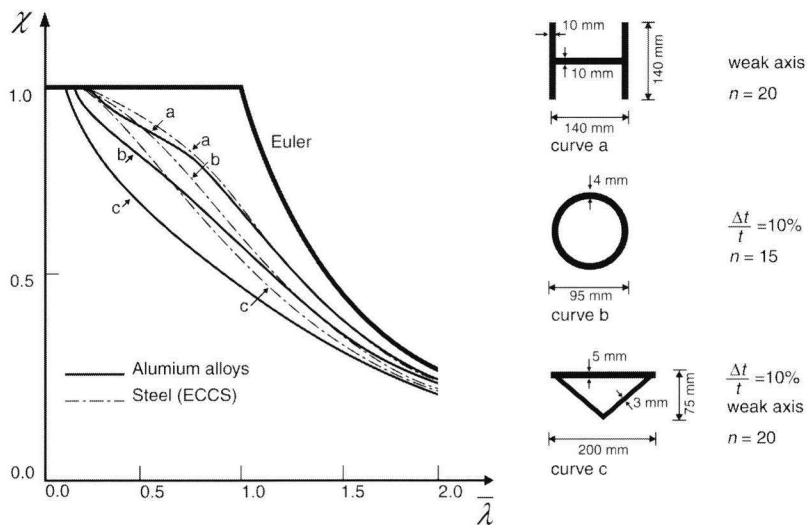


Figure 2-7 ECCS aluminium-alloy buckling curves (Mazzolani 1985)

The design strength N_d is obtained from the cross-sectional capacity $N_{0.2} (=f_{0.2} \cdot A)$:

$$N_d = \chi \cdot N_{0.2} \quad \text{eq. 2-16}$$

After a thorough comparison with tests, numerical simulations and various codes it was decided to quit the use of curve c, but instead add a reduction factor to incorporate the asymmetry of the cross-section. The presented approach is applied in the current Eurocode 9 (CEN 1999).

2.3 Uniformly compressed plates – Plate buckling

2.3.1 General description

When a plate is subjected to compression, shear, or a combination of these stresses, theoretical critical loads can be determined. Contrarily to the uniformly compressed column of the previous section, plates exhibit a stable equilibrium with a substantial amount of post-buckling strength. This behaviour is visualised in Figure 2-8; reference is made to the observations of section 2.1.3. Numerous researchers have investigated the plate-buckling phenomenon in the past and some excellent summarising books exist. See for example: Timoshenko and Gere (1961), the Japanese handbook (CRCJ 1971), Walker (1975), Kirby and Nethercot (1979), Murray (1984), Narayanan (1987), Rhodes (1991), Galambos (1998), and Yu (2000).

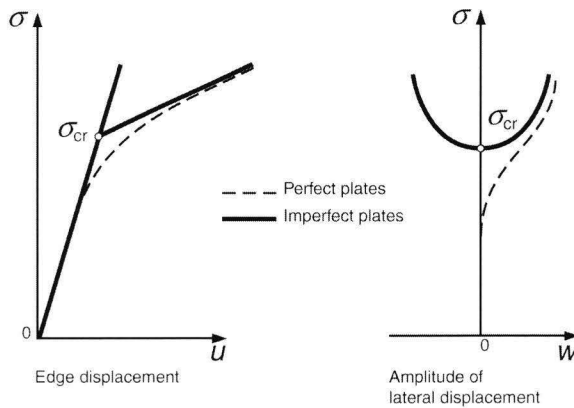


Figure 2-8 Equilibrium paths for initially perfect and imperfect plates subjected to in-plane compression.

The key parameter for plate buckling is the critical plate-buckling stress σ_{cr} . The following equation relates σ_{cr} to the modulus of elasticity E , Poisson's ratio ν , plate width b , plate thickness t and the buckling coefficient k_{cr} , which depends on both the loading and support conditions.

$$\sigma_{cr} = k_{cr} \frac{\pi^2 E}{12(1-\nu^2)} \left(\frac{t}{b}\right)^2 \quad \text{eq. 2-17}$$

Contrarily to columns, the theoretical critical load is not necessarily a satisfactory basis for design, since the ultimate strength can be much greater than the critical load, due to post-buckling strength. In the determination of design rules, both the critical stress and the post-buckling strength are important parameters.

2.3.2 Plate buckling – Determination of the critical stress

Differential equations

Von Kármán derived the original differential equations for plate buckling, following original work on large deflections by Kirchhoff (1877), and a study of the use of stress functions by Föppl (1907). These equations were derived for the rectangular plate of Figure 2-9. The equations allow various boundary and loading conditions at the plate edges. The resulting stress pattern in the plate is described by σ , the lateral load by p .

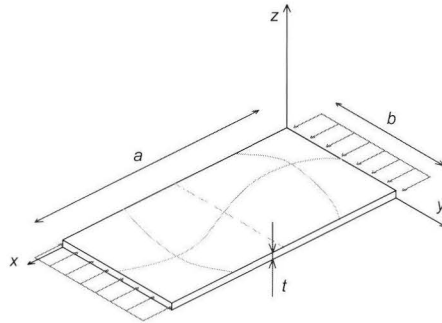


Figure 2-9 Geometry and loads of the plate considered

This resulted in the so-called Von Kármán equations for large deflections of plates. Unfortunately, these are fourth-order, non-linear equations and rigorous solutions are only available for a few theoretical situations. By using the energy method these can be written, freely after Brush and Almroth (1975), in the following compact form:

$$\frac{\partial \sigma_x}{\partial x} + \frac{\partial \sigma_{xy}}{\partial y} = 0 \quad \text{eq. 2-18a}$$

$$\frac{\partial \sigma_{xy}}{\partial x} + \frac{\partial \sigma_y}{\partial y} = 0 \quad \text{eq. 2-18b}$$

$$D \left(\frac{\partial^4 w}{\partial x^4} + 2 \frac{\partial^4 w}{\partial x^2 \partial y^2} + \frac{\partial^4 w}{\partial y^4} \right) - t \left(\sigma_x \frac{\partial^2 w}{\partial x^2} + 2 \sigma_{xy} \frac{\partial^2 w}{\partial y^2} + \sigma_y \frac{\partial^2 w}{\partial x \partial y} \right) = p \quad \text{eq. 2-18c}$$

$$\text{where} \quad D = \frac{E t^3}{12 (1 - \nu^2)} \quad \text{eq. 2-19}$$

The equilibrium equations of linear plate theory can be obtained by omitting the cubic terms of equation 2-18c. Though the actual stress distribution is based on the deformations u , v , and w , the reduced equation 2-18c becomes uncoupled and refers only to w . Much of the relative simplicity of classical thin-plate theory is a consequence of this uncoupling, as the critical stress can be obtained from equation 2-18c alone.

As an example, initial buckling of a uniformly compressed plate with no lateral loading ($p = 0$) is regarded. Thus, equation 2-18c reduces to the following equation, which was originally derived by Saint Venant (1883):

$$\frac{\partial^4 w}{\partial x^4} + 2 \frac{\partial^4 w}{\partial x^2 \partial y^2} + \frac{\partial^4 w}{\partial y^4} = \frac{t}{D} \left(\sigma_x \frac{\partial^2 w}{\partial x^2} + 2\sigma_{xy} \frac{\partial^2 w}{\partial y^2} + \sigma_y \frac{\partial^2 w}{\partial x \partial y} \right) \quad \text{eq. 2-20}$$

Though the critical load can be determined by integration of the differential equation, this is only possible for a limited number of specific boundary and loading conditions. A more general approach is the energy method. It can be used to find critical loads in a very direct and simple way, if a good approximation of the deflected plate is made, see e.g. Allen and Bulson (1980). The solution is exact if the chosen deflected shape equals the true deflected shape. Other methods such as the method of Virtual Displacements, Galerkins method, and the Lagrangian multiplier method, can also be used.

Evaluation of the critical load by integration of the differential equation is explained for a supported rectangular plate under axial compression. This problem was solved first by Bryan (1890); see for example Allen and Bulson (1980) or Timoshenko (1961). All four plate-edges are supported, i.e. out-of-plane translations are restricted whereas rotations are allowed, while one pair of opposite edges is subjected to a uniform compressive stress σ . Thus $\sigma_x = \sigma$, whereas $\sigma_{xy} = \sigma_y = 0$, and equation 2-20 reduces to:

$$\frac{\partial^4 w}{\partial x^4} + 2 \frac{\partial^4 w}{\partial x^2 \partial y^2} + \frac{\partial^4 w}{\partial y^4} = \frac{\sigma t}{D} \frac{\partial^2 w}{\partial x^2} \quad \text{eq. 2-21}$$

It is assumed that the deflected shape w of the simply supported rectangular plate may be represented by a double sinoidal series, in which m and n are the numbers of half sinus waves in the x - and y -direction respectively, and with amplitude C :

$$w = C \sin \frac{m\pi x}{a} \sin \frac{n\pi y}{b} \quad \text{eq. 2-22}$$

Substitution of w in equation 2-21 results:

$$\left[\left(\frac{m\pi}{a} \right)^4 + 2 \left(\frac{m\pi}{a} \right)^2 \left(\frac{n\pi}{b} \right)^2 + \left(\frac{n\pi}{b} \right)^4 - \frac{\sigma t}{D} \left(\frac{m\pi}{a} \right)^2 \right] C \sin \frac{m\pi x}{a} \sin \frac{n\pi y}{b} = 0 \quad \text{eq. 2-23}$$

This equation can be solved for $C = 0$. Thus, it can be concluded that no deflections occur in the elastic range. However, once the term in brackets becomes zero, at a critical value of σ_{cr} , the amplitude of the deflections is no longer defined and instability occurs. The lowest value of edge load to accomplish this is the elastic critical load σ_{cr} :

$$\sigma_{cr} = \frac{D \pi^2}{tb^2} \left[m \left(\frac{b}{a} \right) + \frac{n^2}{m} \left(\frac{a}{b} \right) \right]^2 \quad \text{eq. 2-24}$$

Though this relation was already solved in 1880, the fact that plates with supported edges can accept additional load after buckling was not discovered until the late 1920s through experimental studies made in connection with the structural design of airplanes.

Initial buckling of elastic plates

Introducing the plate-slenderness parameter $\varphi (= a/b)$ as well as the buckling coefficient k_{cr} , equation 2-24 reduces to equation 2-17, which determines the critical stress:

$$\sigma_{cr} = k_{cr} \frac{D\pi^2}{tb^2} \quad \text{eq. 2-25}$$

Where k_{cr} for the presented case of a simply supported rectangular plate under uniform compression equals:

$$k_{cr} = \frac{m^2}{\varphi^2} + \frac{\varphi^2}{m^2} + 2 \quad \text{eq. 2-26}$$

Figure 2-10 presents k_{cr} for a simply supported plate, as a function of the plate slenderness φ . In structural engineering the long plate having a relatively large a/b ratio is of particular interest as such plates can be used to describe the behaviour of plates in cross-sections, for example the webs of square hollow sections. In those cases, k_{cr} reduces to the well-known value of 4.0.

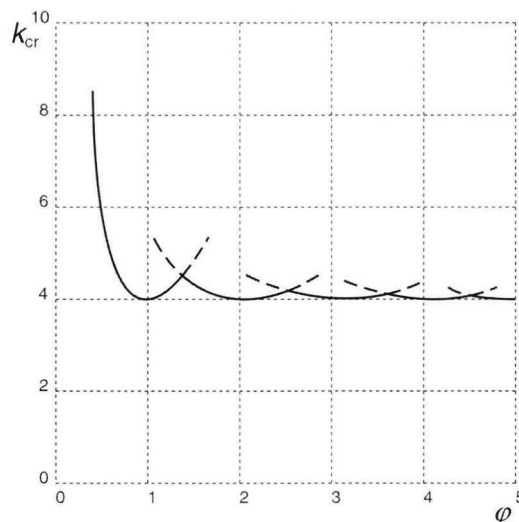


Figure 2-10 Buckling coefficient k_{cr} of a simply supported plate

Comparably for simply supported rectangular outstands under uniform compression, k_{cr} can be determined from:

$$k_{cr} = \frac{1}{\varphi^2} + \frac{6(1-\nu)}{\pi^2} \tag{eq. 2-27}$$

Various authors have studied different boundary conditions. Their results were summarised for the first time by Gerard and Becker (1957). An overview is given in Figure 2-11. The five cases represent the most common cases of supports, where *c* stands for clamped, *ss* for simply support, and *free* for an unsupported edge.

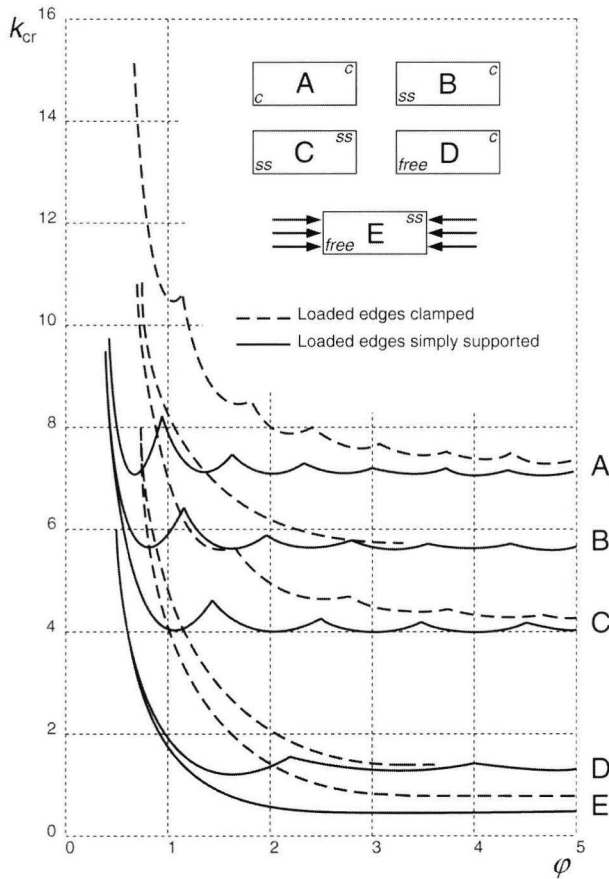


Figure 2-11 Buckling coefficients k_{cr} of uniformly compressed rectangular plates with various boundary conditions (Gerard and Becker 1957)

Initial buckling of inelastic plates

As presented in section 2.2.1 for columns, the inelastic material characteristic of aluminium alloys has a significant influence on the stability behaviour. Based on equation 2-21, and introducing the plasticity reduction factor η , Bleich (1952) introduced the following differential equation for inelastic buckling of uniformly compressed plates:

$$\eta \frac{\partial^4 w}{\partial x^4} + 2\sqrt{\eta} \frac{\partial^4 w}{\partial x^2 \partial y^2} + \frac{\partial^4 w}{\partial y^4} = \frac{\sigma \tau}{D} \frac{\partial^4 w}{\partial x^2} \quad \text{eq. 2-28}$$

This results in the following expression for the critical stress of a flat plate under uniform compressive stress in either the elastic or the inelastic range:

$$\sigma_{cr} = k_{cr} \frac{\sqrt{\eta D} \pi^2}{\tau b^2} \quad \text{eq. 2-29}$$

Note that the value of η depends on the support and loading conditions. For example, $\eta = E_T/E$ for a uniformly compressed simply supported plate and $\eta = E_s/E$ for a simply supported outstand; where E_T and E_s are the tangent and secant modulus of the non-linear material characteristic. Additional information is presented in: Bulson (1969), Gerard and Becker (1957), Johnson (1964), Kalyanaraman (1979) and Stowell (1958).

2.3.3 Plate buckling - Post-buckling and ultimate strength

As introduced in section 2.3.1, supported plates will not collapse when the buckling strength is reached. Instead, they will develop a considerable amount of post-buckling resistance. The overall behaviour of plates is presented in Figure 2-12, relating the average axial stress σ_{av} to the deflections w (Figure 2-12a), respectively the average axial strain ε_{av} (Figure 2-12b). These curves due to Hu, Lundquist, and Batdorf (1946) are shown for various values of w_0/τ , where w_0 is the initial deviation from flatness. The figures show that the behaviour of plates containing small initial deviations from flatness w_0 is similar to that of columns. The lateral deflection w increases throughout the loading sequence, but has – markedly – only influence in the region of the elastic critical stress. Post-buckled deflections are not greatly affected by initial irregularities. Similar curves have been produced for various types of edge support, by using energy methods. The reader should consult the work of Coan (1951) and Yamaki (1959). Finite element and finite difference techniques have enabled a wide range of plate loading and plate geometries to be studied.

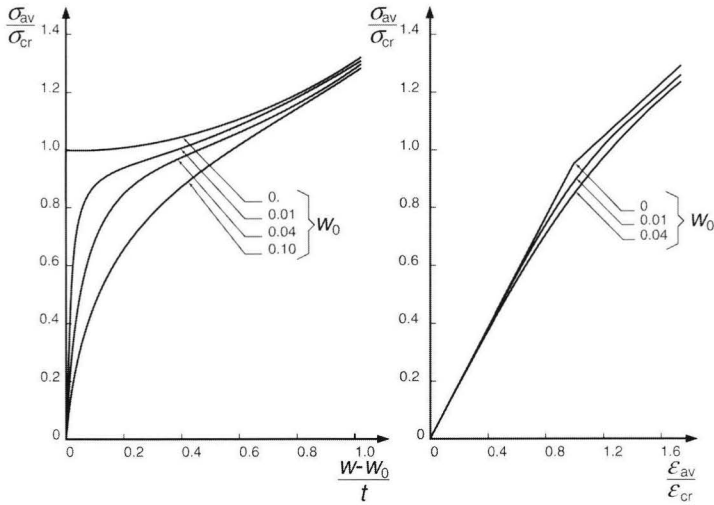


Figure 2-12 Overall behaviour of a uniformly compressed plate with initial imperfections

Coefficients and parameters for rectangular plates under a wide variety of load distribution and edge conditions have been tabulated by Williams and Walker (1975) and (1977). In addition, they defined the non-linear relationships in the post-buckled range in explicit and simple mathematical form. The curves of Figure 2-12a) can be described by:

$$\frac{\sigma_{edge}}{\sigma_{cr}} = \frac{\sigma_{av}}{\sigma_{cr}} + 0.66 \left(\left(\frac{w}{t} \right)^2 - \left(\frac{w_0}{t} \right)^2 \right) + 0.018 \left(\left(\frac{w}{t} \right)^2 - \left(\frac{w_0}{t} \right)^2 \right)^2 \quad \text{eq. 2-30}$$

The various stages of axial stress are presented in Figure 2-13. The axial stress distribution is uniform prior to buckling, as shown in Figure 2-13A. After buckling, the stiffness of the plate centre reduces and a non-uniform stress distribution is developed (B). The redistribution of stress continues until the stress at the edge reaches the yield strength and the plate begins to fail (C).

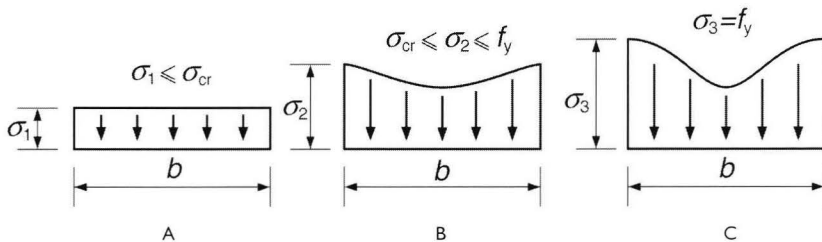


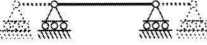




Figure 2-13 Stages of stress distribution in simply supported compressed plates (Yu 2000)

Figure 2-12b shows that the initial post-buckling stiffness, E^* , of plates is linear in nature. Table 2-1 presents the results for a number of conditions of loading and edge support, as summarised by Allen and Bulson (1980).

<i>Table 2-1 Values for the initial post-buckling stiffness of plates</i>		
<i>Simply supported edges:</i>		
Sides straight but free to move laterally	$E^* = 0.5 E$	
Sides straight not free to move laterally	$E^* = 0.746 E$	
Sides free to wave	$E^* = 0.408 E$	
<i>Clamped edges:</i>		
Sides straight but free to move laterally	$E^* = 0.497 E$	
One edge simply supported, one edge free	$E^* = 0.444 E$	

The initial buckled form of a supported plate has one transverse sinusoidal half-wave. As the compressive load is increased, the central portion of the transverse deformation becomes flattened. The well-known effective width approach is based on the stress distribution associated with this form due to yield initiation of the plate edges. Another change of the deflected shape is possible when a simply supported plate is free to translate laterally. Mode jumping, a dynamic snap from one shape to another, may occur by a sudden change of the longitudinal wavelength. The exact analysis of transition between the two modes is not known at present. Sherbourne et al. (1971) determined the terminal wavelength for flat plates at the ultimate capacity.

2.3.4 Plate buckling - Effective width approach

As the differential equations were unsuitable for application in daily practice, Von Kármán et al. (1932) introduced the concept of effective width. This concept was elaborated by many others, including the important work of Winter (1948). As numerous research pointed out that the accuracy of these Winter-equations are sufficient, it is Winter's work that provides the background for most current design approaches.

The effective width approach assumes that, instead of the actual non-uniform stress distribution, the total load is carried by a fictitious effective width b_{eff} , subject to a uniformly distributed stress equal to the maximum stress σ_{max} that occurs at the unloaded plate edges, as shown in Figure 2-14.

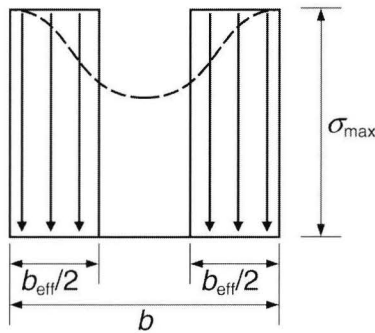


Figure 2-14 Effective width of stiffened compression element (Yu 2000)

The effective width b_{eff} is selected so that the area under the curve of the actual non-uniform stress distribution is equal to the sum of the two parts of the equivalent rectangular shaded area with a total width b_{eff} and an intensity of stress equal to the edge stress σ_{max} , that is:

$$\int_0^b \sigma \, dx = b_{eff} \sigma_{max} \quad \text{eq. 2-31}$$

It may also be considered that the effective width represents a particular plate that buckles when the compressive stress reaches the yield point of steel. This resulted in the *Von Kármán formula*:

$$\frac{b_{eff}}{b} = \sqrt{\frac{\sigma_{cr}}{f_y}} \quad \text{eq. 2-32}$$

Based on his extensive investigation on cold-formed steel sections, Winter (1947) indicates that the equation is equally applicable to the element in which the maximum stress σ_{\max} is below the yield point f_y . In addition, it was verified that the equation was suitable for plates with different boundary conditions according to Figure 2-11. By introducing empirical correction factors, to account for an accumulation of imperfections, this led to the *modified Winter formula* (Winter 1947, 1948, 1970):

$$\frac{b_{\text{eff}}}{b} = \sqrt{\frac{\sigma_{\text{cr}}}{\sigma_{\max}}} \left(1 - 0.22 \sqrt{\frac{\sigma_{\text{cr}}}{\sigma_{\max}}} \right) \quad \text{eq. 2-33}$$

Notably, the equation depends on the ratio between critical and maximum stress. Therefore, the relative plate slenderness $\bar{\lambda}_{\text{pl}}$ is introduced. Comparably to the column slenderness of equation 2-13, the relative plate slenderness can be determined by:

$$\bar{\lambda}_{\text{pl}} = \sqrt{\frac{\sigma_{\max}}{\sigma_{\text{cr}}}} \quad \text{eq. 2-34}$$

Therefore, the effective width can be defined as:

$$b_{\text{eff}} = \left(\frac{1}{\bar{\lambda}_{\text{pl}}} - 0.22 \frac{1}{\bar{\lambda}_{\text{pl}}^2} \right) b \quad \text{or} \quad \rho = \frac{1}{\bar{\lambda}_{\text{pl}}} - 0.22 \frac{1}{\bar{\lambda}_{\text{pl}}^2} \quad \text{eq. 2-35}$$

It is this equation, or comparable ones, that present a practical description of the actual post-buckling strength of individual plates. Furthermore, it presents the basis for the local buckling behaviour of cross-sections as used in the design rules of the design codes, as outlined in section 2.4.

2.4 Cross-sectional instability – Local and distortional buckling

2.4.1 General description

Section 2.3 treated the behaviour of individual plate elements. In practice, cross-sections of structural components may be considered as being composed out of plate elements. It is clear that the buckling behaviour of a plate assembly is governed by interaction of these plates. This section discussed the mechanics of such an interaction and its simplification in design. As already described in section 1.2, cross-sectional instability of a plate assembly can be divided into either:

- *Local buckling*
This mode involves out-of-plane deformation of the component plates with the nodes remaining essentially straight. This mode is to some extent comparable with plate buckling as elaborated in section 2.3. Noteworthy, the wavelength of the buckle is of the same order of magnitude as the widths of the plate elements.
- *Distortional buckling*
The buckling process may involve in-plane bending of one or more of the constituent plate elements as well as out-of-plane bending of the plate assembly, as occurs in a purely local mode. Depending on the context, such modes are referred to as: *stiffener buckling*, *local torsional*, *distortional*, or *orthotropic*. Though the associated wavelengths may be considerably larger than those of local buckling, but there is a half-wavelength at which the critical stress is a minimum.

2.4.2 Local buckling

To account for cross-sectional instability, the cross-section of a member is often schematised as being built up out of plate elements. It is often assumed that connections between plate elements act as hinges. Subsequently, the critical stresses of each individual plate element can be determined according to section 2.3.2. The critical buckling stress of a plate assembly may be taken as the smallest value of the critical stresses of the plate elements. However, such a calculation must be used with caution for the following reasons:

- The results can be very conservative when the plate structure consists of elements with widely varying slenderness. This is the result of neglecting the rotational constraints at the nodes.
- The results are inapplicable unless it is ensured that all the plate elements buckle locally (i.e. the nodes remain essentially straight). Note that if distortional buckling occurs, the result of such a simplified calculation will be on the unsafe side.

While the differential equations of individual plates are known (see section 2.3.2), it is possible to compile these to a set of equations that results the critical stress of the plate combination. Classic analytical solutions to the elastic buckling of stiffened plates begin with the work of Timoshenko and Gere (1966). Others have compiled and extended this large body of work, notably: Bleich (1952), Klöppel and Scheer (1960), and Troitsky (1976). Note, that a more practical approach of determining the critical stress is the application of specific computer programs, see section 2.4.4. A substantial amount of data can be found in references like the Japanese Handbook of Structural Stability (CRCJ 1971). As an example of the stiffening effect of connecting plate elements, Figure 2-15 results the local buckling coefficients $k_{cr,w}$ for I-sections and rectangular hollows. For given values of the geometry, it is possible to determine the buckling coefficient $k_{cr,w}$ with respect to the web. Each of these charts is divided into two portions by a dashed line running across it (Kroll et al. 1943). This line divides the graph into two regions where either flange- or web buckling dominates. If the structural design is based on the lowest critical stress of an individual plate, this line presents the structurally most efficient solution, in that there occurs a complete participation of all plates in the local-buckling process.

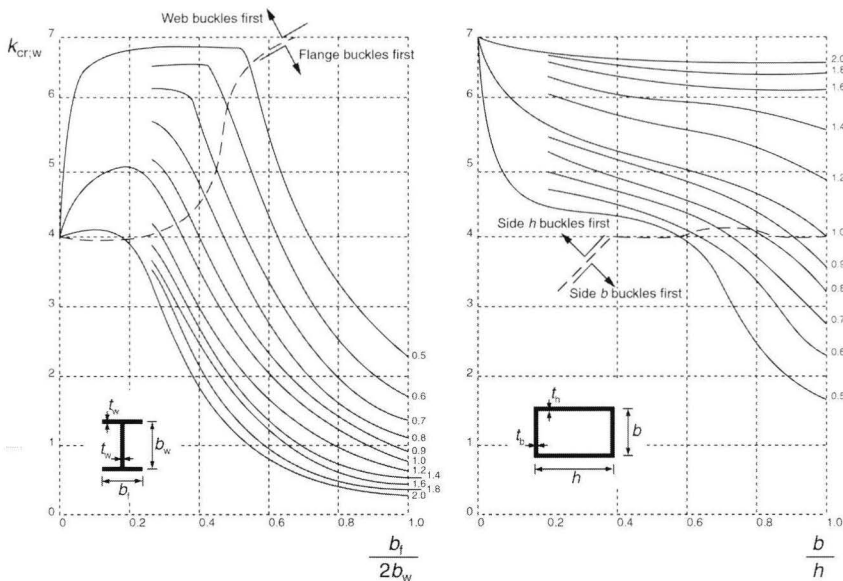


Figure 2-15 Plate buckling coefficients for I- and rectangular box section columns (Kroll et al. 1943)

Though it is possible to determine the critical stress of the cross-section and its plate elements, it is not that simple to determine the according post-buckling strength. Interaction between the (post-) buckling behaviour of the elements of a plate assembly is inescapable because of the equilibrium and compatibility conditions that must be satisfied at the nodes. As previously mentioned this results a set of differential equations to be solved. Note that as the size of the initial deflections makes it possible to assume that normal displacements are zero for each plate element meeting at a corner, it is possible to simplify these conditions considerably (Benthem 1959). Nevertheless, the interactions between plate elements along the nodes become very complex. The problem is further compounded when interaction between overall and local buckling is considered; it is also possible that local buckling modes interact. For reference to executed research is referred to Galambos (1998) and Yu (2000). However, no general approach has come forth and application of the effective width approach, based on the buckling behaviour of individual plates, is still the most common approach.

2.4.3 Distortional buckling

Distortional buckling highly depends on the interaction between the plate elements. Thus, it is very difficult to develop a general approach. Most research on distortional buckling is concerned with cold-formed steel sections, which allows only a limited freedom of cross-sectional shapes. Thus, distortional buckling is generally investigated by the study of specific geometries, resulting design rules for those situations only. Essentially, design rules are limited to plates stiffened with end- or intermediate stiffeners. However, these have been slightly modified and optimised for specific cross-sections like: channels, edge stiffened channels, and trapezoidal sheeting. The difference with aluminium extrusions is clear. Almost any cross-sectional shape may occur and though stiffening elements exists, they are often applied for reasons other than structural. The existing design rules are therefore of limited relevance only. Thus, this section focuses on the backgrounds and the influencing parameters. Reference is made to general literature like: Galambos (1998), Yu (2000), Eurocode 3 (CEN 1993), and Eurocode 9 (CEN 1999).

Comparably to local buckling of the previous section, the critical stress can be obtained by solving the differential equations. However, a nowadays more common approach is to use the numerical tools explained in section 2.4.4. For example, it is often economical to increase the compressive strength of a plate element by introducing longitudinal stiffeners. Seide and Stein (1949), Bleich and Ramsey (1951), and Timoshenko and Gere (1961) present charts and tables for determining the critical stress of plates simply supported on all edges and having one, two, or three equally spaced longitudinal stiffeners. In all these solutions, the stiffeners are assumed to have zero torsional rigidity.

Therefore, they are directly applicable to open-section stiffeners. When applied to stiffeners with substantial torsional stiffness, these methods are conservative. Stiffeners with large torsional rigidity also provide partial or complete fixity of the edges of subpanel plating, thereby increasing their critical stresses. It has been shown by Lind (1973) and Fukumoto et al. (1977) that the stiffener type affects the buckling mode, as well as the ultimate carrying capacity of the stiffened plate. Both Tvergaard (1973) and Fok et al. (1977) showed that local imperfections of stiffeners significantly influence the overall buckling behaviour of stiffened plate panels.

Cold-formed steel design considers post-buckling behaviour to obtain optimal and economic solutions. Therefore, the elastic critical loads are not directly applicable for design. Analytical solutions for the ultimate strength are cumbersome due to large deflections and non-linear material behaviour. Again, solutions are available only for specific cases. The first approach is to disregard local buckling and determine the longitudinal membrane stress distribution at failure, as it is dominated by the distortional mode. This distribution highly resembles the prototypical effective width case (Schafer and Peköz 1998a). A second approach is to consider that stiffeners on thin plates are less effective than actual webs. This effect can be taken into account by considering an effective wall thickness of the stiffener. This principle, introduced by Höglund (1980), is implemented in the current European steel codes (PREN 1993 1-3). A final remark can be made with respect to the amount of post-buckling strength. Distortional buckling of stiffened plates resembles a combination of plate buckling and flexural buckling of the stiffeners. Thus it is not surprising that the post-buckling strength lies in-between that of individual plates and column buckling. Because of the limited post-buckling strength and to prevent mode interaction a design approach could be to prevent the occurrence of distortional buckling by the provision of stiffeners with adequate rigidity. For example, Desmond et al. (1981 a and b) proposed such an approach for intermediate and edge stiffeners. A substantial amount of publications is available with respect to the distortional buckling behaviour of specific cold-formed steel structures. Reference will be made only to three well-respected groups: Hancock, Kwon and Bernard (1994), subsequently Kesti and Davies (1999), and finally Schafer and Peköz (1998b).

Though these approaches may be appropriate for specific situations, there is no general approach for the post-buckling behaviour of arbitrary cross-sections and distortional buckling is a field of research with ongoing interest.

2.4.4 Numerical investigation

As it is often not possible or too laborious to solve plate-buckling problems analytically, numerical methods are often used instead. Note that there is no fundamental difference between the results of a differential equation solved with the energy method, or using one of the following approaches. Various methods exist though the most commonly used procedures are the finite element method (FE) and finite strip method (FS).

Most general-purpose finite element programs include an Euler Eigenvalue analysis. Though the computational costs used to be extraordinary high, the capacity of nowadays computers is such that the approach is generally available for research purposes of both the bifurcation load, as well as for the total non-linear behaviour. Thus, FE provides an excellent tool to study the distortional and local buckling behaviour of plate assemblies. For more information on FE stability see for example: Kitipornchai and Chan (1990), Hinton (1992) and the DIANA Manual (De Witte et al. 1996).

The finite strip method was developed as an alternative for FE to reduce calculation costs. With this approach, the structural member is divided into a discrete number of longitudinal strips, instead of being divided into a discrete number of elements. The finite strip method as developed by Cheung (1976), uses simple polynomials in the transverse direction and continuous Fourier series functions in the longitudinal direction. Though accurate for analysing the buckling of prismatic structural members and stiffened plates under compression, it has some disadvantages when analysing the buckling of beams loaded in bending and/or shear, see also Van Erp (1989). The improved spline finite strip method, developed by Fan (1982) does not suffer from the problems mentioned above (Lau and Hancock 1986). Notably, two specifically fit-to-purpose FS-packages have been developed, namely CU-FSM and Thin-Wall. These are very user-friendly and require only limited calculation time.

Summarised, as the FE-packages tend to be more general applicable than FS; they are better suited for detailed research on post-buckling behaviour, including inelastic material and interaction of buckling modes. However, the developed FS-packages are specifically built to determine the elastic critical load. Therefore, they are a very good alternative for practical purposes.

2.5 Interaction of buckling modes

2.5.1 General description

Simultaneous or nearly simultaneous buckling loads (due to local, distortional, and overall buckling) may result in a non-linear interaction between the buckling modes. The interaction between long-wave and short wave buckling modes has been shown to have a destabilising influence on the post-buckling behaviour (Koiter 1945). Consequently, unavoidable imperfections may significantly reduce the load carrying capacity of thin-walled beams. Two strategies to study buckling interaction:

- The stiffness of the locally buckled member is calculated first, and then this stiffness is used to evaluate the overall buckling.
- The analysis of the interaction is performed based on the general Koiter theory (Koiter 1945).

The studies of interaction buckling under bending by Cherry (1960), Reis and Roorda (1977), Wang et al. (1977), and Bradford and Hancock (1984), belong to the first category. In all these cases, the concept of the effective width was used to account for the post-buckling stiffness of the locally buckled plate component. Koiter (1976), Tvergaard (1973), Pignataro (1985), Sridharan and Benito (1984) used the second approach.

The first approach is very popular among engineers and yields reliable results for a variety of cases. However, this approach is very difficult, if possible, in the case of structural elements with complex cross-sections. Furthermore, it is not suited to properly explain the mechanics of the interaction phenomena. The second, more fundamental, approach is not only applicable to every type of structure but is also much more suited to obtain an insight into the interaction phenomena.

2.5.2 Interaction between local and overall buckling

The single-symmetric column that is not fully effective is a unique and difficult problem. Not only does local buckling reduce the effective section properties, but also the effective centroid shifts along the axis of symmetry. Thus, an initially concentrically loaded column becomes a beam-column. To test such a column with an axial load that is truly centric throughout its loading history is difficult at the least. Furthermore, practically, such columns may not exist at all, as many columns that have no obvious end moments applied may in fact be beam-columns.

The first detailed investigations of the interaction between global and local buckling of a column are due to Bijlaard and Fisher (1952), Van der Neut (1969) and Graves Smith (1969). Van der Neut created a simple mechanical model of a column whose two plate flanges were capable of independent local buckling. This model exhibited a rather strong interaction with overall buckling, resulting in a marked sensitivity to imperfections. Graves-Smith (1969) treats the post-buckling behaviour within the scope of the large-deflection plate theory and accounts for both the local and overall effects of inelasticity. The overall buckling load is computed using the tangent modulus approach based on the stiffness of the locally buckled plate elements. Although the method is general, the author treats only the case of a square tubular column and the interaction appeared to be of minor importance.

Several other authors, notably Koiter (1976), Tvergaard (1973), Pignataro et al. (1985), Sridharan and Benito (1984), and Hancock (1978) contributed to the further study of buckling interaction of compressed members. The interaction problem was investigated using the finite strip method by Hancock (1981), and Sridharan and Benito (1984). Thomasson (1978), and König and Thomasson (1980) treat the post-local-buckling behaviour with an effective width approach and the column strength is determined based on an initial column imperfection. Mulligan and Peköz (1983) studied singly symmetrical columns. DeWolfe et al. (1974) and Kalyanaraman et al. (1977) used an effective width approach to find stiffnesses that depend on the value of the axial load. The stiffnesses thus obtained are used with a modified tangent modulus approach to obtain the overall buckling load.

Summarised, the commonly applied approach for interaction between local and overall buckling is apply column theory by using an effective cross-section. The effective cross-section is calculated based on the local buckling behaviour of the individual plate elements.

2.5.3 Interaction between local and distortional buckling

The interaction between local and distortional buckling, couples two relatively unknown effects. As explained in section 2.4.2, the commonly used description of the local buckling behaviour of cross-sections is rather inaccurate. Furthermore, the post-buckling strength of distortional buckling modes is not constant and in most cases unknown as well. As the amount of possible cross-sections and possible types of buckling modes is extremely large, research is limited to the study of specific (cold-formed steel) cross-sections.

Part of the extensive experimental program on distortional buckling described by Hancock, Kwon, and Bernard (1994) was to determine whether adverse interaction occurred if local and distortional buckling were simultaneous or nearly simultaneous. For the stiffened channel (rack) sections testes, no interaction was found. However, tests on trapezoidal deck sections showed a substantial adverse interaction. For this specific situation, the problem was solved by application of an effective width approach. Comparable research by Schafer and Peköz (1998b) concluded that distortional buckling could have a substantial adverse effect on the local buckling behaviour of specimens with edge stiffened flanges; even if its according critical stress was larger than that due to local buckling.

Both studies concluded that in case of comparable critical stresses due to distortional and local buckling, the distortional buckling mode dominates the actual behaviour. The presented research result design approaches for the interaction, though both are limited to a specific set of cross-sections.

2.6 Evaluation of the existing literature on stability

The previous sections discussed the various buckling modes that are of interest to uniformly compressed aluminium extrusions. Starting from the relatively simple phenomenon of overall buckling of columns, the complexity increases with plate-, local-, and distortional buckling, and finally buckling interactions. The complexity further increases due to interaction with material inelasticity and imperfections.

Overall (flexural and flexural-torsional) buckling is well described, resulting accurate design rules. All parameters can be accounted for through the development of column curves that are determined for actual cross-sections with specific data for the inelastic material and the applied imperfection.

Plate buckling of individual plates is describes accurately as well. Note that the plate buckling curves are determined with respect to the failure loads of the plate. However, the entire load-displacement curve can be obtained. This shows the interesting fact of the almost linear initial post-buckling stiffness.

The critical stress due to local buckling can be determined using analytical charts for specific cross-sections, or numerical approaches for arbitrary cross-sections that consist of plate elements. However, the actual post-buckling stiffness is unknown. Though the commonly used approach of regarding each element as an individual plate shows sufficient accuracy for traditional cross-sections, it does lack a firm background.

Distortional buckling has been studied only for specific geometries, mainly applied in cold-formed steel products. Though the critical stress due to distortional buckling can be determined, numerically, for arbitrary cross-sections, its post-buckling stiffness cannot. Thus, design approaches and buckling curves are available only for a limited set of cross-sectional shapes.

Buckling interaction is a very complex phenomenon. Though design rules are available for specific situations regarding interaction between local and overall buckling, the accuracy of such approaches is low, their range of validity unknown. Furthermore, experimental investigation shows that distortional buckling may have an adverse effect on cross-sections susceptible to local buckling.

Thus, it can be concluded that cross-sectional instability remains a field for further investigation. The present design models for local and distortional buckling are limited, both with respect to the allowable cross-sectional shapes as well as to their accuracy. Therefore, this thesis provides a more accurate investigation of the actual local buckling behaviour of aluminium extrusions with arbitrary cross-sections. Thus aiming at a more accurate prediction model for local buckling, as well as the opening up to distortion buckling and buckling interactions.

3 Experimental investigation on cross-sectional stability of aluminium extrusions

Chapter abstract

To investigate cross-sectional instability, and in order to obtain a prediction model, experimental data are essential. Therefore, this chapter summarises the results of existing experimental work as well as that of a substantial experimental program executed at Eindhoven University of Technology. This program was set up specifically to investigate cross-sectional instability of uniformly compressed aluminium extrusions for a wide range of cross-sectional shapes. This chapter presents those results. Respective sections will describe the executed test program, the method of testing, the imperfection measurements, the determination of the material characteristics, and finally the results of the compression tests. The obtained experimental database is used to develop and validate the finite element and prediction models of the following chapters.

3.1 Summary of existing experimental work

3.1.1 General

To study the actual cross-sectional stability behaviour of aluminium extrusions, it is essential to have experimental validation. Therefore, experiments are executed that focus on local buckling in both the elastic and inelastic range, though some attention is paid to distortional buckling. Furthermore, as buckling lengths are often large, due to for example flange buckling, interaction with overall buckling cannot be excluded.

The largest existing experimental program on cross-sectional instability is that of Salerno University, Italy, executed in the preparation of the Eurocode 9. This program consists of tests on three types of cross-sections: square hollows (SHS), rectangular hollows (RHS) and U-shaped (US) sections. The specifics of this program are described in section 3.1.2. A second test program was executed at Helsinki University, Finland. This program included a limited number of additional experiments on RHS-specimens as well as tests on more complex cross-sections (CS). This test program is described in section 3.1.3.

However, from the start of the current research it was emphasized that practical insight into the actual buckling behaviour could only be obtained by executing additional tests. Based on the ongoing insight obtained from these tests, gaps were found in the existing work. As a result, a substantial amount of experiments is executed. These are presented in section 3.2 and appendices B and C.

3.1.2 Salerno (SHS, RHS, US)

A large test program on square hollow sections (SHS), rectangular hollow sections (RHS) and U-sections (US) was executed at Salerno University, Italy, as mentioned above. The aim of these tests was to determine and validate the design rules of the Eurocode 9 (CEN 1999) and to set up the behavioural classes. For detailed information is referred to Landolfo et al. (1999) and Mazzolani et al. (1996), (1997) and (1998).

The complete experimental program deals with specimens made of 6000 and 7000 series alloys. In addition, different tempers have been considered. Two types of RHS members can be recognized, RHS with sharp corners and RHS with rounded corners. One specimen (RHS27) has an intermediate plate element stiffening the largest side of the cross-section.

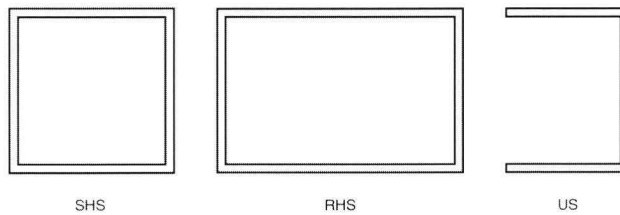


Figure 3-1 Cross-sections tested in the Salerno program

Two identical tests (A and B) were executed for each cross-section. The compression tests were executed (Mazzolani et al. 1998) with a Schenck RBS4000-E2 testing machine (maximum load 4000 kN, piston stroke +/- 100 mm). For each profile a minimum of two stub column tests have been carried out under displacement control. The axial displacements have been measured by means of three inductive displacement transducers (stroke +/- 10 mm, sensitivity 80 mV/V). The mean value of the three measurements has been considered. The specimens were clamped at the base and free to rotate at the top. Neither top nor base rotation of specimens has been observed as, according to the authors, all specimens failed due to pure local buckling without any coupling phenomena. Note that numerous specimens failed at the supports, indicating at least some influence of the support conditions.

The geometrical properties, the material characteristics, and the experimental results are presented in appendix A. Note that no imperfection measurements were executed. The results of the Salerno program will be used in Chapter 6 to validate the results of the newly developed prediction model.

3.1.3 Helsinki (RHS, CS)

The Helsinki program (Hassinen 2000) aimed at verification of the Eurocode 9 design rules by providing additional data on more complex sections. The program consists of: 17 rectangular hollows, 19 angles and 6 RHS-specimens with openings, see Figure 3-2. The specimens were made of the aluminium alloy 6063 T6. The length of the specimens was varied in order to cover the slenderness ratios used in practice. In the tests, the specimens were completely fixed with the frame of the testing machine. The specimens were loaded into uniform compression, by using displacement control.

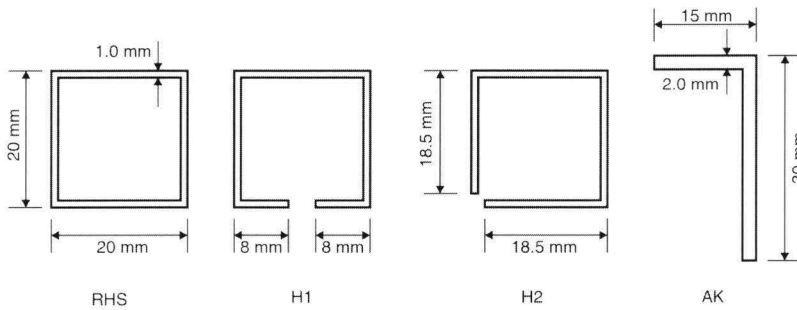


Figure 3-2 Cross-sections tested in the Helsinki program.

Comparable to section 3.1.2, the geometrical properties, material characteristics and experimental results are presented in appendix A. Two or three identical tests (A, B and C) were executed on each type of cross-section. Note that imperfections were not measured. The results of the Helsinki program will be used in Chapter 6 to validate the results of the newly developed prediction model.

3.2 Executed tests – Eindhoven program

3.2.1 Test series

The Eindhoven test program consists of three series of uniformly compressed aluminium extrusions. The material was specified as AlMgSi0.5 (6063-T6). Subsequent series regard: rectangular hollow sections (RHS), U-sections (US) and complex sections (CS) as presented in Figure 3-3. The tests on RHS-specimen are reported in both Mennink (1999b) and Mennink et al. (2000). The tests on US-specimen are described in detail in Peters and Mennink (2000) as well as in Mennink et al. (2001). Finally, the results on the CS-specimen are described in Schillemans (2001) and in Mennink and Schillemans (2002).

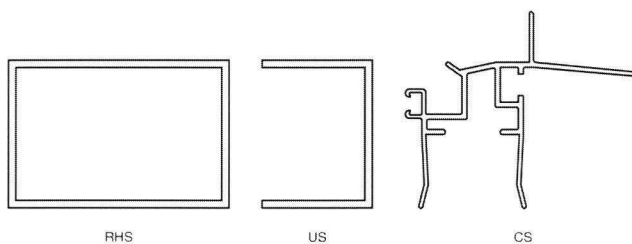


Figure 3-3 Examples of cross-sections tested in the Eindhoven program

The first test series consists of 17 compression tests on rectangular hollow sections (RHS). The aim of these tests was twofold: first, to determine the accuracy of the applied test set-up, by variation of support conditions and specimen length. Secondly, to obtain experimental data on local buckling of internal plates (webs) while taking account for the influence of connecting plates.

The second test series consisted of 21 compression tests on U-shaped (US) sections. The specimens were obtained from rectangular hollow sections by cutting. The aim of this series was to obtain experimental data about local buckling of outstands (flanges), including the stiffening influence of a connecting internal plate element (web). U-sections have two characteristic aspects. First of all, as the critical length of outstands is much larger than its plate width one would need very tall specimen to obtain more than one buckle over the specimen length. Secondly, flange buckling of U-sections may result in such a reduction of overall bending stiffness that in order to prevent the occurrence of column buckling one would need very compact, short, specimens. As these two aspects contradict, it is almost impossible to accommodate both. Moreover, it is very hard to determine in advance the influence of even one aspect. Therefore, it was chosen to use a constant, arbitrary chosen, specimen length of $L = 300$ mm. Though the influence of support conditions as well as overall buckling may both still occur, this approach highly simplified the test set-up and thus enhanced the quality of the execution.

The third test series consisted of 40 tests on extrusions with 12 types of complex cross-sectional shapes (CS). The specimens were obtained from commercially available extrusions used in greenhouses. The aim of these tests was to obtain experimental data on the cross-sectional instability behaviour of cross-sections that cannot be investigated by the current design codes. Well over a hundred cross-sections were studied in advance to determine the appropriateness of these specimens with respect to cross-sectional instability. The finite strip program CU-FSM, see section 2.4.4, allowed the determination of the critical stresses for cross-sectional and overall instability. The twelve cross-sections were chosen, as their critical stress σ_{cr} is substantially less than the 0.2% proof stress $f_{0.2}$. Their cross-sections are presented in Figure 3-4. Various specimen lengths were determined in order to obtain either solely cross-sectional instability or interaction with overall modes.

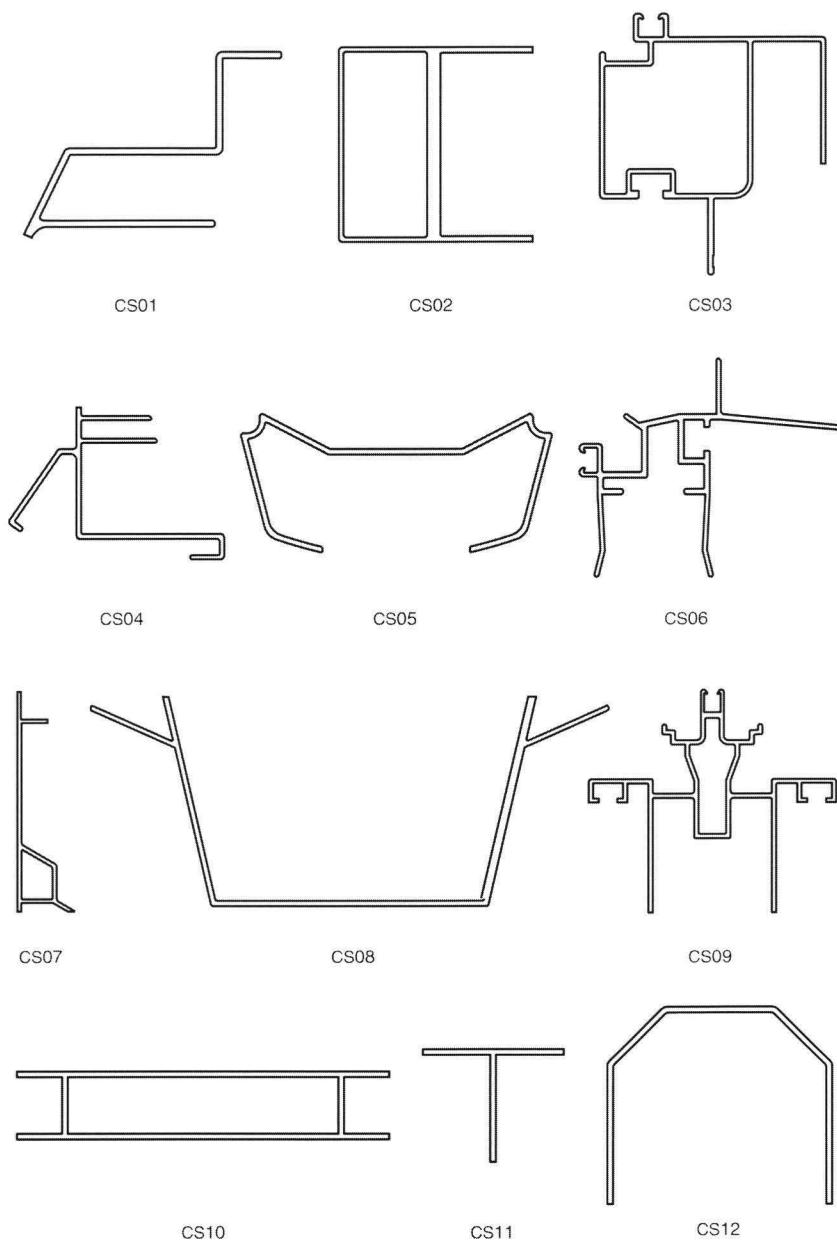


Figure 3-4 Complex sections (CS) tested in the Eindhoven program

3.2.2 Dimensions and geometrical properties

A clear distinction exists between the relative simple RHS and US-specimen versus the complex specimens. The geometry and dimensions of simple cross-sections can easily be determined; those of complex cross-sections cannot. In addition, the input for the finite element and prediction models of the following chapters requires a schematisation of the cross-section to a combination of lines and nodes.

The four sides of the RHS and the three sides of the US test specimens are numbered according to Figure 3-5. In order to execute numerical analyses, the cross-sections are reduced to their heart lines and represented by a series of plates and nodes. These are specified by the plate widths (b and h , respectively b_1 , b_2 and b_3) and thicknesses (t) of each plate. In addition, the axial length (L) is measured. The resulting dimensions are presented in appendix B. The external dimensions and plate thicknesses have been measured using electronic sliding callipers. These callipers have an accuracy of 0.02 mm for dimensions less than 150 mm and an accuracy of 0.1 mm for larger dimensions. Presented results are averages of at least three measurements. Tolerances between actual and nominal values have been compared to the German code (DIN 1987) in Mennink (1999b) and Peters and Mennink (2000). It was concluded that the maximum allowable tolerances were not exceeded. As the extrusion process allows a very accurate production, no measurements were performed on the deviation from the shape of the cross-section.

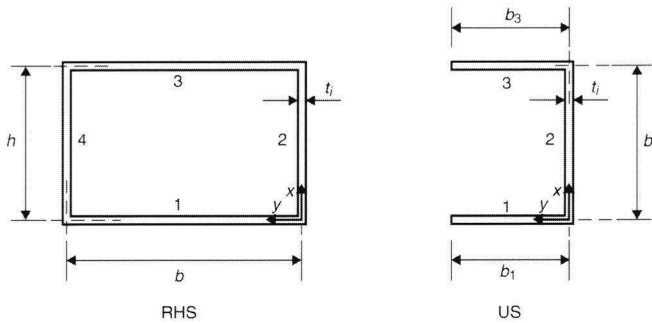


Figure 3-5 Determination of the cross-sectional properties of rectangular hollow (RHS) and U-shaped (US) sections

It is far more difficult to measure the dimensions of the complex (CS) sections. The difficulty is to determine the specific plates. Spark erosion is used to obtain a slice of the profile, which is subsequently scanned to a digital image. See the example of Figure 3-6. Nodes and lines are added to this image by hand to obtain plate elements. The dimensions of all complex sections are specified in appendix B and in Mennink and Schillemans (2002).

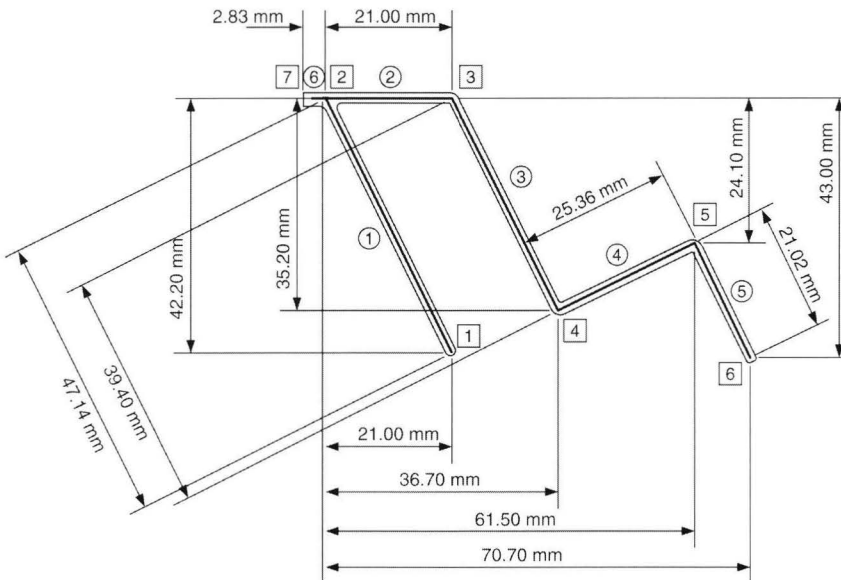


Figure 3-6 Determination of the actual dimensions of the complex sections of the Eindhoven program (Specimen CS01)

The presented approach allows the determination of the geometrical properties of arbitrary (slender) cross-sections. They were determined with the program CU-FSM, as referred to in section 2.4.4. This is obtained by reducing the actual cross-section to the heart-lines of their respective plate elements. Mennink (1999c and 2000) concluded that the deviation between the actual and schematised geometrical properties of the regarded RHS and US specimens is negligible. The presented approach thus provides the necessary input for the finite element and prediction models of the following chapters.

3.3 Test set-up

3.3.1 Methods of testing

In general, three types of test set-ups can be distinguished to determine the buckling behaviour of uniformly compressed elements. As presented in Figure 3-7, these are: pin-ended columns, clamped edges, and individual plates. As the test set-up (test rig and load application) has a significant influence on the test results, this section provides an overview of these methods. With respect to the text, reference is made to the following literature: Rasmussen (2000), Singer et al. (1998), and Venkataramaiah and Roorda (1982).

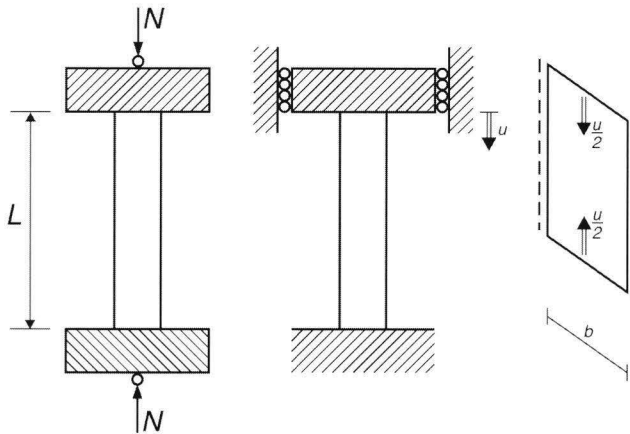


Figure 3-7 Test set-up configurations for the execution of compression tests

The traditional test set-up for overall buckling is the application of pin-ended columns. The column is loaded into axial compression through the gravity centre of the cross-section, most often by displacement control. The assumption is that the buckling length of the column is exactly known. Thus, the approach is well suited for flexural buckling. Note that the fabrication of “perfect” hinges proves to be troublesome. The influence of (small) edge moments can be studied by applying eccentric loads. In case of cross-sectional instability, the gravity centre shifts towards the effective part of the cross-section (see section 2.4). The resulting eccentricity of the applied load causes a bending moment in the cross-section and subsequently a decreased stiffness of the post-buckling branch. This test set-up is thus not well suited to determine cross-sectional instability, or its interaction with overall instability.

The second approach is to use columns with clamped edges. The load is then applied by means of a uniform edge displacement. This results in uniform compression in the elastic range, but provides bending moments when overall buckling occurs. Because of the clamped edges, the buckling length is known exactly, while it is easier to fabricate clamped edges than it is to fabricate hinges. Note that additional equipment is needed to measure the edge moment. This test set-up has the following advantage. If the gravity centre of the cross-section shifts, as described in section 2.4, the centre of the applied load will shift as well. This approach is better suited to regard cross-sectional instability. Especially while the specimen is less susceptible to overall buckling, as the critical length of a clamped column is twice as large, the critical load four times as large, as that of a pin-ended column.

Finally, the third approach specifically studies a part (often a plate) taken out of the cross-section. This part is then loaded into compression by providing support conditions along its edges. This approach is very well suited to regard the behaviour of individual plate elements, as it is not susceptible to aspects like overall buckling, the shift of gravity centre and reduced support conditions. Obviously, this approach is very well -and only- suited to investigate local (and to a limited extent) distortional buckling. Note that the support conditions are of extreme importance and require specific tools. Fabrication and calibration of these is often a very difficult task.

The most important parts of the test set-up are the edge supports. Fixation due to clamping, bonding, or welding (not advisable for aluminium because of heat-softening), combined with a uniform edge displacement results in local stress concentrations at these supports. In case of tests on stocky specimens, this results in failure at the supports. A different approach is to place the test specimen between two end plates without any additional supports. The only support results from friction, which can even be reduced by the use of Teflon layers. Subsequently, the stress concentrations are less as the support against edge translations and rotations is minimal. Note that such a support cannot resist tensile stresses that may occur due to buckling.

It can be concluded that the type of test set-up depends on the aim of the research. As the Eindhoven program aims at cross-sectional instability, clamped edges were used. The presented remarks are used in subsequent sections to evaluate and compare the experimental results.

3.3.2 Test set-up Eindhoven experimental program

The test set-up used in the Eindhoven experimental program is presented in Figure 3-8. The specimens are placed, freely, within fixed supports. Thus, the specimens resemble clamped columns that are loaded into compression by a uniform axial edge displacement.

The tests have been executed on a 250-kN bench. The bench is operated on displacement control of the hydraulic cylinders, which is steered by the measurement of the axial shortening of the specimens. Two perfectly flat support plates were fixed to the test rig; their flatness and parallelity was verified with an accuracy of 0.01 mm. The specimens were placed freely in between these plates. Double layers of Teflon were applied in-between the RHS-specimen and the support plates, in order to minimise friction and thus obtain an almost undisturbed displacement field. Teflon led to a remarkable improvement of the results of cross-sections failing through squashing, as presented in section 3.6.2. Unfortunately, the reduction of friction also allows the occurrence of slip. As this could result in unwanted effects on overall and flange buckling, Teflon was not applied in the tests on US and CS specimens.

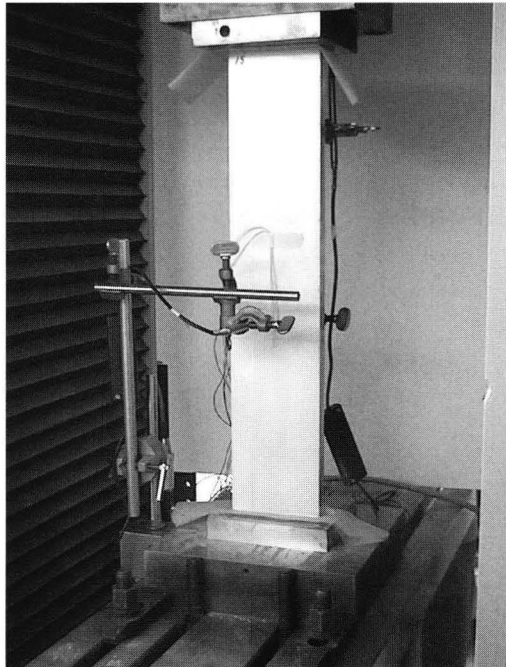


Figure 3-8 Test set-up compression tests Eindhoven program

In order to obtain uniform axial shortening, both edges of the test specimens have to be flat, as well as parallel to each other. The RHS as well as the U-sections have been machined with an accuracy of 0.01 mm. Despite the effort on accuracy, some edges still showed a few small wires from the machining. Therefore, the spark erosion process was used to obtain flat edges for the complex sections. This process resulted in an even more accurate flatness (no wires, accuracy of 0.005 mm). However, the resulting parallelity of the edges was substantially less and resulted for some cases even in visual gaps in the order of 0.1 mm.

3.3.3 Test equipment

Measurements were made using four different types of equipment. The test bench measured the applied load, displacements were measured with so-called LVDT's, axial strains with strain gauges, and displacement patterns with ESPI. A short overview of these equipments as well as their use is presented below.

Displacements were measured using so-called LVDT's, which stands for "Linear Variable Differential Transformer". The axial shortening of the test specimen was measured by LVDT's placed on a rig and resting against the upper support plate (see Figure 3-8). Respectively one, three and four LVDT's were used during the test series of respectively the RHS, the US, and the CS-specimen. From the results of the LVDT's it is possible to draw conclusions with respect to the axial strain as well as the accuracy of the uniform edge displacement. Out-of-plane deformations were measured as well. Though these results are not accurate enough to be used as amplitude of the actual deflections, they provide insight into the load at bifurcation.

Strain gauges were placed in axial direction at different plates of the test specimens. The strain gauges have a length of 6.0 mm, and are accurate to a strain of at least 0.004 mm/mm. They resulted load-strain curves, which allow the investigation of local and overall buckling. It has to be noted that in most cases the maximum deflections (buckles) did not occur at the strain gauges. Their results are therefore only useful in the elastic region and when compared to the numerical finite element results of the following chapter.

An ESPI (Electronic Speckle Pattern Interferometer) system was used for the RHS and U-sections, see also Jones and Wykes (1983). This laser system allows the measurement of displacement increments for a field; a specimen length of 200 mm could be regarded accurately. Note that it is too laborious to obtain the total deformations during loading. Therefore, the ESPI-results provide only increments in displacements. It was used to visualise the out-of-plane deformations in the elastic range. In fact, it provided information about the elastic local buckling behaviour.

3.4 Imperfection measurements

3.4.1 Imperfection measurements on rectangular hollow and U-sections

Geometrical imperfections of aluminium extrusions are in general very small. This is a result of the accuracy of the extrusion manufacturing process as explained in section 2.2.3. Therefore, only a limited investigation was executed on the actual size and shape of the initial imperfections of the RHS and US test specimen. The test set-up used is presented in Figure 3-9. The test specimens are placed on a perfectly flat plate, while a displacement indicator (further called LVDT) is positioned over the centre of the specimen. This position is used as origin, at which the value of the displacement indicator is set to zero. Assuming an imperfection pattern with peaks in the middle of the plate, the specimen is slid in both the axial and lateral directions of the plate. This procedure is repeated for all sides of the specimen. The maximally registered value, referred to as e_0 , provides an indication of the magnitude of the imperfections. As previously stated this approach is rather inaccurate and provides only an indication of the magnitude of the initial imperfections. Finite element analyses showed that if failure occurred due to flexural buckling, the magnitude of the imperfections did have an influence on the failure load of up to 10%. Therefore, more accurate imperfection measurements were executed on the CS-specimens.

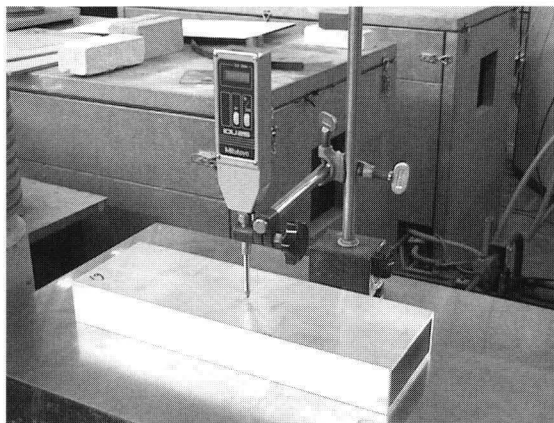


Figure 3-9 Set-up imperfection measurements - Rectangular hollows

3.4.2 Imperfection measurements on complex cross-sections

To obtain more insight into the actual imperfections, extensive measurements were performed on the initial deflections of the complex cross-sections. A computerized bench was used to accurately measure the flatness of each plate of a cross-section, see Figure 3-10. Each specimen was placed on the bench and the flatness of each plate was measured for a large number of points.

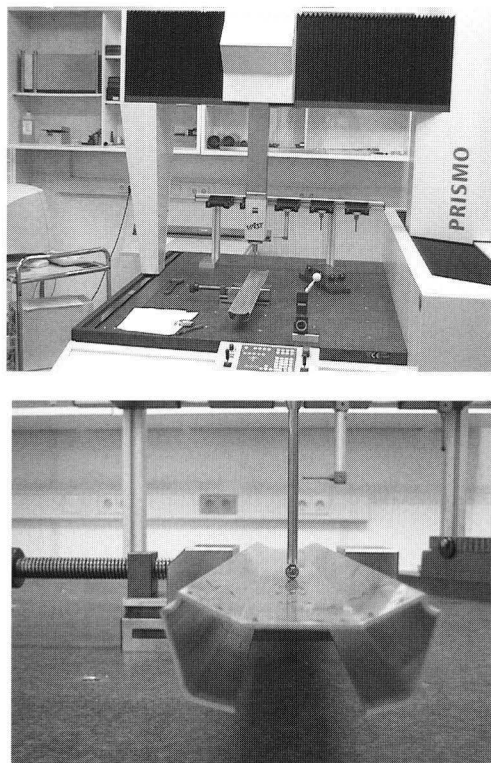


Figure 3-10 Set-up imperfection measurements – Complex cross-sections

Two examples of measured deformation patterns are given in Figure 3-11. These present the shape of the largest flange (plate 1) of specimen CS01-2, respectively that of the web (plate 2) of section CS10-2 (see appendix B). A more complete presentation of the imperfections is given in Schillemans (2001) and in Mennink and Schillemans (2002). The flange of the CS01-2 specimen shows an obvious curvature of the entire specimen, as well as a less pronounced twist. Local initial imperfections are small; with the exception of “large” (0.06 mm) imperfections at the specimen edges. The shape of the CS10-2 shows a dent over the entire specimen length. In both cases, the imperfection pattern is governed by overall imperfections.

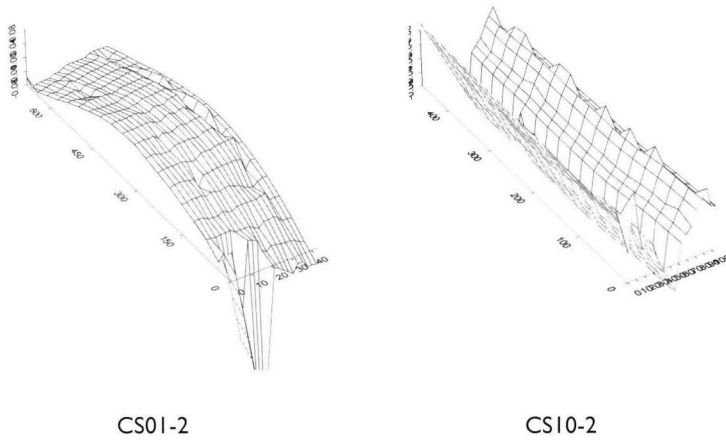


Figure 3-11 Measured imperfection patterns of complex test specimen

3.4.3 Determination of the imperfection amplitude

Imperfection patterns may be characterised by their shape and amplitude. Section 4.1.2 will explain that the finite element analyses apply imperfection shapes according to the deflected shape of the first Eigenmode of the specimen. Thus, the aim of the imperfection measurements is to provide the according amplitude, denoted by e_0 .

The amplitude e_0 is determined from the measured imperfections of that plate for which the deformation pattern of the Eigenmode of the FE-analysis results the largest deformations. This plate is either internal (web) or outstand (flange). Note that the critical length of the Eigenmode approximates the specimen length for overall buckling, distortional, and flange buckling, whereas for local buckling of internal plates, it approximates the plate width. Therefore, a distinction is made between overall and local imperfections.

The RHS and US-specimens were slid in axial and lateral direction. For the RHS-specimens the maximum values measured in these directions provide some measure for the overall ($e_{0,ov}$), respectively local ($e_{0,loc}$) imperfections. All U-sections fail through either flange or overall buckling. Therefore, no distinction is made and the maximum value of the measured deflections is used as imperfection amplitude (e_0).

For the CS-specimens, ($m =$) 3 to 4 measurements were made in the lateral (x -) direction and ($n =$) 20 to 30 in the axial (y -) direction. Thus, 60 to 120 measurements were made for each individual plate. Each measurement (ij) is described by its coordinate in the x -, and (axial) y - direction. The measured deflection is described by z_{ij} . Note that the origin of the x -, y -axis is positioned at measurement (1;1).

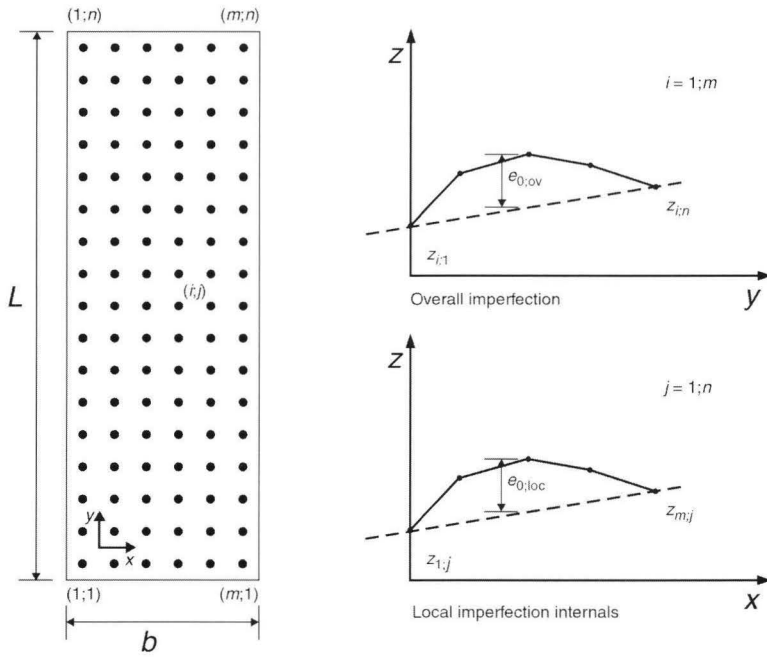


Figure 3-12 Determination of the imperfection amplitude e_0

The overall imperfection amplitude $e_{0,ov}$ (due to overall, distortional, or flange buckling) is determined based on the imperfections at the two longitudinal edges ($i=1$, and $i=m$), see Figure 3-12:

$$e_{0,ov} = \text{MAX}_{j=1..n} \left(z_{i;j} - z_{i;1} - \frac{z_{i;n} - z_{i;1}}{y_{i;n}} y_{i;j} \right) \quad \text{eq. 3-1}$$

However, if the deflection z at one of the four edge points is extreme, it is allowed to use the value of z of an adjacent point. See for example the deflection pattern of CS01-2 in Figure 3-11.

The amplitude $e_{0,loc}$ due to local imperfections of internals is determined based on the maximum local imperfection for each cross-section j :

$$e_{0,loc} = \text{MAX}_{j=1..n} \left(\text{MAX}_{i=1..m} \left(z_{i;j} - z_{1;j} - \frac{z_{m;j} - z_{1;j}}{x_{m;j}} x_{i;j} \right) \right) \quad \text{eq. 3-2}$$

Note that large local deviations may occur at the specimen edges. As these are of no interest for the local buckling behaviour, they have to be disregarded. Practically, cross-sections within an axial distance of $b/2$ from the edges are neglected in determining e_0 .

3.4.4 Results imperfection measurements

The results of the imperfection measurements are summarised in Table 3-1. Already the table shows that initial imperfections are small; $e_0 < 0.35$ mm, which is generally less than 5% of the plate thickness. Commercial tolerances allow overall imperfections of $L/500$ in some extruded aluminium members, though $L/1000$ is rarely exceeded (Mazzolani 1985). With the lengths given in the tables of appendix B, Mennink (1999b), Peters and Mennink (2000), and Mennink and Schillemans (2002) concluded that the overall imperfections never exceed $L/1000$ and are in average even less than $L/3600$.

Table 3-1 *Amplitudes of the measured imperfections, Eindhoven program*

RHS			US				CS		
Test	$e_{0,ov}$	$e_{0,loc}$	Test	e	Test	e	Test	$e_{0,ov}$	$e_{0,loc}$
RHS01	-	-	US01	0.07	US18	0.24	CS01	0.10	0.01
RHS02	0.07	0.00	US02	0.23	US19	0.00	CS02	0.04	0.06
RHS04	0.03	0.00	US03	0.00	US20	0.07	CS03	0.05	0.00
RHS05	0.05	0.00	US04	0.16	US21	0.04	CS04	0.02	0.02
RHS06	0.11	0.02	US05	0.21	US22	0.04	CS05	0.12	0.10
RHS07	0.09	0.05	US06	0.09	US23	0.00	CS06	0.30	0.04
RHS08	0.25	0.08	US07	0.00	US24	0.00	CS07	0.06	0.01
RHS09	0.30	0.08	US08	0.13	US25	0.22	CS08	0.20	0.31
RHS10	0.15	0.04	US09	0.15	US26	0.31	CS09	0.08	0.01
RHS11	0.15	0.03	US10	0.12	US27	0.00	CS10	0.08	0.11
RHS12	0.21	0.20	US11	0.03	US28	0.00	CS11	0.29	0.02
RHS13	0.25	0.08	US12	0.00	US29	0.24	CS12	0.08	0.11
RHS14	0.35	0.20	US13	0.04	US30	0.15			
RHS15	0.06	0.03	US14	0.04	US31	0.00			
RHS16	0.06	0.10	US15	0.00	US32	0.00			
RHS17	0.20	0.06	US16	0.00	US33	0.07			
RHS19	0.10	0.04	US17	0.31	US34	0.09			

3.5 Material characteristics

3.5.1 Test set-up tensile tests

The most commonly applied test in metal structures is the tensile test, executed to determine the material characteristics. In practice, one is concerned with strength and tensile tests are used to determine both the 0.2% proof stress $f_{0.2}$ and the ultimate stress f_u . However, as the determined material characteristics will be used as input for finite element analyses of Chapter 4, the actual stress-strain relation in both the elastic and inelastic ranges have to be determined more accurately. This includes the modulus of elasticity E , and the 0.1% and 0.2% proof stresses $f_{0.1}$ and $f_{0.2}$.

Tensile tests have been executed according to NEN-EN 10002-1 (NNI 1991). The geometry of the specimens was specified as: "Niet-proportionele proefstaaf (Non-proportional test specimen) type 1", as presented in Figure 3-13.

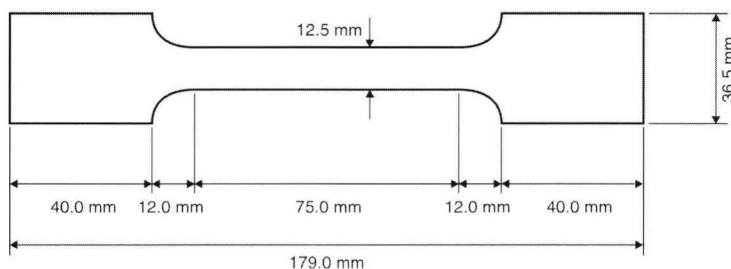


Figure 3-13 Dimensions of the tensile test specimens

A 20 kN Zwick Z020 test bench was used (see Figure 3-14). The load is applied by displacement control. The test specimen is clamped at its edges by so-called wedge grips (The gripping force changes via a moveable wedge, in a constant ratio to the tensile force. This ratio is fixed by the wedge angle). These are screwed to the frame so they can be considered as fixed supports. Though these clamps are aligned, it is possible that small bending moments occur. Two strain gauges are applied at the centre of the opposite sides of the specimen. They have a measuring length of 6.0 mm, and are accurate to a strain of at least 0.004 mm/mm. In order to determine a substantial part of the plastic range, a displacement meter was used as well with an initial length of $L_0 = 50$ mm and its measuring range set to 2.0 mm.

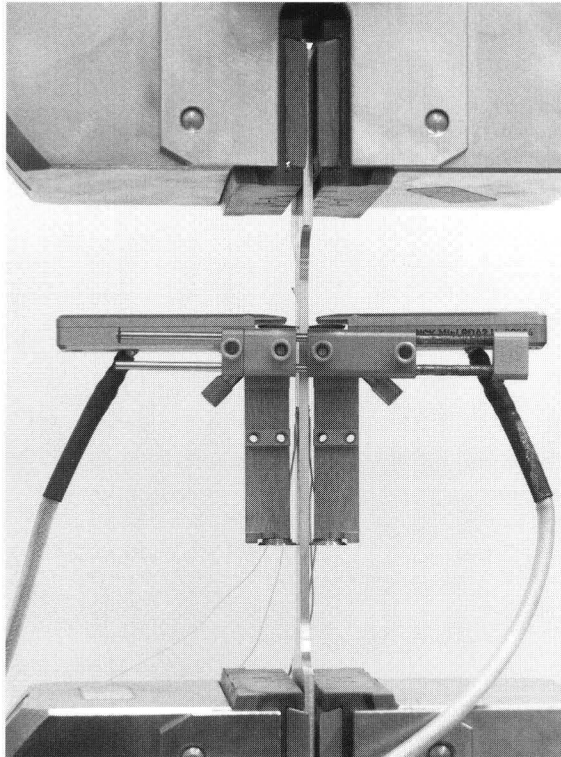


Figure 3-14 Test set-up tensile tests

3.5.2 Determination of tensile test results

The tensile tests result the applied force (N), the measured strains (ε) of the two strain gauges and a displacement u measured with the displacement indicator. By neglecting the influence of lateral contraction, these are transformed to three curves representing the engineering stresses and strains of Figure 3-15. Division of N by the measured area (thickness * width) results in the engineering stress σ_e ; division of u by the measurement length L_0 results in the engineering strain ε_e . Initial setting of the test set-up causes an initial non-linear measurement of u . Therefore a horizontal shift u_0 has been applied, such that the initial stiffness of its σ_e - ε_e curve coincides with that of the average of the strain gauges. Taking account of the lateral and thickness contraction results the true stresses and strains, σ_t and ε_t . Though its influence is negligible for the elastic and inelastic range (<1.0%), the following equation is used as described in for example Hertzberg (1996). These results are included in the diagrams of appendix C.

$$\varepsilon_t = \ln(1 + \varepsilon_e) \quad \text{and} \quad \sigma_t = \sigma_e (1 + \varepsilon_e) \quad \text{eq. 3-3}$$

The load is applied using displacement control with a velocity of 0.36 mm/min and increased until an average stress of 150 N/mm² is obtained. The specimen is unloaded (0.36 mm/min) until an average stress of 30 N/mm². Then it is reloaded (0.36 mm/min) until a strain of at least 0.006 mm/mm is reached. The loading velocity is then increased to 1.4 mm/min until the specimen fails. The unloading and reloading branches are clearly visible in the figure and show a substantial amount of plastic strains, even at low stresses. The commonly used approach to determine E is to draw a straight line through the “elastic” part of the material characteristic, even if no load-cycle is executed, and obtain E from its angle. Obviously, the accuracy of such an approach is limited. As the intention of the tests is to determine E within a 5% accuracy, a more accurate procedure is used as outlined below.

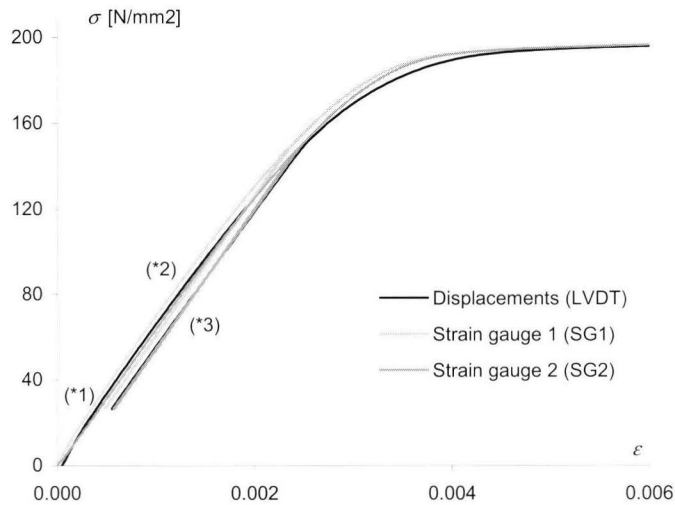


Figure 3-15 Results tensile test – stress-strain relation

The stress-strain relation of the material characteristic is transformed to stiffness-strain (E - ε) relations (see Figure 3-16). The E - ε graph to the left presents the tangential stiffness E_T of both strain gauges. It is observed that initial loading results in substantial difference in stiffness between the strain gauges, (*1) in Figure 3-16, which coincides with an initial bending moment. Subsequent load (or strain) increase results in the non-linear curve (*2). Non-linear behaviour occurs at relatively low loads. Therefore, the specimen is unloaded and subsequently reloaded which results the parallel horizontal lines at (*3). The specimens show almost linear elastic behaviour during this phase.

The righter $E-\varepsilon$ diagram presents the average tangential stiffness of the strain gauges and the secant stiffness of the displacement measurements. Note that the secant stiffness highly depends on the previously described horizontal shift u_0 . The secant stiffness of the unloading and reloading branch (*4) is of no physical meaning as it consists partially of plastic strain. Contrarily, the results of the unloading and reloading branch of the strain gauges (*3) show a linear behaviour that is well suited to determine the modulus of elasticity E . The vertical lines at positions I and II coincide approximately with a stress of $\sigma_I = 30$ and $\sigma_{II} = 100 \text{ N/mm}^2$. These describe the range in which E is determined.

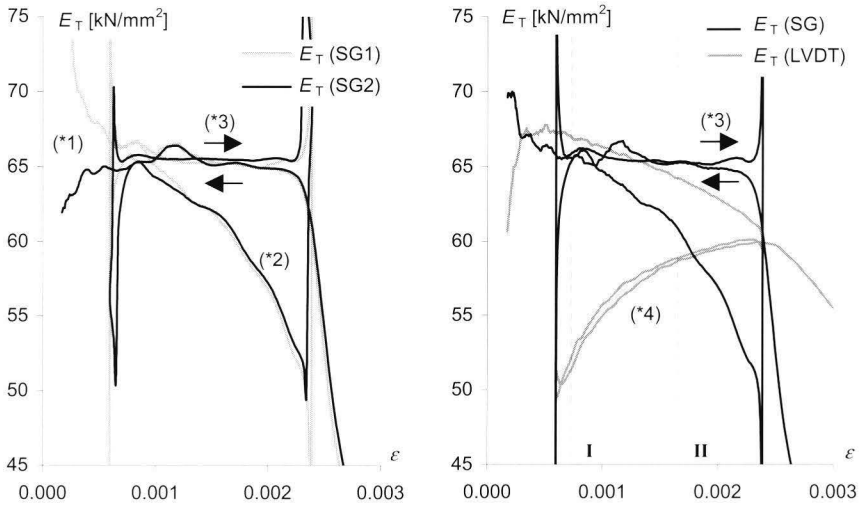


Figure 3-16 Results tensile tests – tangential stiffness CS05

The average value of E is determined from the reloading branch of the strain gauges by:

$$E = \frac{\sigma_{II} - \sigma_I}{\varepsilon_{II} - \varepsilon_I} \quad \text{eq. 3-4}$$

The material parameters are determined according to the average stress-strain curve of the strain gauges. The values of $f_{0,1}$ and $f_{0,2}$ are obtained from the actual material characteristic of Figure 3-15, for measurement i :

$$f_{0,1} = \sigma_i \quad \text{when} \quad \frac{\sigma_i}{E} + 0.001 = \varepsilon_i \quad \text{eq. 3-5}$$

$$f_{0,2} = \sigma_i \quad \text{when} \quad \frac{\sigma_i}{E} + 0.002 = \varepsilon_i \quad \text{eq. 3-6}$$

Finally, the maximum stress of the stress-strain curve is taken equal to f_u . Note that the actual determination of the ultimate strength f_u is still a matter of debate. However, as this value is not used within this thesis it is not elaborated on.

3.5.3 Remarks

Aluminium shows a substantial amount of inelasticity, even in the “elastic” range. In order to determine an accurate value of the modulus of elasticity E , it is therefore necessary to execute tensile tests with at least one load cycle. The presented approach for the subsequent calculation of E proves to be more accurate than traditional curve fitting. The results of the tensile tests, as summarised in appendix B, show a remarkable consistent value of E (66 kN/mm²). This is substantially lower than the generally used value of 70 and its accorded bandwidth of 68 to 72. Thus, the question arises whether the generally used value of 70 is accurate, at least for the 6000-alloys.

3.6 Results compression tests

This section summarises the results of the three series of compression tests. The following types of results are presented: deformations, strength, and stiffness. To limit the amount of data only those results are presented that provide insight into specific aspects of the buckling behaviour. Note, all load-displacement curves are presented in appendix C.

3.6.1 Deformation patterns and failure modes

Figure 3-17 present representative failure modes for the rectangular hollows (RHS), U-shaped (US), and complex (CS) test specimens. Based on the definitions of section 1.2, the following modes can be distinguished:

- *Squashing (S)*
The occurrence of large plastic axial strains and stresses above $f_{0.2}$ is defined as squashing. An example is RHS05.
- *Flexural buckling (F)*
Flexural buckling of a two-sided clamped column results a kink at half the specimen length. However, application of Teflon-layers for the RHS-specimen, partially allows translations at the edge supports. As a result, the position of the kink lies approximately at three-quarters of the specimen length (RHS12). The Teflon layers are therefore not advisable when investigating overall buckling, as the buckling length cannot be accurately determined.
- *Torsional (T) and flexural-torsional (FT) buckling*
Torsional buckling results in a rotation of the cross-section (CS11-2); flexural-torsional buckling results a combination of deflections and rotations (US14).

- *Local buckling (L)*
The occurrence of out-of-plane deformations for axial stresses below $f_{0.2}$ is defined as local buckling (RHS14, US04, US01, CS10-3). The buckle that localises at the ultimate load can occur at any position on the specimen-length. However, if a buckle occurs at the specimen edges this indicates an unwanted influence of the support conditions. It has to be noted that flange buckling of the U-sections (US01) results in buckling lengths comparable to the specimen length; in which case the supports may have a substantial influence.
- *Distortional buckling (D)*
Distortional buckling results in substantial cross-sectional deformations, which was observed for several of the complex specimen. This phenomenon is most clearly visible for the CS05 specimen.
- *Interaction of local and flexural buckling (L/F)*
When inelastic localisation (of local buckles) occurs, the cross-sectional stiffness reduces such that an interaction of buckling modes may occur (US10). However, it is also possible that this interaction leads to an adjustment of the flexural buckling length and, probably, the buckling load (RHS09).

Notably, the 40 tests of the complex series show all types of instability modes, as well as various types of interactions. The occurring modes have been described according to the previous definitions and are summarised in appendix B

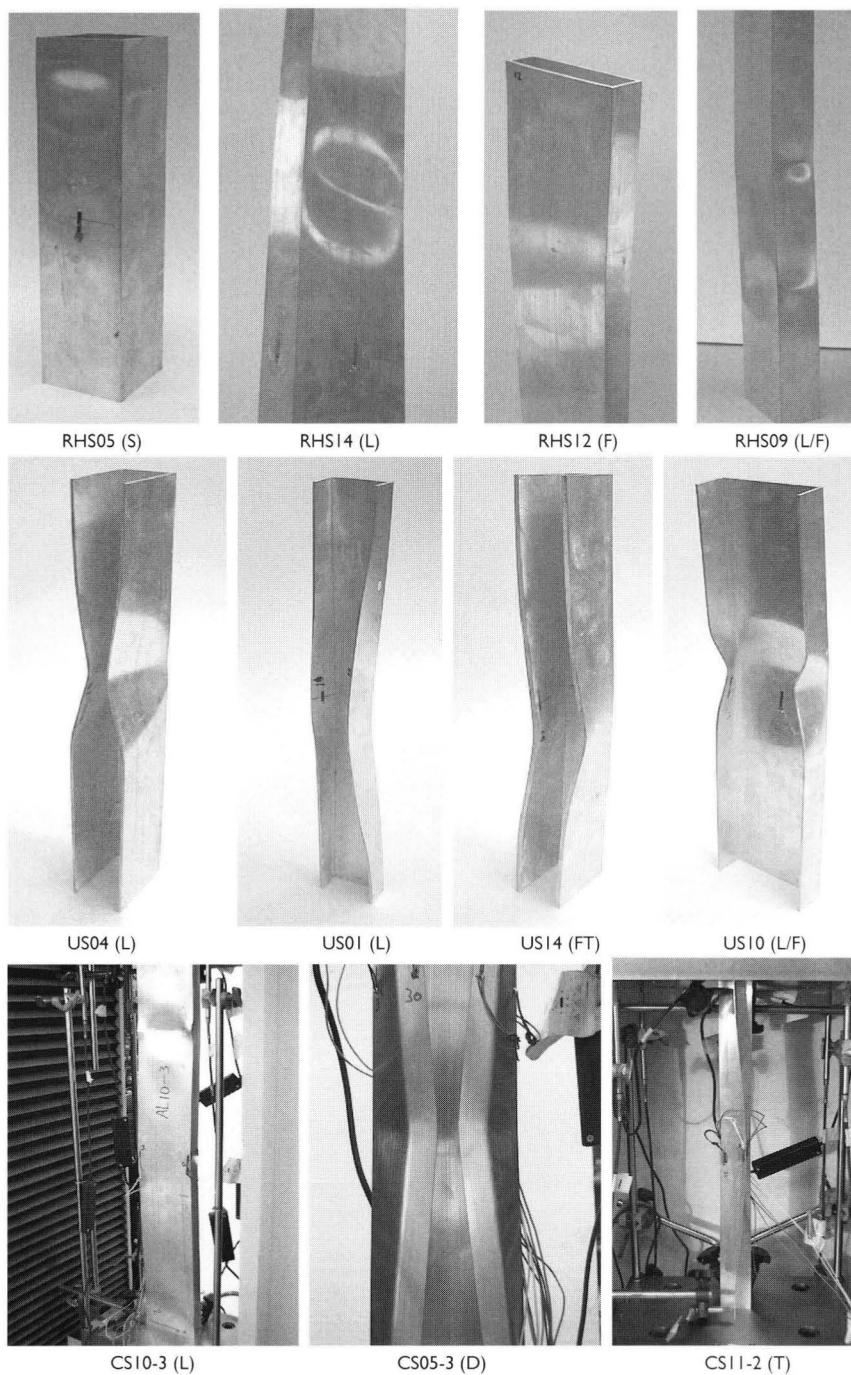


Figure 3-17 Characteristic failure modes observed in the Eindhoven test program

Application of the ESPI-equipment allowed the measurement of deformations in the elastic range. For specimen RHS07 the results are presented in Figure 3-18. The pictures show the lower half of side I of the specimen. The thirst three pictures are taken at 10% of the maximum load, the fourth at 25%. The horizontal lines of the axial displacements represent the axial deformations. As they are horizontal and occur at constant intervals, they show that the column is in uniform compression. Axial compression leads to lateral expansion, represented by the vertical lines of the lateral deformations. It is also visible that the influence of the supports is negligible. However, large disturbances did occur for the specimens without Teflon layers, causing the specimen to fail prematurely (Mennink 1999b). The circle lines in the out-of-plane deflections are the first occurrence of buckles. The diagrams show that buckling is already initiated at loads far less than the bifurcation load. In addition, the buckling pattern is initiated at the edge support, though failure occurs at a buckle at half the column length. From the continuous buckling pattern it is possible to determine the buckling length, for RHS07 $L_{cr} = 60$ mm.

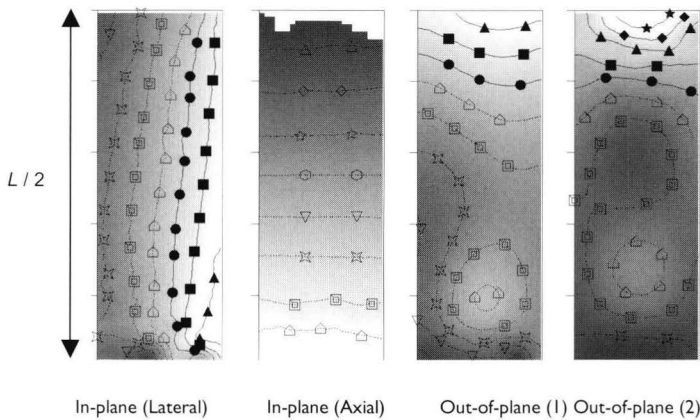


Figure 3-18 ESPI-results (RHS10)

3.6.2 Axial strength

This section evaluates the experimentally determined load-displacement curves. These curves relate the measured reaction force (N) in kN to the applied axial shortening (u) in mm, as presented in Figure 3-19A. However, to obtain comparable results the N - u diagrams are replaced by σ_{av} - ϵ_{av} diagrams presented in Figure 3-19B. These diagrams relate the average axial stress σ_{av} ($=N/A$) to the average axial strain ϵ_{av} (u/L).

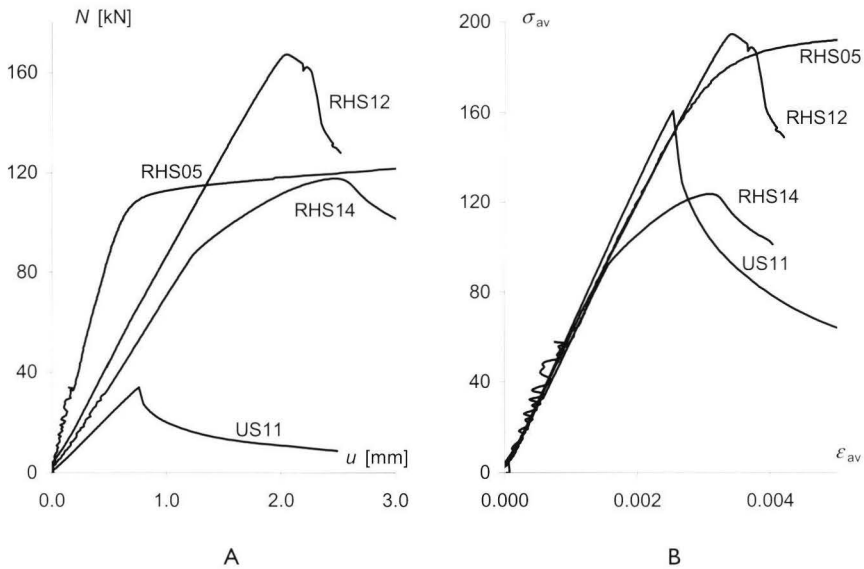


Figure 3-19 Characteristic load-displacement diagrams, Eindhoven program

The curves presented in Figure 3-19B are representative for the possible failure modes, as explained below. Two representative loads can be determined: the load at initial buckling N_{cr} , and the ultimate or failure load N_u . Though initial buckling is, obviously, only relevant in case of local buckling (e.g. RHS14). These loads as well as the according failure mode are summarised in appendix B, while appendix C presents all curves, as well as the procedure used to determine N_{cr} .

- **Squashing (S)**
The behaviour of a compression test on compact cross-sections (RHS05) resembles that of a tensile test. An accurately executed compression test will follow the material characteristic until the sudden occurrence of out-of-plane deformations, at substantial plastic strains.
- **Flexural (F) or flexural-torsional (FT) buckling**
If the dominant failure mode is overall buckling (RHS12, US11), the load-displacement curve shows little deviations from the elastic curve up to the ultimate load. Though column theory indicates a horizontal plateau (RHS12), most specimens fail with a sharp peak (US11). This occurs while the applied supports cannot support tensile forces.
- **Local (L) or distortional (D) buckling**
Sections susceptible to cross-sectional instability (RHS14) approach linear-elastically the bifurcation load N_{cr} . Subsequently, these cross-sections progress gradually into inelastic failure, which can be governed by overall buckling.

3.6.3 Axial stiffness

Additional information can be found from the results of the strain gauges. These were applied at mid-length of the specimen, and one at each plate. Two representative specimens are presented in the diagrams of Figure 3-20. These diagrams, for RHS14 and RHS07, include four strain gauges in grey; RHS14 also presents the average result of the LVDT in black.

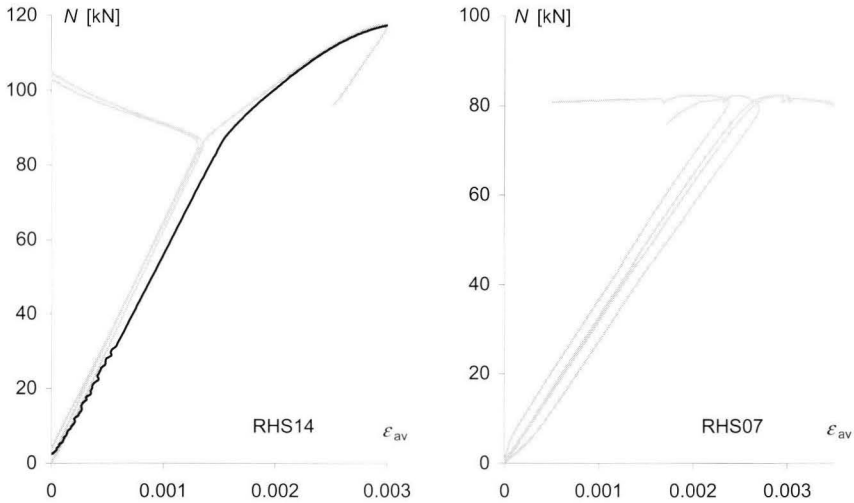


Figure 3-20 Characteristic load-strain curves: strain gauges in grey, LVDT in black

For RHS14 the strain gauges are identical up to the bifurcation load ($N_{cr} = 87.1$ kN), indicating uniform compression. Contrarily, the horizontal gap between the curves of RHS07 indicates load eccentricity. Assuming linear elastic theory, the horizontal difference $\Delta\varepsilon$ (arbitrarily determined at a quarter of N_u) between the curves can be used to obtain an indication of the difference in axial stress over the cross-section.

$$\Delta\sigma = E \Delta\varepsilon \quad \text{eq. 3-7}$$

The LVDT results show in general a less stiff behaviour than those of the strain gauges do. This is caused by the more accurate measurement of the strain gauges as well as the influence of inaccuracies during load initiation.

The stiffness of the load-strain curves has been analysed in appendix B as the compression stiffness E_c , and is, together with $\Delta\sigma$, summarised in section 4.5. It is concluded that the deviation between the stiffness of the tensile and compression tests is small.

3.7 Observations with respect to experimental research on stability

The previous sections presented the results of the Eindhoven experimental program as well as a summary of existing tests. As each of the three test programs (Salerno, Helsinki and Eindhoven) used a different testing procedure, the question arises which is the most appropriate:

- The Salerno tests used one fixed and one hinged support. However, no support rotations were observed which, according to the authors, is because the sections failed due to pure local buckling. Without rotations, there is no difference with the Helsinki and Eindhoven program that both used fixed supports. Nevertheless, as no rotations are intended, it seems more appropriate to fix the supports.
- Overall buckling and flange buckling of a clamped column can result in tensile forces at the supports. Clamped supports were applied only the Helsinki tests, whereas the Eindhoven (and Salerno) specimens were freely placed within the test arrangement. As a result, some of the Eindhoven tests failed suddenly (e.g. US1 I in Figure 3-19). On the other hand, the fabrication of clamped edges is very difficult for specimens with arbitrary complex shapes.
- In case of inelastic buckling, failure through local buckling will occur at the supports. This was observed in some of the Eindhoven and several of the Salerno tests. This is caused by an increase of the local stresses at the supports through friction with the support plates. The Eindhoven tests showed that application of double layers of Teflon improved these results, though caused in increased susceptibility to overall buckling as well.

It is concluded that the appropriateness of the various approaches is comparable with respect to cross-sectional stability. However, clamped edge conditions are preferable (Helsinki) in case of overall buckling, whereas friction should be reduced (Eindhoven) in case of squashing. However, the influence of aspects like material characteristics and imperfections is difficult to measure from experimental results and further conclusions will be drawn in Chapter 4 based on the results of finite element analyses.

4 Numerical research

Chapter abstract

This chapter presents the validation of a finite element (FE) model, using the specimens of the TUE-experiments of Chapter 3. Once validated, FE-analyses have the advantage that they provide more detailed information than experiments can. For example, they provide stress and strain distributions and deformation patterns of the entire specimen. The applied FE-model and input parameters like cross-section, imperfections, and material characteristics are explained; the results of parameter analyses are presented. Subsequently, the FE-model is validated by comparison of its results to those of the experiments. Thus validated, the FE-model is used in Chapter 5 in the development and validation of a general prediction model for local buckling of aluminium extrusions.

4.1 Executed FE-analyses

4.1.1 General

The aim of this chapter is to validate a finite element (FE) model, with respect to the cross-sectional stability behaviour of aluminium extrusions. Therefore, FE-analyses have been executed on almost all tests executed within the TUE experimental program, as described in Chapter 3. This section (see section 4.1) describes the applied geometry, imperfections, and material characteristics. Subsequent sections provide the set-up of the FE-model, a parameter study, and the results of the FE-analyses.

As specified in section 3.2.1 the experimental program consists of compression tests on 17 rectangular hollow sections (RHS), 21 U-shaped sections (US) and 40 tests on complex sections (CS). However, not all are analysed: Tests RHS01, RHS02, RHS04, RHS17, and RHS19 failed through squashing. Tests RHS15 and RHS16 have a varying plate thickness as well as internal radii. Tests CS09-1 to CS09-3 have very complex cross-sections, and thus inaccurate cross-sectional properties, while no tensile test was executed. This leaves 68 tests that have been simulated numerically.

As presented in section 3.2.2, the applied dimensions used in the FE-simulations are taken as closely as possible to those actually measured, by reducing the cross-sections to their heart-lines. The applied dimensions have been presented in appendix B.

4.1.2 Applied imperfections

Section 2.2.3 concluded that four major types of geometrical imperfections may occur: initial deflections and curvature, load eccentricities, eccentricities due to asymmetric cross-sections, and thickness deviations.

Initial deflections and curvatures are characterised by their shape and amplitude e_0 . The imperfection measurements of section 3.4 provide an indication of the amplitude of the imperfections. However, most measurements are not accurate enough to determine the shape of the imperfection pattern. Therefore, a simplified procedure is used that is in line with the commonly used research approach presented in section 2.2.3. The deformation pattern belonging to the lowest positive Eigenvalue of the specimen is applied for the shape of the imperfection pattern. Subsequently, the amplitude of this pattern is calibrated to the measured value of e_0 . The assumption is that failure will

occur according to this mode and that the applied imperfection pattern thus provides a lower bound solution. Note that this is not true for all cases, as both mode interaction and mode jumping may occur. However, the measured imperfections as presented in section 3.4 are very small and section 2.2.3 explained that in that case their influence is limited. Though some overall buckling phenomena may be very susceptible to small imperfections, this thesis focuses on cross-sectional instability. As this is characterised by a substantial amount of post-buckling strength, the influence of imperfections due to initial deflections is limited (see section 2.2.3). Note that the direction of these patterns (inward or outward) is not defined. It is therefore decided to apply the same direction as that observed from the deformed test specimens. The approach has been validated by the parameter analyses of section 4.3.

Load eccentricities (represented by $\Delta\sigma$) were measured in the experiments (see section 3.6.3). However, it is not known if these are caused by leaning, crookedness of the column, or due to non-parallelity of the loaded edges. Therefore, the influence of this deviation is not accounted for. As some of the experiments show substantial load eccentricities, it partially explains the deviations between the experimental and finite element results.

The influence of asymmetrical cross-sections and thickness deviations is accounted for by the application of the actually measured geometry and measured plate thicknesses. Note that the accuracy of the thickness measurement, as well as the accuracy of the extrusion process, reduces with decreasing plate thickness.

Thus, geometrical imperfections have been applied by using the actual geometry of the cross-section, the actually measured plate thicknesses, and by application of the amplitude of the measured initial plate deflections to the deformations of the first Euler Eigenmode.

4.1.3 Applied material characteristic

The stress-strain curves of the tensile tests, as obtained in section 3.5, are applied as material characteristic in the FE-analyses. The analyses are executed using a Von Mises yield criterion and a work-hardening stress-strain relation. The used procedure is described in Mennink (2002b). Section 3.4.4 concluded that the accuracy of the measured stiffness (E) from tensile tests is limited (5-10%). While both the buckling stress and post-buckling stiffness are linearly related to E , this may be an important cause for deviations between the experimental and finite element results.

4.2 Set-up finite element model

4.2.1 Mesh

The test specimens are simulated using a mesh of so-called curved shell elements. Each part of the test specimen is modelled as a rectangular plate, which is divided into rectangular elements. An example is shown in Figure 4-1.

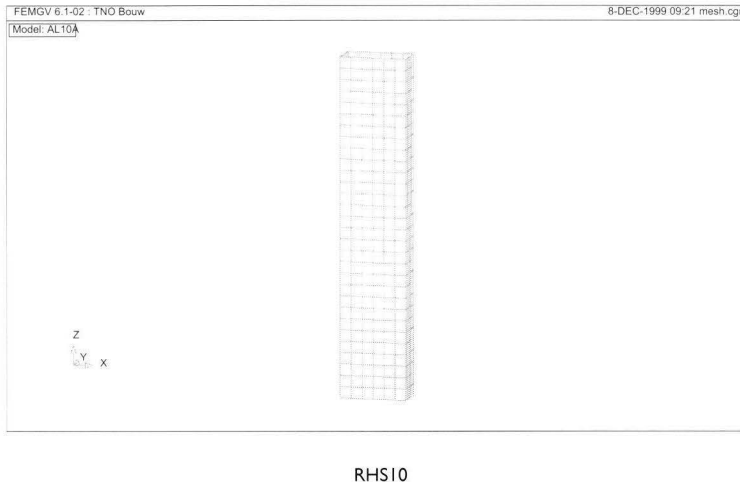


Figure 4-1 Mesh schematisation of specimen RHS10

Elements

The specimens are modelled in DIANA (De Witte et al. 1996), using CQ40S eight-node quadrilateral iso-parametric curved shell elements (see Figure 4-2), which are based on quadratic interpolation and a 2×2 point Gauss integration scheme over the element area. Straight normals are assumed, but not necessarily normal to the reference surface. Transverse shear deformation is included according to the Mindlin-Reissner theory; see for example Hertzberg (1996). The elements present a reduced deformation pattern. Instead of 6 degrees of freedom, each node has three translations as well as two rotations. Thus resulting forty degrees of freedom per element. The allowable deformations are presented in Figure 4-2. Typically, the strain ε_{xx} varies quadratic in x -direction and linear in y -direction, while the strain ε_{yy} varies linear in x -direction and quadratic in y -direction.

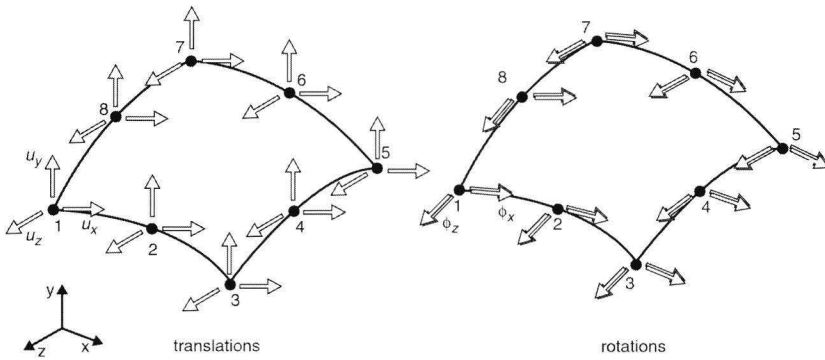


Figure 4-2 Degrees of freedom of the CQ40S-element

Application of seven thickness integration points in each of the Gauss points provides sufficiently accurate results. This is necessary to accurately describe a non-linear stress distribution over the plate thickness; compare Figure 4-3 A and B, as concluded in Mennink (1999a).

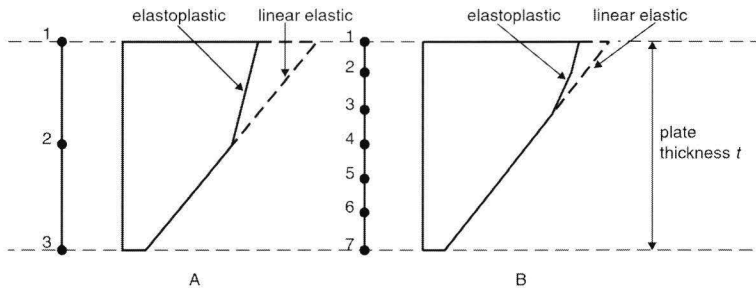


Figure 4-3 Elastoplastic stress distribution over the plate thickness, for a given combination of bending and compression strains, using respectively three and seven thickness integration points

Mesh density

Essential in the determination of the mesh density is the deformation pattern and the localisation of inelastic behaviour. The CQ40S-elements are able to accurately describe a quadratic deformation (deflection) pattern. For sine-shaped deflections, according to elastic buckling analyses, it would be sufficient to apply two elements for each half-sine. However, as inelastic stresses are determined only at the Gauss integration points, more elements and integration points are necessary to describe the deformations due to plastic localisation of a buckle.

A parameter analysis on the mesh density is presented in section 4.3.3. Analyses have been executed using respectively 4, 6, and 10 elements over the plate width; as square elements were used, the number of elements in longitudinal direction was defined. These analyses showed that four elements are sufficiently accurate for the description of the elastic range and the ultimate load, but overestimate the post-buckling strength. Therefore, meshes used in the RHS and US analyses apply a 6*6 mesh for each buckle.

For the complex sections (CS) the mesh density was reduced from a 6*6 mesh to a 4*4 mesh, as the total number of plates within these cross-sections would otherwise result in a huge number of elements. Nevertheless, all slender plates were attributed six elements over the plate thickness, whereas compact plates received only two. The number of elements in axial direction is based the number of elements resulting from application of 4*4 mesh for each buckle, or that of an arbitrary chosen element length-width ratio of 3. For each specimen the mesh density is summarised in Mennink (2002b).

Support / loading conditions

In the experiments, the specimens are positioned on steel support plates, as explained in section 3.2.2. Though this resembles a fixed end support, it is based on friction only. Nevertheless, parameter analyses (Mennink 1999a) concluded that the influence of the support conditions is negligible for specimens with sufficient length or if buckling occurs in the elastic range.

As Teflon-layers were applied, the RHS tests have been simulated using supports that allow the edge cross-sections to expand and translate, but prohibit any rotations as well as axial deformations. Contrarily, Teflon-layers were not applied at the US and CS-specimens. Though slip between specimen and support plate might have occurred, it has not been observed. Therefore, all translations and rotations have been restricted at the supported edges of the US and CS-specimens.

4.2.2 General calculation procedure

Calculation commands

The finite element analyses were executed according to the DIANA code, release 7.2 (De Witte et al. 1996). The analyses are divided into three steps, which are performed respectively by the DIANA modules: LINSTA, EULER and NONLIN. The first module, LINSTA, is used for linear elastic analysis under static circumstances. In addition, this module is essential as a preliminary analysis for the stability and geometrical and physical non-linear analyses.

The stability analysis (EULER) results in a set of sequential buckling modes. Each mode presents a buckling load and an according deformation pattern. The deformation pattern of the first Euler buckling mode is used as imperfection pattern for the geometrical non-linear analysis, as explained in section 4.1.2. Geometrical and physical non-linear analyses (NONLIN) require input from the LINEAR and EULER analyses; the physical non-linear behaviour is described using the actual material characteristic (see section 4.1.3).

Load step size

In physical and geometrical non-linear analyses, the influence of the load step size can be significant. The axial shortening (u) of the specimen is applied as a uniform edge displacement of the top cross-section of the test specimen. The size of the load steps depends on two reasons. First, the accuracy increases with smaller load steps, especially when physical non-linear behaviour occurs. In case of sudden changes in the mechanical behaviour (development of a buckle), large load steps could even lead to failure of the numerical process. The second, more practical, reason is that results are obtained only at the load steps; small load steps are required to obtain detailed information. The size of the load steps (Δu) has been chosen such that the resulting curves of the load-deflection ($N-w$) diagram are fluent; see e.g. Figure 4-11. Parameter analyse has proven this approach to be sufficiently accurate.

4.3 Parameter analyses

4.3.1 General

Parameter analyses have been executed on the two specimens of Figure 4-4 (Mennink 1999a). The dimensions of the RHS-specimen are chosen such as to obtain a compact cross-section with limited influence of buckling; the SHS-specimen is a semi-slender section exhibiting local buckling behaviour in the inelastic range. The insight obtained from the presented analyses was used to determine the actual FE-procedure as outlined in the previous sections.

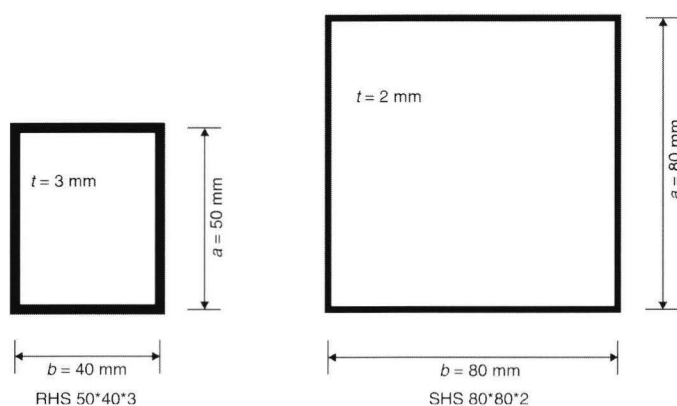


Figure 4-4 Test specimens used in the FE parameter analyses

4.3.2 Experimental input

Initial imperfections

The amplitude of the initial deformations, e_0 , is limited to 0.005 times the plate width, as described in the prENV 755-9 (CEN 1995). For the RHS and SHS-specimens, this equals a maximum deviation from flatness of respectively 0.25 mm (0.005×50) and 0.20 mm (0.005×40). To investigate the influence of the amplitude of the initial imperfections three DIANA analyses were performed with amplitudes of: 1.0, 0.5, and 0.2 mm for the RHS-specimen, respectively 0.4, 0.2, and 0.1 mm for the SHS-specimen. The results are presented in Figure 4-5A and B. An increase of the imperfections results in a decrease of the stiffness and strength. With deviations of failure loads of less than 3%, it can be concluded that the influence of initial imperfections on local buckling is small for the allowable initial deformations.

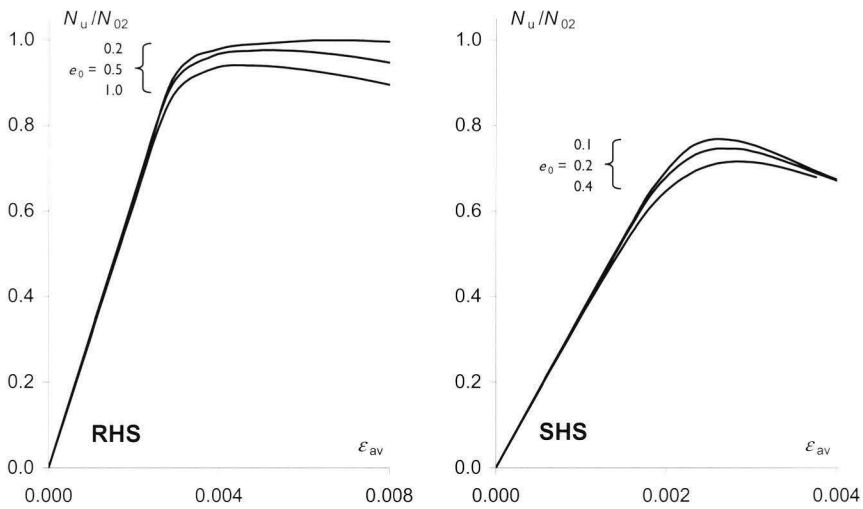


Figure 4-5 Parameter analyses - Influence of the size of initial imperfections

Material characteristic

Only a limited set of FE-analyses has been executed to investigate the influence of the material characteristic on the buckling behaviour. Therefore, no details are presented, and reference is made to Mennink (1999a). Elastic buckling (though not the entire post-buckling strength) is governed by the modulus of elasticity E . However, as many common aluminium alloys have a proportional limit $f_{p,0.2}$ of less than 75% of the 0.2% proof stress $f_{0.2}$. The influence of inelasticity may be quite substantial. In general, the conclusion can be drawn that the accuracy of the FE-analysis depends highly on the accuracy of the tensile test.

4.3.3 Mesh density

The influence of the mesh density has been studied for two densities. At first FE-analyses were executed that applied 6 elements over the plate width, secondly 12 elements were applied. For example, the meshes of the RHS-specimen are presented in Figure 4-6. The resulting load-displacement curves are presented in Figure 4-7. The load-displacement curves clearly show the negligible influence of the mesh density. Therefore, it is concluded that a 6*6 mesh density is sufficiently accurate.

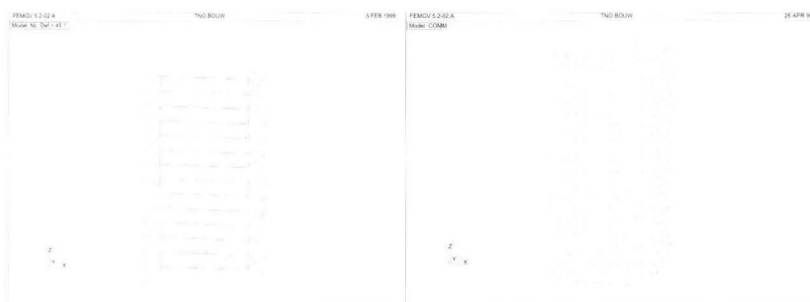


Figure 4-6 Mesh density – RHS

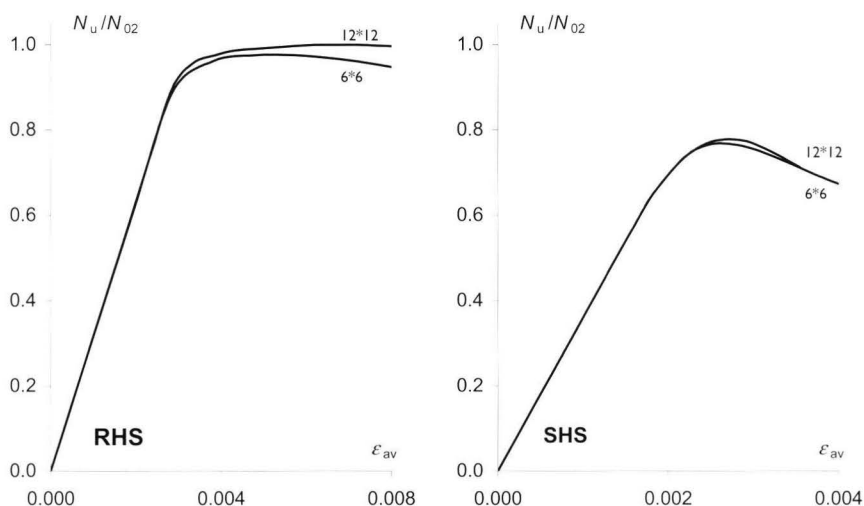


Figure 4-7 Comparison of a 12*12 element mesh with that of a 6*6 mesh

4.4 Results FE-analyses

4.4.1 Deformation patterns and failure modes

Paragraph 3.5.1 presented the deformed specimen of the experiments. Comparably, Figure 4-8 presents the according deformation patterns of the FE-analyses at the failure load. It also includes the specification of the test specimen and failure mode (L=local, F=flexural, T=torsional, D=distortional buckling, whereas S=squashing). Comparison of the presented deformation patterns to the experiments of Figure 3-17 shows that the failure modes are identical.

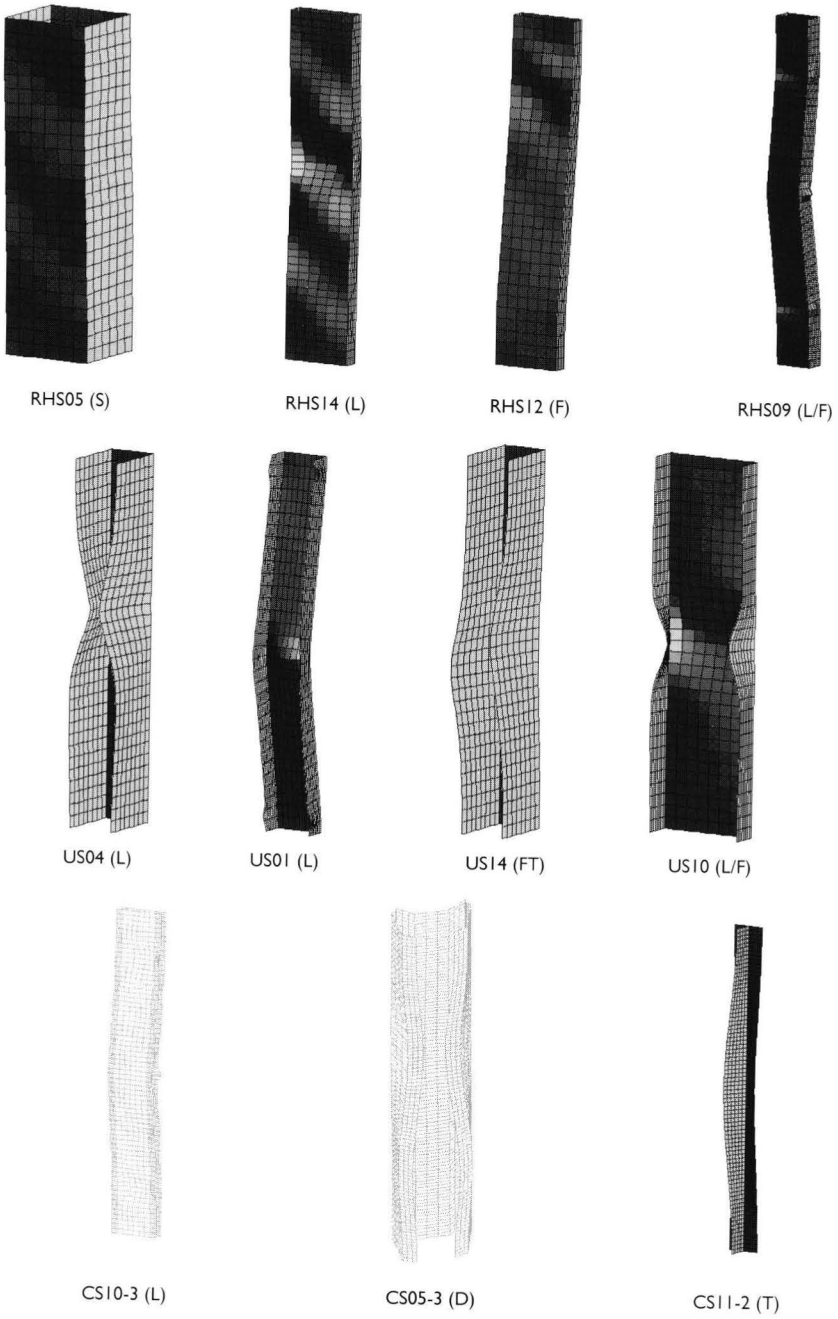


Figure 4-8 Deformations at failure – FE-results

4.4.2 Axial strength

Three characteristic strength-strain curves could be determined, each referring to a type of stability: squashing, overall buckling, and cross-sectional instability. These are explained respectively by the results of test specimen: RHS05, US1 I, and CS1 I-2. This section includes the load-displacement ($N-u$) and load-deflection ($N-w$) curves of the FE-analyses and those of the according experiments. Appendix C presents all curves.

The results of RHS05 are presented in Figure 4-9. The $N-u$ diagram presents the material characteristic, the results of the experiment, and the results of the FE-analyses. Note that for this specimen, the actual material characteristic was unavailable; the presented material is that applied in the FE-analysis. From the results it is quite clear that the deviation between FE-analysis and its applied material characteristic is small, even for substantial plastic strains. The deviation between experimental and numerical results is therefore mainly attributed to the deviation between the actual (unknown) and the applied material characteristics. Important is that failure occurs suddenly at large strains. The load deflection ($N-w$) diagram relates the amplitude of the out-of-plane deformations of the FE-analyses to the axial resistance. The values of $N_{0.2}$ from the material characteristic and $N_{u,exp}$ from the experiment are included for comparison. From this diagram it can be concluded that large deflections occur suddenly at failure.

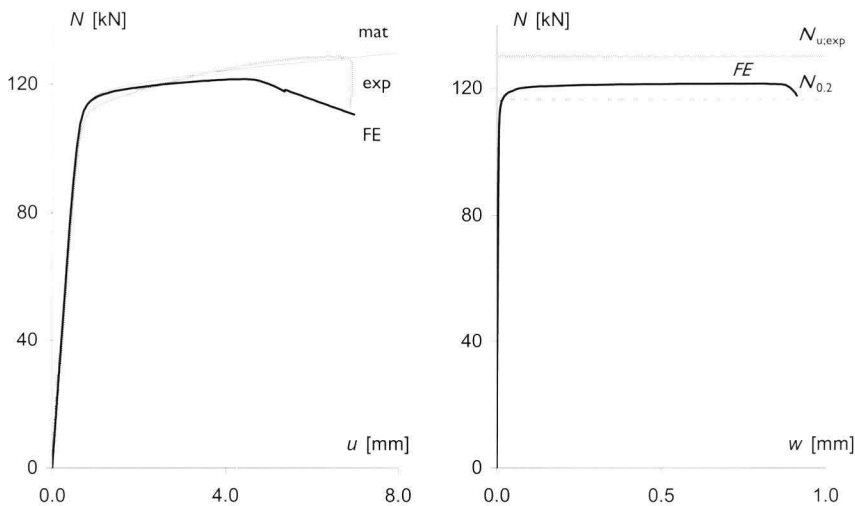


Figure 4-9 Comparison of the experimental and numerical non-dimensionalised load-displacement and load deflection curves (RHS05)

The results of the second specimen, US10, are presented in Figure 4-10. The $N-u$ diagram present the experimental result, two curves with FE-results using different imperfections, as well as the material characteristic. The $N-w$ diagram presents the FE-results as well as the experimental failure load ($N_{u,exp}$). The experiment fails through flexural buckling with a distinct peak, which is associated with small imperfections. Therefore, two FE-analyses have been executed, representing the actual and small imperfections by using imperfection amplitudes e_0 of respectively 0.12 and 0.01 mm. The difference in failure loads of the FE-analyses (12%) shows the distinct influence of imperfections on flexural buckling. Note that subsequent sections present the results of the actual imperfections. Elastic buckling of symmetrical columns would theoretically result in a horizontal plateau in the load-deflection ($N-w$) diagram. However, the FE-analyses only show such behaviour in case of relatively large imperfections, as the U-sections exhibit both asymmetric and inelastic buckling behaviour, see also Figure 2-6.

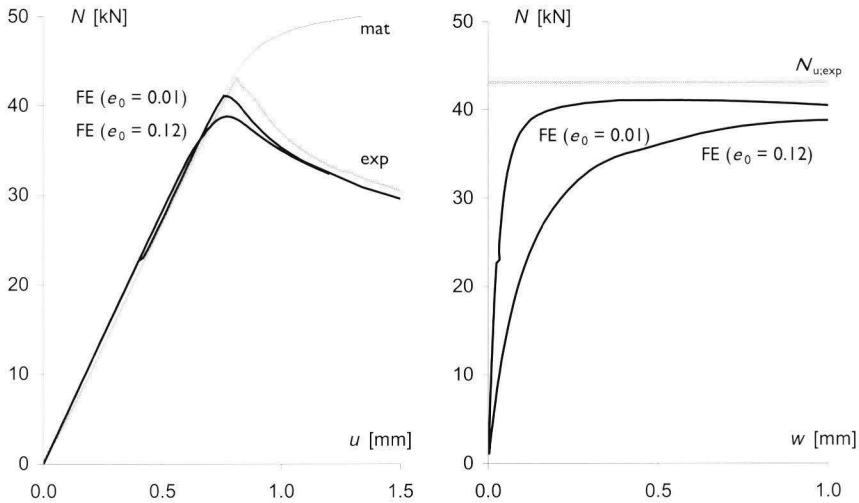


Figure 4-10 Comparison of the experimental and numerical load-displacement and load-deflection curves (US10)

Finally, the T-section (CS11-2) shows the behaviour associated with local buckling. The specimen buckles at the bifurcation load N_{cr} and shows a substantial amount of post-buckling strength. Failure occurs due to the interaction with flexural buckling. It is noted that there is no clear distinction between flange-buckling and torsional buckling.

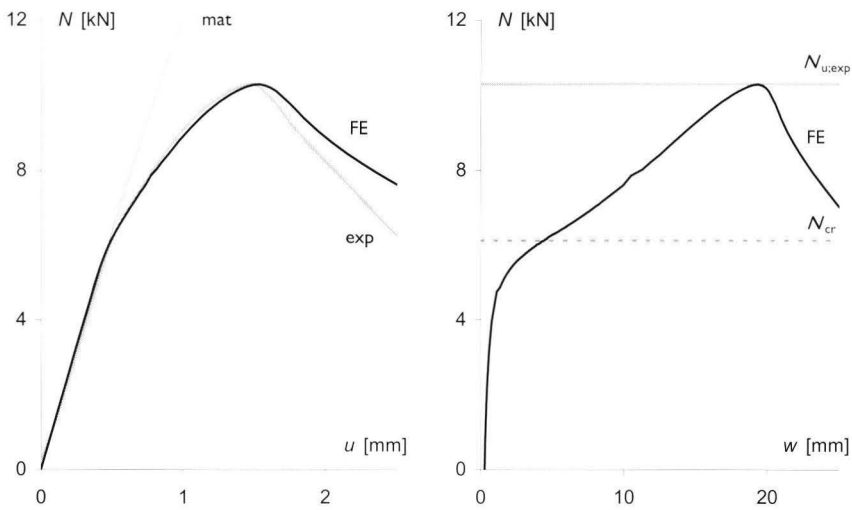


Figure 4-11 Comparison of the experimental and numerical non-dimensionalised load-displacement and load-deflection curves (CSI I-2)

The results of all FE-analyses and experiments are presented in appendix B and C. A global evaluation of these figures shows comparable results. However, for a more detailed comparison a distinction is made between three characteristic loads:

- *Initial buckling load (N_{cr})*
The Euler buckling load provides an indication of the bifurcation load, where cross-sectional instability occurs.
- *Failure load (N_u)*
This value refers to the maximum load obtained during either the FE-analysis or its matching test.
- *Tensile load (N_t)*
In some cases the FE-analyses result in tensile forces in the supports. Obviously, these cannot be accommodated in the experiment. Therefore, the stiffness of the experiment reduces and failure might occur. In fact, the ultimate load of the experiment will be somewhere in-between N_t and N_u of its respective FE-analysis.

The determination of N_{cr} , N_t and the axial stiffness E_c is explained in section 4.4.4. The actual comparison is presented in section 4.5.

4.4.3 Axial stiffness

In general, no distinction is made between the material characteristics of aluminium alloys under tensile or compressive forces. Therefore, the results of the elastic range of the compression and tensile tests should be comparable. Furthermore, as presented in section 2.3.3, the tangential stiffness of the post-buckling range is an important parameter in the determination of the post-buckling behaviour of plates. To illustrate this, Figure 4-12 presents for specimen CS1 I-2 the tangential stiffnesses (E_T) of the tensile test, the compression test (both strain gauges and LVDT's), and that of the FE-analysis. The resulting curves show excellent agreement. Comparably to section 3.5, a value for the "compressive" modulus of elasticity (E_c) is determined based on the elastic results of the strain gauges. The figure also shows that plate buckling results a stiffness reduction, and that the results of the finite element analyses largely agrees with that of the LVDT's.

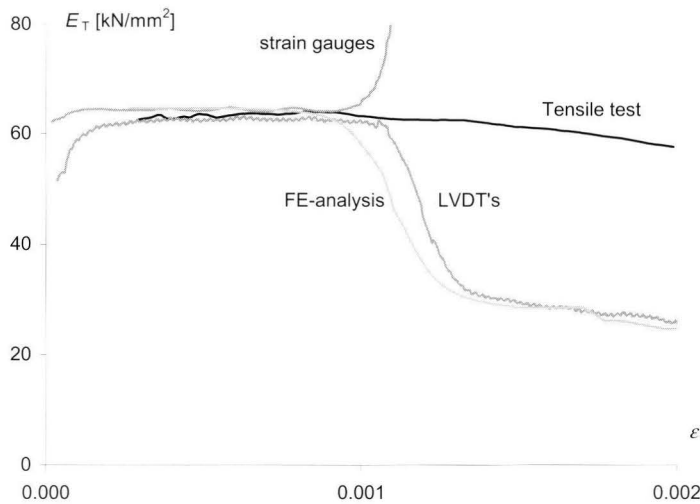


Figure 4-12 Comparison of the tangential stiffnesses of the compression test (strain gauges and LVDT's), tensile test and FE-analysis (CS1 I-2)

4.4.4 Determination of the characteristic FE-results

This section outlines how to obtain the characteristic values of the FE-results: the critical Euler load N_{cr} , the ultimate load N_u , the load when (in the FE-analyses) tensile stresses occur at the supports N_t and the elastic stiffness of the specimen E_c . The resulting values are summarised in section 4.5.

As the load is applied by control of the axial shortening u , the characteristic loads are determined from the axial support reactions. The critical load N_{cr} is obtained from an Eigenvalue analysis using the EULER routine (see section 4.2.2). Quite similarly, the ultimate load N_u equals the maximum value of the support reactions. It is assumed that the bifurcation load (initial buckling) occurs either at N_{cr} (elastic buckling) or else at N_u (inelastic buckling). Contrarily to the experiments, the supports applied in the FE-analyses are able to resist tensile stresses. This has the advantage that a truly clamped column is simulated. However, when tensile stresses do occur, the maximum load of the FE-analysis may exceed that of the according experiment. Therefore, N_t presents the lowest value of the axial load of the FE-analysis at which tensile stresses occur at the supports. Finally, the tangential stiffness of the FE-analyses is determined identically to that of the compression tests. Thus, the following equation is used:

$$E_c = \frac{\sigma_{11} - \sigma_1}{\varepsilon_{11} - \varepsilon_1} \quad \text{eq. 4-1}$$

Where σ_1 and σ_{11} coincide with normalised axial stresses of 10 respectively 50 N/mm², while ε_1 and ε_{11} are the according values of the average axial strain.

4.5 Comparison of experimental and FE-results

4.5.1 Overview of results

The previous sections visualised the various types of FE-results. The resulting characteristic values of FE-analyses executed on RHS-, US-, and CS-specimen of the Eindhoven program, are summarised in Table 4-1 and Table 4-2. These are used to validate the FE-model to the experiments.

Three tables present the characteristic values of both the experiments and FE-analyses and consist of: the load eccentricity ($\Delta\sigma$), the compression stiffness (E_c), the bifurcation and failure loads (N_{cr} and N_u) and their according modes, as well as the tensile load (N_t) at which tensile forces occur at the supports. Finally, the rightmost columns compare the bifurcation and ultimate loads. If bifurcation occurs in the experiment, the value of $N_{cr,FE}/N_{cr,exp}$ is presented. With respect to failure the lowest value of $N_{u,FE}/N_{u,exp}$ or $N_{t,FE}/N_{u,exp}$ is presented. The presented results are evaluated in section 4.5.2.

Table 4-1 Comparison of experimental and FE-results – RHS and US-specimen

RHS	EXP						FEM						FE / Exp	
			Bif.		Failure			Bif.		Failure			Bif.	Fail.
Spec.	$\Delta\sigma$	E_c	Md.	N_{cr}	Md.	N_u	E_c	Md.	N_{cr}	Md.	N_u	N_t		
RHS01	29.0	69.9			S	130.1								
RHS02	8.1	68.6			S	129.7								
RHS04	12.3	67.1			S	125.1								
RHS05	12.0	67.9			S	128.5	65.3	L	600.3	S	121.5			0.95
RHS06	6.8	70.8			L	83.8	66.4	L	92.5	L	86.9			1.04
RHS07	19.9	70.6			L	82.2	66.4	L	89.6	L	84.9			1.03
RHS08	14.5	69.5			L	86.5	67.1	L	87.0	L	83.1			0.96
RHS09	5.8	70.0			L-F	84.2	66.3	L	83.0	L-F	83.0			0.99
RHS10	8.8	68.0			L	173.3	66.4	L	216.1	L	172.4			1.00
RHS11	23.4	67.7			L	159.8	66.5	L	210.6	L	164.6			1.03
RHS12	0.6	69.4			L-F	167.2	67.5	L	190.2	L-F	163.8			0.98
RHS13	15.8	74.2			L-F	173.3	67.5	F	163.6	F	141.4			0.82
RHS14	3.3	65.1	L	87.1	F	117.6	64.1	L	78.7	L-F	131.7			0.90 1.12
RHS15*	3.4	70.1			F	85.2								
RHS16*	8.0	71.0			L-F	80.9								
RHS17	5.9	68.8			S	218.7								
RHS19	3.4	67.7			F	223.9								

US	EXP						FEM						FE / Exp	
			Bif.		Failure			Bif.		Failure			Bif.	Fail.
Spec.	$\Delta\sigma$	E_c	Md.	N_{cr}	Md.	N_u	E_c	Md.	N_{cr}	Md.	N_u	N_t		
US01	2.5	68.8			L-T	31.0	69.3	L	78.4	F	29.4			0.95
US02	9.3	72.3	L	23.8	F	40.6	62.4	L	23.5	L	40.0			0.99 0.98
US04	5.5	67.6	L	24.9	L	40.8	63.2	L	24.4	L	40.3			0.98 0.99
US05	3.7	68.4			L-F	38.4	69.1	L	52.5	L	35.1			0.91
US06	14.5	68.7	L	27.1	L	39.0	69.2	L	28.7	L	38.1			1.06 0.98
US08	4.2	71.1	L	28.6	L	38.8	68.9	L	26.4	L	36.4			0.92 0.94
US10	5.9	67.2			L-F	43.1	69.3	L	43.0	L	38.8			0.90
US11	1.4	65.3			F	33.9	69.5	F	37.0	F	33.5			0.99
US13	4.0	67.6			F	52.4	66.6	F	212.0	F	51.2			0.98
US14	4.0	70.0			D-T	110.6	66.7	L	166.8	L-T	108.2			0.98
US17	11.5	65.5			D-T	71.1	66.7	T	285.9	T	67.0			0.94
US18	8.1	67.6			D-T	99.2	66.7	L	210.5	L	95.7			0.96
US20	9.8	69.8			D-T	98.5	66.8	L	205.0	L-T	96.2			0.98
US21	37.5	63.4			F	66.0	51.0	F	103.2	F	65.7			1.00
US22	6.4	62.8			F	92.4	66.9	L	301.0	L-F	89.4			0.97
US25	22.3	68.4			D-T	59.8	66.0	L	147.2	L-T	56.2			0.94
US26	14.8	68.8	L	59.3	L	74.1	65.2	L	58.5	L	72.8			0.99 0.98
US29	29.5	69.7			L	67.7	66.1	L	106.0	L	64.4			0.95
US30	30.5	65.2	L	61.6	L	71.5	66.1	L	67.2	L	69.7			1.09 0.97
US33	7.5	62.9			F	73.6	66.3	L-F	90.8	L-F	67.1			0.91
US34	10.5	61.9			L-F	77.3	65.8	L	92.2	L-F	75.5			0.98

S = squashing / L = Local buckling / D = Distortional buckling / F = Flexural buckling / T = Torsional buckling

Table 4-2 Comparison of experimental and FE-results – CS-specimen

CS	EXP						FEM						FE / Exp	
			Bif.		Failure			Bif.		Failure			Bif.	Fail.
Spec.	$\Delta\sigma$	E_c	Md.	N_{cr}	Md.	N_u	E_c	Md.	N_{cr}	Md.	N_u	N_t		
CS01-1	2.2	63.6	L	22.7	F-T	33.8	65.5	L	22.7	FT	32.9		1.00	0.97
CS01-2	4.9	64.1	L	23.6	F-T	36.5	65.5	L	22.7	FT	32.9		0.96	0.90
CS02-1	0.8	63.6			F	65.6	64.5	L	76.0	L	67.9			1.03
CS02-2	3.1	63.2			L	65.4	64.5	L	76.0	L	67.9			1.04
CS02-3	3.0	64.7			F	64.8	64.4	L	75.6	L	66.7			1.03
CS02-4	1.0	63.1			F	64.5	64.4	L	75.6	L	66.7			1.03
CS03-1	7.0	60.4	L	32.2	L	68.4	65.3	L	32.8	L	73.5		1.02	1.07
CS03-2	7.0	66.5	L	29.7	L	68.7	65.3	L	32.8	L	73.5		1.10	1.07
CS03-3	2.7	62.3	L	31.2	L	66.6	65.3	L	32.5	L	72.0		1.04	1.08
CS04-1	25.5	59.7			F-T	36.1	64.7	L	30.9	L	39.1			1.08
CS04-2	11.5	61.9			F-T	34.9	64.7	L	30.9	L	35.7			1.02
CS04-3	4.9	65.2			L	29.8	64.6	FT	29.8	FT	28.1			0.94
CS04-4	19.6	70.7	L/T	18.6	L	21.8	64.6	FT	20.1	FT	23.6	21.7	1.08	0.99
CS05-1	1.8	64.8			D-F	39.3	65.6	D	45.9	D	38.4			0.98
CS05-2	19.3	63.1			D-F	38.0	65.6	D	45.9	D	38.4			1.01
CS05-3	5.5	63.7			D-F	39.3	65.6	D	43.1	D	37.2			0.95
CS06-1	6.6	66.1	L	29.0	F-T	43.2	65.2	L	29.9	L	44.5		1.03	1.03
CS06-2	6.7	62.2	L	26.6	F-T	40.5	65.1	L	29.8	L	43.5		1.12	1.07
CS06-3	12.0	59.6	L	26.4	F-T	38.7	65.0	L	29.6	L	40.9		1.12	1.06
CS06-4	7.1	59.7	FT	25.7	L	28.2	65.2	FT	28.8	FT	32.1	28.8	1.12	1.02
CS07-1	5.0	66.4			F	35.1	66.5	D	42.0	F	37.5			1.07
CS07-2	28.1	60.8	D	34.5	F	36.4	66.5	D	42.0	F	37.5		1.22	1.03
CS08-1	18.2	60.2			L	94.7	67.0	L	95.4	L	95.6			1.01
CS08-2	16.7	60.1			L	93.4	67.0	L	95.4	L	95.6			1.02
CS08-3	3.5	63.3			L	96.0	65.7	L	94.7	L	95.5			1.00
CS09-1	1.9	78.5	L	47.4	L	76.5								
CS09-2	8.5	91.8	L	51.7	L	77.9								
CS09-3	3.0	80.1	L	48.2	L	79.5								
CS10-1	8.9	66.5	L	43.4	F	58.9	68.8	L	44.2	L	61.4		1.02	1.04
CS10-2	5.1	68.1	L	44.5	F	59.3	68.8	L	44.2	L	61.4		0.99	1.04
CS10-3	9.4	68.8	L	47.0	F	55.6	68.7	L	43.8	L	59.8		0.93	1.08
CS10-4	26.2	66.4	L	44.7	F	58.0	68.7	L	43.8	L	58.1		0.98	1.00
CS11-1	2.7	64.2	T	6.7	L	10.4	64.3	T	6.7	T	10.7		1.01	1.03
CS11-2	1.9	64.2	T	5.8	L	10.3	64.6	T	6.1	T	10.3	10.3	1.06	1.00
CS11-3	0.1	64.3	T	5.9	L	9.6	67.1	T	5.9	T	9.6	9.5	1.00	0.99
CS11-4	3.8	63.9	T	5.8	L	8.8	64.6	T	5.7	T	8.6	8.4	0.99	0.96
CS12-1	19.5	62.3	L	13.1	D	30.2	62.5	L	13.7	D	29.2	28.5	1.04	0.94
CS12-2	25.2	48.9	L	10.9	D	29.6	63.9	L	14.8	L	35.0	33.5	1.36	1.13
CS12-3	11.0	62.9	L	12.2	D	28.7	61.9	L	13.6	D	28.8		1.11	1.00
CS12-4	19.0	64.0	L	12.4	D	27.8	60.7	L	13.5	D	28.2		1.09	1.02

S = squashing / L = Local buckling / D = Distortional buckling / F = Flexural buckling / T = Torsional buckling

4.5.2 Comparison of bifurcation and failure loads

The most practical approach to compare the experimental and FE-results of the previous paragraph, is to present them in the non-dimensionalised shape of Figure 4-13. This figure presents for each of the test specimen the ultimate load (N_u) divided by the squash load $N_{0.2}$ ($=A f_{0.2}$). In addition, the figure includes the unity line that coincides with zero deviation, as well as a 10% upper and lower limit. The following remarks are made:

- The accuracy of the FE-results is good, as comparison to the experimental results ($N_{u,FE}/N_{u,exp}$) results an average of $\mu = 1.00$ and a standard deviation of $\sigma = 0.06$, when considering all specimens.
- The CS-specimens show a larger scatter than that of the RHS and US-specimens. This is attributed to the complex geometry and the limited plate thickness (1.0 mm).
- Note that the largest deviation between FE and experiment occur for specimen that either fail suddenly through flexural buckling (RHS13, RHS14), or else show an inaccurate execution (CS12-2, $E_c = 48.9 \text{ kN/mm}^2$).

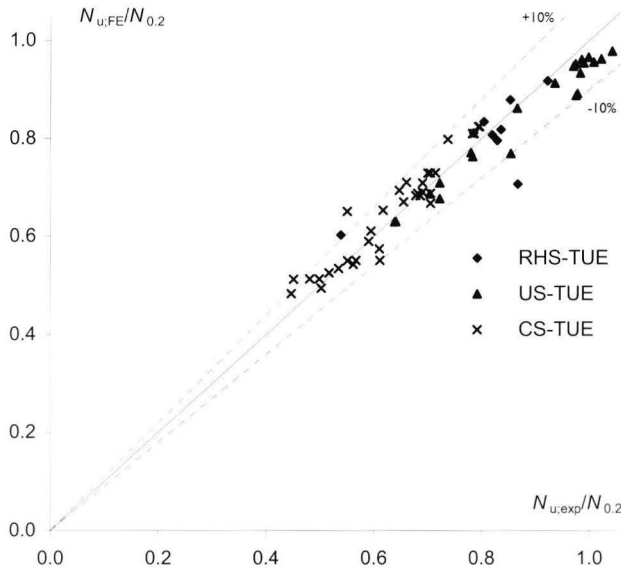


Figure 4-13 Comparison of experimental and FE-results – Ultimate loads

To obtain insight in the accuracy of the predicted buckling behaviour, the elastic critical load of the Euler analysis ($N_{cr,FE}$) is compared to the bifurcation load ($N_{cr,exp}$) observed in the experiments. However, as the elastic critical load is meaningless in the inelastic range, the critical load ($N_{cr,FE}$) is limited to the squash load ($N_{0.2}$) of the respective specimen. Flexural buckling as well as inelastic local buckling will lead to immediate failure (e.g. Figure 4-10). Therefore, if bifurcation is not observed in the experiments ($N_{cr,exp}$), the failure load is taken instead ($N_{u,exp}$). The subsequent results are presented in Figure 4-14. The accuracy of the determined bifurcation loads is obviously limited. Nevertheless, the comparison shows a distinct correlation ($\mu = 1.06$; $\sigma = 0.09$).

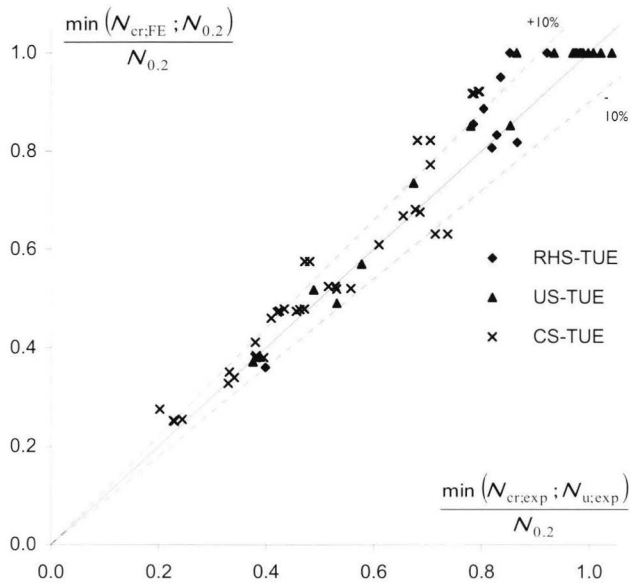


Figure 4-14 Comparison of experimental and FE-results – Bifurcation loads

4.5.3 Observations

The following observations can be made from the comparison of the results of the previous sections:

- The FE-analyses result deformation patterns that coincide with those observed in the experiments. However, the direction of the buckle is fitted to that observed in the experiments. This can be an important aspect as asymmetrical buckling may occur for especially the US and CS-specimen.
- The load-displacement diagrams show three types of behaviour: squashing, sudden failure, and bifurcation buckling. The actual behaviour due to squashing highly depends on the material characteristic and support conditions. Sudden failure occurs due to overall buckling, inelastic local buckling, or mode interactions. Sudden failure highly depends on the imperfections. It was observed that in general, the observed influence of initial deflections was negligible and less than that of the numerically applied ones. Finally, the behaviour due to bifurcation buckling is well described and the influence of both imperfections and inelastic material is less than that observed for squashing and sudden failure.
- The tangential stiffness of the FE-analyses is identical to that of the material characteristic. Generally, these coincide with the results of the strain gauges as well. The stiffness of the LVDT is in most cases less, which can be attributed to the influence of the support conditions and loading inaccuracies.
- Load eccentricity ($\Delta\sigma$) generally results in a constant bending moment in the elastic range. In most cases, the eccentricity is limited to $\Delta\sigma < 20 \text{ N/mm}^2$. Experiments with larger load eccentricities result in values of $N_{u,\text{exp}}$ less than that of the FE-analyses.
- The FE-analyses accurately predict the ultimate load of the experiments, $N_{u,\text{FE}}/N_{u,\text{exp}}$ results an average of $\mu = 1.00$ and a standard deviation of $\sigma = 0.06$. Notably, the largest deviations occur for specimens of which the experiments are considered less accurate. Comparably, the bifurcation or critical load is reasonably well predicted, though for obvious reasons less accurate ($\mu = 1.06$ and $\sigma = 0.09$).

It is concluded that the FE-analyses provide an accurate description of the actual buckling behaviour of aluminium extrusions with arbitrary cross-sections. Therefore, this model is well suited to determine and validate the prediction model of the following chapter.

5 Investigation of plate buckling and local buckling of cross-sections - Development of a general prediction model

Chapter abstract

As introduced in Chapter 1, existing design rules present a non-realistic description of the actual local buckling behaviour of cross-sections. In addition, they are unable to cover cross-sectional instability of arbitrary cross-sectional shapes, since there is no general approach to cover distortional buckling. As a result, it is unclear whether they provide accurate, overly conservative or even unsafe results. This chapter presents a thorough investigation of the actual local buckling behaviour of plates and cross-sections. Based on FE-results, experimentally validated in Chapter 4, this research is step-wise extended from elastic and inelastic plate buckling, to local buckling of elastic and inelastic cross-sections. The resulting model is validated in Chapter 6. This results in a new prediction model that is based on the actual buckling behaviour.

5.1 General

This section describes the notations used throughout this chapter, which allow the investigation of the results of the FE-analyses in a uniform approach. They also determine the parameters for a clear and univocal prediction model. Therefore, this section is essential in understanding the development of the prediction model.

As explained in Chapter 3, and used in Chapter 4, the actual cross-section is reduced to plates and nodes. This results in the following hierarchy: *plate* (*pl*), *plate-group* (*pg*), and *section* (*sec*), as explained in Figure 5-1. The prediction model requires the collection of the plates into two plate groups (*pg1* and *pg2*) that consist of plates with comparable buckling characteristics. For example, the RHS and IS-specimens are divided into the two plate groups: “flanges” (*pg1*) and “web(s)” (*pg2*). As a rule, plate-group 1 consists of those plates most susceptible to buckling; group 2 of the remainder of the cross-section. The determination of the plate groups is explained in detail in section 5.4.4.

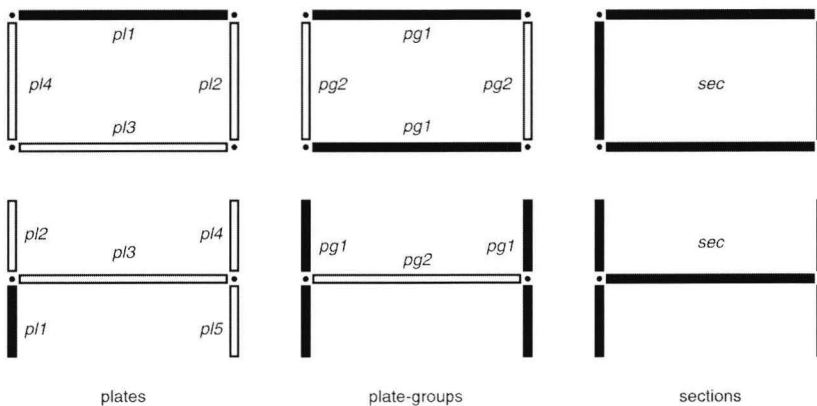


Figure 5-1 Cross-sections - General notation

For reasons of simplicity, a distinction is made between elastic and inelastic buckling. Elastic buckling refers to the behaviour of “perfect” plates or cross-sections with an ideal linear elastic material characteristic according to Hooke’s law ($\sigma = E \epsilon$). The presented FE-results are those of a geometrical non-linear analysis with very small imperfections of 1/1000 of the plate thickness that are merely used to initiate a certain buckling pattern. Comparably, the influence of a non-linear elastic or inelastic material characteristic is referred to as inelastic buckling. Where presented results are those of a geometrical and physical non-linear analysis, again with very small imperfections. Parameters related to these inelastic results, generally include a “T” in the subscript.

The simulated specimens, each with a specific cross-sectional shape, cross-sectional area A , and axial length L , are loaded into uniform compression by an axial shortening u . The summation of the resulting axial support reactions is referred to as the axial load of the cross-section N_{sec} , or $N_{pl,i}$ for an individual plate i ($N_{sec} = \sum N_{pl,i}$). FE-analyses are executed according to their validation in Chapter 4. In addition, the supports are taken such as to resemble an infinitely long plate or column with an even number of buckles over the specimen length.

As very small imperfections are used in the FE-analyses, buckling occurs suddenly. This point is defined as *initial buckling*. The according average axial stress is σ_{cr} , the according axial strain ε_{cr} . Note that this generally coincides with the first Euler Eigen-mode of the FE-analyses. The occurrence of *secondary buckling*, which will be explained in section 5.4.4, is described by $\sigma_{cr,2}$ and $\varepsilon_{cr,2}$.

The FE-analyses result in load-displacement (N - u) relations for the cross-section and its plates. In order to obtain a prediction model, it is necessary to use a format that provides comparable results. Therefore, these N - u relations are transformed to relations between the average axial stresses and strains (σ_{av} - ε_{av}). These parameters are represented by equations 5-1 to 5-3. Division of axial force by cross-sectional area results in a representative value of the average axial stress (σ_{av}); the average axial strain (ε_{av}) is found through the division of axial shortening by length. Finally, a characteristic stiffness parameter is the tangential stiffness (E^*) that can be found by taking the tangent to the average stress-strain relations. However, to investigate specific aspects it is often more appropriate to present the load-displacement relation in a non-dimensional ($\underline{\sigma}_{av}$ - $\underline{\varepsilon}_{av}$) relation, with respect to initial buckling of the cross-section:

$$\sigma_{av} = \frac{N}{A} \qquad \underline{\sigma}_{av} = \frac{\sigma_{av}}{\sigma_{cr}} \qquad \text{eq. 5-1}$$

$$\varepsilon_{av} = \frac{u}{L} \qquad \underline{\varepsilon}_{av} = \frac{E \varepsilon_{av}}{\sigma_{cr}} \qquad \text{eq. 5-2}$$

$$E^* = \frac{d \sigma_{av}}{d \varepsilon_{av}} \qquad \underline{E}^* = \frac{E^*}{E} \qquad \text{eq. 5-3}$$

These notations are used throughout this chapter. Note, that reference to a specific geometrical part is made by an addition to the subscript of the parameter (e.g. $\sigma_{av,pl4}$). Whenever additional parameters are used, e.g. with respect to inelasticity, reference will be made to the appropriate paragraphs and equations.

5.2 Elastic plate buckling

As the behaviour of a cross-section is the summation of that of its composing plates, the key to determine the actual local buckling behaviour is to provide an accurate description of the plate-buckling problem. This section evaluates the elastic plate buckling of uniformly compressed plates, based on FE-results. Comparable to Chapter 4, the analyses are executed using a geometric non-linear analysis with elastic material characteristics and negligible imperfections. For a detailed description of the FE-analyses is referred to Mennink (2002b). The executed FE-analyses regard “infinitely” long elastic plates; loaded into compression by axial shortening and with various support conditions at the unloaded edges. If no remarks are made, the presented analyses have been executed on plates with a width b of 48 mm, a length L of 480 mm, and a plate thickness t of 0.8 mm. The critical plate buckling stresses (σ_{cr}) can be calculated according to equation 2-17. The result of this section is a new and more accurate prediction model for elastic plate buckling of individual plates.

5.2.1 Elastic buckling of simply supported plates

The most commonly investigated case of plate buckling is that of simply supported plates; a plate loaded into uniform axial compression whose unloaded edges provide no rotational stiffness. More specific, three types of supports can occur:

- ss-free* both unloaded edges are roll-supported, but are free to wave;
- ss-straight* both unloaded edges are roll-supported, but remain straight;
- ss-fixed* both unloaded edges are hinge-supported.

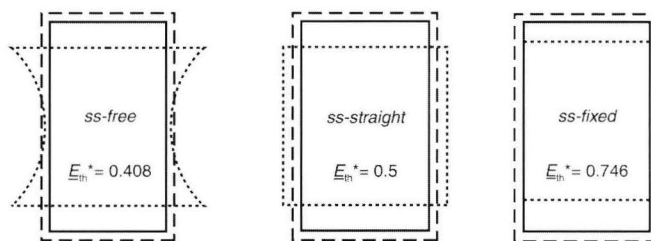


Figure 5-2 Support conditions of simply supported plates, including the theoretical initial post-buckling stiffness E_{th}^* (Allen and Bulson 1980)

FE-results

The FE-results of these three cases are presented in their non-dimensional form in Figure 5-3. As outlined in section 5.1, these diagrams relate the non-dimensional values for the average axial stress $\underline{\sigma}_{av}$ and tangential stiffness E^* to that of the axial strain $\underline{\epsilon}_{av}$. The E^* - $\underline{\epsilon}_{av}$ diagram also includes the theoretical values (E_{th}^*) of the initial post-buckling stiffness according to Allen and Bulson (1980).

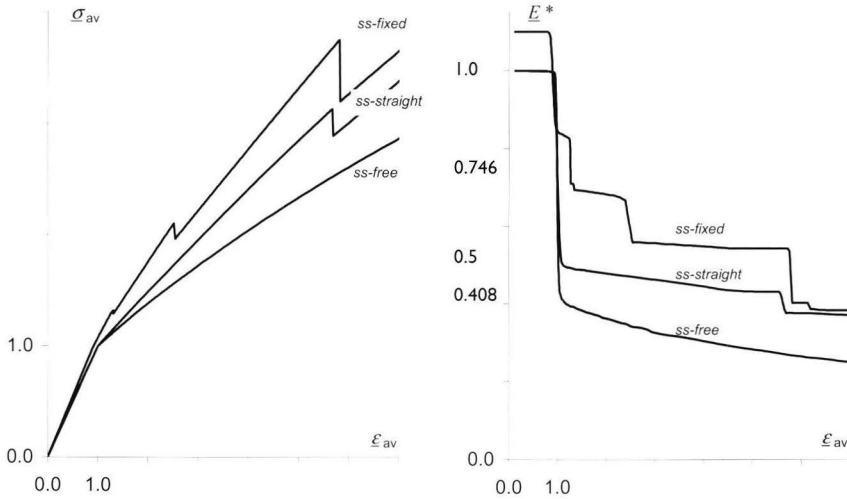


Figure 5-3 Elastic buckling of uniformly compressed plates with various types of "simply supported" edge conditions

Initial buckling at the critical stress ($\underline{\sigma}_{av} = \underline{\epsilon}_{av} = 1.0$) results in a sudden drop in stiffness E^* and its subsequent gradual decrease. The sudden strength reductions for *ss-straight* and *ss-fixed* are caused by mode jumping. Note that lateral contraction is restraint for *ss-fixed*, causing an increase of the axial stresses and tangential stiffness with a factor $1/(1-\nu^2)$. With ν equal to 0.3, this results in a factor of 1.1. Lateral contraction also results, compared to *ss-straight*, in a decrease of the critical stress. The initial values of the reduced stiffness coincide with the theoretical values E_{th}^* for the *ss-free* and *ss-straight* cases, though not for that of *ss-fixed*. However, literature also states that these values are sufficiently accurate up to twice (Galambos 1998) or even five times (Allen and Bulson 1980) the critical strain. Obviously, this seems an overestimation of the actual behaviour, which shows a gradual and almost linear reduction. The deviation between theory and FE is explained by the limited validity of the theory while it is based on energy solutions of a simplified set of differential equations (see section 2.3.3). The influence of plate slenderness, imperfections, and mode jumping are discussed below.

Plate slenderness and initial imperfections

The influence of the plate slenderness on the plate buckling behaviour of the *ss-straight* and *ss-free* cases is presented in Figure 5-4A. In addition to the plates of Figure 5-2 that have a thickness of 0.8 mm, additional analyses have been performed with a plate thickness of respectively 0.4 and 1.2 mm. It is clear that the influence of plate slenderness is negligible on the overall behaviour. Figure 5-4B presents the influence of initial imperfections on the behaviour of an *ss-free* plate. As explained in section 5.1, the presented FE-analyses apply negligible imperfections. For the plates of Figure 5-2, an imperfection amplitude e_0 of 0.0008 mm ($= t/1000$) has been applied. In addition, Figure 5-4B presents the results of plates with imperfections of respectively: 0.008, 0.08, and 0.8 mm. It is clear that the influence of imperfections is negligible for values of e_0 of less than one-tenth of the plate thickness.

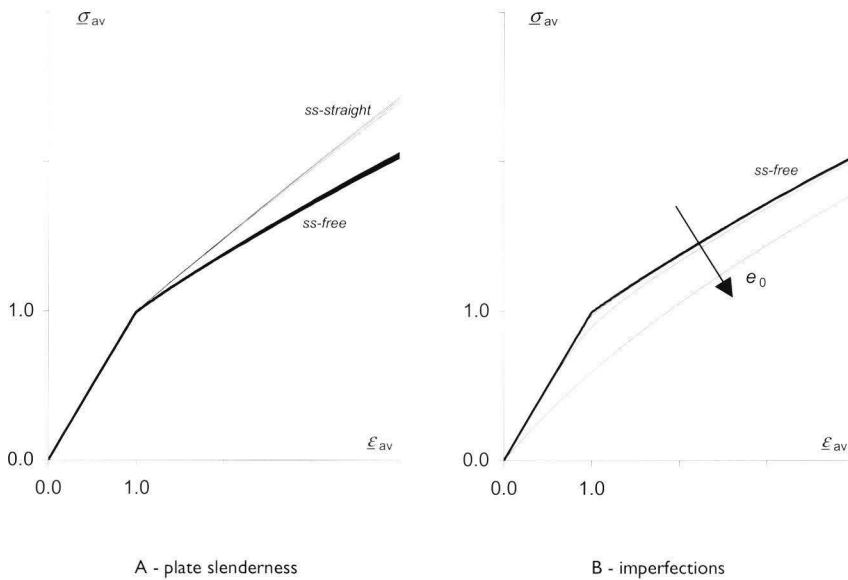


Figure 5-4 Influence of plate slenderness and imperfections on the elastic buckling behaviour of simply supported plates

Mode jumping

The sudden drop in strength and stiffness observed in Figure 5-3 for *ss-straight* and *ss-fixed* is caused by mode jumping. This complex and difficult phenomenon is rarely investigated, or observed in experiments on plate buckling. Noteworthy, Figure 3 of Stein (1959) shows the experimental result of a stiffened panel that exhibits mode jumping comparable to that of the presented FE-results.

This section presents the results of a limited investigation by Mennink (2002b). Figure 5-5A magnifies the behaviour of the *ss-fixed* situation. The first Eigenmode results a total number of $n_0 = 6$ buckles over the regarded plate length that is used as imperfection pattern. As very small imperfections are applied, the initial branch is almost linear and initial buckling occurs at $\underline{\sigma}_{av} = 1.0$. Obviously, the according buckling pattern has total of $n = 6$ buckles. Mode jumping occurs at $\underline{\sigma}_{av} = 1.3$ and results a deformation pattern with $n = 8$ buckles over the regarded length. Figure 5-5B shows that further load increase results in mode jumping to respectively 10 and 14 buckles.

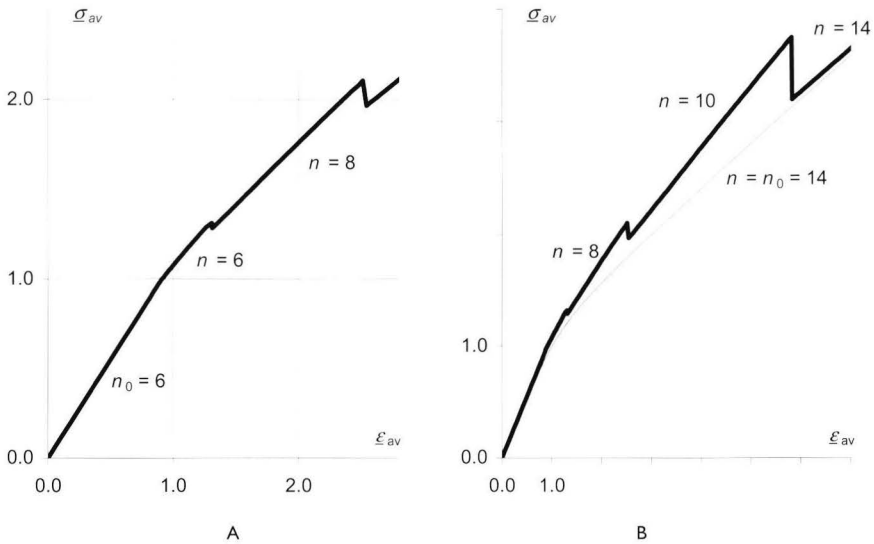


Figure 5-5 Investigation of mode jumping for an elastic *ss-fixed* plate by comparison of the number of buckles n over its plate length

Further investigation shows that each subsequent buckling pattern coincides with a higher-order Eigenmode of the plate. Therefore, several additional FE-analyses have been executed using initial imperfection patterns according to these modes. For example, Figure 5-5B presents the results of an FE-analysis using a mode with $n_0 = 14$. The according post-buckling strength shows excellent agreement with that observed from the *ss-fixed* case for large strains. Though not presented, comparable analyses showed excellent agreement with the post-buckling branches according to $n = 8$, and $n = 10$. Note that such curves (without mode jumping) could be determined analytically from the differential equations as well.

For relatively long plates, the critical stresses of higher-order modes are only marginally larger than σ_{cr} (see Figure 2-11). However, their post-buckling stiffnesses are less and each mode coincides with a subsequent part of *ss-fixed*. Thus, mode jumping is the sudden transition of one buckling mode to another, to obtain a stable situation that

requires less energy. The sudden drop in strength is explained by the energy needed to execute the transition to the deformation pattern of the new mode. From a practical point of view, one would wish to prevent the occurrence of mode jumping. Apparently, this is possible by stating that no mode jumping occurs for *ss-free* or *ss-straight* plates if $\underline{\varepsilon}_{av}$ is less than 7.0, respectively 5.6. Note that the *ss-free* analysis was extended to a value of $\underline{\varepsilon}_{av}$ of 60 without the occurrence of mode jumping.

5.2.2 Elastic buckling of clamped plates

Comparable to simply supported plates, three types of clamped conditions can occur at the unloaded edges. Contrarily to the simply supported cases, only one value, $E_{th}^* = 0.497$, for the initial post-buckling stiffness is specified (Allen and Bulson 1980).

<i>cl-free</i>	unloaded edges are clamped, free to move, and free to wave
<i>cl-straight</i>	unloaded edges are clamped, free to move, but remain straight
<i>cl-fixed</i>	unloaded edges are clamped and fixed

Figure 5-6 presents the FE-results of these three cases, relating the non-dimensionalised values of average axial stress $\underline{\sigma}_{av}$ and tangential stiffness E^* , to that of the average axial strain $\underline{\varepsilon}_{av}$. Figure 5-6B also presents the theoretical value $E_{th}^* = 0.497$.

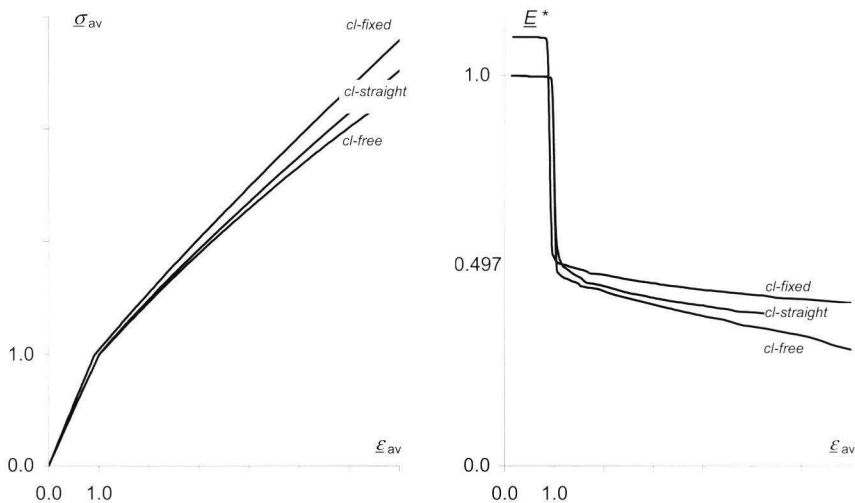


Figure 5-6 Elastic buckling of clamped plates

From the $\underline{\sigma}_{av}$ - $\underline{\varepsilon}_{av}$ diagram is observed that, contrarily to the simply supported cases, the support conditions have a limited influence on the post-buckling stiffness. Again, E_{th}^* coincides with the initial tangential stiffness E^* at $\underline{\varepsilon}_{av} = 1.0$, after which it reduces almost linearly.

5.2.3 Elastic buckling of outstands

Outstands “flanges” are supported at one unloaded edge and are free at the other. Four types of supports can occur at the supported edges, though literature specifies only one value for the theoretical tangential stiffness $E_{th}^* = 0.444$ (Allen and Bulson 1980).

- out-ss-free* roll-supported edge free to wave in-plane;
- out-ss-fixed* hinge-supported edge;
- out-cl-free* clamped edge free to wave in-plane;
- out-cl-fixed* clamped edge.

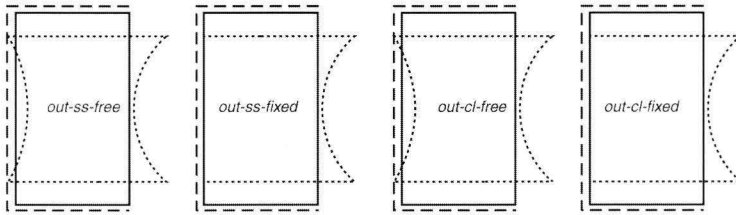


Figure 5-7 Support conditions of outstands

Figure 5-8 presents the according FE-results that show only a limited influence of the support conditions. From the $E^*-\underline{\epsilon}_{av}$ diagram can be observed that at the critical stress, the tangential stiffness drops approximately to its theoretical value, after which it is either constant or reduce almost linearly. Note that mode jumping occurs for the *out-cl-free* case at $\underline{\epsilon}_{av} = 6.2$, as explained in section 5.2.1.

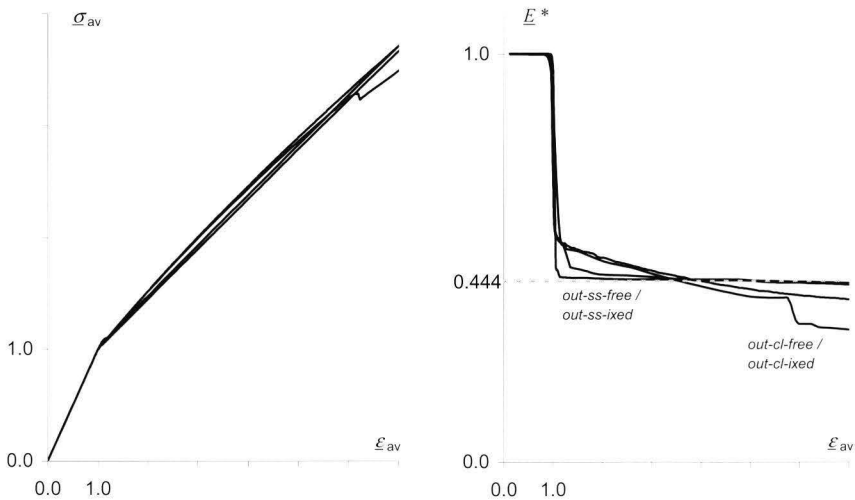


Figure 5-8 Elastic buckling of outstands

5.2.4 Evaluation of elastic plate buckling

The previous sections described the elastic buckling behaviour of uniformly compressed plates with a wide range of boundary conditions at the unloaded edges. This section summarises and evaluates the key aspects of these results, which results in an accurate prediction model for elastic plate buckling.

Existing local buckling approaches (see section 2.3) are based on a simply supported plate whose unloaded edges are straight, but free to deform: case *ss-straight* for internal plates (see section 5.2.1) and *out-ss-fixed* for outstands (see section 5.2.3). A comparison of all cases shows that a lower bound is given by the behaviour of the *ss-free* case; a simply supported internal plate whose unloaded sides are free to wave (see section 5.2.1). Therefore, these three cases (see Figure 5-9) are compared and evaluated.

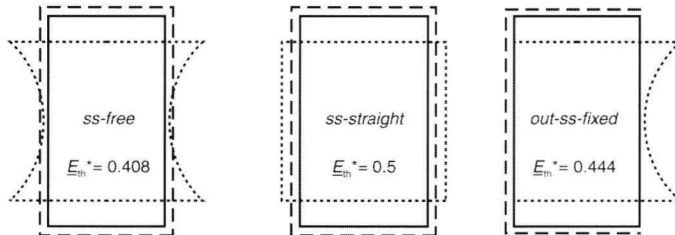


Figure 5-9 Support conditions of the representative cases of plate buckling

The FE-results of the three cases are presented in Figure 5-10 (black lines). Notably, the results of *ss-straight* and *out-ss-fixed* are nearly identical. To determine a general prediction model, two straight lines have been fitted through the results of *ss-straight* and *ss-free* in Figure 5-10B (grey with crosses). Integration results the fitted curves presented in diagram A, whereas a third set represents the Von Kármán buckling formulae. Table 5-1 presents the according equations.

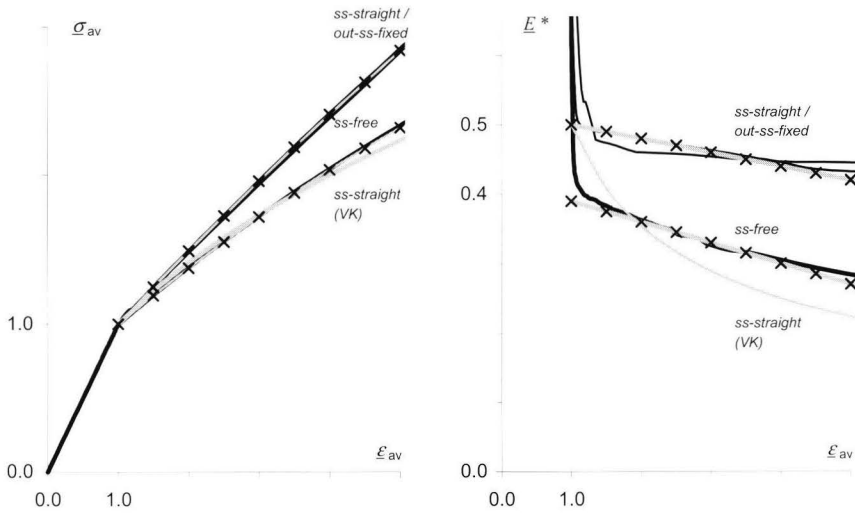


Figure 5-10 Comparison of the actual elastic plate buckling behaviour (black) with fitted curves (grey with cross) and the Von Kármán equations (grey)

The following conclusions can be drawn from these results as well as those of the previous sections:

- The *ss-straight* and *out-ss-fixed* cases show almost identical results. This supports the original derivation for the effective width concept by Von Kármán (see section 2.3.4) that a simply supported plate with straight edges can be described by two identical outstands.
- The fitted curves have been determined such as to provide accurate results for limited strains ($\epsilon_{cr} < \epsilon < 4 \epsilon_{cr}$), and conservative values for larger strains. This range coincides with a commonly used slenderness range of: $1.0 < \bar{\lambda}_{pl} < 2.0$.
- The Von Kármán equations, *ss-straight (VK)*, are based on an analytical solution of a simplified set of differential equations (see section 2.3.3) for an *ss-straight* plate. However, though the initial post-buckling stiffness is accurate ($E^* = 0.5$) its subsequent behaviour is not. More particularly, as the differential equations are simplified with respect to the in-plane stresses, the predicted behaviour resembles the *ss-free* case instead.
- Though not presented in the diagrams, mode jumping occurs for *ss-straight* at $\epsilon < 5.6 \epsilon_{cr}$ (see section 5.2.1).

<i>Table 5-1</i>	<i>Representative equations for elastic post-buckling of plates</i>	
<i>ss-straight (pm)</i>	$\underline{E}_{pm}^* = 0.52 - 0.02\underline{\varepsilon}_{av}$	eq. 5-4
	$\underline{\sigma}_{pm} = 0.49 + 0.52\underline{\varepsilon}_{av} - 0.01\underline{\varepsilon}_{av}^2$	eq. 5-5
	$\sigma_{pm} = 0.49E \varepsilon_{cr} + 0.52E \varepsilon_{av} - 0.01E \frac{\varepsilon_{av}^2}{\varepsilon_{cr}}$	eq. 5-6
<i>ss-free (pm)</i>	$\underline{E}_{pm}^* = 0.42 - 0.03\underline{\varepsilon}_{av}$	eq. 5-7
	$\underline{\sigma}_{pm} = 0.6 + 0.42\underline{\varepsilon}_{av} - 0.015\underline{\varepsilon}_{av}^2$	eq. 5-8
	$\sigma_{pm} = 0.6E \varepsilon_{cr} + 0.42E \varepsilon_{av} - 0.015E \frac{\varepsilon_{av}^2}{\varepsilon_{cr}}$	eq. 5-9
<i>ss-straight (VK)</i>	$\underline{E}_{VK}^* = 0.5\sqrt{\frac{1}{\varepsilon_{av}}}$	eq. 5-10
	$\underline{\sigma}_{VK} = \sqrt{\varepsilon_{av}}$	eq. 5-11
	$\sigma_{VK} = E\sqrt{\varepsilon_{av} \varepsilon_{cr}}$	eq. 5-12

From the previously obtained insight it is concluded that the elastic post-buckling behaviour of plates with various boundary conditions can be accurately described by a linearisation of the tangential post-buckling stiffness E^* . This approach results an accurate description of the actual post-buckling strength and stiffness that is markedly better than existing theory.

Summarising procedure for elastic plate buckling

This procedure describes the elastic buckling behaviour of uniformly compressed internal plates and outstands where unloaded edges remain straight, as well as internal plates whose unloaded edges are free to wave. The presented approach can be extended for other types of support conditions based on the results of the previous sections. The presented procedure predicts the average axial stress (σ_{pm}) in the plate for a given value of axial strain (ε). In fact, the procedure results the predicted curves (grey with cross) of Figure 5-10.

1. Determine the **elastic critical stress** (σ_{cr})

For internal plates: $k_{cr} = 4$ or using eq. 2-26

For outstands: $k_{cr} = 0.43$ or using eq. 2-27

$$\sigma_{cr} = k_{cr} D \left(\frac{t}{b} \right)^2 \quad \text{where} \quad D = \frac{\pi^2 E}{12(1-\nu^2)}$$

2. Determine the **characteristic strains** ε_{cr} and ε_{lim}

$$\varepsilon_{cr} = \frac{\sigma_{cr}}{E} \quad (\text{initial buckling})$$

$$\varepsilon_{lim} = 5.6\varepsilon_{cr} \quad (\text{limiting strain with respect to mode jumping})$$

- 3.A Predict the average **axial stress** (σ_{pm}) in the linear elastic region ($\varepsilon \leq \varepsilon_{cr}$)

$$\sigma_{pm}(\varepsilon) = E\varepsilon$$

- 3.B Predict the average **axial stress** (σ_{pm}) in the post-buckling region ($\varepsilon_{cr} < \varepsilon < \varepsilon_{lim}$)
Outstands and internal plates with straight unloaded edges:

$$\sigma_{pm}(\varepsilon) = 0.49 E\varepsilon_{cr} + 0.52 E\varepsilon - 0.01 E \frac{\varepsilon^2}{\varepsilon_{cr}}$$

Internal plates with unloaded edges free to wave:

$$\sigma_{pm}(\varepsilon) = 0.6 E\varepsilon_{cr} + 0.42 E\varepsilon - 0.015 E \frac{\varepsilon^2}{\varepsilon_{cr}}$$

4. Predict the **axial resistance** (N_{pm}) as a function of ε and the plate dimensions

$$N_{pm}(\varepsilon) = \sigma_{pm}(\varepsilon) b t$$

5.3 Inelastic plate buckling

This section investigates the influence of material inelasticity on plate buckling. The actual plate buckling behaviour is studied with FE-analyses using two characteristic materials. Subsequently, the theoretical inelastic buckling stress and curve have been used to evaluate the results. The FE-analyses are executed for uniformly compressed internal plates whose unloaded edges are free to wave (*ss-free*, section 5.2.1). Though the approach can be extended to different types of plates and support conditions, section 5.5 will show that this is not essential. The obtained insights are summarised into a procedure that predicts the inelastic buckling behaviour of plates.

5.3.1 Material characteristic

The non-linear material characteristic of aluminium is generally described by the Ramberg-Osgood relationship presented by equation 2.2.2. The main parameters are the modulus of elasticity E , the 0.2% proof stress $f_{0.2}$ and the Ramberg-Osgood parameter n . The value of E is generally assumed equal to 70000 N/mm². For heat-treated alloys the following boundaries hold: $20 < n < 40$ (Mazzolani; 1985) and $140 < f_{0.2} < 350$ N/mm² (CEN 1999).

$$\varepsilon = \frac{\sigma}{E} + 0.002 \left(\frac{\sigma}{f_{0.2}} \right)^n \quad \text{eq. 2-15}$$

To determine the inelastic buckling behaviour, two material characteristics will be studied. The first material (*mat1*) is a representation of the actual materials as found in the executed tests (see appendix B). The second material (*mat2*) represents a lower bound for the possible material characteristics, having both the lowest 0.2% proof stress as well as the most “inelastic” value for n .

Name	E (N/mm ²)	$f_{0.2}$ (N/mm ²)	n
<i>mat1</i>	70000	200	30
<i>mat2</i>	70000	140	20

The according material characteristics are visualised in Figure 5-11. Diagram A presents the stress-strain relation, diagram B the relation between the axial strain and the non-dimensionalised tangential stiffness E_T (according to eq. 5-14). Diagram A is used to determine that strain ($\epsilon_{0.2}$) which results in 0.2% plastic strain. Diagram B provides the proportional limit (ϵ_p); as the curve is exponential it is arbitrarily decided to determine ϵ_p at $E_T = 0.99$. This results in $\epsilon_p = 0.022$ for *mat1* and $\epsilon_p = 0.013$ for *mat2*.

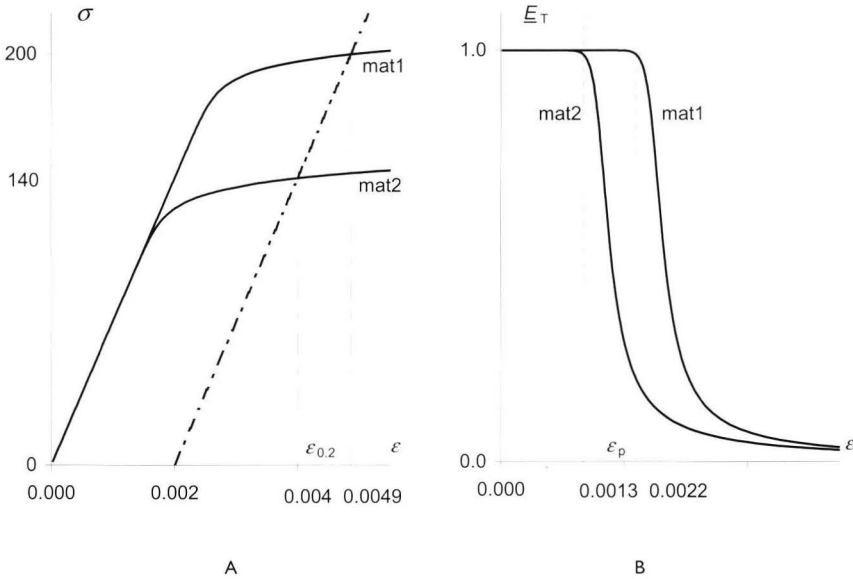


Figure 5-11 Material characteristics applied in the physical non-linear FE-analyses to determine the inelastic buckling behaviour of plates and cross-sections

5.3.2 Theory

The elastic prediction model of section 5.2.4 is based on the elastic critical stress (σ_{cr}) and the predicted elastic post-buckling stiffness (E_{pm}^*). This section determines the inelastic critical stress $\sigma_{cr,T}$, based on the tangential stiffness of the material characteristic E_T . Note, the presented approach is largely based on the work by Shanley (1947), as described by Mazzolani (1985).

The tangential stiffness E_T of the material characteristic can be determined by differentiation of the Ramberg-Osgood relation with respect to σ :

$$\frac{\partial \epsilon}{\partial \sigma} = \frac{1}{E} + \frac{0.002n}{f_{0.2}} \left(\frac{\sigma}{f_{0.2}} \right)^{n-1} \quad \text{eq. 5-13}$$

Inverting results:

$$E_T = \frac{\partial \sigma}{\partial \varepsilon} = \frac{1}{\frac{1}{E} + \frac{0.002n}{f_{0.2}} \left(\frac{\sigma}{f_{0.2}} \right)^{n-1}} \quad \text{eq. 5-14}$$

Shanley's approach assumes that the inelastic buckling load (or stress) is obtained by replacing the elastic modulus of elasticity with its tangential equivalent:

$$\sigma_{\text{cr};T} = \frac{E_T(\sigma_{\text{cr};T})}{E} \sigma_{\text{cr}} \quad \text{eq. 5-15}$$

This equation can be rewritten as a function of the 0.2% proof stress $f_{0.2}$, which is commonly used in buckling curves. Introduction of the inelastic buckling coefficient χ_T results:

$$\sigma_{\text{cr};T} = \chi_T(\sigma_{\text{cr}}) f_{0.2} \quad \text{or} \quad \chi_T(\sigma_{\text{cr}}) = \frac{\sigma_{\text{cr};T}}{f_{0.2}} \quad \text{eq. 5-16}$$

Instead of using the elastic critical stress, the relative plate slenderness $\bar{\lambda}$ is introduced:

$$\bar{\lambda} = \sqrt{\frac{f_{0.2}}{\sigma_{\text{cr}}}} \quad \text{or} \quad \sigma_{\text{cr}} = \frac{f_{0.2}}{\bar{\lambda}^2} \quad \text{eq. 5-17}$$

This results for *elastic* ($\sigma_{\text{cr};T} = \sigma_{\text{cr}}$), respectively *inelastic* material:

$$\chi = \frac{1}{\bar{\lambda}^2} \quad \text{eq. 5-18}$$

$$\chi_T = \frac{E_T}{E} \frac{1}{\bar{\lambda}^2} \quad \text{eq. 5-19}$$

Substitution of E_T (eq. 5-14) and $\sigma = \sigma_{\text{cr};T}$ yields:

$$\chi_T = \frac{1}{1 + \frac{0.002En}{f_{0.2}} \chi_T^{n-1} \frac{1}{\bar{\lambda}^2}} \quad \text{eq. 5-20}$$

Or if written in $\bar{\lambda}^2$:

$$\bar{\lambda}^2 = \frac{1}{\chi_T + \frac{0.002En}{f_{0.2}} \chi_T^n} \quad \text{eq. 5-21}$$

For the two prescribed material characteristics, *mat1* and *mat2*, this results in the buckling curves of Figure 5-12. Unfortunately, it is not possible to determine χ_T in a closed form solution.

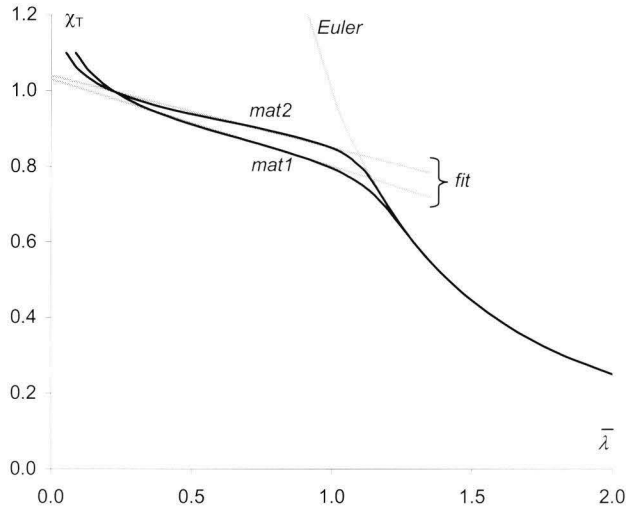


Figure 5-12 Actual and fitted buckling curves for the determination of the inelastic critical stress

The buckling curves can be divided into two branches. Elastic (or Euler) buckling is described by equation 5-18, whereas the inelastic branches are fitted by:

$$\text{mat1:} \quad \chi_T = 1.04 - 0.19\bar{\lambda} \quad \text{eq. 5-22}$$

$$\text{mat2:} \quad \chi_T = 1.03 - 0.23\bar{\lambda} \quad \text{eq. 5-23}$$

Thus the inelastic critical stress $\sigma_{cr,T}$ is obtained from σ_{cr} by:

$$\text{mat1:} \quad \sigma_{cr,T} = \min \left(\left(1.04 - 0.19 \sqrt{\frac{f_{0.2}}{\sigma_{cr}}} \right) f_{0.2} ; \sigma_{cr} \right) \quad \text{eq. 5-24}$$

$$\text{mat2:} \quad \sigma_{cr,T} = \min \left(\left(1.03 - 0.23 \sqrt{\frac{f_{0.2}}{\sigma_{cr}}} \right) f_{0.2} ; \sigma_{cr} \right) \quad \text{eq. 5-25}$$

These two equations allow the determination of the inelastic critical stress for the two materials specified. The applicability of $\sigma_{cr,T}$ with respect to the actual buckling behaviour is studied next.

5.3.3 Actual behaviour

This section investigates the actual inelastic plate buckling behaviour, by presenting the results of geometrical and physical non-linear FE-analyses. The regarded plates are uniformly compressed internals (*ss-free*, section 5.2.1) with a plate width of 48 mm. For each material (*mat1* or *mat2*), six FE-analyses have been executed with different plate thickness t . The values of t have been chosen to result characteristic values of χ_T , see Table 5-3, by using the equations of the previous paragraph. Based on the results of these FE-analyses, it is possible to investigate the influence of inelasticity on initial buckling ($\sigma_{cr,T}$) and the tangential stiffness (E^*).

Table 5-3 Characteristic data - Inelastic FE-analyses

<i>mat1</i> $f_{02} = 200 \text{ N/mm}^2 / n = 30$		<i>mat2</i> $f_{02} = 140 \text{ N/mm}^2 / n = 20$	
χ_T	t [mm]	χ_T	t [mm]
0.25	0.67	0.25	0.57
0.50	0.95	0.50	0.80
0.65	1.09	0.65	0.91
0.75	1.17	0.75	0.98
0.85	1.35	0.85	1.44
0.90	1.83	0.90	2.00

Note: $E = 70,000 \text{ N/mm}^2 / b = 48\text{mm} / L = 480\text{mm}$

Figure 5-13 and Figure 5-14 represent the FE-results of analyses executed with respectively *mat1* and *mat2* material characteristics.

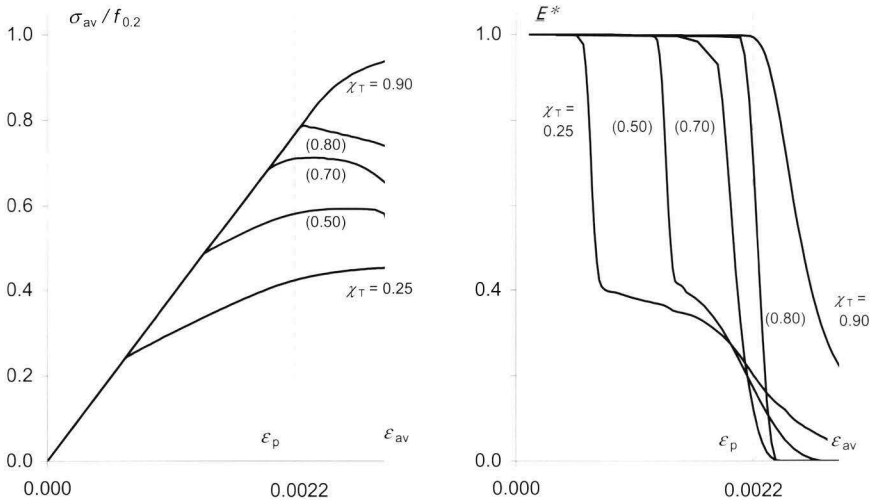


Figure 5-13 Investigation of the behaviour of individual *ss-free* plates as a function of the inelastic buckling coefficient χ_T (*mat1*)

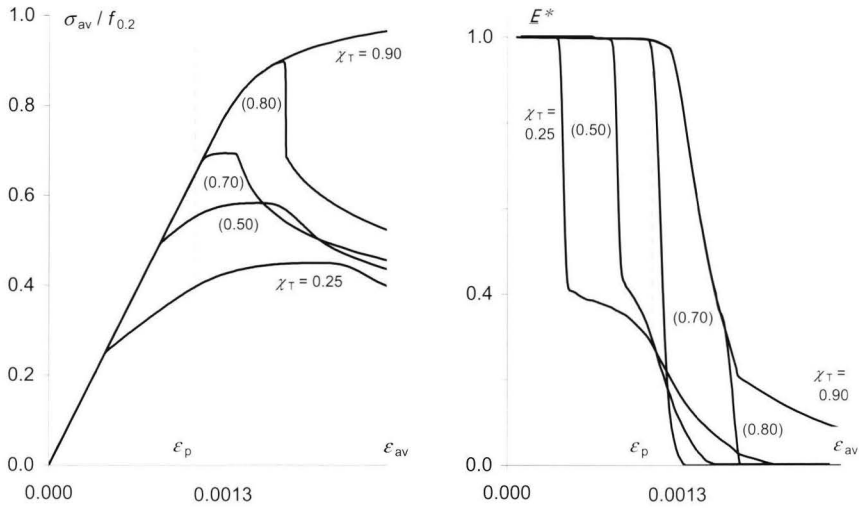


Figure 5-14 Investigation of the behaviour of individual ss-free plates as a function of the inelastic buckling coefficient χ_T (mat2)

Based on these graphs, the following remarks are made to understand and describe the inelastic plate buckling behaviour.

- The proportional limit of the material, represented by ϵ_p and f_p , roughly divides elastic from inelastic buckling. Elastic buckling ($\epsilon_{cr} < \epsilon_p$) may show a considerable amount of post-buckling strength, whereas inelastic buckling ($\epsilon_p < \epsilon_{cr}$) does not.
- Inelastic buckling does not exhibit any post-buckling strength. An explanation can be found in the fact that buckling causes bending over the plate thickness and thus an increase, respectively decrease, of the stresses at the inner and outer plate surfaces. Because of the shape of the material characteristic, this results in a reduction of the plate bending stiffness. Therefore, initial buckling automatically results a strength reduction.
- The non-dimensional stress at failure ($\sigma_u / f_{0.2}$) is larger than χ_T . Thus, the calculated inelastic buckling strength provides a lower bound for the actual inelastic buckling (failure) load. As presented in section 2.3.2, the actual inelastic critical stress depends on the plate geometry, whereas the applied equations are merely a conservative and generally applicable assumption. Note that while the presented FE-results are those of an initially perfect plate, a conservative prediction of $\sigma_{cr,T}$ also compensates the strength reduction due to initial imperfections.

- The presented average strain ε_{av} ($=u/L$) is the division of axial shortening by specimen length. As long as each buckle (half-wave) is identical, as has been checked in the elastic analyses, this is a correct interpretation. However, the occurrence of plastic stresses results in the localisation of one buckle. As a result, ε_{av} would underestimate the local strains and overestimate the according stiffness. However, an investigation by Mennink (2002b) led to the conclusion that localisation occurred only after the maximum load was reached. Thus, it has no influence on the development of a prediction model.
- The E^* - ε_{av} curves show that inelasticity results in a substantial reduction of the post-buckling stiffness. Typically, the curves cross each other at the proportional limit ε_p .
- Section 5.2.4 concluded that, elastically, the tangential post-buckling stiffness E^* could be approximated by a linear relation; this is obviously not the case with respect to inelastic buckling in the range beyond ε_p .
- No mode jumping was observed while the necessary large strains (see section 5.2.1) were never reached due to inelastic failure.

5.3.4 Evaluation of inelastic plate buckling

The previous section provided a qualitative description of inelastic plate buckling based on FE-results. Based on these results, this section will extend the prediction model for elastic plate buckling obtained in section 5.2.4 with inelasticity.

A distinction is made between the buckling behaviour of slender plates with post-buckling capacity and semi-compact plates with none. The apparent limit of elastic buckling is the proportional strain ε_p . To investigate the post-buckling capacity, the FE-results of the slender plates (Table 5-3; $\chi_T = 0.25, 0.50$ and 0.65) are summarised in Figure 5-15 for both materials. In addition, the σ_{av} - ε_{av} diagram includes the predicted strength σ_{pm} of the newly developed model at ε_p (closed diamonds), according to the procedure described at the end of this section.

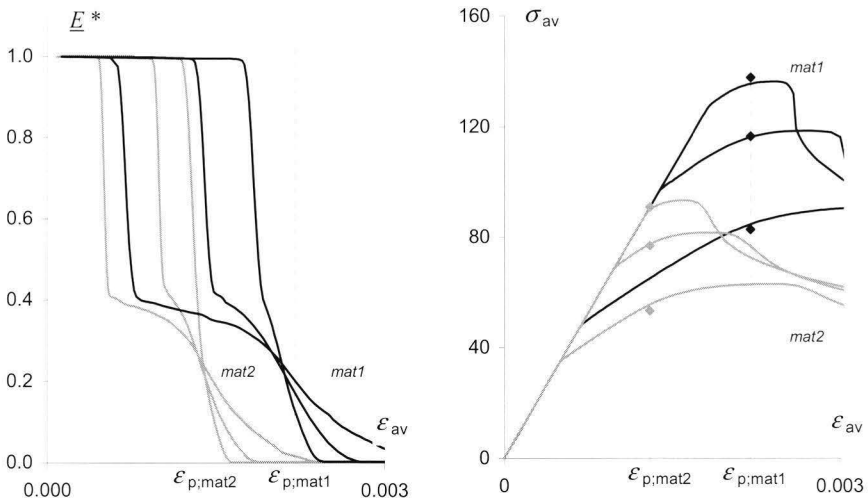


Figure 5-15 Comparison of the actual inelastic post-buckling resistance of an *ss-free* plate with the newly developed prediction model

The E^* - ε_{av} diagram shows the influence of inelasticity on the tangential stiffness. The most slender plates ($\chi_T = 0.25$) initially show elastic post-buckling behaviour of an individual *ss-free* plate, which is subsequently reduced due to inelasticity. The less slender plates ($\chi_T = 0.50$ and 0.65) are directly influenced by inelasticity. Nevertheless, the initial post-buckling stiffness is for all plates equal to $E^* = 0.4$. Notably, the curves intersect at ε_p ; the according stiffness is equal to $E^* = 0.22$. A practical approach is to linearise E^* from 0.4 at ε_{cr} to 0.22 at ε_p . This results in the inelastic equations of Table 5-4, which are comparable to those of Table 5-1. Note that the elastic critical stress σ_{cr} can be used (instead of $\sigma_{cr,T}$), as post-buckling strength is restricted to plates that show initial buckling below the proportional limit ε_p .

Table 5-4	Equations for the post-buckling behaviour of inelastic <i>ss-free</i> plates	
	$\underline{E}_{pm}^* = 0.42 - 0.2 \frac{\underline{\varepsilon}_{av} - 1}{\underline{\varepsilon}_p - 1}$	eq. 5-26
	$\underline{\sigma}_{pm} = 0.58 + 0.42 \underline{\varepsilon}_{av} - 0.1 \frac{(\underline{\varepsilon}_{av} - 1)^2}{\underline{\varepsilon}_p - 1}$	eq. 5-27
	$\sigma_{pm} = 0.58 E \varepsilon_{cr} + 0.42 E \varepsilon_{av} - 0.1 E \frac{(\varepsilon_{av} - \varepsilon_{cr})^2}{\varepsilon_p - \varepsilon_{cr}}$	eq. 5-28

Summarising procedure for inelastic plate buckling

This procedure describes the inelastic buckling behaviour of internal plates (case *ss-free*, section 5.2.1). The procedure is based on the elastic critical stress (σ_{cr}) of plates which, with $k_{cr} = 4.0$ for internal plates, results:

$$\sigma_{cr} = k_{cr} D \left(\frac{t}{b} \right)^2 \quad \text{where} \quad D = \frac{\pi^2 E}{12(1-\nu^2)}$$

$$\varepsilon_{cr} = \frac{\sigma_{cr}}{E}$$

ELASTIC BUCKLING with post-buckling strength

Elastic buckling occurs if the elastic critical stress is less than the proportional limit ($\sigma_{cr} < f_p$). The average axial stress in the plate (σ_{pm}) is predicted for any value of axial strain less the proportional limit (ε_p). This results in a line in Figure 5-15 from the origin, to the point of initial buckling, to the predicted failure load at ε_p (diamond).

$$\sigma_{pm}(\varepsilon) = E \varepsilon \quad \text{for } \varepsilon \leq \varepsilon_{cr}$$

$$\sigma_{pm}(\varepsilon) = 0.58 E \varepsilon_{cr} + 0.42 E \varepsilon - 0.1 E \frac{(\varepsilon - \varepsilon_{cr})^2}{\varepsilon_p - \varepsilon_{cr}} \quad \text{for } \varepsilon_{cr} < \varepsilon < \varepsilon_p$$

INELASTIC BUCKLING

Buckling in the inelastic range ($f_p \leq \sigma_{cr}$) results in sudden failure. Thus, the predicted strength follows the material characteristic until the inelastic critical strength ($\sigma_{cr,T}$) is reached and failure occurs.

For arbitrary materials, $\sigma_{cr,T}$ can be determined by using buckling curves presented in design codes, or the equations for χ_T as specified in section 5.3.2:

$$\sigma_{cr,T} = \chi_T(\sigma_{cr}) f_{0.2}$$

The relation between axial stress and axial strain is given by:

$$\varepsilon = \frac{\sigma_{pm}}{E} + 0.002 \left(\frac{\sigma_{pm}}{f_{0.2}} \right)^n \quad \text{for } \sigma \leq \sigma_{cr,T}$$

FAILURE LOAD

For practical purposes, it is of key interest to predict the failure or ultimate load. For an individual plate with cross-section $A_{pl} (= b t)$, the elastic or inelastic ultimate load is determined by:

$$N_{u,pm} = (0.68 E \varepsilon_{cr} + 0.32 E \varepsilon_p) A_{pl} \quad \text{if } \sigma_{cr} < f_p$$

$$N_{u,pm} = \chi_T(\sigma_{cr}) f_{0.2} A_{pl} \quad \text{if } f_p \leq \sigma_{cr}$$

5.4 Elastic local buckling of cross-sections

In extension to the plate buckling behaviour described in the previous sections, this section regards elastic local buckling of uniformly compressed cross-sections. The actual behaviour of cross-sections is studied for square hollow sections (SHS), rectangular hollow sections (RHS) and I-sections (IS). Based on the obtained insight, a theoretical approach is developed to determine the optical stresses due to initial and secondary buckling. Section 5.4.5 summarises the results and provides a prediction model that accurately describes the actual elastic local buckling behaviour of aluminium extrusions.

5.4.1 Square hollow sections (SHS)

A first set of FE-analyses is executed on square hollow sections (SHS). These sections are regarded because their geometry consists of four identical plates. Therefore, it allows the comparison with the elastic plate-buckling problem of internal plates of section 5.2.

Figure 5-16 presents in black the FE-results of four SHS-specimens with different plate slenderness (see Mennink 2002b). For comparison, the diagrams include in grey the FE-results of a simply supported plate (*ss-free*, section 5.2.1).

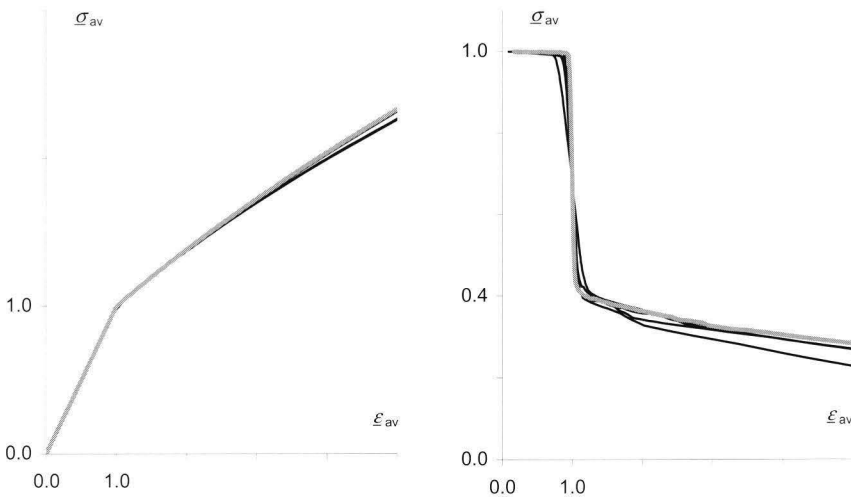


Figure 5-16 Comparison of the elastic local buckling behaviour of four SHS-specimen (black) and an *ss-free* plate (grey)

The presented curves show a remarkable agreement, though slight deviations occur for large strains. Apparently, interaction between plates in SHS-specimen is negligible and their behaviour can be described by that of an individual *ss-free* plate.

5.4.2 Rectangular hollow sections (RHS)

The local buckling behaviour of specimens consisting of internal plates is studied for a 50*80 mm RHS-specimen with various plate thicknesses. The thickness of the 80 mm plates is equal to 1.0 mm whereas the thickness of the 50 mm plates is varied, as described in detail in Mennink (2002b). Initial buckling occurs at the critical stress of the cross-section σ_{cr} , due to instability of the most slender plates. As these plates are supported by the remainder of the cross-section, they will be referred to as plate group 1 (*pg1*). Subsequent load increase may lead to secondary buckling, at $\sigma_{cr,2}$, due to instability of the supporting plates of group 2 (*pg2*). The value of σ_{cr} is obtained from an Eigenvalue analysis; the determination of $\sigma_{cr,2}$ is described in detail in section 5.4.4.

The FE-results of RHS3 are presented in Figure 5-17. In addition to the average stresses of the cross-section, the figure includes those of the *pg1*- and *pg2* plates. Finally, it includes two curves of individual *ss-free* plates (see section 5.2.1) that have been scaled to represent the behaviour of the *pg1*-plates ($\sigma_{cr,pl} = \sigma_{cr}$) respectively that of the *pg2*-plates ($\sigma_{cr,pl} = \sigma_{cr,2} = 3.8 \sigma_{cr}$).

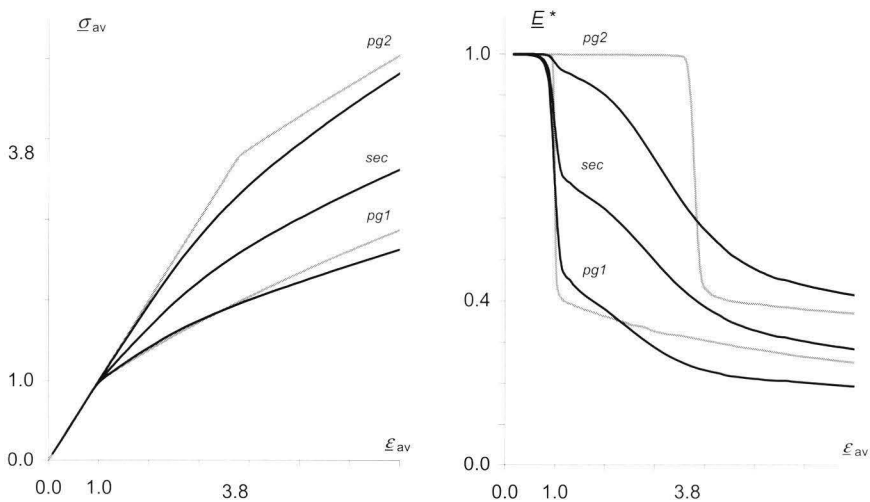


Figure 5-17 Local buckling of specimen RHS3, comparison of the various parts of the section (black) with that of individual *ss-free* plates (grey)

The behaviour of the *pg1*-plates is to some extent comparable with that of an individual *ss-free* plate. Contrarily, the supporting *pg2*-plates behave more like *ss-free* plates with initial plate imperfections (see Figure 5-4B), due to the deflections caused by initial buckling. Once the “imperfect” *pg2*-plates become susceptible to (secondary) buckling, they are less capable of providing support to the *pg1*-plates. As a result, the post-buckling stiffness of the *pg1*-plates reduces, even below that of an individual *ss-free* plate.

The FE-results of the supported *pg1*-plates of all RHS-specimen are summarised in Figure 5-18. In addition, the figure includes from top to bottom the results of: *cl-fixed* (acting as an upper bound), *ss-free* (which presented the average of the SHS-specimen), and a new set of equations that are a fitted lower bound (see Table 5-5).

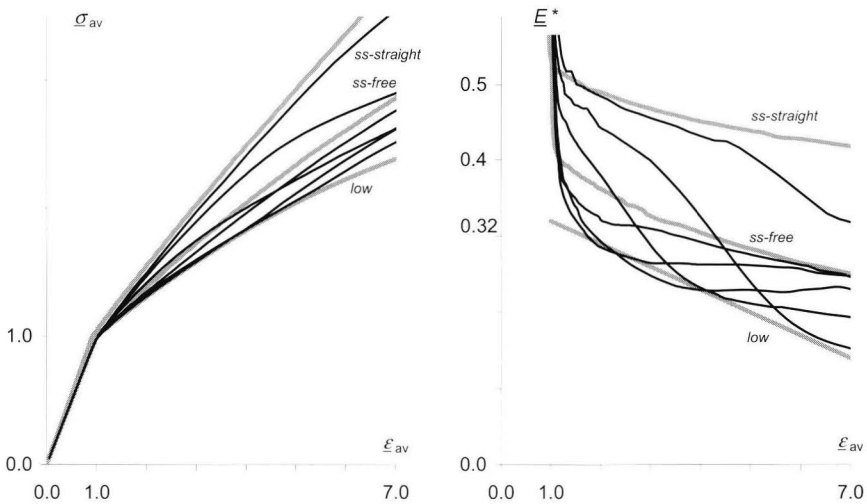
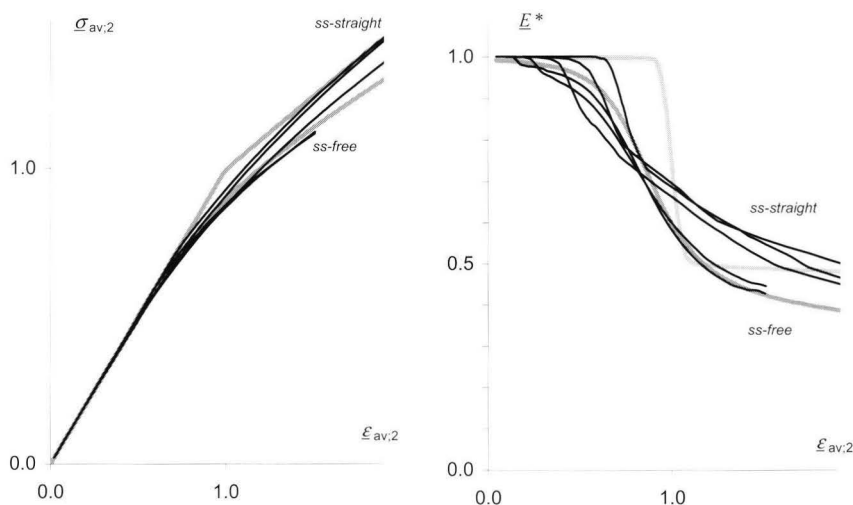


Figure 5-18 Investigation of the scatter in local buckling behaviour of the supported *pg1*-plates of all considered RHS-specimen (black) with that of individual plates (grey)

Table 5-5	Equations for the lower bound of RHS-buckling	
	$\underline{E}_{low}^* = 0.35 - 0.03\underline{\epsilon}_{av}$	eq. 5-29
	$\underline{\sigma}_{low} = 0.67 + 0.35\underline{\epsilon}_{av} - 0.015\underline{\epsilon}_{av}^2$	eq. 5-30
	$\sigma_{low} = 0.67E \epsilon_{cr} + 0.35E \epsilon_{av} - 0.015E \frac{\epsilon_{av}^2}{\epsilon_{cr}}$	eq. 5-31

As explained for RHS3, the supporting *pg2*-plates resemble imperfect plates. Therefore their results are presented in Figure 5-19 using $\underline{\sigma}_{av,2}$ ($=\sigma_{av}/\sigma_{cr,2}$) and $\underline{\varepsilon}_{av,2}$ ($=\varepsilon_{av}/\varepsilon_{cr,2}$) on the axes. The secondary buckling stress $\sigma_{cr,2}$ of the supporting plates is fully explained in section 5.4.4. The curve of an individual imperfect *ss-free* plate ($e_0 = t/10$) is presented as a lower bound, that of an *ss-straight* plate as an upper bound.



*Figure 5-19 Investigation of the scatter in local buckling behaviour of the supporting *pg2*-plates of all considered RHS-specimen (black) with individual “perfect” *ss-straight* and “imperfect” *ss-free* plates (grey)*

The results of both Figure 5-18 and Figure 5-19 show a remarkable agreement with the conclusions drawn from specimen RHS3. Starting with plate group 2, the following remarks can be made:

- It is obvious that all *pg2*-plates resemble the behaviour of imperfect individual plates. The amount of “imperfection” depends on a complex interaction between cross-sectional properties and critical stresses that is not investigated.
- Not all specimens show the characteristic S-curve of imperfect plates, especially not at low strains. This is because “imperfections” occur only once initial buckling of the cross-section has taken place.
- The three specimens with the most slender *pg1*-plates (RHS6, RHS5 and RHS4) exceed *ss-free* and resemble the upper bound of *ss-straight*. Apparently, the buckled *pg1*-plates restrict the in-plane deformations of the *pg2*-plates.

Additional remarks from the behaviour plate group 1 are:

- As long as the supporting *pg2*-plates show little effect of buckling, the *pg1*-plates of the compact specimen (RHS1, RHS2 and RHS3) resemble *cl-fixed*. However, once the support of the *pg2*-plates fails, so thus the stiffness of the *pg1*-plates.
- The post-buckling stiffness of the *pg1*-plates has a distinct range. In the presented results, *ss-straight* and *low* define the upper and lower boundaries, while *ss-free* coincides with the average of this range. Note that *ss-free* coincides as well with the behaviour of the SHS-specimens.

Summarised, this section provided a qualitative description of the interaction between the supported (*pg1*) and supporting (*pg2*) plates in RHS specimens. It is concluded that average, upper, and lower bounds can be specified for the *pg1*-plates. Furthermore, the supporting *pg2*-plates show a remarkable resemblance with imperfect plates.

5.4.3 I-sections (IS)

The interaction between internal plates and outstands is investigated for an I-section with 30 mm wide flanges, a 25 mm wide web and 1 mm thick flanges. The web thickness is varied (see Mennink 2002b) such that plate group 1 (*pg1*) consists of the flanges, whereas plate group 2 (*pg2*) consists of the web. The results of specimen ISI.3 are presented in Figure 5-20. For comparison, a simply supported outstand at initial buckling (*out-ss-free*), as well as a supported internal at $\sigma_{cr,2}$ (*ss-straight*) are included.

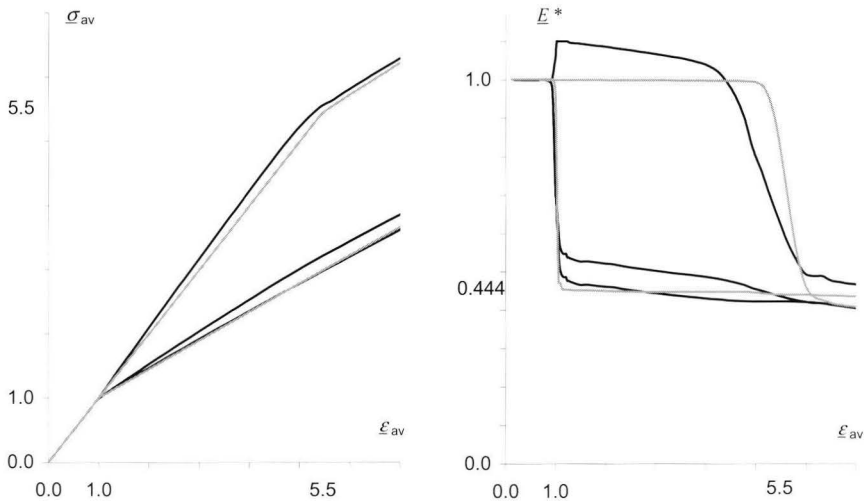


Figure 5-20 Local buckling of specimen ISI-3, comparison of the various parts of the cross-section (black) with that of an individual *out-ss-free* outstand at σ_{cr} and an *ss-straight* internal at $\sigma_{cr,2}$ (grey)

These figures result in the following interesting remarks:

- In general, it is assured that the buckling stress of a plate is increased by the rotational support of connecting plates (compare *ss-free* and *cl-free*). However, as only one web exists to support all four flanges, at initial buckling, it is assumable that this rotational stiffness is limited. As a result, the flanges behave almost exactly as simply supported outstands. Note that the critical length and stress do not coincide with plate buckling ($\sigma_{cr} = 1.7 \sigma_{cr,pl}$). Thus, it can be concluded that the supporting influence is a combination of rotational constraint and buckling length.
- The initial post-buckling stiffness of the web exceeds the value of 1.0. This can be explained by the fact that the average axial stresses are taken from the cross-section at half the specimen length. Thus, its results are local. Contrarily, the average axial strains are global, as they are obtained from the axial shortening of the specimen. Apparently, the local strains are larger. This can be explained by considering load redistribution over the cross-section at initial buckling; the flanges will partly unload unto the web because of their reduced stiffness.
- Initial buckling results in the occurrence of four half-waves over both the web and the flanges (see Figure 5-21A). However, load increase results in radically different deformation patterns. At $\varepsilon_{av} = 5.5$ (B) a second mode occurs. Though the buckles seem to localise, this is not entirely true. In fact, secondary buckles develop on top of those of mode I. Further load increase results in the sudden development of very local additional short-wave buckles (C). Meanwhile, the deformation pattern of the flanges hardly changes, though the buckles become steeper. The occurrence of these buckles is explained in section 5.4.4.

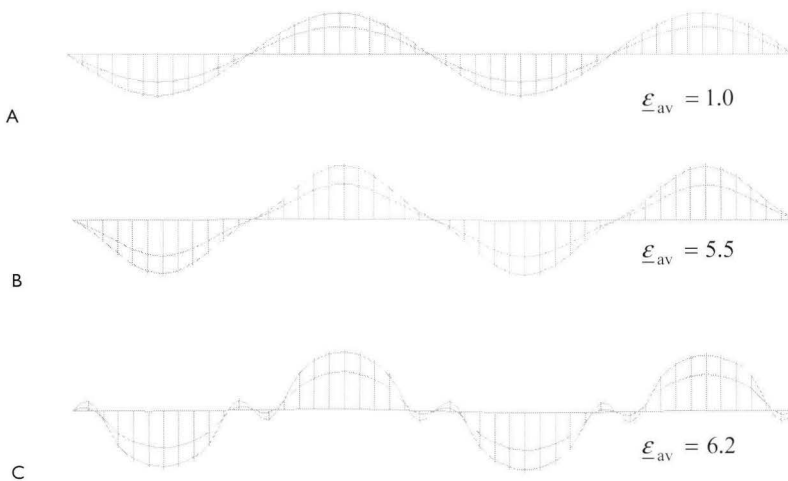


Figure 5-21 Relative out-of-plane deflections of the web of IS1.3 at various loads

The FE-results of five I-sections, with web thicknesses decreasing from IS1.1 to IS1.5 are presented in Figure 5-22 for the flanges ($pg1$) and in Figure 5-23 for the webs ($pg2$). For comparison, the results of several individual plates are presented.

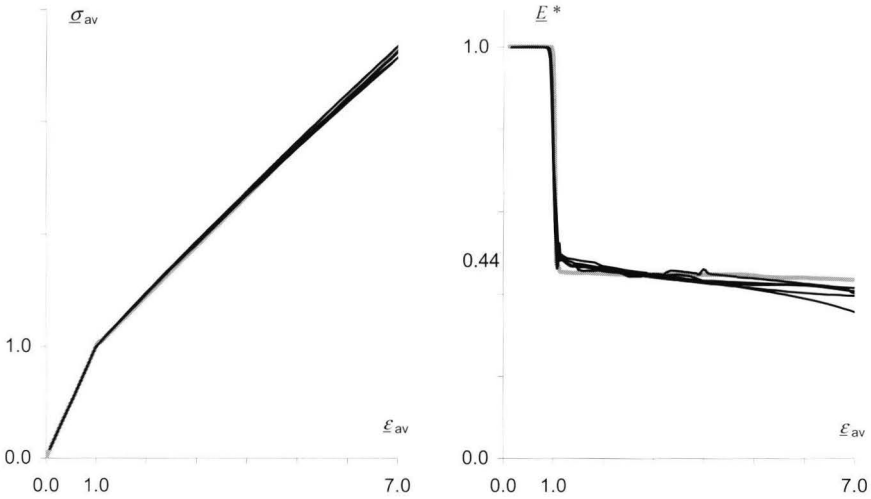


Figure 5-22 Investigation of the scatter in local buckling behaviour of the supported $pg1$ -plates of all considered IS-specimen (black), for comparison out-ss-free is added (grey)

The figure clearly shows that the behaviour of the supported outstands coincides with that of an individual outstand. The fact that the tangential stiffnesses coincide is in agreement with the comparable behaviour of the variously supported outstands of Figure 5-8. However, contrarily to the RHS-specimen, no subsequent stiffness reduction occurs at secondary buckling.

Figure 5-23 relates the behaviour of the supporting webs ($pg2$) to the critical stress according to secondary buckling $\sigma_{cr,2}$. Thus, it presents $\epsilon_{av,2}$ ($= \epsilon_{av} / \epsilon_{cr,2}$) on the horizontal axis and $\sigma_{av,2}$ ($= \sigma_{av} / \sigma_{cr,2}$) on the vertical axis. As previously described, the critical length of the additional buckles cannot be measured accurately. Thus, it is not possible to determine $\sigma_{cr,2}$ directly. However, from the RHS-specimen is known that the supporting ($pg2$) plates behave like imperfect plates (see Figure 5-19). Assuming that this is true for I-sections as well, it is possible to determine $\sigma_{cr,2}$ such that similar E^* - ϵ_{av} curves are obtained. In addition, the figures include in black the characteristics results of the *out-ss-free* and *ss-straight* cases as described in section 5.2.1.

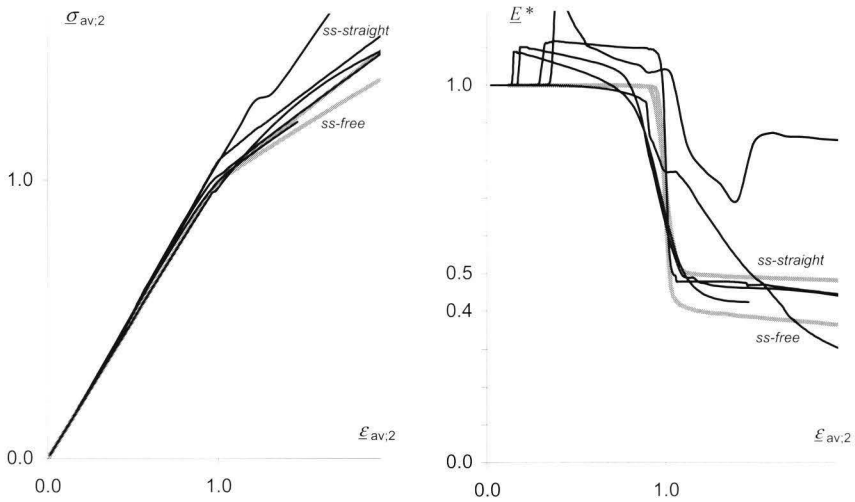


Figure 5-23 Investigation of the scatter in local buckling behaviour of the supporting $pg2$ -plates of all considered IS-specimen (black), comparison with the individual plates ss -free and ss -straight (grey)

The figures clearly show that the post-buckling behaviour of the ($pg1$) flanges is hardly influenced by secondary buckling of the ($pg2$) webs. Its behaviour is described best by that of the *out-ss-free* case, which happens to coincide with the *ss-straight* case. Furthermore, it seems that the flanges restrain any in-plane deformations of the web. As a result, secondary buckling of the internals is described best by the behaviour of an *ss-straight* plate.

5.4.4 Theory – Local buckling modes

So far, this chapter has shown that the buckling and post-buckling behaviour of actual cross-sections can be described comparably to that of individual plates. However, this only works if a correct interpretation is given of the plate-buckling problem; assuming “hinge-supported” plates is inaccurate. This section explains the observed modes for the RHS and IS-specimen and outlines a procedure to determine the actual initial and secondary buckling modes of a cross-section, and the according critical stresses, based on an interpretation of the actual plate buckling behaviour.

Initial buckling

In general, two approaches exist to determine the initial buckling mode of a cross-section. First, it is commonly assumed that the first mode of an Eigenvalue analysis, executed either analytically (see section 2.4.2) or numerically (see section 2.4.4), is representative for the actual initial buckling mode. This has been verified for the local buckling behaviour of aluminium extrusions, by comparison of FE and experimental results in Chapter 4. Secondly, most design codes regard the local buckling behaviour of a cross-section based on the individual plate buckling behaviour of its composing plates. This section will investigate the initial buckling behaviour by comparing these two approaches for the two example specimens of Figure 5-24. For both specimens, plate group 1 ($pg1$) consists of the flanges and plate group 2 ($pg2$) of the web(s). In addition, the figure includes the deflected (buckled) shape of the cross-section according to an Eigenvalue analysis, as well as the according critical length (L_{cr}), and stress (σ_{cr}).

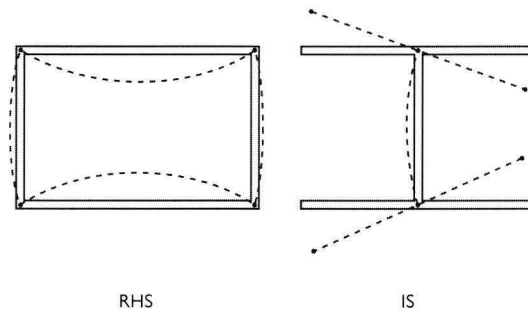


Figure 5-24 RHS and IS examples, deflected shapes in striped lines

The critical stress of individual plates is determined from equation 2-17. In which the buckling coefficient k_{cr} depends on the rotational stiffness transferred at the plate connections, and the critical length (L_{cr}) of the cross-section.

$$\sigma_{cr} = k_{cr} \frac{\pi^2 E}{12(1-\nu^2)} \left(\frac{t}{b}\right)^2 \tag{eq. 2-17}$$

Figure 5-25 presents k_{cr} as a function of the critical length for various support conditions (see section 2.3.2). Upper and lower limits for the rotational stiffness at plate connections are given by a full clamp (c), respectively a simply supported (ss) or hinged connection. Initial buckling will result in one “buckle” over L_{cr} . The coefficient k_{cr} of the internal flange of the RHS-specimen is therefore positioned in the specified area between curves A and C, whereas k_{cr} of the flanges of the IS-specimen is positioned in the area between D and E. While the pg/l -flanges cause initial buckling, their according critical stress should coincide with that of the cross-section ($\sigma_{cr} = \sigma_{cr,pgl}$). Substitution of σ_{cr} (RHS) and σ_{cr} (IS) for σ_{cr} in equation 2-17, as well as the according widths (b) and thicknesses (t), results the buckling coefficients k_{cr} (RHS) and k_{cr} (IS). While the critical lengths (L_{cr}) are known from the Eigenvalue analyses, k_{cr} can be plotted in Figure 5-25 for the two examples. Obviously, the actual values of k_{cr} (5.2 and 0.8) are substantially higher than those generally used (4.0 for internal plates, 0.425 for outstands).

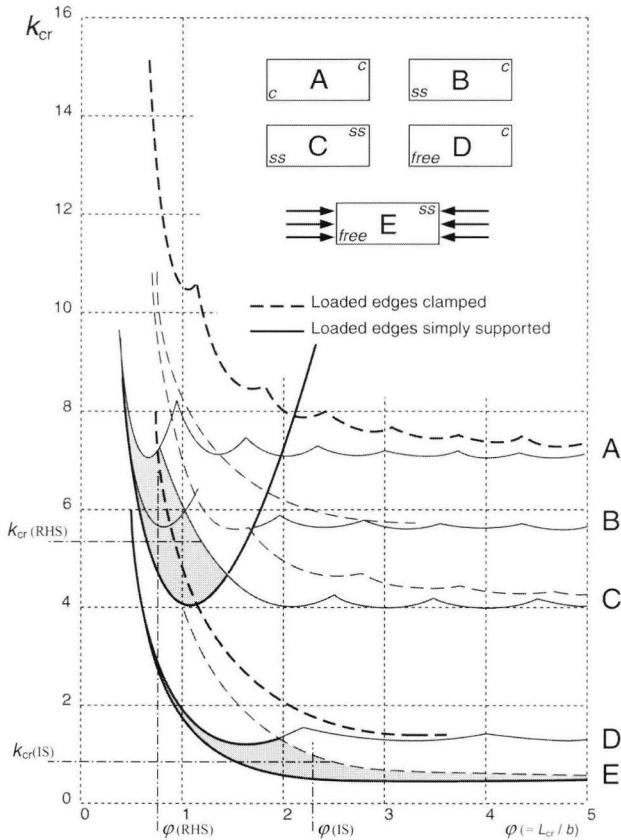


Figure 5-25 Determination of the initial and secondary buckling stresses

Determination of the supported (pg1) and supporting (pg2) plate groups

The examples have been chosen such that it is clear that the flanges cause initial buckling. However, this is not necessarily clear for complex cross-sections. Therefore, this section provides a generally applicable procedure to distinct the supported plates of plate group 1 (pg1) from the supporting plates of plate group 2 (pg2).

The simplest procedure to distinct the supported from the supporting plates is to determine the critical stress of each plate individually, based on eq. 2-17 and assuming that $k_{cr} = 4.0$ for internals, respectively 0.425 for outstands. Those plates with the lowest value of σ_{cr} are the supported plates, all others are supporting. However, Figure 5-25 shows that this approach may severely underestimate the actual critical stresses.

A far more accurate procedure is possible when an Eigenvalue analysis is executed. Again, the critical stresses are determined for each plate i . As $k_{cr,i}$ is positioned at $\varphi_i = L_{cr} / b_i$, lower bounds are found at the intersection of φ_i and the highlighted part of curve C for internals, respectively curve E for outstands. Using the equations of section 2.3.2 these curves are described by:

$$\text{Internals: } k_{cr,i} = \frac{1}{\varphi_i^2} + \varphi_i^2 + 2 \quad \text{eq. 5-32}$$

$$\text{Outstands: } k_{cr,i} = 0.456 + \frac{1}{\varphi_i^2} \quad \text{eq. 5-33}$$

Now it is possible to determine for each plate i in a cross-section a lower bound for the buckling coefficient $k_{cr,i}$, and the critical stress $\sigma_{cr,i}$. However, the actual cross-section – and therefore all supported plates – buckles at $\sigma_{cr,sec}$. Thus plate group 1 (pg1) consists of all plates of which the critical stress ($\sigma_{cr,i}$) is less than that of the cross-section (σ_{cr}), subsequently plate group 2 (pg2) consists of all remaining plates. This approach allows a univocal distinction between plate group 1 and plate group 2.

Mode jumping

Section 5.2 showed that the elastic buckling behaviour of individual plates was influenced by the occurrence of mode jumping. It was shown that the occurrence depended on the support conditions with respect to both translations and rotations at the unloaded edges. Obviously, the interaction between plates in actual cross-sections may cause comparable situations. Mode jumping could thus occur for cross-sections as well.


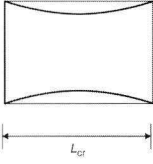

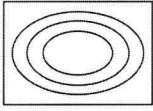

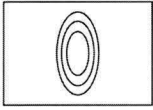
The approach used in the prediction model for elastic plate buckling is to prevent mode jumping by limiting the model to strains below ε_{lim} . With respect to both internals and outstands it can be concluded that mode jumping did not occur for clamped plates where it did for the simply supported ones. Assuming this can be generalised: an increase of the rotational stiffness (clamped versus simply-supported) results in an increase of the limit strain. Thus, a lower bound is found for mode jumping in cross-sections by the limit strain obtained from plates.

Secondary buckling

The FE-analyses on RHS and IS-specimen showed that when loaded beyond initial buckling, the supporting plates might buckle as well. From here on, this phenomenon is referred to as secondary buckling. Simplified, the supporting *pg2*-plates will buckle themselves. Even though both the RHS and IS-specimen showed this phenomenon, their deformation patterns were entirely different. Thus prompting a further distinction, this is explained below and visualised in Table 5-6.

The plate groups of the RHS example were based on the critical stress of the various plates. Obviously, the flanges (largest plates) caused initial buckling, whereas the webs provided support. The cross-sectional deformations caused by the buckling behaviour of the flanges “force” the webs to buckle into a comparable deformation pattern. The given equations for k_{cr} are therefore suitable as well to describe the buckling behaviour of the *pg2*-plates. This approach has been used to determine the critical stress $\sigma_{cr,2}$ for the RHS-specimen in Figure 5-19, which showed such an excellent agreement. This type of buckling is referred to as *secondary buckling type A*.

Secondary buckling of specimen IS1.3 (see Figure 5-21), is markedly different. With large values of φ , the approach presented above, would result in extremely high values of k_{cr} and the incorrect conclusion that secondary buckling does not occur. Though the web is forced into a certain displacement field by initial flange buckling, one should consider that this shape is relatively shallow because of its large buckling length. In fact, the web is no more than a slightly curved plate that is fixed into position by the buckled flanges. Again referring to Figure 5-25 this behaviour is comparable to case A. More specifically the striped lines of case A, while in most cases the various buckling lengths won't match. Obviously, a safe lower bound for this approach is to use $k_{cr} = 7.0$ at $\varphi > 5.0$. This has been verified against the FE-analyses on IS-specimen in Mennink (2002b) and is subsequently referred to as *secondary buckling type B*.

Table 5-6	Characteristic local buckling modes – IS example	
		<p>Initial buckling Buckling of the supported plates ($pg1$) at L_{cr} coincides with buckling of the cross-section</p>
		<p>Secondary buckling – type A Buckling of the supporting plates ($pg2$) at L_{cr}</p>
		<p>Secondary buckling – type B Formation of an additional buckle on the supporting plates ($pg2$) at a different buckling length</p>

Based on the FE-analyses of the previous sections it is obvious that the current approach is essential in the determination of the actual buckling behaviour. The presented approach provides a generally applicable and workable method for the determination of the plate groups and initial and secondary buckling stresses.

5.4.5 Evaluation of elastic local buckling of cross-sections

The previous sections described the elastic local buckling behaviour of uniformly compressed cross-sections with various cross-sectional shapes. It was shown that their buckling and post-buckling behaviour is more complex than that of individual plates (see section 5.2). Nevertheless, its behaviour could be simplified and it is possible to determine a generally applicable prediction model by taking into account the following characteristic aspects:

- The cross-section is divided into two plate groups. A distinction is made between those plates that cause initial buckling ($pg1$) and those that provide support ($pg2$), (see section 5.4.4).
- The critical stress σ_{cr} coincides with the bifurcation load according to a numerical or analytical Eigenvalue analysis of the cross-section. As imperfections are small, it is assumed that the entire cross-section behaves elastically up to σ_{cr} .
- Secondary buckling of the supporting $pg2$ -plates occurs at $\sigma_{cr,2}$, which can be determined conservatively according to section 5.4.4.

- The post-buckling behaviour of the supported plates ($pg1$) is comparable to that of individual plates. For internals, the behaviour was evaluated in section 5.4.2. The average behaviour was presented by equations fitted on the behaviour of an individual ss -free plate, an upper bound on that of an ss -straight plate, as presented in Table 5-1. The equations for a lower bound (low) are presented in Table 5-5. For outstands (see section 5.4.3) the behaviour is described best by that of an out - ss -free plate.
- The post-buckling behaviour of supporting ($pg2$) internals resembles the behaviour of an imperfect individual ss -straight plate. That of outstands resembles an individual out - ss -free plate. Note that the behaviour of a perfect ss -straight and out - ss -free plate almost coincide (see section 5.2.4). Therefore, further reference is made only to ss -straight.

Figure 5-26 presents the results of the supported $pg1$ -plates of all FE-analyses made on SHS, RHS, and IS-specimen. In addition, they include the three prediction curves.

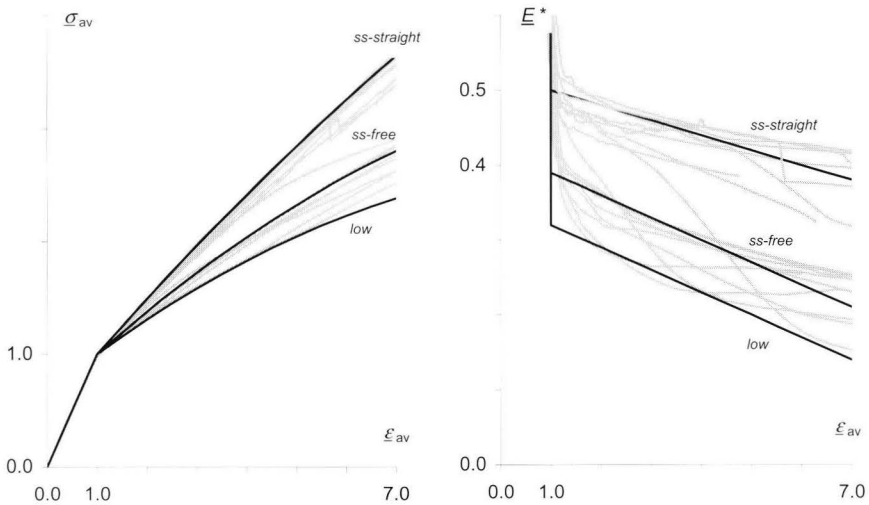


Figure 5-26 Comparison of the local buckling behaviour of the supported $pg1$ -plates of all analysed cross-sections (grey) with three predicted curves (black)

The diagrams clearly show the appropriateness of the three curves. As presented in the previous sections, the IS-results are positioned around the upper *ss-straight* curve, the SHS-results surround the middle *ss-free* curve, while the RHS-results cover the entire range. As previously presented, the scatter of the RHS is caused by the distinct interaction of web and flange buckling. Contrarily, interaction is limited for the I-sections. Obviously, no interaction occurs for the SHS-specimen.

The *pg2*-plate of all FE-analyses on RHS and IS-specimens are presented in Figure 5-27. In addition, the diagrams include the behaviour of an individual *ss-straight* and *ss-free* plate. Note that the diagrams are slightly unclear because of two aspects, previously explained in section 5.4.4. First, the influence of load redistribution results in values of E^* larger than unity. Secondly, the occurrence of higher-order buckling modes and mode jumping results in unclear patterns for the post-buckling stiffness.

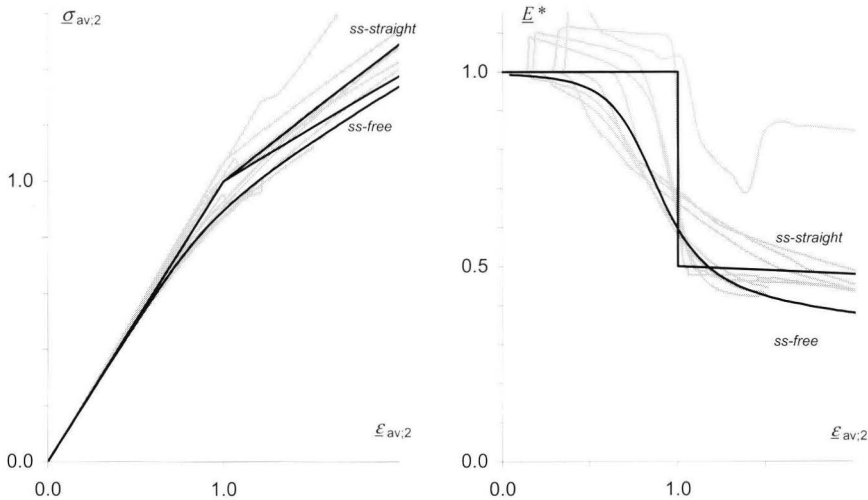


Figure 5-27 Comparison of the local buckling behaviour of the supported *pg2*-plates of all RHS and IS specimen

The diagrams show that the *pg2*-plates behave like imperfect plates. These imperfections are caused by the deformations resulting from buckling of the *pg1*-plates. Again, there is the distinction between RHS and IS-specimen. The RHS-specimens generally show a large influence of imperfectness, whereas the influence is very small for the IS-specimen. A further observation is that the post-buckling stiffness lies somewhere in between that of the *ss-straight* and *ss-free* curves.

With respect to the prediction model, the following choices are made in order to determine a general and practically applicable prediction model:

- For the *pg1*-plates, it is decided to represent the behaviour of internal plates (“webs”) by *lower* and that of outstands (“flanges”) by *ss-straight*. Thus providing a lower bound for the internal plates, which show a considerable scatter, while providing accurate results for outstands.
- The behaviour of the *pg2*-plates is determined based on *ss-straight*. It is specifically chosen to use the most accurate prediction curve instead of the conservative curve of the imperfect *ss-free* plate, as plate interaction is already incorporated conservatively for the *pg1*-plates.

The resulting prediction model for elastic local buckling of cross-sections is presented in the chart at the end of this section. The results of this new prediction model (*pm*), and an approach according to existing theories (*ss*), are presented in Figure 5-28. The *ss*-model determines the behaviour of the cross-section as a summation of the individual behaviour of its simply supported plates, assuming “hinges” at the plate connections. According to section 5.2.4, internals were modelled with *ss-free*, outstands with *ss-straight*. As both models determine the resistance of the cross-section as a function of its axial shortening, their accuracy depends on the load level. The diagrams therefore relate the predicted axial resistance (N_{pm} or N_{ss}) to that of the FE-analysis (N_{FE}), as a function of the non-dimensionalised axial strain $\underline{\epsilon}_{av}$.

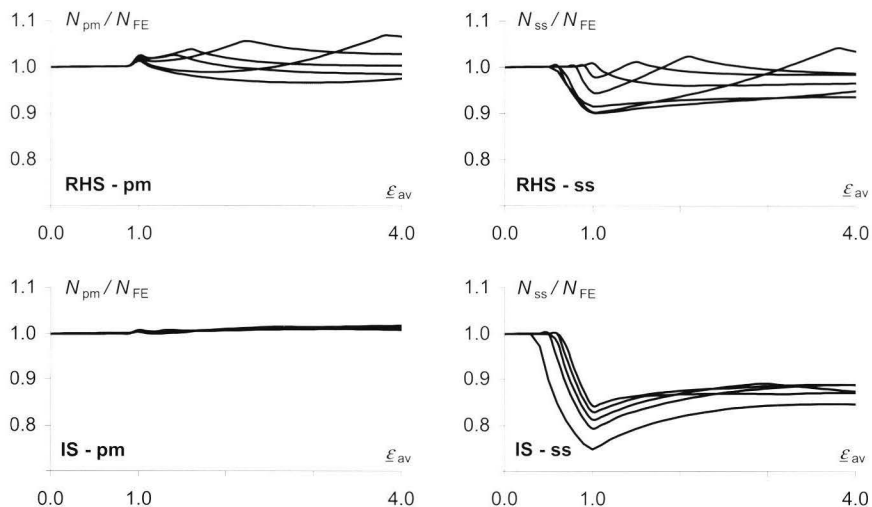


Figure 5-28 Comparison of new (*pm*) and existing (*ss*) approaches – average strength of the cross-section

Several remarks must be made:

- The accuracy of both models is comparable for the RHS-specimen. Because of the inaccurate prediction of the point of initial buckling of the *ss*-model, its largest deviations (up to 10%) occur at $\underline{\varepsilon}_{av} = 1.0$. In both models peaks occur at $\sigma_{cr,2}$, while the “imperfectness” of the *pg2*-plates is not modelled. However, in the most interesting region at $\underline{\varepsilon}_{av} = 1.0$ the new prediction model performs markedly better.
- The new prediction model shows very accurate results for the IS-specimens (IS-pm). This is mainly contributed to the accurate description of outstand behaviour, whereas the influence of interaction with the web is small. Contrarily, the *ss*-model (IS-ss) shows substantial deviations, up to 25% at $\underline{\varepsilon}_{av} = 1.0$, caused by an inaccurate prediction of σ_{cr} .
- The IS-specimens also show that the combination of outstands and internals results in such a large difference between σ_{cr} and $\sigma_{cr,2}$ that the relevance of $\sigma_{cr,2}$ in the practical range ($\underline{\varepsilon}_{av} < 4.0$) is negligible. Obviously, this might not be true for complex cross-sections or for specimens with unusual ratios between web and flange widths or thicknesses.

It can be concluded that an accurate prediction model is developed for the elastic local buckling behaviour. Contrarily to existing approaches, it is based on a thorough investigation of the actual behaviour of cross-sections.

Summarising procedure for elastic local buckling of cross-sections

1. Execute an **Eigenvalue analysis**

Either using analytical solutions or, more appropriate for arbitrary cross-sections, using finite-element or finite-strip programs. The analysis must result in the critical length L_{cr} and critical stress σ_{cr} of the cross-section.

2. **Schematise the cross-section** to nodes and plates

Each individual plate i has width (b_i) and thickness (t_i). Plates are connected at nodes that are positioned at the intersection of the heart-lines of the plates

Determine
$$D = \frac{\pi^2 E}{12(1-\nu^2)}$$

3. **Determine the elastic critical stress of each plate** ($\sigma_{cr,i}$)

Plate slenderness:
$$\varphi_i = \frac{L_{cr}}{b_i}$$

For internals
$$k_{cr,i} = \frac{1}{\varphi_i^2} + \varphi_i^2 + 2 \quad \text{but:} \quad k_{cr1,i} \leq 7$$

For outstands:
$$k_{cr,i} = 0.456 + \frac{1}{\varphi_i^2}$$

Critical stress
$$\sigma_{cr,i} = k_{cr,i} D \left(\frac{t}{b} \right)^2$$

4. **Determine plate groups**

▪ **Plate group 1 (pg1) - Supported plates**

The first plate group consists of all plates that buckle at the critical stress of the cross-section (σ_{cr}). These can be determined from:

$$\sigma_{cr,i} \leq \sigma_{cr}$$

Note: it is always allowed to add additional plates to this group.

▪ **Plate group 2 (pg2) - Supporting plates**

The second group of plates consists of all those plates that are not within plate group 1.

- Determine the secondary buckling stress $\sigma_{cr,2}$
The value of $\sigma_{cr,2}$ is equal to the lowest critical stress of the plates j that are within plate group 2:

$$\sigma_{cr,2} = \min_{j \in pg2} (\sigma_{cr,j})$$

5. **Determine the characteristic axial strains**

Initial buckling:
$$\varepsilon_{cr} = \frac{\sigma_{cr}}{E}$$

Secondary buckling or limit strain:
$$\varepsilon_{cr,2} = \min\left(\frac{\sigma_{cr,2}}{E}; 5.6\varepsilon_{cr}\right)$$

Limit strain:
$$\varepsilon_{lim} = 5.6\varepsilon_{cr}$$

6. **Definition of the post-buckling formulae**

For *pg1*-internals:

$$\sigma_{pb}(\varepsilon; \varepsilon_{cr}) = 0.67E \varepsilon_{cr} + 0.35E \varepsilon - 0.015E \frac{\varepsilon^2}{\varepsilon_{cr}}$$

For *pg2*-internals or both *pg1* and *pg2*-outstands:

$$\sigma_{pb}(\varepsilon; \varepsilon_{cr}) = 0.49E \varepsilon_{cr} + 0.52E \varepsilon - 0.01E \frac{\varepsilon^2}{\varepsilon_{cr}}$$

7. Predict the average **axial stress** (σ_{pm}) for $\varepsilon \leq \varepsilon_{cr}$

$$\sigma_{pm}(\varepsilon) = E\varepsilon$$

8. Predict the average **axial stress** (σ_{pm}) in the plate groups for $\varepsilon_1 < \varepsilon < \varepsilon_2$

Plate group 1
$$\sigma_{pm;pg1}(\varepsilon) = \sigma_{pb}(\varepsilon; \varepsilon_1)$$

Plate group 2
$$\sigma_{pm;pg2}(\varepsilon) = E\varepsilon$$

9. Predict the average **axial stress** (σ_{pm}) in the plate groups for $\varepsilon_2 < \varepsilon < \varepsilon_3$

Plate group 1
$$\sigma_{pm;pg1}(\varepsilon) = \sigma_{pb}(\varepsilon; \varepsilon_1)$$

Plate group 2
$$\sigma_{pm;pg2}(\varepsilon) = \sigma_{pb}(\varepsilon; \varepsilon_2)$$

10. Predict the **axial strength** (N_{pm}) as a function of ε

$$N_{pm}(\varepsilon) = \sigma_{pm;pg1}(\varepsilon)A_{pg1} + \sigma_{pm;pg2}(\varepsilon)A_{pg2}$$

5.5 Inelastic local buckling of cross-sections

Comparably to section 5.3 for inelastic plate buckling, this section investigates the influence of inelasticity on the local buckling behaviour of cross-sections. Again, the two material characteristics (*mat1* and *mat2*) have been used that represent an average and a lower bound for the inelastic behaviour of aluminium alloys.

5.5.1 Rectangular hollow sections (RHS)

Geometrical and physical non-linear FE-analyses have been executed on all RHS-specimen specified in section 5.4.2. The inelastic results of RHS3, using *mat1*, are presented in Figure 5-29 by their average stress-strain (σ_{av} - ϵ_{av}) and stiffness-strain (E_T^* - ϵ_{av}) curves. In addition the diagrams include the strains according to the inelastic critical stress ($\epsilon_{cr,T}$) and proportional limit (ϵ_p).

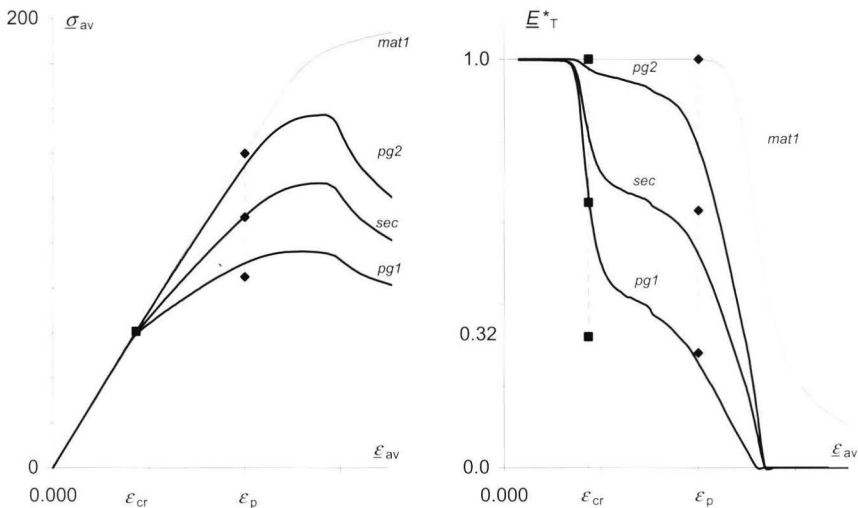


Figure 5-29 Comparison of the inelastic local buckling behaviour of specimen RHS3 with the results of the elastic prediction model at ϵ_{cr} and ϵ_p

Comparison with Figure 5-17 shows that the inelastic and elastic analyses show identical results in the elastic range ($\epsilon < \epsilon_p$). Therefore, the results of the elastic prediction model of section 5.4.5 are presented. At initial buckling (blocks), the slender *pg1*-plates start to buckle and the tangential stiffness reduces. Subsequently, the results are presented at the proportional limit (diamonds). Comparably to the inelastic behaviour of individual plates, section 5.3.4, the proportional limit coincides with the sudden (inelastic) stiffness reduction. Such stiffness reduction reduces the critical loads of higher order buckling modes and the cross-section might become susceptible to all kinds of mode interactions.

Figure 5-30 and Figure 5-31 present for all RHS-specimen the results of the entire cross-section with respectively *mat1* and *mat2* material characteristics. Comparably to Figure 5-29, the diagrams include the calculated inelastic critical stresses (blocks) and the results of the elastic prediction model at the proportional limit (diamonds).

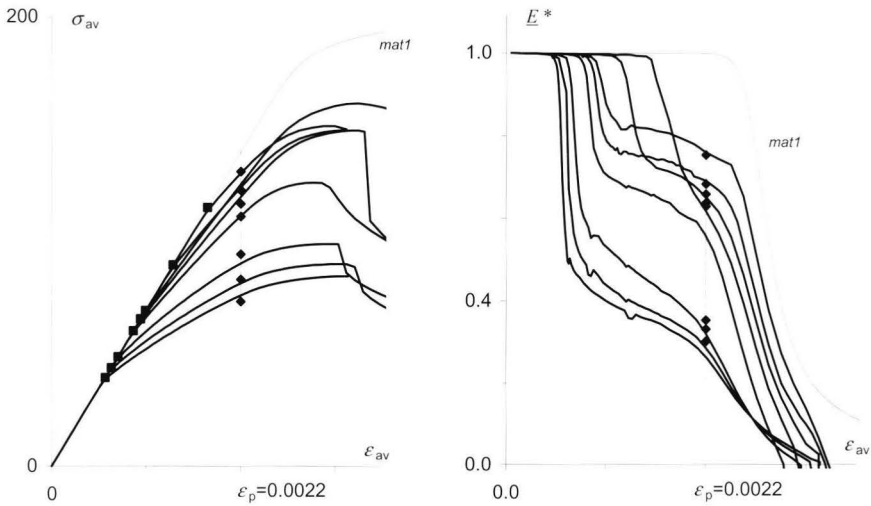


Figure 5-30 Comparison of the inelastic (*mat1*) local buckling behaviour of all RHS-cross-sections, with $\sigma_{cr,T}$ (blocks) and the elastic model at ε_p (diamonds)

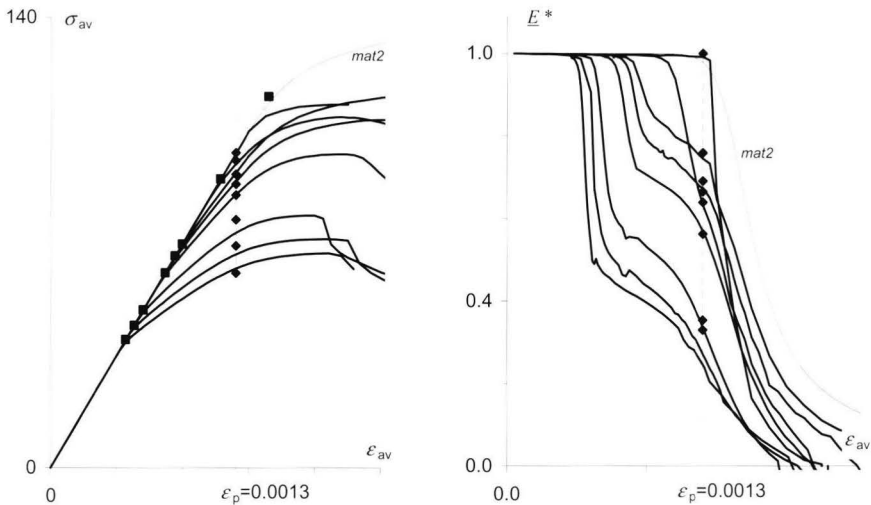


Figure 5-31 Comparison of the inelastic (*mat2*) local buckling behaviour of all RHS-cross-sections, with $\sigma_{cr,T}$ (blocks) and the elastic model at ε_p (diamonds)

The following remarks can be made with respect to these figures. Concerning the critical stresses, the post-buckling capacity and the failure load:

- The inelastic critical stress according to initial buckling ($\sigma_{cr,T}$) can be determined from the elastic critical stress (σ_{cr}) and the inelasticity coefficient χ_T derived in section 5.3.2. However, for cross-sections exhibiting post-buckling strength, the occurring strain is restricted to the proportional limit ($\varepsilon_{av} < \varepsilon_p$) and the influence of inelasticity is negligible ($\sigma_{cr,T} = \sigma_{cr}$). For semi-compact sections (initial buckling in the inelastic range) the calculated inelastic critical stress ($\sigma_{cr,T}$) provides a measure for the failure load.
- The inelastic critical stress due to secondary buckling ($\sigma_{cr,2,T}$) is obtained comparably. Note, that the visible influence of secondary buckling is limited, as $\sigma_{cr,2}$ is in most cases much larger than σ_{cr} .
- The predicted post-buckling capacity can be visualised by drawing an almost linear line in Figure 5-30, from the point of initial buckling (block) to the predicted strength at the proportional limit (diamond). As these results are essentially elastic, the excellent agreement specified in 5.4.5 is obtained.
- The E^* - ε_{av} diagrams also show that once the limiting strains are reached, the curves dive downwards. As it is not clear how to incorporate this into a simple approach it is decided to limit the predicted strength to that obtained at the proportional limit ε_p . Though at first sight this may seem rather conservative as some cross-sections show a considerable increase in strength beyond ε_p , in fact it is not. As presented in section 5.4.4, various types of secondary buckling may occur, which are essentially based on the tangential stiffness. These modes may occur suddenly as E^* drops beyond ε_p . The same is true for any other type of instability including distortional and overall buckling phenomena. For practical application, the strength according to ε_p thus presents both a conservative prediction of the ultimate strength, as well as an accurate prediction of the actual behaviour.

5.5.2 I-sections (IS)

This section presents the results of geometrical and physical non-linear FE-analyses executed on the IS-specimen specified in section 5.4.3. Comparably to Figure 5-18, Figure 5-32 and Figure 5-33 present the average results of the cross-section for all IS-specimen with respectively *mat1* and *mat2* material characteristics.

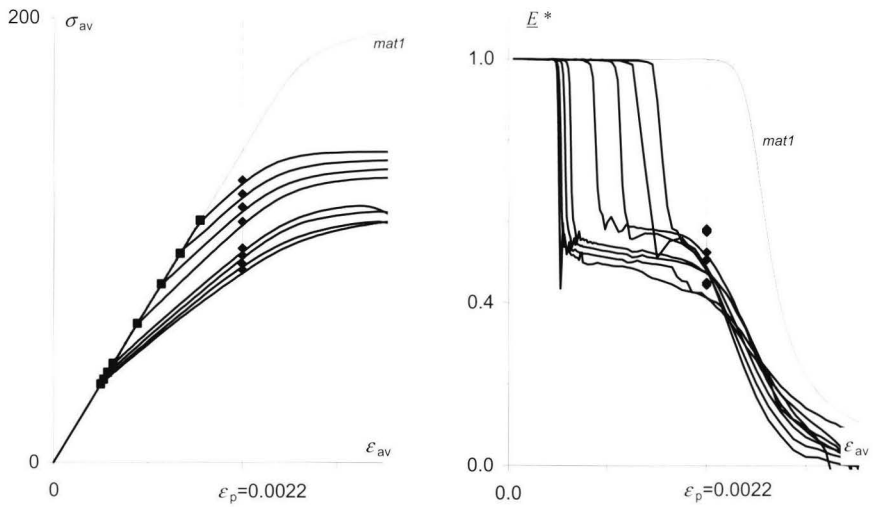


Figure 5-32 Comparison of the inelastic (mat1) local buckling behaviour of all IS-specimen with $\sigma_{cr,T}$ (blocks) and the elastic model at ϵ_p (diamonds)

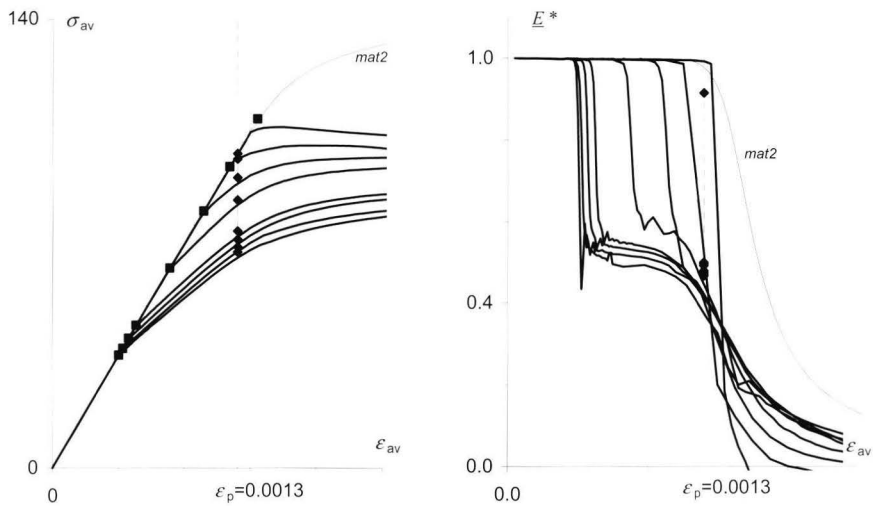


Figure 5-33 Comparison of the inelastic (mat2) local buckling behaviour of all IS-specimen with $\sigma_{cr,T}$ (blocks) and the elastic model at ϵ_p (diamonds)

It is clear from the diagrams that the comments made with respect to the inelastic buckling behaviour of RHS-specimens of the previous section are valid as well for IS-specimen. Thus, it is concluded that the approaches specified for inelastic plate buckling (see section 5.3.4) and elastic buckling of cross-sections (see section 5.4.5) can be combined to result the approach outlined in the following section.

5.5.3 Inelastic local buckling of actual cross-sections

The previous sections present the theoretical buckling behaviour of simple cross-sections. Specifically, the behaviour of SHS, RHS and IS-specimen is investigated. These sections have in common that they are doubly symmetrical and consist of only two sets of identical plates (webs and flanges). This section investigates the actual local buckling behaviour of less perfect specimen, explained for test specimens US02 and CS04-1 of the Eindhoven test program.

The first cross-section studied is that of the TUE-US02 specimen which includes actual imperfections, load eccentricities and thickness deviations. Figure 5-34 presents the FE-results for each plate, relating the average axial stress σ_{av} to the average axial strain ϵ_{av} . In addition, the figure presents the behaviour of the cross-section (sec) and the applied material characteristic (mat). For comparison, the results of the prediction model are presented as well. The tangential critical stress (block) indicates initial buckling. The predicted stresses at the proportional limit (diamonds) indicate failure.

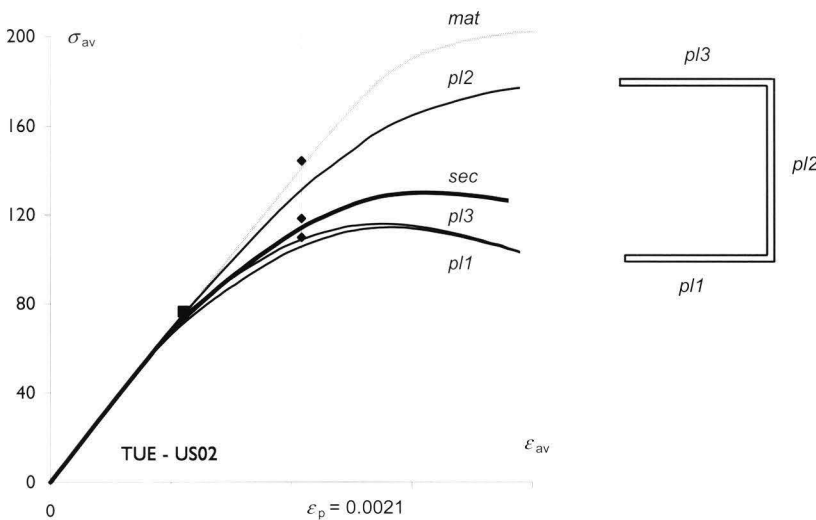


Figure 5-34 Comparison of the actual local buckling behaviour of a simple non-perfect specimen (TUE-US02) with the model at ϵ_{cr} and ϵ_p

The critical stress of the cross-section coincides with initial buckling, though slightly less accurate than it does for the “perfect” specimens of section 5.5. The 4% thickness deviation between both flanges ($pl1$ and $pl3$) results in slight deviations. Finally, the predicted stresses are accurate, and provide lower bounds for the failure load.

Figure 5-35 presents the results of the far more complex TUE-CS04-I specimen. Initial buckling is caused by plate 9, whereas secondary buckling should occur due to plate 11. Again, the block indicates the predicted moment of initial buckling, whereas diamonds present the predicted values at the limiting strain for the section, plate 9 and plate 11.

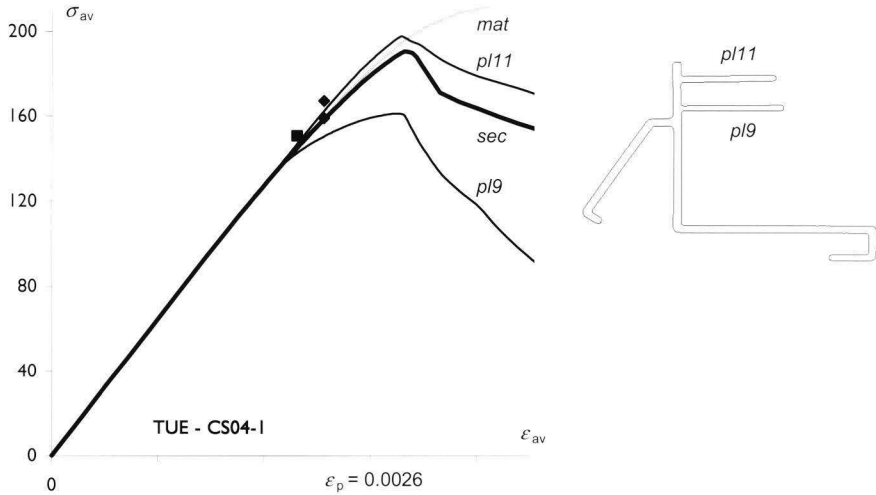


Figure 5-35 Investigation of the actual local buckling behaviour of a complex non-perfect specimen (TUE-US02)

Evaluation results in three points of interest that distinct complex from simple cross-sections. First, the post-buckling strength of plate 9 is limited. Apparently, the load is transferred to the remaining section, which is possible as the influence of plate 9 on the total cross-section is limited. Secondly, failure occurs at $\epsilon_{av} = 0.0034$ due to secondary buckling of plate 11. However, the predicted inelastic critical stress is less. Obviously, the remaining cross-section provides additional support. Finally, the elastic critical stress of the cross-section without plate 9, results an elastic critical stress larger than that estimated for the secondary buckling mode due to plate 11. Such an approach would put the “block” right at the failure stress. Calculation of the failure load (predicted stress multiplied by cross-sectional area) results accurate results as well. Apparently, one should consider that in some cases it could be more economical to neglect parts of the cross-section, than it is to apply a low value of the critical stress.

It is concluded that the local buckling behaviour of actual cross-sections, thus including various kinds of imperfections, is accurately described by the prediction model. Furthermore, the prediction model is applicable to both simple and complex cross-sections.

Summarising procedure for inelastic local buckling of cross-sections

This model predicts the axial resistance of the cross-section N_{pm} for a given value of axial strain ε .

1. Execute an **Eigenvalue analysis**

Either using analytical solutions or, more appropriate for arbitrary cross-sections, using finite-element or finite-strip programs. The analysis must result the critical length L_{cr} and critical stress σ_{cr} of the cross-section.

2. **Schematise the cross-section** to nodes and plates

Each individual plate i has a width (b_i) and thickness (t_i). Plates are connected at the nodes. Nodes are positioned at the intersection of the heart-lines of the individual plates.

3. Determine the **elastic critical stress of each plate** ($\sigma_{cr,i}$)

Determine
$$D = \frac{\pi^2 E}{12(1-\nu^2)}$$

Plate slenderness:
$$\varphi_i = \frac{L_{cr}}{b_i}$$

For internals
$$k_{cr,i} = \frac{1}{\varphi_i^2} + \varphi_i^2 + 2 \quad \text{but: } k_{cr,i} \leq 7$$

For outstands:
$$k_{cr,i} = 0.456 + \frac{1}{\varphi_i^2}$$

Critical stress
$$\sigma_{cr,i} = k_{cr,i} D \left(\frac{t}{b} \right)^2$$

4. Determine **plate groups**

▪ **Plate group 1 (pg1) - Supported plates**

The first plate group consists of all plates that, were they not supported by other plates, would buckle before the critical buckling stress of the cross-section is reached ($\sigma_{cr,i} \leq \sigma_{cr}$). Note: it is always allowed to add additional plates to this group.

▪ **Plate group 2 (pg2) - Supporting plate**

The second plate group consists of all plates that are not within plate group 1. The secondary buckling stress is equal to the lowest critical stress of any plate j within plate group 2:

$$\sigma_{cr,2} = \min(\sigma_{cr,j})$$

▪ Determine the cross-sectional areas

For each plate i of plate group 1, respectively plate j of plate group 2, the cross-sectional area is determined from its plate width and thickness. Subsequently, this results the following representations of the cross-sectional areas:

$$\text{Plate group 1} \quad A_{pg1} = \sum_i b_i t_i$$

$$\text{Plate group 2} \quad A_{pg2} = \sum_j b_j t_j$$

$$\text{Cross-section} \quad A = A_{pg1} + A_{pg2}$$

ELASTIC BUCKLING with post-buckling strength

The cross-section will show post-buckling resistance if the elastic critical stress is less than the proportional limit ($\sigma_{cr} < f_p$). Its resistance is determined from:

5. Plate group 1 ($\sigma_{pm;pg1}$)

The axial stress ($\sigma_{pm;pg1}$) is predicted for the axial strain less than the proportional limit ($\varepsilon < \varepsilon_p$) and results a line (see Figure 5-29) from the origin, to the point of initial buckling (block), to the predicted failure load (diamond) at ε_p .

$$\sigma_{pm;pg1}(\varepsilon) = E \varepsilon \quad \text{for } \varepsilon \leq \varepsilon_{cr}$$

If plate group 1 consists of at least one internal plate:

$$\sigma_{pm;pg1}(\varepsilon) = 0.67E \varepsilon_{cr} + 0.35E \varepsilon - 0.015E \frac{\varepsilon^2}{\varepsilon_{cr}} \quad \text{for } \varepsilon_{cr} < \varepsilon < \varepsilon_p$$

Else, if plate group 1 consists solely of outstands:

$$\sigma_{pm;pg1}(\varepsilon) = 0.49E \varepsilon_{cr} + 0.52E \varepsilon - 0.01E \frac{\varepsilon^2}{\varepsilon_{cr}} \quad \text{for } \varepsilon_{cr} < \varepsilon < \varepsilon_p$$

6. Plate group 2 ($\sigma_{pm;pg2}$)

The plates of plate group 2 behave elastic up to either the proportional limit is reached, or secondary buckling occurs:

$$\sigma_{pm;pg2}(\varepsilon) = E \varepsilon \quad \text{for } \varepsilon \leq \min(\varepsilon_p; \varepsilon_{cr;2})$$

If secondary buckling occurs in the elastic range an additional post-buckling resistance is available:

$$\sigma_{pm;pg2}(\varepsilon) = 0.49E \varepsilon_{cr;2} + 0.52E \varepsilon - 0.01E \frac{\varepsilon^2}{\varepsilon_{cr;2}} \quad \text{for } \varepsilon_{cr;2} < \varepsilon < \varepsilon_p$$

7. Predict the **axial resistance** (N_{pm}) as a function of ε

$$N_{pm}(\varepsilon) = \sigma_{pm;pg1}(\varepsilon)A_{pg1} + \sigma_{pm;pg2}(\varepsilon)A_{pg2}$$

INELASTIC BUCKLING

Buckling in the inelastic range ($f_p \leq \sigma_{cr}$), results in sudden failure. Thus, the predicted strength follows the material characteristic until the inelastic critical strength ($\sigma_{cr,T}$) is reached and failure occurs.

For arbitrary materials, $\sigma_{cr,T}$ can be determined by using buckling curves presented in design codes, or the equations for χ_T as specified in section 5.3.2:

$$\sigma_{cr,T} = \chi_T(\sigma_{cr}) f_{0.2}$$

The relation between axial stress and axial strain is given by:

$$\varepsilon = \frac{\sigma_{pm}}{E} + 0.002 \left(\frac{\sigma_{pm}}{f_{0.2}} \right)^n \quad \text{for } \sigma \leq \sigma_{cr,T}$$

FAILURE LOAD

For practical purposes, it is of key interest to predict the failure or ultimate load. For elastic buckling the failure load can be determined by:

$$N_{u;pm} = \sigma_{pm;pg1}(\varepsilon_p) A_{pg1} + \sigma_{pm;pg2}(\varepsilon_p) A_{pg2} \quad \text{if } \sigma_{cr} < f_p$$

For inelastic buckling results:

$$N_{u;pm} = \chi_T(\sigma_{cr}) f_{0.2} A \quad \text{if } f_p \leq \sigma_{cr}$$

Note: the equations for elastic buckling can be simplified by considering a limited slenderness range. For example by assuming that $\sigma_{cr} > f_p / 4$, which is true for all presented experiments, the equation for the elastic resistance ($\sigma_{cr} < f_p$) reduces to:

$$N_{u;pm} = (0.67 \sigma_{cr} + 0.32 f_p) A_{pg1} + (0.49 \sigma_{cr;2} + 0.50 f_p) A_{pg2}$$

If plate group I consists of at least one internal plate (web).

$$N_{u;pm} = (0.49 \sigma_{cr} + 0.50 f_p) A_{pg1} + (0.49 \sigma_{cr;2} + 0.50 f_p) A_{pg2}$$

If plate group I consists of only outstands.

6 Validation of the developed prediction model

Chapter abstract

In the previous chapter a prediction model is developed based on the (theoretical) local buckling behaviour of perfect specimens. Obviously, actual specimens include all kinds of inaccuracies. Therefore, this chapter validates the use of the prediction model based on the experimental results of Chapter 4.

Validation of the developed prediction model

6.1 Determination of representative experiments with respect to local buckling

This chapter presents and compares the results of the developed prediction model of Chapter 5, with the experimental results of the Salerno and Eindhoven experimental programs of Chapter 3. This initial section investigates the appropriateness of these experiments. This results in Table 6-2, which presents the predicted and experimental results of those experiments that are representative for local buckling.

The material characteristics (E , $f_{0,2}$ and n) are important input parameters for the design procedure. The ranges found in the experiments are presented in Table 6-1. The TUE specimens regard aluminium alloys of the 6000-series with a T6 heat treatment with a limited range of material characteristics. The Salerno tests investigated a wider range of materials, including alloys of both the 6000- and 7000-series with, and without, heat-treatments. Finally, the Helsinki tests consisted of only two 6000-series alloys.

Table 6-1 Comparison of the experimentally obtained material characteristics with those applied in the prediction model

	E [kN/mm ²]	$f_{0,2}$ [N/mm ²]	n [-]
TUE	64 - 70	180 - 240	23 - 40
Salerno	60 - 78	111 - 340	11 - 90
Helsinki	64 - 65	178 - 202	18 - 20
<i>Mat1</i>	70	200	30
<i>Mat2</i>	70	140	20

The design procedure of the prediction model is only elaborated for the two materials *mat1* and *mat2*, see Table 6-1. It is decided to use the actual values of E and $f_{0,2}$ in the design procedure, but to determine the inelastic coefficient χ_T based on *mat1* if the actual value of n is larger than 28, or on *mat2* if n is less than 28. As no material characteristics are available for some of the TUE compression tests, these values have been filled in using those of comparable specimen. Note that the values of n have been determined according to section 2.2.2 from $f_{0,1}$, or if $f_{0,1}$ is not available by $n = f_{0,2}/10$.

The prediction model regards elastic and inelastic local buckling of cross-sections. As failure through plastic squashing is not regarded, specimens that fail at loads ($N_{u,exp}$) above the squash load ($N_{0,2} = f_{0,2} \cdot A$) are not considered. Figure 6-1 shows that this concerns a substantial part of the available test data.

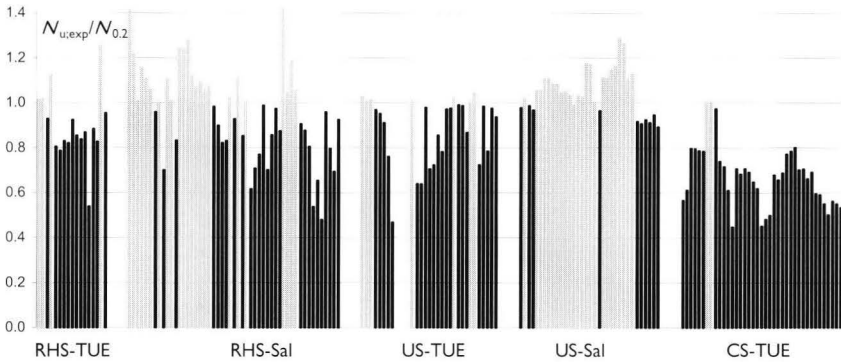


Figure 6-1 Comparison of the experimental load at failure ($N_{u,exp}$) with the squash load ($N_{0.2} = f_{0.2} \cdot A$)

The advantage of the current approach is that the (numerical) Eigenvalue analysis results in both the elastic critical stress and its according mode: flexural (F), torsional (T), flexural-torsional (FT), local (L), or distortional (D) buckling. Chapter 4 showed that this Eigenmode is representative for initial buckling observed in the experiments. Eigenvalue analyses have been executed for all experiments, including those of Salerno and Helsinki. Those specimens are selected of which the Eigenmode (initial buckling) coincides with local buckling.

If any post-buckling resistance is available, secondary buckling may occur. The design procedure provides an approach to determine the secondary critical stress due to local buckling. However, the occurrence of overall and distortional buckling is not accounted for. The FE-analyses executed for the TUE-experiments allow the determination of the deformation patterns at failure. Only those specimens are regarded of which the failure pattern can be associated with local buckling. Such an approach is not possible for the Salerno and Helsinki tests, as no FE-analyses were executed. However, the respective authors of the Salerno tests state these specimens failed through local buckling. Therefore, no additional Salerno tests are excluded.

Table 6-2 presents the experimental (exp) and predicted (pm) results of the remaining, representative, test specimens. Notably, the results of the Helsinki program are not presented as they fail either through inelastic buckling or else through mode interaction. However, a detailed summary of input and results is presented in appendix B.5 and Mennink (2002b) for all specimens. Table 6-2 includes the predicted and experimental failure loads ($N_{u,pm}$ and $N_{u,exp}$), and their non-dimensionalised equivalents ($\rho_{u,pm}$ and $\rho_{u,exp}$), with respect to the squash load using the actual (measured) values of $f_{0.2}$ and A .

$$\rho_u = \frac{N_u}{f_{0.2} A} \tag{eq. 6-1}$$

Table 6-2 Summary of experimental and predicted failure loads for the representative test specimen with respect to local buckling

Test	$N_{u,exp}$ kN	$N_{u,pm}$ kN	ρ_{exp} -	ρ_{pm} -	$N_{u,pm} / N_{u,exp}$	Test	$N_{u,exp}$ kN	$N_{u,pm}$ kN	ρ_{exp} -	ρ_{pm} -	$N_{u,pm} / N_{u,exp}$
RHS-TUE											
RHS04	125.1	128.7	0.93	0.95	1.03	US08	38.8	33.6	0.72	0.62	0.86
RHS06	83.8	87.4	0.80	0.84	1.04	US10	43.1	42.1	0.85	0.83	0.98
RHS07	82.2	87.9	0.78	0.84	1.07	US14	110.6	100.3	0.97	0.88	0.91
RHS08	86.5	86.9	0.83	0.83	1.00	US18	99.2	91.2	0.99	0.91	0.92
RHS09	84.2	82.8	0.82	0.81	0.98	US20	98.5	90.8	0.99	0.91	0.92
RHS10	173.3	162.2	0.92	0.86	0.94	US22	92.4	86.5	1.00	0.93	0.94
RHS11	159.8	161.4	0.85	0.86	1.01	US26	74.1	66.9	0.72	0.65	0.90
RHS12	167.2	169.1	0.84	0.85	1.01	US29	67.7	61.1	0.98	0.89	0.90
RHS14	117.6	111.7	0.54	0.51	0.95	US30	71.5	67.2	0.78	0.74	0.94
RHS15*	85.2	81.7	0.88	0.85	0.96	US33	73.6	65.5	0.97	0.87	0.89
RHS16*	80.9	83.2	0.83	0.85	1.03	US34	77.3	71.1	0.93	0.86	0.92
RHS19	223.9	215.4	0.95	0.92	0.96	US-Sal					
RHS-Sal						C1A	106.7	101.4	0.98	0.93	0.95
SHS7	302.5	286.6	0.96	0.91	0.95	C2A	103.9	98.1	0.98	0.93	0.94
SHS8	83.0	73.6	1.00	0.88	0.89	C2B	107.1	103.5	0.97	0.93	0.97
SHS9	84.7	95.2	0.70	0.79	1.12	C7B	89.5	85.6	0.99	0.94	0.96
SHS12	635.0	626.4	0.83	0.82	0.99	C10A	43.2	38.4	1.00	0.89	0.89
RHS10	263.4	254.3	0.90	0.87	0.97	C10B	41.7	38.4	0.96	0.89	0.92
RHS11	276.0	275.8	0.82	0.82	1.00	C15A	50.3	44.7	0.92	0.81	0.89
RHS12	314.4	303.5	0.83	0.80	0.97	C15B	49.4	44.4	0.91	0.81	0.90
RHS14	82.4	79.2	0.93	0.89	0.96	C16A	333.4	320.6	0.92	0.89	0.96
RHS18	91.1	105.3	0.62	0.71	1.16	C16B	333.0	323.0	0.91	0.88	0.97
RHS19	138.7	157.6	0.71	0.80	1.14	C17A	338.0	321.1	0.95	0.90	0.95
RHS20	510.0	512.4	0.77	0.77	1.00	C17B	319.8	322.6	0.89	0.90	1.01
RHS21	115.9	111.7	0.99	0.95	0.96	US-TUE					
RHS25	669.8	692.2	0.87	0.90	1.03	CS02-1	65.6	65.2	0.80	0.79	0.99
SHS04C	408.2	390.8	0.90	0.87	0.96	CS02-2	65.4	65.2	0.79	0.79	1.00
SHS05C	190.4	176.1	0.88	0.81	0.92	CS02-3	64.8	65.1	0.79	0.79	1.01
SHS06C	147.3	152.1	0.80	0.83	1.03	CS02-4	64.5	65.1	0.78	0.79	1.01
SHS07C	102.8	98.2	0.54	0.51	0.96	CS04-1	36.1	29.5	0.74	0.60	0.82
SHS08C	67.6	79.6	0.65	0.77	1.18	CS04-2	34.9	33.9	0.71	0.69	0.97
SHS09C	38.2	41.2	0.48	0.52	1.08	CS06-1	43.2	42.6	0.69	0.68	0.98
SHS10C	81.9	75.6	0.96	0.88	0.92	CS06-2	40.5	42.6	0.65	0.68	1.05
SHS11C	70.4	72.9	0.79	0.82	1.04	CS06-3	38.7	42.6	0.62	0.68	1.10
RHS01C	146.8	132.6	0.69	0.63	0.90	CS08-1	94.7	96.7	0.68	0.69	1.02
RHS02C	236.3	216.8	0.92	0.85	0.92	CS08-2	93.4	97.6	0.65	0.68	1.05
US-TUE						CS08-3	96.0	96.3	0.69	0.69	1.00
US02	40.6	36.4	0.64	0.57	0.90	CS10-1	58.9	52.5	0.70	0.62	0.89
US04	40.8	37.0	0.64	0.58	0.91	CS10-2	59.3	52.5	0.70	0.62	0.89
US05	38.4	34.4	0.98	0.88	0.90	CS10-3	55.6	52.3	0.66	0.62	0.94
US06	39.0	35.2	0.70	0.63	0.90	CS10-4	58.0	52.3	0.69	0.62	0.90

6.2 Comparison of the prediction model with test results

Comparison of the presented ultimate loads of the experiments ($N_{u,exp}$) with those predicted ($N_{u,pm}$) results in the diagram below. At first sight, the diagram shows an excellent agreement between experiment and model, quantified by a correlation coefficient of 0.995. However, further investigation is necessary.

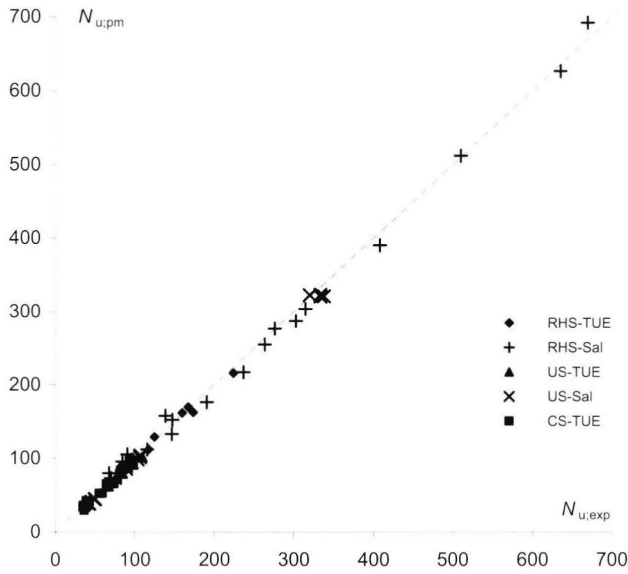


Figure 6-2 Comparison of the experimental ($N_{u,exp}$) and predicted ($N_{u,exp}$) failure loads in kN of specimen failing through local buckling

Though the results of the prediction model are presented as a force, it predicts stresses. In case of elastic buckling it predicts the stress at the proportional limit ε_p ; in case of inelastic buckling it predicts the inelastic critical stress $\sigma_{cr,T}$. The cross-sectional area A is thus merely a magnification factor. Furthermore, the determination of $\sigma_{cr,T}$ is based on the relative load level, compare χ_T used in buckling curves. As a result it is more appropriate to present the results of the prediction model and those measured in the experiments in their non-dimensionalised values $\rho_{u,pm}$ and $\rho_{u,exp}$, as explained in the previous section. These are presented in Figure 6-3, which results in a diagram radically different from that of Figure 6-2.

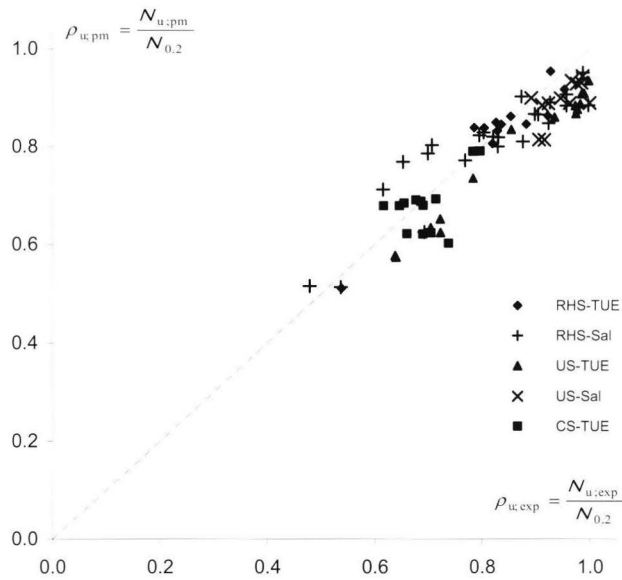


Figure 6-3 Comparison of the experimental and predicted non-dimensional stresses of specimen failing through local buckling

Though the results are essentially the same, this diagram seems to have a far larger scatter, which is emphasized by a correlation coefficient of 0.92. However, the same relative scatter exists, which is found in Figure 6-2 by taking a closer look at the specimens failing at limited loads (50-150 kN). The scatter is investigated in Table 6-3 and Figure 6-4. Table 6-3 presents the correlation coefficient with respect to the ultimate loads (Figure 6-2) and that of the non-dimensionalised stress (Figure 6-3), as well as the average μ and standard deviation σ of the relative load ($N_{u,pm}/N_{u,exp}$).

Table 6-3 Correlation between experimental and predicted failure loads; scatter (μ and σ) of the relative load ($N_{u,pm}/N_{u,exp}$) for n tests

	corr. (F_u)	corr. (ρ)	μ	σ	n
RHS - TUE	1.00	0.95	1.00	0.04	12
RHS - Sal	1.00	0.91	1.00	0.08	23
US - TUE	1.00	0.99	0.91	0.03	15
US - Sal	1.00	0.63	0.94	0.04	12
CS - TUE	0.99	0.67	0.98	0.07	16
All	1.00	0.91	0.97	0.07	78

The diagrams of Figure 6-4 relate the relative load ($N_{u,pm}/N_{u,exp}$) to either the failure load ($N_{u,exp}$) or the non-dimensional stress ($\rho_{u,exp}$) of the experiments. The diagrams show the same scatter range, though at a different position. This is of importance while the development of design rules is often based on the assumption of a scatter with constant bandwidth, for example the worked-out approach in Annex D of Eurocode I (CEN 1991). The distinct non-uniform scatter observed in the topmost diagram should be accounted for.

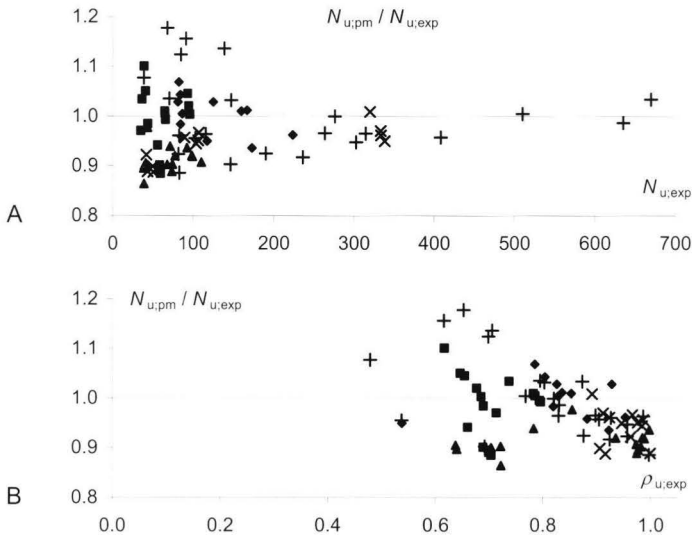


Figure 6-4 Investigation of the scatter between experimental and predicted strength of specimen failing through local buckling

The following remarks can be made with respect to both Table 6-3 and Figure 6-4:

- Though the correlation coefficient is a commonly used tool, it has its limitations. For example, the coefficients found for the US-specimen executed in Salerno are respectively 1.00 and 0.65. Based on a value of 1.00, one would draw the conclusions that the model provided an excellent prediction, whereas a value of 0.65 raises significant doubts. The difference in coefficients is caused by the distribution of the results; representation of the loads results in a line, whereas representation of the load level results a cloud at $\rho_u = 0.9$.

- The prediction model is outlined such as to result lower bound solutions for the failure load. However, five of the RHS-Sal specimens (SHS9, RHS18, RHS19, SHS08C and SHS09C) overpredict the strength by 8 to 18 percent. As they all fail in the inelastic range, this can be explained by either one or the combination of: inaccurate modelling of the actual material characteristic, inaccurate execution of the test, or mode interaction.
- The cross-sections of the CS-TUE specimens are both complex and thin-walled ($t = 1.0$ mm). Thus, their geometrical properties are less accurately determined than those of the RHS- and US-specimen, which results in a larger scatter of the test results.
- Though not included in the presentation while $N_{u,exp} \sim N_{0.2}$, the predicted local buckling strength of the CS03 test specimens is highly inaccurate ($N_{u,exp} = 0.7 N_{0.2}$). However, these cross-sections (Figure 3-4) consist of a very compact tube and one slender outstand. As the set-up of the prediction model is based on the most slender plate this severely underestimates the actual strength. A workaround for such cross-sections is to neglect the outstand entirely which, in this case this, would lead to a failure load of 80% of that of the experiment.

The average μ and standard deviation σ of all tests have been summarised ($\mu = 0.97$; $\sigma = 0.067$). Assuming a normal distribution of the scatter, 95% of all specimens are positioned within a $\pm 2 \cdot \sigma$ range from the average. Based on these results it is concluded that the newly prediction model provides an accurate description of the actual local buckling behaviour.

6.3 Development of design rules

The current research results in a prediction model that accurately described the actual local buckling behaviour of cross-sections. With the experimental work of Chapter 3, and the validated FE-model of Chapter 4, all tools are available for the development of design rules.

The experiments executed within the current research, as well as those obtained from literature, provide a substantial database for test specimens failing through local buckling in the elastic and inelastic range. Any gaps still existing (with respect to for example imperfections, materials and geometry) can be filled in with the use of the FE-model validated in Chapter 5. Note that some conclusions have to be drawn with respect to the accuracy of the FE-model.

With the available test data, the possibility for additional numerical simulations, and the accurate prediction model, the essential parts are available for the determination of a design rules. For example using the approach specified in Annex D of Eurocode I (CEN 1991). The additional input required are the probabilistic data with respect to initial imperfections, material characteristics, load eccentricities, and the deviations between actual and nominal geometrical properties. With these data, design rules can be calibrated.

Finally, validation of the current design rules for local buckling, as used in the Eurocode 9 (CEN 1999), is based on the Salerno tests. As these cover mainly the inelastic range, the validity of these rules is limited. Furthermore, these rules do not include distortional buckling. The presented prediction model does not exhibit these drawbacks. Application of the presented prediction model into the codes would therefore substantially increase the safety of the design, as well as provide more economical products.

7 Conclusions and recommendations

7.1 Conclusions

A thorough investigation of the actual stability behaviour of aluminium extrusions is presented. The work contains a substantial amount of test data, validates the use of finite element analyses, provides insight into the actual behaviour, and results in a generally applicable prediction model.

Applicability of existing design rules for aluminium extrusions

In contrast to the complexity of extrusions applied in practice, most design rules are based on the behaviour of simple symmetrical cross-sections. The behaviour of complex cross-sections is unknown. Cross-sectional stability is generally described by plate buckling of individual plates, neglecting rotational support by assuming hinged plate connections. However, as rotational stiffness does occur and plate connections may translate, the actual local or distortional buckling behaviour may be radically different from the predicted one. As a result, it is unknown whether the outcome of current design rules leads to accurate, overly conservative, or even unsafe results.

Execution of experiments

The most appropriate test set-up to investigate the cross-sectional stability of aluminium extrusions with slender cross-sections is to execute compression tests with fixed support plates. This set-up results in an accurate loading, limits the influence of overall buckling, and takes account of the shift in neutral axis of the effective cross-section. Compact cross-sections will fail at the supports due to edge disturbances caused by friction between specimen and support plates. This friction can be reduced through application of double layers of Teflon. However, as these also allow slip, they are not advisable for specimens that may exhibit an interaction with overall buckling.

Tensile tests, executed for stability research purposes, should focus on the determination of the modulus of elasticity E and the stress-strain relation in the inelastic range. It is therefore essential to accurately measure strains, preferably by means of strain gauges. To determine E , at least one unloading/reloading sequence should be used to eliminate the influence of plastic strains.

Numerical work

The numerical (finite element) and experimental results show excellent agreement. The deformation pattern according to the first numerical Eigenmode coincides with the initial buckling patterns observed in the experiments; the deformation patterns at failure coincide as well. Furthermore, both the critical and ultimate loads of the FE-analyses provide an accurate prediction of those observed in the experiments. Parameter analyses show that the influence of initial plate deflections is negligible compared to overall imperfections, thickness deviations, load eccentricities, and inaccuracies in the measured and modelled material characteristics.

Determination of the actual behaviour

With respect to plate and local buckling, a distinction can be made between elastic and inelastic buckling. Critical stresses less than the proportional limit of the material (f_p) will result in (considerable) post-buckling resistance, whereas buckling in the inelastic range will yield none.

It is shown that the (simplified) differential plate equations provide inaccurate results with respect to post-buckling strength and stiffness. Furthermore, plates are susceptible to mode jumping. An explanation for its occurrence is given.

Initial buckling of cross-sections occurs due to local buckling of the most slender (supported) plates. The remaining (supporting) plates of the cross-section supply support that depends on both the critical length of the cross-section, as well as the rotational stiffness at the plate connections. Subsequent load increase will lead to secondary buckling of the supporting plates. Contrarily to common belief, the according critical stress is highly dependent on the shape of the cross-section, buckled or not. Note that an additional mode, not found in literature, may occur. The occurrence of this mode is explained, its influence predicted.

Nevertheless, it is shown that if the initial and secondary buckling stresses are determined accurately, the post-buckling strength of both the supported and supporting plates can be described by an approach comparable to that of plate buckling.

Though local buckling may be initiated in the elastic range, post-buckling resistance will extend the behaviour into the inelastic range. However, the exponential stiffness reduction of the material in the inelastic range enhances all kinds of secondary buckling modes, due to overall, distortional or local buckling. As a result, failure is in most cases caused by an interaction of buckling modes that limits the post-buckling resistance to the elastic range.

Development and validation of a general prediction model

The obtained insights are used for the development of a general prediction model for local buckling of aluminium extrusions with arbitrary cross-sectional shapes, of which the procedure is presented in section 5.5. This model is based on the actual buckling behaviour. It combines an accurate description of both elastic and inelastic buckling and the elastic post-buckling strength, but provides a safe approach with respect the inelastic post-buckling resistance.

Key aspect of the model is the application and determination of the actual critical stresses due to initial buckling (numerically determined) and secondary buckling (analytically determined). For comparison: existing approaches will always underestimate initial buckling as they are based on the critical stresses of individual plates. Furthermore, the Eigenvalue analysis shows the buckling type. If distortional or flexural buckling is found instead of local buckling this should caution the designer. This provides a safety net for the new model that is not available for analytically based solutions.

In case of inelastic buckling, the specimen fails at the inelastic critical stress. An approach is presented to determine this load based on the elastic critical stress. Though the concept is comparable with existing buckling curves, it should only be used when verified with respect to initial buckling of cross-sections instead of plates.

The occurrence of post-buckling resistance is limited to the elastic range. Though this underestimates the failure strength, it is not extended as inelasticity may cause the sudden and unpredictable occurrence of secondary buckling modes that could lead to unsafe results.

The applicability of the newly developed prediction model is validated with respect to experimental results. The results show an accurate description of the deformation patterns at both initial and secondary buckling (due to local buckling). The failure load is predicted with an average of 97% as well as a standard deviation of 4.8%. Therefore, it is concluded that the newly developed prediction model provides accurate results.

7.2 Recommendations for further research

The current thesis showed that even for complex cross-sections it is still possible to determine relatively simple and practical design tools, based on numerical input. Future research will undoubtedly investigate even more complex combinations of shapes and (interactions between) buckling phenomena. It is therefore essential to develop a solid basis for *generally applicable* prediction models, instead of focussing on specific geometries as is common (and more appropriate) in steel-related research. The presented model is a first step in the development of such a general approach.

Research on stability

Cross-sections used in aluminium are in general non-symmetrical. Thus, even the determination of the overall buckling load is cumbersome. Therefore, it seems appropriate to determine design rules based on a *numerically* determined critical load instead of on simplified design rules. Such an approach could cover any type of loading and support conditions, notably interactions between axial forces and bending forces, and provide more accurate and economical results. Research on overall buckling should therefore be focused on the development and validation of a fixed procedure based on numerical input and generally applicable design curves.

The prediction model developed in this thesis provides an accurate description of the local buckling behaviour of uniformly compressed cross-sections. The model predicts stresses for a certain level of strain. Thus, there are no major limitations to extend the model to other types of loading, as long as account is taken for the change in cross-sectional properties due to effective area and the resulting overall load distribution.

Distortional buckling can be simplified to a combination of local and overall buckling. It is therefore always conservative to assume that no post-buckling strength exists and apply column-buckling curves. However, whenever it is possible to describe the post-buckling stiffness and strength, there are no restrictions to extend the developed prediction model to distortional buckling. Note that the distortional modes associated with initial and secondary buckling have to refer to different parts of the cross-section.

Experimental versus numerical research

Despite the effort taken, the executed experiments are not perfect. The scatter in test results seems as wide (or small) as the deviation between numerical and experimental results. Thus, the question arises whether experiments are trustworthier than (these specific) FE-analyses. Therefore, it is advised to develop an approach that allows the validation of future prediction models and design rules to be based on FE-results, supported by a limited number of experiments.

Extension of the prediction model

There seem to be no major limitations to extend the current prediction model to include additional aspects like buckling interaction, as well as distortional and overall buckling. Though substantial research will be necessary, approaches comparable to the developed prediction model may provide far more accurate results than any extension of existing models will.

Literature

- AA (1994), *Specifications for aluminium structures*, Aluminium Association, Washington D.C., USA
- Allen H.G.; Bulson, P.S. (1980), *Background to Buckling*, McGraw-Hill Book Company, UK
- AISI (1996), *Specification for the Design of Cold-Formed Stainless Steel Structural Members*, American Iron and Steel Institute, Washington D.C., USA
- ASCE (1991), *Specification for the Design of Cold-Formed Stainless Steel Structural Members*, Standard No. ASCE-8-90, American Society of Civil Engineers, New York, USA
- Baehre, R. (1966), *Trycktastravorav elastoplastiskt material-nagrafragefallningar (Comparison between structural behaviour of elastoplastic materials)*, Report No. 16, Tekn. Dr. Arne Johnson Ingenjorsbyra
- Batteman, R.H.; Johnston, B.G. (1967), *Behavior and maximum strength of metal columns*, In: ASCE Journal of the Structural Division, Vol. 93, No. ST2, pp. 205-230
- Beer, H.; Schultz, G. (1970), *Theoretical basis for the European column curves*, In: Construction Metallique, No. 3
- Benthem, J.P. (1959), *The reduction in stiffness of combinations of rectangular plates in compression after exceeding the buckling load*, Technical report NLL-TR S-539, The Netherlands
- Bernard, A.; Frey, F.; Janss, J.; Chassonet, CH. (1973), *Recherches sur le comportement au flambement de barres en aluminium (Research on the buckling behaviour of aluminium columns, In French)*, IABSE Mem., Vol. 33-I, pp. 1-33
- Bernard, E.S.; Coleman, R.; Bridge, R.Q. (1999), *Measurements and assessment of geometricimperfections in thin-walled panels*, In: Thin-Walled Structures 40, pp. 239-262
- Bijlaard, P.P.; Fisher, G.P. (1952), *Column strenght of H sections and square tubes, in post-buckling range of component plates*, Technical note No. 2994, NACA, USSA
- Bjorhovde, R.; Birkemoe, P.O. (1979), *Limit stat design of H.S.S. columns*, In: Canadian Journal of Civil Engineering, Vol. 8, No. 2, pp. 276-291
- Bjorhovde, R.; Tall, L. (1971), *Maximum column strength and the multiple column curve concept*, Fritz Engineering Laboratory Report No. 338.29, Lehigh University, Bethlehem, Pa., USA
- Bleich, F.; Ramsey, L.B. (1951), *A Design Manual on the Buckling Strength of Metal Structures*, Society of Naval Architects, Washington D.C., USA

- Bleich, F. (1952), *Buckling strength of metal structures*, McGraw-Hill Book Company, New York, USA
- Bradford, M.A.; Hancock, G.J. (1984), *Elastic interaction of local and lateral buckling in beams*, In: *Thin-Walled Structures* 2(1), pp. 1-25
- Brush, D.O.; Almroth, B.O. (1975), *Buckling of bars, plates and shells*, McGraw-Hill, New York, USA
- Bryan, G.H. (1890), *On the Stability of a Plane Plate under Thrust in its Own Plane*, In: *Proceedings of the London Mathematical Society*, Vol. 22, London, UK
- Bulson, P.S. (1969), *The Stability of Flat Plates*, American Elsevier Publishing Company, New York, USA
- CEN (1991), *Actions on structures*, Eurocode 1, EN 1991, Brussels, Belgium
- CEN (1995), *Aluminium and aluminium alloys - Extruded rod/bar, tube and profiles- Part 9: Profiles, tolerances on dimension and form*, prENV 755-9, Brussels, Belgium
- CEN (1993), *Design of steel structures*, Eurocode 3, Part 1.1, ENV 1993-1-1, Brussels, Belgium
- CEN (1999), *Design of aluminium structures*, Eurocode 9, Part 1.1, ENV 1999-1-1, Brussels, Belgium
- Chapuis, J.; Galambos, T.V. (1982), *Restrained crooked aluminium columns*, In: *Journal of the Structural Division*, Vol. 108, No. ST3, pp. 511-524
- Cheung, Y.K. (1976), *Finite strip method in structural analysis*, Pergamon Press, London, UK
- Cherry, S. (1960), *The stability of beams with buckled compression flanges*, In: *Structural Engineer* 38(9), pp. 277-285
- Coan, J.M. (1951), *Large-Deflection Theory for Plates With Small Initial Curvature Loaded in Edge Compression*, In: *Journal of Applied Mechanics*, Vol. 19(2), No. 143
- CRCJ (1971), *Handbook of Structural Stability*, Column Research Committee of Japan, Corona publishing Co., Tokyo, Japan
- Desmond, T.P.; Peköz, T.; Winter, G. (1981a), *Edge stiffeners for thin-walled members*, In: *Journal of Structural Engineering*, Vol. 107, No. ST2, pp. 329-354
- Desmond, T. P.; Peköz, T.; Winter, G. (1981b), *Intermediate stiffeners for thin-walled members*, In: *Journal of Structural Engineering*, Vol. 107, No. ST4, pp. 627-648
- DeWolfe, J.T.; Peköz, T.; Winter, G. (1974), *Local and overall buckling of cold-formed members*, In: *Journal of the Structural Division*, Vol. 100, No. ST10, pp. 2017-2306

- DIN (1987), *Precise profiles of alloys of the type AlMgSi0, 5.: tolerances*, DIN 17615-3, Deutsches Institut für Normung e.V., Germany
- Dubina, D.; Ungureanu V. (2002), *Effect of imperfections on numerical simulation of instability behaviour of cold-formed steel members*, In: *Thin-Walled Structures* 40(3), pp. 239-262
- Erp, van, G.M. (1989), *Advanced buckling Analyses of Beams with arbitrary Cross Sections*, PhD Thesis, Eindhoven University of Technology, Eindhoven, The Netherlands
- Essa, H.S.; Kennedy, D.L.J. (1993), *Distortional buckling of steel beams*, Structural Engineering report No. 185, Department of Civil Engineering, University of Alberta, Canada
- Faella, C. (1976), *Influenza delle imperfezioni geometriche sul comportamento instabile delle aste compresse in alluminio (Influence of geometrical imperfections on the buckling behaviour of aluminium compression bars)*, La Ricerca, Italy
- Fan, S.C. (1982), *Spline finite strip in structural analysis*, PhD Thesis, University of Hong Kong, Hong Kong
- Fok, W.C.; Walker, A.C. (1977), *Buckling of Locally Imperfect Stiffeners in Plates*, In: *Journal of the Engineering Mechanics Division*, Vol. 103, No. EM5, pp. 895-911
- Föppl, A. (1907), *Technische Mechanik*, 5, Teubner, Leipzig, Germany
- Fukumoto, Y.; Nethercot, D.A.; Galambos, T.V. (1983), *Experimental data for the buckling of steel structures – NDSS Stability of metal structures*, In: *Proceedings of the 3rd International Colloquium SSRC*, pp. 609-630, Toronto, Ontario, Canada
- Fukumoto, Y.; Usami, T.; Yamaguchi, K. (1977), *Inelastic Buckling of Stiffened Plates in Compression*, IABSE Period. 3/1977, IABSE Proc. P-8/77, pp. 1-15
- Galambos, T.V. (Ed.) (1998), *Guide to Stability design criteria for metal structures 5th Ed.*, John Wiley & Sons, New York, USA
- Gerard, G.; Becker, H. (1957), *Handbook of Structural Stability, Part 1 - Buckling of Flat Plates*, Technical note 3781, NACA, USA
- Gonçalves R.; Camotim D. (2001), *On the allowance of member imperfections in the design/safety checking of steel frames*, In: *Proceedings of the 9th Nordic Steel Construction Conference, NSCC'2001* (Eds. Mäkeläinen, P.; Kesti, J.; Jutila, A.; Kaitila, O.), Helsinki, Finland
- Graves Smith, T.R. (1969), *The ultimate strength of columns of arbitrary length*, In: *Symposium on thin-walled structures*, Crosby-Lockwood, London, UK

- Graves Smith, T.R.; Sridharan, S. (1978), *A finite strip method for the buckling of plate structures under arbitrary loading*, In: International Journal of Mechanical Engineering Science, Vol. 20, pp. 685-693
- Hall, D.H. (1981), *Proposed steel column design criteria*, In: Journal of the Structural Division, Vol. 107, No. ST4, pp. 649-670
- Hancock, G.J. (1978), *Local, distortional and lateral buckling of I-beams*, In: Journal of the Structural Division, Vol. 104, No. ST11, pp. 1781-1798
- Hancock, G.J. (1981), *Interaction buckling of I-section columns*, In: Journal of the Structural Division, Vol. 107, ST1, pp. 165-181
- Hancock, G.J.; Kwon, Y.B.; Bernard, E.S. (1994), *Strength Design Curves for Thin-Walled Sections Undergoing Distortional Buckling*, In: Journal of Constructual Steel Research, Vol. 31(2-3), pp. 169-186
- Hariri, R. (1967), *Post-buckling behaviour of Tee-shaped aluminium columns*, PhD Thesis, University of Michigan, Ann Arbor, Michigan, USA
- Hassinen, P. (2000), *Compression strength of aluminium columns – Experimental and numerical studies*, In: Proceedings of the 3rd International Conference on Coupled Instabilities of Metal Structures, CIMS'2000 (Eds. Camotim D.; Dubina, D.; Rondal J.), ICP, London, UK
- Hertzberg, R.W. (1996), *Deformation and fracture mechanics of engineering materials 4th Ed.*, John Wiley and Sons, New York, USA
- Hinton, E. (1992), *Introduction to Nonlinear Finite Element Analysis*, NAFEMS, Glasgow, UK
- Höglund, T. (1980), *Design of trapezoidal sheeting provided with stiffeners in the flanges and webs*, Document D28, Swedish Council for Building Research, Stockholm, Sweden
- Hopperstad, O.S.; Langseth, M.; Moen, L. (1998), *Strength of aluminium extrusions under compression and bending*, In: Thin-Walled Structures - Research and Development, pp. 85-92 (Eds. Shanmugan, N.E. et al), Elsevier, London, UK
- Hopperstad, O.S.; Langseth, M.; Tryland, T. (1999), *Ultimate strength of aluminium alloy outstands in compression - experiments and simplified analysis*, In: Thin-Walled Structures 34, pp. 279-294
- Hu, P.C.; Lundquist, E.E.; Batdorf, S.B. (1946), *Effect of Small Deviations from Flatness on the Effective Width and Buckling of Plates in Compression*, Technical note 1124, NACA, USA
- Johnston, B.G. (1964), *Inelastic buckling gradient*, In: Journal of the Engineering Mechanics Division, Vol. 90, No. EM5, pp. 31-48

- Jones, R.; Wykes, C. (1983), *Holographic and speckle interferometry*, Cambridge University Press, Cambridge, UK
- Kalyanaraman, V. (1979), *Local Buckling of Cold-Formed Steel Members*, In: Journal of the Structural Division, Vol. 105
- Kalyanaraman, V.; Peköz, T.; Winter, G. (1977), *Unstiffened Compression Elements*, In: Journal of the Structural Division, Vol. 103
- Karman, Von, T.; Sechler, E.E.; Donnell, L.H. (1932), *The Strength of Thin Plates in Compression*, Transactions ASME, Vol. 54, APM 54
- Kesti, J.; Davies, J.M. (1999), *Local and distortional buckling of thin-walled short columns* In: Thin-Walled Structures 34, pp. 115-134
- Kirby, P.A.; Nethercot, D.A. (1979), *Design for Structural Stability*, Granada Publishing, UK
- Kirchhoff, G. (1877), *Mechanik*, Teubner, Leipzig, Germany
- Kitipornchai, S.; Chan, S.L. (1990), *Stability and Non-linear Finite Element Analysis of Thin-Walled Structures*, In: Finite element method applications to thin-walled structures (Ed. Bull, J.), Elsevier, London, UK
- Klöppel, E.H.K.; Scheer, J.; Möller, K.H. (1960), *Beulwerte Ausgesteifter Rechteckplatten.; Kurventafeln zum direkten Nachweis der Beulsicherheit für verschiedene Steifenanordnungen und Belastungen*, Verlag von Wilhelm, Ernst & Sohn, Berlin, Germany
- König, J. (1978), *Transversely loaded thin-Walled C-shaped panels with intermediate stiffeners*, Document D7, Swedish Council for Building Research, Stockholm, Sweden
- König, J.; Thomasson, P.O. (1979), *Thin-Walled C-shaped Panels subject to Axial Compression or to Pure Bending*, In: Thin-Walled Structures (Eds. Rhodes, J.; Walker, A.C.), Granada Publishing
- Koiter, W.T. (1945), *Over de stabiliteit van het elastisch evenwicht* (in Dutch), PhD Thesis, Delft University of Technology, 1945, The Netherlands; English translations issued as: NASA TT F10, 833 (1967), and: AFFDL TR 70-25 (1970)
- Koiter, W.T. (1976), *General theory of mode interaction in stiffened plate and shell structures*, Report WTHD-91, Delft University of Technology, The Netherlands
- Kroll, W.D.; Fisher, G.P.; Heimerl, G.J. (1943), *Charts for the calculation of the critical stress for local instability of columns with I, Z, channel and rectangular tube sections.*, Wartime report L-429, NACA, USA
- Lai, Y.F.W.; Nethercot, D.A. (1992), *Strength of aluminium members containing local transverse welds*, In: Engineering Structures, Vol. 14, No. 4

- Landolfo, R.; Piluso, V.; Langseth, M.; Hopperstad, O.S. (1999), *EC9 provisions for flat internal elements*, comparison with experimental results, In: *Lightweight Steel and Aluminium Structures* (Eds. Mäkeläinen, P.; Hassinen, P.), Espoo, Finland
- Langseth, M.; Hopperstad, O.S. (1997), *Local Buckling of Square Thin-Walled Aluminium Extrusions*, In: *Thin-Walled Structures* 27(1), pp. 117-126
- Lau, S.C.W. (1988), *Distortional Buckling of Thin-Walled Columns*, PhD Thesis, University of Sydney, Australia
- Lau, S.C.W.; Hancock, G.J. (1986), *Buckling of Thin Flat-Walled Structures by a Spline Finite Strip Method*, In: *Thin-Walled Structures* 4, pp. 269-294
- Lindner, J.; Gietzelt, R. (1984), *Imperfektionsannahmen für Stützenschiefstellungen*, In *Stahlbau*, Vol. 52, No. 4, pp. 97-101
- Mazzolani, F.M. (1972), *La caratterizzazione della legge σ - ε e l'instabilità dellacolonne di alluminio (Characterisation of the σ - ε law and buckling of aluminium columns)*, *Constr. Metall.*, No. 3, Italy
- Mazzolani, F.M. (1974), *Proposal to classify the aluminium alloy on the basis of the mechanical behaviour*, ECCS Committee 16, Doc. 16-74-2.
- Mazzolani, F.M. (1985), *Aluminium alloy structures 2nd Ed.*, Chapman & Hall, London, UK
- Mazzolani, F.M.; Faella, C.; Piluso, V.; Rizzano, G. (1996), *Experimental analysis of aluminium alloy SHS-members subjected to local buckling under uniform compression*, 5th Int. Coll. on Structural Stability, SSRC, Rio de Janeiro, Brasil
- Mazzolani, F.M.; Piluso, V.; Rizzano, G. (1997), *Numerical simulation of aluminium stocky hollow members under uniform compression*, 5th International Colloquium on Stability and Ductility of Steel Structures, SDSS'97, Nagoya, Japan
- Mazzolani, F.M.; Faella, C.; Piluso, V.; Rizzano, G. (1998), *Local buckling of aluminium members: Experimental analysis and cross-sectional classification*, Department of Civil Engineering, University of Salerno, Italy
- Mazzolani, F.M.; Frey, F. (1977), *Buckling behaviour of aluminium alloy extruded members*, 2nd International Colloquium on the Stability of Steel Structures, pp. 85-94, Liege, Belgium
- Mennink, J. (1999a), *Preliminary FEM-simulations on aluminium stub columns*, BCO-Report 99.09, Eindhoven University of Technology, Eindhoven (TNO-report 1999-CON-LBC-R7014, TNO Building and Construction Research, Delft), The Netherlands
- Mennink, J. (1999b), *Stub column tests on aluminium extrusions with rectangular hollow sections*, BCO-Report 99.23, Eindhoven University of Technology, Eindhoven, The Netherlands

- Mennink J. (1999c), *Validation of finite element simulations on aluminium stub column tests with rectangular hollow sections*, BCO-Report 99.24, Eindhoven University of Technology, Eindhoven, The Netherlands
- Mennink, J. (2000), *Validation of FEM-calculations on aluminium stub column tests with U-shaped sections*, BCO-Report 00.10, Eindhoven University of Technology, Eindhoven (TNO-report 1999-CON-LBC-R7025, TNO Building and Construction Research, Delft), The Netherlands
- Mennink, J.; Soetens, F.; Snijder, H.H.; Hove, B.W.E.M. van (2000), *Experimental work and FEM-calculations on the interaction of local buckling modes in aluminium sections*, In: Proceedings of the 3rd International Conference on Coupled Instabilities of Metal Structures, CIMS'2000 (Eds. Camotim D.; Dubina, D.; Rondal J.), ICP, London, UK
- Mennink, J.; Soetens, F.; Snijder, H.H.; Hove, B.W.E.M. van (2001), *Buckling experiments and finite element simulations on uniformly compressed aluminium U-sections*, In: Proceedings of the 9th Nordic Steel Construction Conference, NSCC'2001 (Eds. Mäkeläinen, P.; Kesti, J.; Jutila, A.; Kaitila, O.), Helsinki, Finland
- Mennink, J.; Schillemans J. (2002), *Experimental research on the stability behaviour of axially compressed aluminium extrusions with complex cross-sectional shapes*, BCO-Report 02.14, Eindhoven University of Technology, Eindhoven (TNO-report 2002-BC-R0036, TNO Building and Construction Research, Delft), The Netherlands
- Mennink, J. (2002a), *Validation of finite element simulations on aluminium stub column tests with complex cross-sectional shapes*, BCO-Report 02.15, Eindhoven University of Technology, Eindhoven (TNO-report 2002-BC-R0037, TNO Building and Construction Research, Delft), The Netherlands
- Mennink, J. (2002b), *Development of a general prediction model for cross-sectional instability of aluminium extrusions with complex cross-sectional shapes*, BCO-Report 02.16, Eindhoven University of Technology, Eindhoven (TNO-report 2002-BC-R0038, TNO Building and Construction Research, Delft), The Netherlands
- Mofflin, D.S.; Dwight, J.B. (1984), *Buckling of Aluminium Plates in Compression*, In: Behaviour of Thin-Walled Structures (Eds. Rhodes, J.; Spence, J.), pp. 399-427
- Mulligan, G.P.; Peköz, T. (1983), *Influence of local buckling on the behavior of singly symmetric cold-formed steel columns*, Report No. 8302, Department of Structural Engineering, Cornell University, Ithaca, New York, USA
- Murray, N.W. (1984), *Introduction to the theory of thin-walled structures*, Oxford University Press, Oxford, UK
- Narayanan, R. (Ed.) (1987), *Aluminium Structures: Advances, Design & Connections*, Elsevier Applied Science, London, UK

- Neut, A. van der (1969), *The interaction of local buckling and column failure of thin-walled compression members*, In: Proceedings of the 12th International Congress on Theoretical and Applied Mechanics, pp. 389-399, Springer Verlag (And in: Report VTH-149, Department of Aeronautical Engineering, Delft University of Technology, Delft, The Netherlands)
- NNI (1991), *Metalen – Trekproef, Deel 1: Beproevingmethode (bij omgevingstemperatuur)*, NEN 10002-1, Nederlands Normalisatie Instituut, Delft, The Netherlands
- Peters, R.W.H.; Mennink, J. (2000), *Experimenteel onderzoek naar het instabiliteitsgedrag van axiaal belaste aluminium U-profielen* (In Dutch), BCO-Report 00.03, Eindhoven University of Technology, Eindhoven (TNO 00-CON-LBC/R5004, TNO Building and Construction Research, Delft), The Netherlands
- Pignataro, M.; Luongo, A.; Rizzi, N. (1985), *On the effect of the local-overall interaction on the postbuckling of uniformly compressed channels*, In: Thin-Walled Structures 3, pp. 1470-1486
- Ramberg, W.; Osgood, W.R. (1943), *Description of stress-strain curves by three parameters*, Technical note 902, NACA, USA
- Rasmussen, K.J.R. (2000), *Experimental techniques in the testing of thin-walled structural members*, Proceedings of the 3rd International Conference on Coupled Instabilities of Metal Structures, CIMS'2000 (Eds. Camotim, D.; Dubina, D.; Rondal J.), ICP, London, UK
- Reis, A.; Roorda, J. (1977), *The interaction between lateral-torsional and local plate buckling in thin-walled beams*, Second International Colloquium on the Stability of Steel Structures, Liege, Belgium
- Rhodes, J. (Ed.) (1991), *Design of cold formed steel members*, Elsevier Applied Science Publishers, London, UK
- Saint Venant (1883), *Théorie de l'élasticité des corps solides*, Clebsch, Germany
- Schafer, B.W. (1997), *Cold-Formed Steel Behavior and Design: Analytical and Numerical Modelling of Elements and Members with Longitudinal Stiffeners*, PhD Thesis, Cornell University, Ithaca, New York, USA
- Schafer, B.W.; Peköz, T. (1998a), *Cold-Formed Steel Members with Multiple Longitudinal Intermediate Stiffeners In the Compression Flange*, In: Journal of Structural Engineering, In: Journal of Structural Engineering, Vol. 124, No. 10
- Schafer, B.W.; Peköz, T. (1998b), *Laterally Braced Cold-Formed Steel Flexural Members with Edge Stiffened Flanges*, In: Proceedings of the Fourteenth International Specialty Conference on Cold-Formed Steel Structures, St. Louis, Missouri, USA

- Schillemans, J. (2001), *Experimenteel en numeriek onderzoek naar het instabiliteitsgedrag van axiaal belaste aluminium extrusieprofielen met complexe doorsnedevormen* (Dutch), BCO-Report 01.24, Eindhoven University of Technology, Eindhoven, The Netherlands
- Seide, P.; Stein, M. (1949), *Compressive Buckling of Simply Supported Plates with Longitudinal Stiffeners*, Technical note 1825, NACA, USA
- Shanley, F.R. (1947), *Inelastic column theory*, In: Journal of Aeronautical Science, Vol. 14, No. 5
- Sherbourne, A.N.; Marsh, C.; Lian, C.Y. (1971), *Stiffened Plates in Uniaxial Compression*, IABSE Publ., Vol. 31-1, pp. 145-178, Zurich, Switzerland
- Singer, J.; Arbocz, J.; Weller, T. (1998), *Buckling experiments: experimental methods in buckling of thin-walled structures, Vol. 1. Basic concepts, columns, beams and plates*, John Wiley and Sons, New York, USA
- Soetens, F.; Mennink, J. (1999), *Aluminium building and civil engineering structures*, In: Light-weight steel and aluminium structures (Eds. Mäkeläinen, P.; Hassinen, P.), Espoo, Finland
- Sridharan, S.; Benito, R. (1984), *Static and dynamic interactive buckling*, In: Journal of Engineering Mechanics, ASCE, Vol. 110, No. 1, pp. 49-65
- Sutter, K. (1959), *Die theoretischen Knickdiagramme bei Aluminiumlegierungen* (Theoretical stress-strain diagram for aluminium alloys), Technische Rundschau, Nos 20-24, Bern, Switzerland
- Stein, M. (1959), *Loads and deformations of buckled rectangular plates*, Technical report R40, NASA, USA
- Steinhardt, G. (1971), *Aluminium in engineered construction* (German), In: Aluminum, No. 47
- Stowell, E.Z. (1958), *A Unified Theory of Plastic Buckling of Columns and Plates*, Technical note 1556, NACA, USA
- Thomasson, P.O. (1978), *Thin-walled C-shaped panels in axial compression*, Swedish Council for Building Research, Document D1, Stockholm, Sweden
- Timoshenko, S.P.; Gere, M.J. (1961), *Theory of elastic stability 2nd Ed.*, McGraw-Hill, New York, USA
- Trahair, N.S.; Bradford, M.A. (1988), *The behaviour and design of steel structures 2nd Ed.*, Chapman&Hall, London, UK
- Troitsky, M.S. (1976), *Stiffened Plates - Bending, Stability and Vibrations*, Elsevier, New York, USA

- Tvergaard, V. (1973), *Imperfection-Sensitivity of a Wide Integrally Stiffened Panel Under Compression*, In: International Journal of Solids and Structures, Vol. 9, pp. 177-192
- Venkataramaiah, K.R.; Roorda, J. (1982), *Analysis of the local plate buckling experimental data*, Proceedings of the 6th International Specialty Conference on Cold-Formed Steel Structures (Eds. Yu, W.W.; Senne, J. H.), pp. 45-74, St. Louis, Missouri, USA
- Walker, A.C. (Ed.) (1975), *Design and analysis of cold-formed sections*, International Textbook Company, London, UK
- Wang, S.T.; Yost, M.I.; Tien, Y.L. (1977), *Lateral buckling of locally buckled beams using finite element techniques*, Computers & Structures, Vol. 7, No. 7, pp. 469-475
- Williams, D.G.; Walker, A.C. (1975), *Explicit solutions for the design of initially deformed plates subject to compression*, In: Proceedings of the Institution of Civil Engineers, Part 2, Vol. 59
- Williams, D.G.; Walker, A.C. (1977), *Explicit solutions for plate buckling analysis*, Proceedings of the American Society of Civil Engineers, Vol. 103, No. EM4
- Winter, G. (1947), *Strength of thin steel compression flanges*, bulletin 35/3, Cornell University Engineering Experiment Station, Ithaca, New York, USA
- Winter, G. (1948), *Performance of thin steel compression flanges*, preliminary publication, 3rd Congress for the Association for Bridge and Structural Engineering, Liege, Belgium
- Winter, G. (1970), *Commentary on the 1968 Edition of the Specification for the Design of Cold-Formed Steel Structural Members*, American Iron and Steel Institute (AISI), USA
- Witte, F. de et al (1996), *DIANA Finite Element Analysis, User's Manual release 7.2*, TNO Building and Construction Research, Delft, The Netherlands
- Yamaki, N. (1959), *Postbuckling behaviour of rectangular plates with small initial curvature loaded in edge compression*, In: Journal of Applied Mechanics, Vol. 26(3), ASME transactions, USA
- Yu, W.W. (2000), *Cold-formed steel design 3rd Ed.*, John Wiley & Sons, New York, USA

Appendix A - Results of the Salerno and Helsinki experiments

A.1 Geometry of the Salerno program

US - Salerno											
Test	Spec.	L	b_1	b_2	b_3	t_1	t_2	t_3	A	I_{11}	I_{22}
		mm	mm	mm	mm	mm	mm	mm	mm ²	10 ³ mm ⁴	10 ³ mm ⁴
C1A	39*48*4	96.5	45.55	34.90	46.05	4.00	4.10	3.80	504.38	13.13	11.73
C1B	40*48*4	96.5	46.25	35.90	45.35	4.00	3.90	3.80	497.34	13.05	11.55
C2A	100*17*4	96.4	15.40	95.90	15.20	4.10	3.80	3.90	486.84	56.09	0.82
C2B	100*19*4	96.4	16.53	95.90	16.63	4.00	3.95	4.00	511.45	59.55	1.03
C3A	50*49*4	97.6	46.85	46.20	46.85	3.90	3.90	3.90	545.61	22.75	13.33
C3B	50*47*4	97.6	45.10	46.15	45.20	4.00	4.00	3.90	541.28	22.31	12.28
C4A	40*29*3	97.2	27.65	37.55	25.85	2.60	2.50	2.50	230.39	5.91	1.82
C4B	40*27*3	97.2	25.85	37.60	27.55	2.50	2.50	2.50	227.50	5.83	1.79
C5A	60*17*3	97.2	15.80	57.50	15.90	2.50	2.60	2.50	228.75	10.67	0.50
C5B	60*19*3	97.2	17.65	57.45	17.65	2.60	2.50	2.50	233.64	11.38	0.67
C6A	40*38*4	72.6	35.55	36.40	35.65	3.90	3.90	3.90	419.64	10.80	5.93
C6B	40*39*4	72.6	36.65	36.10	36.65	3.90	3.90	3.90	426.66	10.88	6.39
C7A	70*32*4	68.2	29.80	65.95	29.90	4.30	4.00	3.80	505.56	35.84	4.64
C7B	70*34*4	68.2	32.25	66.00	32.45	3.90	3.90	4.10	516.22	37.55	5.67
C8A	50*23*3	72.2	21.70	46.85	21.70	2.90	3.00	3.00	268.58	9.60	1.30
C8B	50*23*3	72.2	21.10	47.00	21.10	3.00	3.00	3.00	267.60	9.60	1.22
C9A	34*29*3	67.7	27.15	31.00	26.95	3.00	2.90	3.00	252.20	4.63	2.05
C9B	34*28*3	67.7	26.20	31.00	25.90	3.10	3.00	2.90	249.33	4.51	1.88
C10A	40*28*2	71.7	26.60	38.10	27.50	2.00	2.00	2.00	184.40	4.85	1.48
C10B	40*28*2	71.7	26.60	38.10	27.60	2.00	2.00	2.00	184.60	4.86	1.49
C11A	80*19*4	72.8	16.95	76.30	16.95	3.90	3.90	3.90	429.78	33.70	1.01
C11B	80*17*4	72.8	15.30	76.30	15.20	3.90	3.80	3.90	408.89	31.39	0.76
C12A	40*22*2	72.0	20.40	37.25	19.80	2.40	2.40	2.50	187.86	4.45	0.81
C12B	40*22*3	72.0	20.35	37.35	19.75	2.50	2.50	2.40	191.65	4.52	0.82
C13A	40*18*4	68.5	16.05	36.05	16.05	4.00	4.10	3.90	274.60	5.74	0.73
C13B	40*18*4	68.5	15.95	36.05	15.95	3.90	4.10	4.00	273.81	5.71	0.72
C14A	80*38*4	77.5	35.70	75.90	35.90	4.00	4.20	4.20	612.36	57.61	8.08
C14B	80*38*4	77.5	35.70	75.60	35.90	4.20	4.00	4.00	595.94	56.38	7.95
C15A	80*38*2	77.5	37.45	78.25	37.35	1.90	1.90	2.00	294.53	29.91	4.28
C15B	80*38*2	77.5	36.95	78.15	36.75	1.90	1.90	2.00	292.19	29.50	4.11
C16A	100*58*7	146.8	54.60	95.50	53.80	4.60	6.60	4.40	1118.18	159.18	32.39
C16B	100*59*7	146.8	56.00	95.50	55.40	4.40	6.60	4.60	1131.54	162.26	34.84
C17A	120*47*5	146.0	45.15	113.80	46.25	6.50	4.50	6.50	1106.20	247.81	24.80
C17B	120*48*5	146.0	45.55	113.60	46.75	6.50	4.50	6.50	1111.15	248.73	25.45

Results of the Salerno and Helsinki experiments

SHS / RHS - Salerno													
Test	Spec.	L_A	L_B	b	h	t_1	t_2	t_3	t_4	A	I_{11}	I_{22}	
		mm	mm	mm	mm	mm	mm	mm	mm	mm ²	10 ³ mm ⁴	10 ³ mm ⁴	
SHS1	15*15*2	44.5	46.0	13.10	13.10	1.90	1.90	1.90	1.90	100	0.29	0.29	
SHS2	40*40*4	120.0	115.7	36.03	35.95	4.05	4.10	4.15	4.05	588	12.75	12.74	
SHS3	50*50*3	149.4	149.4	48.05	46.90	3.10	3.05	3.10	3.15	589	22.54	21.74	
SHS4	50*50*4	149.4	149.3	46.15	46.08	4.45	4.20	4.10	4.30	786	27.92	27.91	
SHS5	70*70*4	209.5	209.5	66.05	65.95	4.10	4.20	4.20	4.00	1089	79.29	78.97	
SHS6	80*80*4	239.0	239.0	75.63	75.60	4.30	4.35	4.20	4.20	1289	123.16	122.73	
SHS7	100*100*4	296.0	299.0	96.10	95.85	3.90	3.95	4.00	3.85	1507	231.69	231.12	
SHS8	60*60*2	179.0	179.0	58.15	58.08	2.30	2.25	2.25	2.25	526	29.67	29.56	
SHS9	80*80*2	239.5	239.0	78.35	78.10	2.10	2.10	2.10	2.00	649	66.47	65.97	
SHS10	100*100*6	303.0	303.0	94.25	93.93	6.00	6.00	5.95	6.10	2263	336.11	332.32	
SHS11	150*150*5	437.0	451.0	145.35	145.13	5.20	5.00	4.75	4.70	2854	1008.17	998.05	
SHS12	150*150*5	451.5	452.0	144.78	144.80	5.20	5.00	5.00	5.25	2961	1035.83	1033.56	
RHS1	34*20*3	46.8	46.8	31.00	17.00	3.00	3.00	3.00	3.00	288	3.95	1.60	
RHS2	40*30*4	73.6	120.4	35.90	25.90	4.10	4.00	3.90	4.00	494	9.79	6.01	
RHS3	50*20*4	52.3	52.3	45.95	15.95	3.90	4.40	4.20	3.90	505	13.55	2.70	
RHS4	50*30*3	80.7	149.0	46.93	27.23	3.00	3.25	3.05	2.90	451	14.43	6.32	
RHS5	50*40*3	104.5	211.0	47.55	37.60	2.80	2.60	2.60	2.80	460	16.32	11.48	
RHS6	60*34*3	88.8	179.0	57.20	31.10	3.00	3.00	3.00	3.00	530	24.63	9.83	
RHS7	60*40*3	179.5	176.0	57.65	37.55	2.60	2.60	2.50	2.50	486	24.06	12.63	
RHS8	80*40*4	234.5	233.5	76.35	36.10	4.00	3.90	4.00	3.90	892	70.74	23.04	
RHS9	100*40*4	236.0	236.0	95.85	36.10	4.00	4.00	4.00	3.90	1052	124.24	28.18	
RHS10	120*50*4	361.0	361.0	116.03	46.45	4.15	4.30	4.15	4.25	1360	241.77	59.23	
RHS11	150*40*4	225.0	224.5	146.45	36.70	4.10	4.00	4.10	4.10	1498	374.06	43.94	
RHS12	180*40*4	242.0	237.0	177.00	36.60	4.20	3.90	4.20	4.30	1787	623.18	53.36	
RHS13	100*50*4	299.0	298.0	96.15	46.30	4.00	3.90	3.90	4.00	1125	143.10	47.34	
RHS14	60*40*2	191.0	176.0	58.05	37.95	2.00	2.00	2.30	2.10	405	20.12	10.84	
RHS15	80*40*4	234.5	233.9	76.00	36.05	4.00	3.90	3.90	3.90	882	69.54	22.63	
RHS16	80*40*2	239.0	238.0	78.13	38.18	2.30	2.15	1.85	2.00	483	40.67	13.66	
RHS17	60*40*2	180.0	178.0	57.90	38.05	2.00	2.00	1.90	2.00	378	19.07	10.01	
RHS18	100*25*2	125.0	127.0	98.00	23.40	2.30	2.30	2.30	2.30	558	61.93	6.68	
RHS19	120*60*2.5	359.0	355.0	117.30	58.30	2.70	2.60	2.70	2.60	937	176.93	62.45	
RHS20	200*100*5	601.0	601.0	195.10	95.05	5.00	4.80	4.70	5.00	2824	1486.76	497.67	
RHS21	47*40*2.5	140.0	141.0	44.13	37.13	2.80	2.95	2.95	2.80	467	14.52	11.21	
RHS22	180*70*4.5	540.0	540.0	174.85	65.43	4.50	4.65	4.65	4.65	2208	872.80	193.18	
RHS23	153*70*4.5	411.0	411.5	146.15	66.75	4.35	6.85	5.35	6.85	2332	741.02	191.13	
RHS24	200*180*15.1	531.2	535.0	191.28	163.90	15.30	9.15	15.30	9.30	8877	4619.23	4552.73	
RHS25	120*100*4.5	361.0	361.0	113.73	95.60	4.60	6.70	4.90	6.85	2376	535.80	345.61	
RHS26	200*180*6	601.0	601.0	194.90	175.40	6.00	6.50	6.20	5.70	4518	2781.36	2377.91	
RHS27	219*68*4.5	508.0	508.0	213.80	63.30	4.40	6.00	5.00	6.00	2769	1633.81	226.46	
SHS01C	100*100*6	376.3	376.3	94.47	93.36	5.99	5.95	5.90	5.91	2231	330.90	325.51	
SHS02C	100*100*6	376.9	376.9	94.49	93.18	5.98	5.93	5.86	5.90	2221	329.61	322.91	
SHS03C	100*100*6	376.0	376.0	94.19	93.93	5.91	5.89	6.04	5.94	2237	330.29	329.99	
SHS04C	100*100*4	383.8	383.8	98.98	98.47	3.76	3.63	3.91	3.62	1473	241.77	236.91	
SHS05C	100*100*3	387.7	387.7	96.68	96.64	2.87	2.84	2.86	2.80	1099	171.80	170.55	
SHS06C	100*100*3	388.0	388.0	97.06	96.10	2.78	2.85	2.82	2.84	1090	171.49	167.61	
SHS07C	100*100*2	392.0	392.0	97.57	97.55	1.95	1.91	1.96	1.95	758	120.63	119.89	
SHS08C	100*100*2	392.2	392.2	97.62	97.67	1.90	1.98	1.96	1.98	764	122.08	120.61	
SHS09C	100*100*1.5	393.8	393.8	98.96	98.95	1.48	1.45	1.42	1.44	573	93.57	93.44	
SHS10C	80*80*2.5	310.0	310.0	77.63	77.62	2.46	2.46	2.50	2.48	768	77.27	77.13	
SHS11C	80*80*2	310.1	310.1	78.25	78.17	2.02	2.05	2.05	2.06	640	65.44	65.02	
RHS01C	120*60*2.5	470.5	470.5	117.00	58.35	2.60	2.11	2.30	2.89	865	164.44	56.98	
RHS02C	100*60*3	387.9	387.9	96.19	58.06	2.99	2.93	2.89	2.89	904	121.80	57.19	

A.2 Test results of the Salerno program

US - Salerno						
Test	Tensile test					Comp. N_u kN
	E kN/mm ²	$f_{0.1}$ N/mm ²	$f_{0.2}$ N/mm ³	f_t N/mm ⁴	n	
C1B	70.2	213.3	216.6	242.2	45	109.8
C2A	70.2	213.3	216.6	242.2	45	103.9
C2B	70.2	213.3	216.6	242.2	45	107.1
C3A	68.5	211.5	216.0	236.6	33	124.1
C3B	68.5	211.5	216.0	236.6	33	123.2
C4A	62.8	229.4	234.6	258.9	31	59.7
C4B	62.8	229.4	234.6	258.9	31	59.0
C5A	62.8	229.4	234.6	258.9	31	58.0
C5B	62.8	229.4	234.6	258.9	31	59.3
C6A	63.5	216.3	222.0	258.6	27	97.0
C6B	63.5	216.3	222.0	258.6	27	99.1
C7A	70.2	169.9	175.7	202.9	21	91.6
C7B	70.2	169.9	175.7	202.9	21	89.5
C8A	64.9	222.5	222.5	244.8	29	61.5
C8B	64.9	222.5	222.5	244.8	29	60.8
C9A	77.8	204.8	212.5	235.0	19	62.9
C9B	77.8	204.8	212.5	235.0	19	61.9
C10A	69.3	230.0	234.3	253.3	38	43.2
C10B	69.3	230.0	234.3	253.3	38	41.7
C11A	63.5	216.3	222.0	258.6	27	105.8
C11B	63.5	216.3	222.0	258.6	27	100.5
C12A	67.5	246.0	251.3	276.9	33	54.1
C12B	67.5	246.0	251.3	276.9	33	55.9
C13A	72.3	223.6	223.6	244.3	19	79.0
C13B	72.3	223.6	223.6	244.3	19	77.3
C14A	71.7	194.2	194.2	220.3	27	131.1
C14B	71.7	194.2	194.2	220.3	27	130.7
C15A	65.1	186.7	186.7	203.9	28	50.3
C15B	65.1	186.7	186.7	203.9	28	49.4
C16A	68.8	315.7	323.0	342.8	30	333.4
C16B	68.8	315.7	323.0	342.8	30	333.0
C17A	68.8	315.7	323.0	342.8	30	338.0
C17B	68.8	315.7	323.0	342.8	30	319.8

SHS / RHS - Salerno							
Test	Tensile test					Comp. test	
	E kN/mm ²	$f_{0.1}$ N/mm ²	$f_{0.2}$ N/mm ³	f_t N/mm ⁴	n	$N_u(A)$ kN	$N_u(B)$ kN
SHS1	67.5	207.8	214.4	241.3	22	30.6	29.7
SHS2	72.3	215.6	223.6	244.3	19	160.8	158.4
SHS3	64.9	217.2	222.5	244.8	29	132.4	131.3
SHS4	64.1	198.1	202.6	225.2	31	186.6	180.9
SHS5	70.2	169.9	175.7	202.9	21	213.8	208.7
SHS6	71.7	189.2	194.2	220.3	27	264.4	263.8
SHS7	70.8	204.8	209.8	228.3	28	300.2	304.8
SHS8	72.0	149.3	158.2	186.6	12	82.7	83.3
SHS9	65.1	182.1	186.7	203.9	28	84.7	84.7
SHS10	65.3	286.0	293.5	323.7	27	728.5	731.5
SHS11	75.3	186.5	208.9	252.1	11	605.5	592.5
SHS12	68.4	245.5	258.4	300.1	13	626.5	643.5
RHS1	62.8	212.4	218.7	250.9	24	78.7	77.5
RHS2	69.8	197.5	202.0	214.3	31	124.3	122.4
RHS3	68.4	205.3	210.7	233.3	27	134.8	136.8
RHS4	70.9	209.8	217.4	242.5	20	109.8	109.2
RHS5	69.7	218.4	221.6	244.5	48	108.5	109.1
RHS6	77.8	204.8	212.5	235.0	19	122.4	122.9
RHS7	62.8	229.4	234.6	258.9	31	120.6	118.7
RHS8	63.5	216.3	222.0	258.6	27	212.0	212.0
RHS9	70.2	213.3	216.6	242.2	45	222.6	224.9
RHS10	68.9	209.8	215.8	227.3	25	271.2	255.6
RHS11	68.8	213.4	224.6	255.5	14	290.8	261.2
RHS12	74.5	204.6	212.3	246.8	19	313.2	315.6
RHS13	68.5	211.5	216.0	236.6	33	248.1	248.2
RHS14	62.4	215.2	219.6	242.8	35	85.1	79.7
RHS15	69.3	184.0	188.9	212.4	27	185.7	185.2
RHS16	60.0	222.4	225.4	260.5	53	92.5	92.8
RHS17	69.3	230.0	234.3	253.3	38	89.4	88.6
RHS18	68.0	258.3	264.8	285.0	28	92.7	89.4
RHS19	69.3	205.5	209.7	229.4	34	137.7	139.6
RHS20	65.2	224.2	235.2	282.8	15	513.5	506.5
RHS21	67.5	246.0	251.3	276.9	33	115.3	116.5
RHS22	72.0	317.3	320.0	353.4	84	493.2	497.0
RHS23	71.9	306.7	309.2	329.9	91	621.5	612.0
RHS24	71.4	336.9	340.0	362.1	77	2939.0	2934.0
RHS25	68.8	315.7	323.0	342.8	30	669.0	670.5
RHS26	71.6	131.6	132.7	184.8	84	865.0	852.0
RHS27	69.0	294.1	297.9	325.0	53	831.0	808.5
SHS01C	70.1		312.1	325.2	31	726.2	
SHS02C	72.9		178.7	292.7	18	470.1	
SHS03C	68.2		311.2	352.1	31	733.6	
SHS04C	70.5		306.6	349.4	31	408.2	
SHS05C	69.0		197.9	240.1	20	190.4	
SHS06C	71.3		168.3	282.5	17	147.3	
SHS07C	68.3		252.3	281.4	25	102.8	
SHS08C	72.5		135.7	242.6	14	67.6	
SHS09C	70.6		139.3	263.3	14	38.2	
SHS10C	74.8		111.4	226.2	11	81.9	
SHS11C	69.1		138.5	259.1	14	70.4	
RHS01C	68.3		245.2	282.8	25	146.8	
RHS02C	65.6		283.2	290.2	28	236.3	

A.3 Geometry and test results of the Helsinki program

RHS - Helsinki											
Test	Spec.	L	b	h	t_1	t_2	t_3	t_4	A	I_{11}	I_{22}
		mm	mm	mm	mm	mm	mm	mm	mm ²	mm ⁴	mm ⁴
RHS200	20*20*1	100	18.83	18.94	0.86	0.99	0.87	0.97	69.7	4256	4033
RHS240	20*20*1	140	18.83	18.94	0.86	0.99	0.87	0.97	69.7	4256	4033
RHS290	20*20*1	190	18.83	18.94	0.86	0.99	0.87	0.97	69.7	4256	4033
RHS390	20*20*1	290	18.83	18.94	0.86	0.99	0.87	0.97	69.7	4256	4033
RHS550	20*20*1	450	18.83	18.94	0.86	0.99	0.87	0.97	69.7	4256	4033
RHS670	20*20*1	570	18.83	18.94	0.86	0.99	0.87	0.97	69.7	4256	4033
RHS960	20*20*1	860	18.83	18.94	0.86	0.99	0.87	0.97	69.7	4256	4033
RHS1340	20*20*1	1240	18.83	18.94	0.86	0.99	0.87	0.97	69.7	4256	4033

RHS - Helsinki										
Test	Spec.	Tensile test					Compression test			
		E	f_{02}	f_t	N_u (A)	Mode	N_u (B)	Mode	N_u (C)	Mode
		kN/mm ²	N/mm ²	N/mm ²	kN	A	kN	B	kN	C
RHS200	20*20*1	65.2	178.3	214.9	12.81	L	12.67	L		
RHS240	20*20*1	65.2	178.3	214.9	12.59	L	12.31	L	12.5	L
RHS290	20*20*1	65.2	178.3	214.9	12.56	L	12.62	F		
RHS390	20*20*1	65.2	178.3	214.9	12.4	F	11.88	F	11.8	F
RHS550	20*20*1	65.2	178.3	214.9	11.95	F	11.68	F		
RHS670	20*20*1	65.2	178.3	214.9	11.39	F	11.2	F		
RHS960	20*20*1	65.2	178.3	214.9	9.41	F	9.48	F		
RHS1340	20*20*1	65.2	178.3	214.9	5.45	F	6.16	F		

CS - Helsinki											
Test	Spec.	Geometry			Tensile				Compression		
		L	A	I_{22}	E	f_{02}	f_t	N_u (A)	Mode	N_u (B)	Mode
		mm	mm ²	mm ⁴	kN/mm ²	N/mm ²	N/mm ²	kN	A	kN	B
AK180	30*15*2	80	85.71	868	64.1	201.8	233.1	15.76	L	15.58	L
AK200	30*15*2	100	85.71	868	64.1	201.8	233.1	14.22	L	16.46	L
AK230	30*15*2	130	85.71	868	64.1	201.8	233.1	14.78	L	15.72	L
AK280	30*15*2	180	85.71	868	64.1	201.8	233.1	13.79	FT	13.81	FT
AK350	30*15*2	250	85.71	868	64.1	201.8	233.1	11.58	FT	11.88	FT
AK420	30*15*2	320	85.71	868	64.1	201.8	233.1	9.66	FT	10.14	FT
AK500	30*15*2	400	85.71	868	64.1	201.8	233.1	8.44	FT	8.26	FT
AK600	30*15*2	500	85.71	868	64.1	201.8	233.1	6.46	FT	6.57	FT
AK800	30*15*2	700	85.71	868	64.1	201.8	233.1	3.8	FT	3.45	FT
H1-200	20*20*1	200	63.98	3647	65.2	178.3	214.9	11.52	D	11.64	D
H1-290	20*20*2	290	63.98	3647	65.2	178.3	214.9	11.37	D		
H2-200	20*20*3	200	65.9	3414	65.2	178.3	214.9	9.5	L	10.09	L
H2-290	20*20*4	290	65.9	3414	65.2	178.3	214.9	9.04	L		

Appendix B - Results of the Eindhoven program

B.1 Cross-sectional properties RHS and US specimen

RHS - Eindhoven											
Test	Spec.	L	b	h	t_1	t_2	t_3	t_4	A	I_{11}	I_{22}
		mm	mm	mm	mm	mm	mm	mm	mm ²	10 ³ mm ⁴	10 ³ mm ⁴
RHS01	50*50*3	50.0	47.03	47.04	2.92	2.98	3.00	2.97	558	206	206
RHS02	50*50*3	100.3	46.99	47.02	2.92	2.98	2.98	2.96	557	205	205
RHS04	50*50*3	149.7	46.86	46.84	3.10	3.11	3.14	3.17	587	215	214
RHS05	50*50*3	200.0	46.86	46.86	3.09	3.17	3.14	3.12	587	215	214
RHS06	80*40*2	239.9	77.87	38.08	1.91	1.95	1.99	1.98	453	380	128
RHS07	80*40*2	390.1	77.90	38.10	1.91	1.98	2.00	1.98	455	383	129
RHS08	80*40*2	560.0	77.85	38.12	1.94	1.99	1.94	1.92	451	378	128
RHS09	80*40*2	720.1	77.84	38.11	1.90	1.88	1.93	1.95	444	372	126
RHS10	100*50*3	500.0	97.11	47.31	2.83	2.79	2.83	2.83	816	1059	358
RHS11	100*50*3	700.2	97.14	47.34	2.80	2.83	2.82	2.81	813	1059	356
RHS12	120*30*3	599.5	117.08	27.17	2.93	3.04	3.00	3.01	859	1357	139
RHS13	120*30*3	720.0	117.07	27.19	2.95	2.99	2.98	3.04	858	1355	139
RHS14	160*40*2.5	800.0	157.52	37.60	2.43	2.42	2.44	2.45	950	2722	293
RHS15	100*18*2.1	500.0	97.32	15.93	2.20	2.55	2.15	2.65	506	530	29
RHS16	100*18*2.1	700.1	97.24	15.93	2.20	2.58	2.20	2.76	513	538	29
RHS17	80*40*4	239.1	76.07	35.87	4.00	3.92	3.88	3.97	882	699	224
RHS19	100*40*4	300.0	95.85	35.82	3.85	3.86	3.91	3.89	1021	1207	269

US - Eindhoven											
Test	Spec.	L	b_1	b_2	b_3	t_1	t_2	t_3	A	I_{11}	I_{22}
		mm	mm	mm	mm	mm	mm	mm	mm ²	10 ³ mm ⁴	10 ³ mm ⁴
US01	40*20*2	300.1	17.90	38.03	17.97	1.94	2.03	2.06	149.0	35.3	4.94
US02	40*60*2	300.1	58.13	38.06	58.12	1.93	2.01	2.05	307.8	93.0	113.7
US04	40*60*2	300.1	58.20	38.02	58.12	2.00	2.00	2.03	310.4	93.9	114.6
US05	40*30*2	300.1	27.94	38.04	27.99	2.00	2.05	2.03	190.7	50.2	16.4
US06	40*50*2	300.1	48.11	38.01	48.10	2.04	2.01	1.96	268.8	78.7	68.8
US08	40*50*2	300.4	48.05	38.02	48.14	1.92	1.94	1.97	260.9	76.5	66.7
US10	80*25*2	300.0	22.96	78.13	22.95	2.01	1.95	2.01	244.6	218.4	11.7
US11	80*15*2	300.1	13.17	78.08	13.03	2.08	2.00	2.10	210.9	162.8	2.58
US13	40*20*4	300.0	16.79	36.05	16.68	4.01	4.02	3.88	277.0	58.8	8.12
US14	40*60*4	300.1	57.18	36.02	57.19	3.89	3.95	3.81	582.6	158.7	208.1
US17	40*30*4	300.1	26.79	36.02	26.91	3.94	4.00	3.99	357.0	84.9	28.5
US18	40*50*4	300.0	47.05	36.00	47.07	4.00	3.94	3.92	514.6	136.6	125.9
US20	40*50*4	300.4	47.39	36.02	47.05	3.89	3.90	4.00	513.0	136.5	126.3
US21	80*15*4	300.2	12.01	75.91	12.01	4.00	3.90	3.93	391.3	279.5	4.12
US22	80*25*4	300.2	21.95	76.02	21.98	3.95	3.96	3.95	474.6	395.9	20.6
US25	50*30*3	300.2	27.46	47.17	27.25	2.97	2.92	2.74	294.0	112.5	23.5
US26	50*70*3	300.2	67.68	47.06	67.72	2.72	2.94	3.00	525.6	239.8	264.8
US29	50*40*3	300.1	37.55	47.07	37.29	3.03	2.94	2.70	352.9	144.2	54.6
US30	50*60*3	300.2	57.67	47.18	57.65	2.70	2.91	3.03	467.7	209.1	172.2
US33	100*20*3	300.1	17.46	97.19	17.45	2.94	2.93	2.91	386.9	465.4	8.52
US34	100*30*3	300.1	27.61	96.96	27.68	2.92	2.70	2.92	423.2	584.7	29.5

B.2 Cross-sectional properties CS specimen

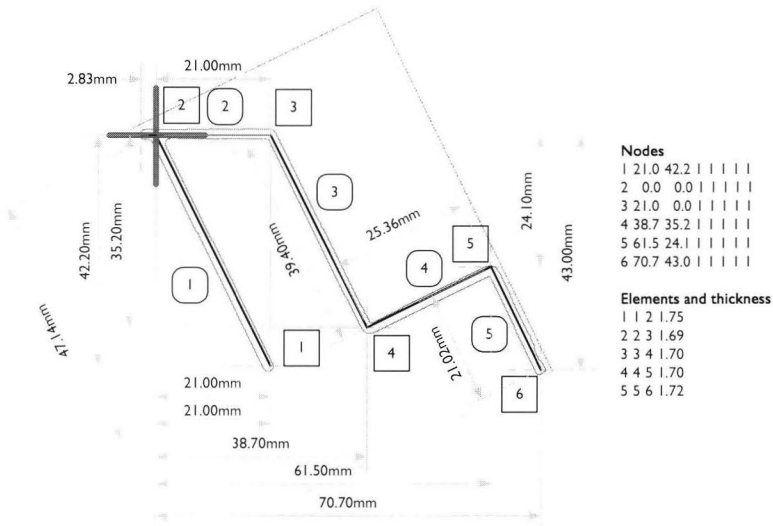


Figure B.2-1 Cross-section specimen CS01

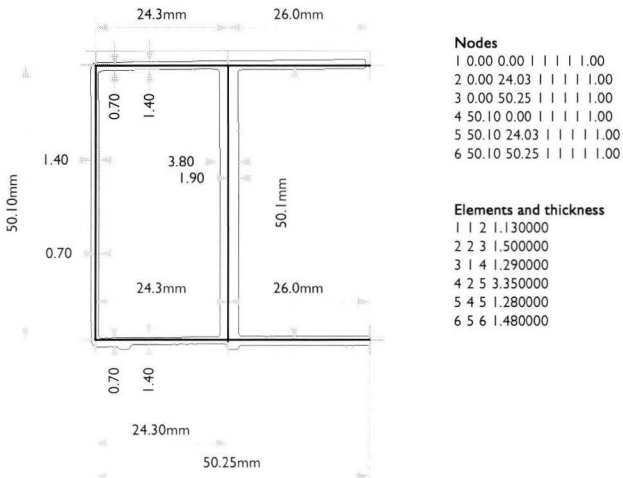


Figure B.2-2 Cross-section specimen CS02

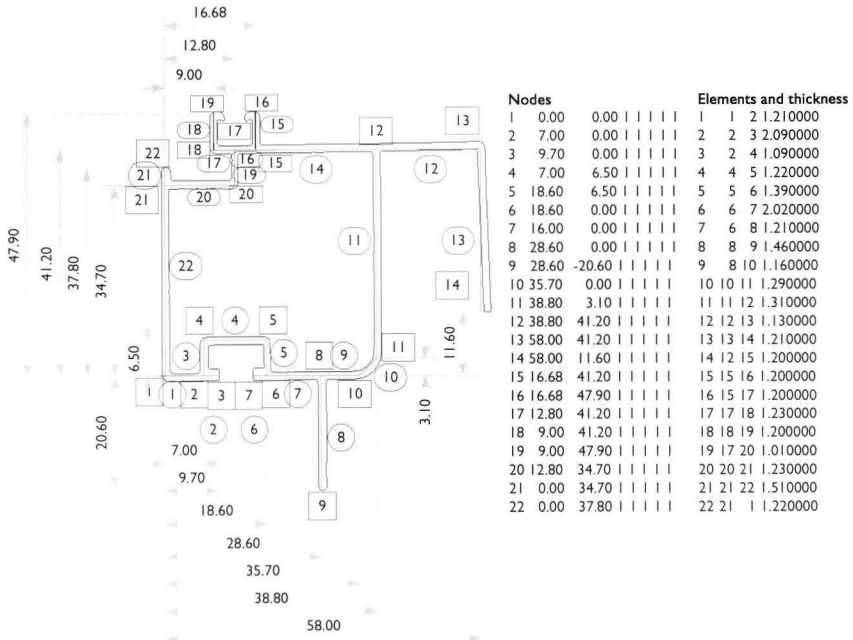


Figure B.2-3 Cross-section specimen CS03

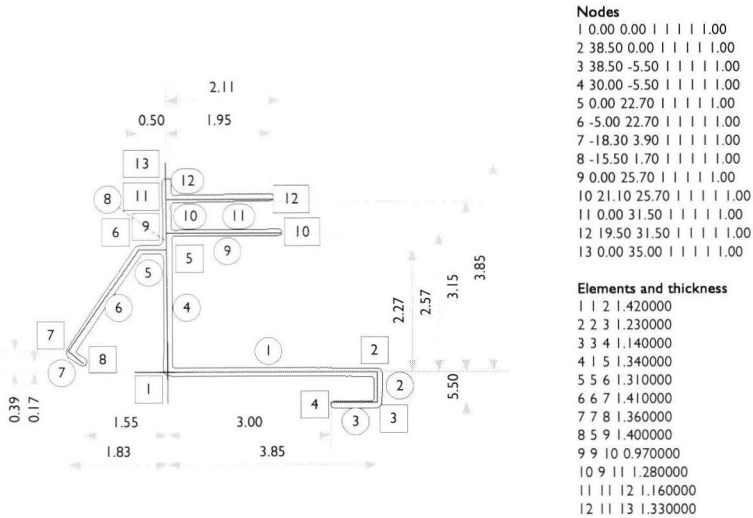


Figure B.2-4 Cross-section specimen CS04

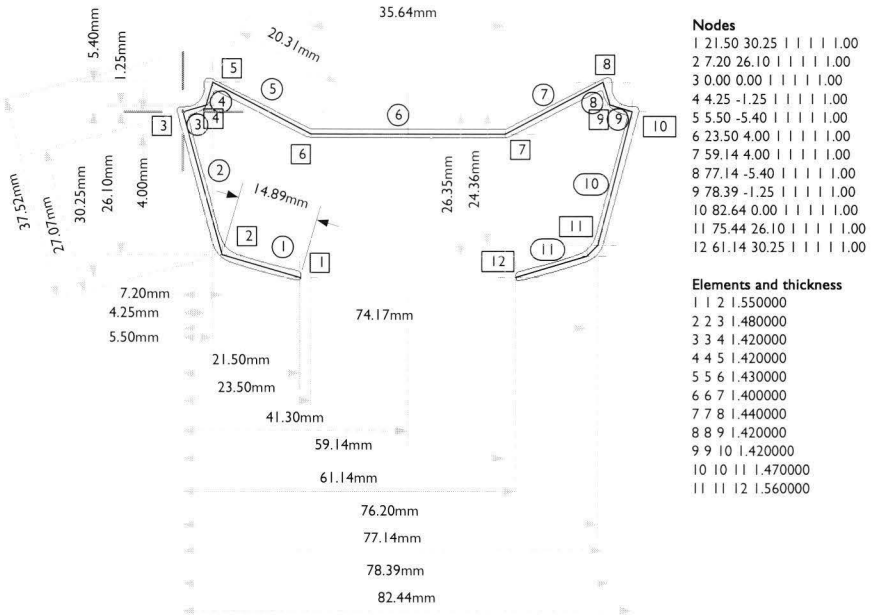


Figure B.2-5 Cross-section specimen CS05

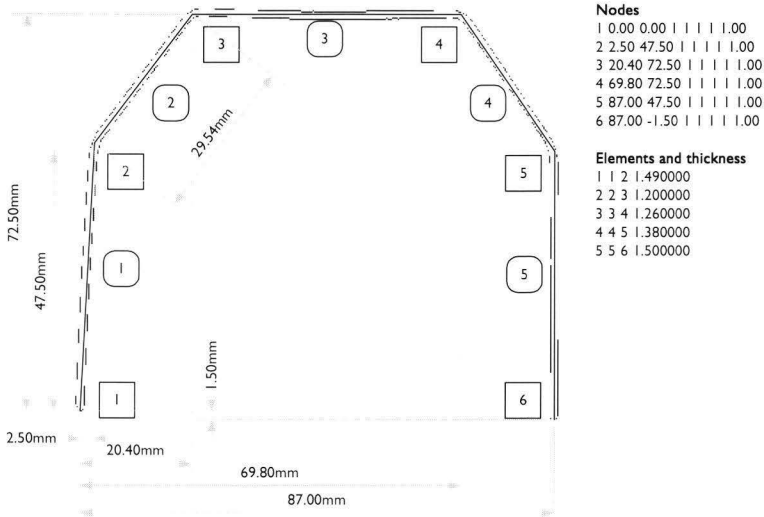


Figure B.2-6 Cross-section specimen CS12

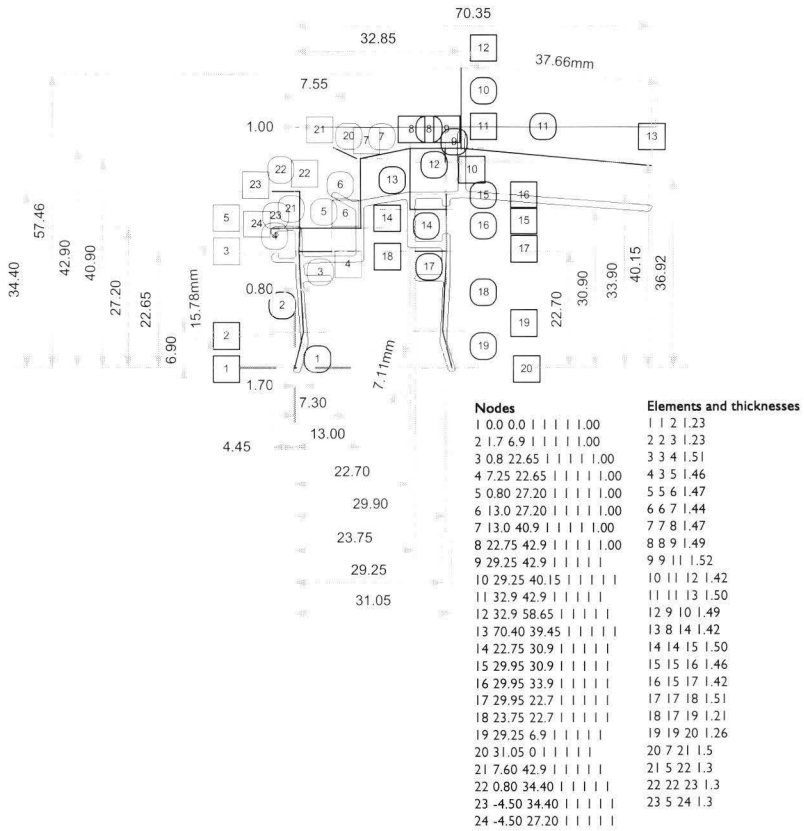


Figure B.2-7 Cross-section specimen CS06

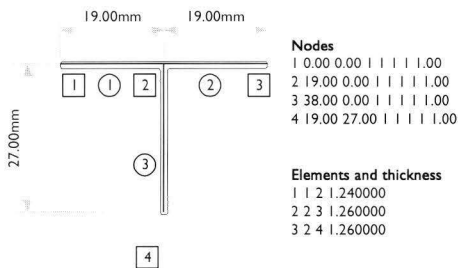


Figure B.2-8 Cross-section specimen CS11

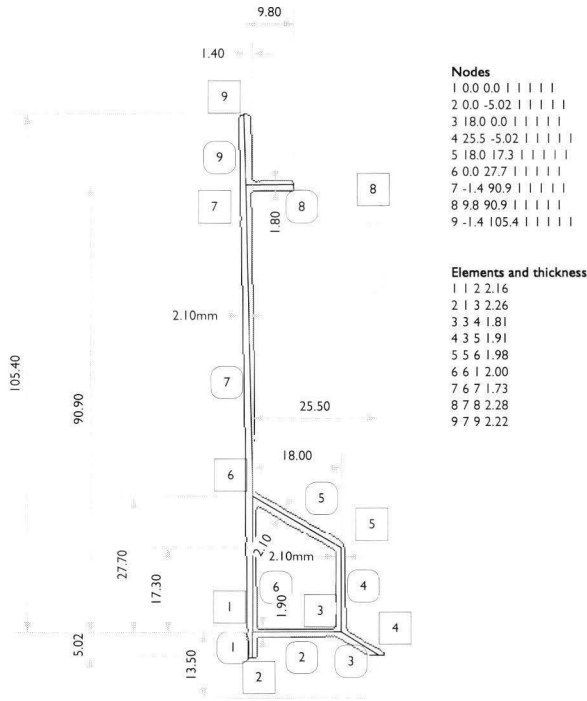


Figure B.2-9 Cross-section specimen CS07

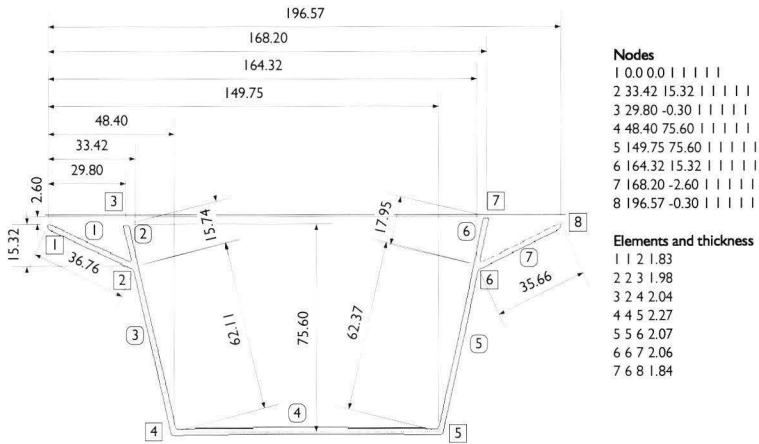


Figure B.2-10 Cross-section specimen CS08

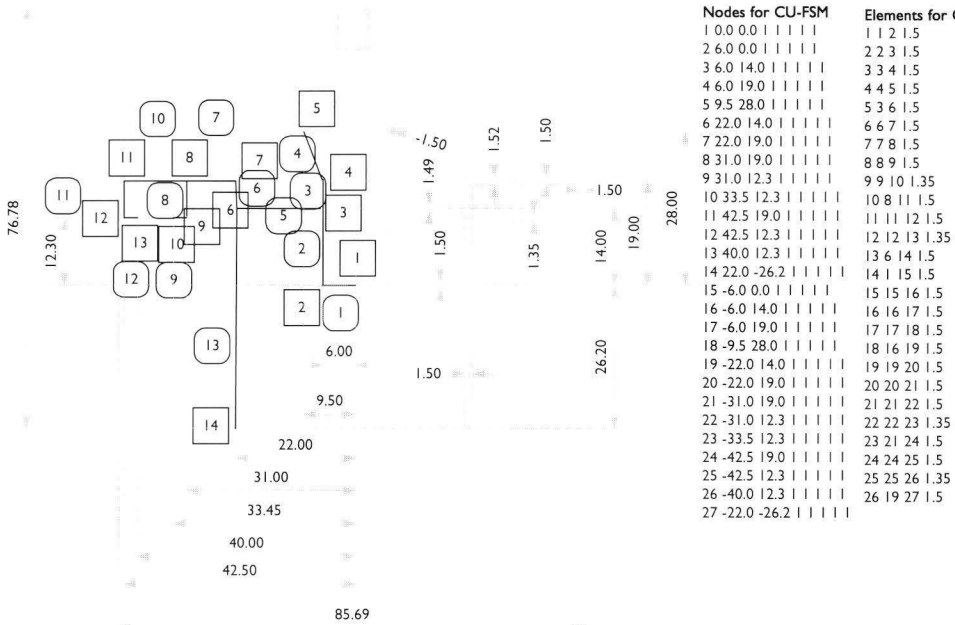


Figure B.2-11 Cross-section specimen CS09

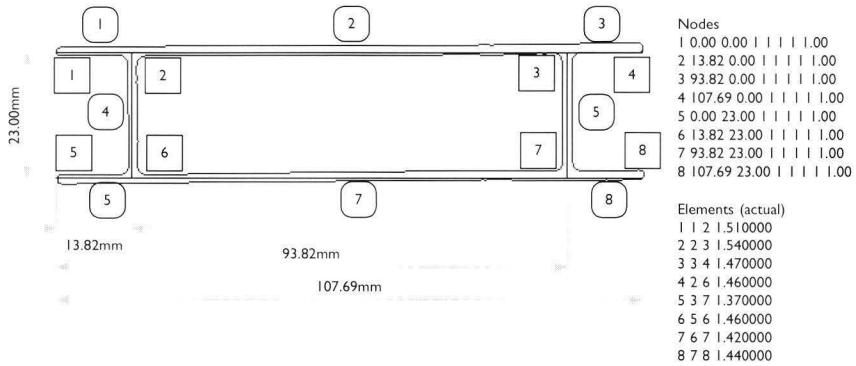


Figure B.2-12 Cross-section specimen CS10

B.3 Experimental results

RHS - Eindhoven											
Test	Imp.		Tensile test					Compression test			
	$e_{0,ov}$	$e_{0,loc}$	E	$f_{0,1}$	$f_{0,2}$	f_t	n	E_c	$\Delta\sigma$	Mode	N_u
	mm	mm	kN/mm ²	N/mm ²	N/mm ²	N/mm ²		kN/mm ²	N/mm ²		kN
RHS01	-	-	70.0		230.0		30	69.9	29.0	S	130.05
RHS02	0.07	0.00	70.0		230.0		30	68.6	8.1	S	129.67
RHS04	0.03	0.00	70.0		230.0		30	67.1	12.3	S	125.08
RHS05	0.05	0.00	65.4		198.5		28	67.9	12.0	S	128.52
RHS06	0.11	0.02	70.0		230.0		30	70.8	6.8	L	83.80
RHS07	0.09	0.05	70.0		230.0		30	70.6	19.9	L	82.21
RHS08	0.25	0.08	66.5	226.6	231.5	261.1	32	69.5	14.5	L	86.51
RHS09	0.30	0.08	66.5	226.6	231.5	261.1	32	70.0	5.8	L/F	84.23
RHS10	0.15	0.04	66.6	225.8	230.5	258.6	34	68.0	8.8	L	173.28
RHS11	0.15	0.03	66.6	225.8	230.5	258.6	34	67.7	23.4	L	159.76
RHS12	0.21	0.20	67.6	227.8	233.1	254.2	30	69.4	0.6	L/F	167.19
RHS13	0.25	0.08	67.6	227.8	233.1	254.2	30	74.2	15.8	L/F	173.30
RHS14	0.35	0.20	70.0		230.0		30	65.1	3.3	F	117.64
RHS15	0.06	0.03	66.4	187.5	191.0	217.5	39	70.1	3.4	F	85.22
RHS16	0.06	0.10	66.4	187.5	191.0	217.5	39	71.0	8.0	L/F	80.88
RHS17	0.20	0.06	65.4	193.6	198.5	225.8	28	68.8	5.9	S	218.70
RHS19	0.10	0.04	70.0		230.0		30	67.7	3.4	F	223.9

S - Squashing / L - Local / D - Distortional / F - Flexural / T - Torsional
 Note: bifurcation occurs for RHS14 at $N_{cr} = 87.1$ kN

US - Eindhoven												
Test	Imp.	Tensile test					Compression test					
		e	E	$f_{0,1}$	$f_{0,2}$	f_t	n	E_c	$\Delta\sigma$	N_{cr}	Mode	N_u
		mm	kN/mm ²	N/mm ²	N/mm ²	N/mm ²		kN/mm ²	N/mm ²	kN		kN
US01	0.07	69.2	202.2	206.2	228.8	35	68.8	2.5			L + T	30.96
US02	0.23	69.2	202.2	206.2	228.8	35	72.3	9.3	23.85		F	40.62
US04	0.16	69.2	202.2	206.2	228.8	35	67.6	5.5	24.89		L	40.84
US05	0.21	69.2	202.2	206.2	228.8	35	68.4	3.7			L + F	38.42
US06	0.09	69.2	202.2	206.2	228.8	35	68.7	14.5	27.06		L	39.03
US08	0.13	69.2	202.2	206.2	228.8	35	71.1	4.2	28.57		L	38.84
US10	0.12	69.2	202.2	206.2	228.8	35	67.2	5.9			L + F	43.07
US11	0.03	69.2	202.2	206.2	228.8	35	65.3	1.4			F	33.92
US13	0.04	66.6	191.6	195.0	217.0	40	67.6	4.0			F	52.36
US14	0.04	66.6	191.6	195.0	217.0	40	70.0	4.0			D + T	110.58
US17	0.31	66.6	191.6	195.0	217.0	40	65.5	11.5			D + T	71.11
US18	0.24	66.6	191.6	195.0	217.0	40	67.6	8.1			D + T	99.25
US20	0.07	66.6	191.6	195.0	217.0	40	69.8	9.8			D + T	98.55
US21	0.04	66.6	191.6	195.0	217.0	40	63.4	37.5			F	66.03
US22	0.04	66.6	191.6	195.0	217.0	40	62.8	6.4			F	92.36
US25	0.22	65.9	191.2	195.4	225.5	32	68.4	22.3			D + T	59.84
US26	0.31	65.9	191.2	195.4	225.5	32	68.8	14.8	59.30		L	74.11
US29	0.24	65.9	191.2	195.4	225.5	32	69.7	29.5			L	67.72
US30	0.15	65.9	191.2	195.4	225.5	32	65.2	30.5	61.59		L	71.52
US33	0.07	65.9	191.2	195.4	225.5	32	62.9	7.5			F	73.64
US34	0.09	65.9	191.2	195.4	225.5	32	61.9	10.5			L+F	77.29

S - Squashing / L - Local / D - Distortional / F - Flexural / T - Torsional

CS - Eindhoven													
Test	Imp.		Tensile test					Compression test					
	$e_{0,ov}$	$e_{0,loc}$	E	$f_{0,1}$	$f_{0,2}$	f_t	n	E_c	$\Delta\sigma$	Mode	N_{cr}	Mode	N_u
	mm	mm	kN/mm ²	N/mm ²	N/mm ²	N/mm ²		kN/mm ²	N/mm ²		kN		kN
CS01-1	0.10	0.01	64.8	215.0	221.9	247.9	22	63.6	2.19	L	22.67	F-T	33.82
CS01-2	0.10	0.01	64.8	215.0	221.9	247.9	22	64.1	4.87	L	23.62	F-T	36.46
CS02-1	0.04	0.06	65.5	217.2	223.7	249.6	24	63.6	0.83			F	65.61
CS02-2	0.04	0.06	65.5	217.2	223.7	249.6	24	63.2	3.06			L	65.42
CS02-3	0.04	0.06	65.5	217.2	223.7	249.6	24	64.7	3.05			F	64.77
CS02-4	0.04	0.06	65.5	217.2	223.7	249.6	24	63.1	0.97			F	64.48
CS03-1	0.05	0.00	64.4	201.9	204.7	216.7	50	60.4	6.97	L	32.23	L	68.38
CS03-2	0.05	0.00	64.4	201.9	204.7	216.7	50	66.5	7.01	L	29.69	L	68.65
CS03-3	0.05	0.00	64.4	201.9	204.7	216.7	50	62.3	2.70	L	31.23	L	66.60
CS04-1	0.02	0.02	65.2	233.7	239.0	262.2	31	59.7	25.48			F-T	36.07
CS04-2	0.02	0.02	65.2	233.7	239.0	262.2	31	61.9	11.54			F-T	34.92
CS04-3	0.02	0.02	65.2	233.7	239.0	262.2	31	65.2	4.90			L	29.83
CS04-4	0.02	0.02	65.2	233.7	239.0	262.2	31	70.7	19.56	L/T	18.58	L	21.84
CS05-1	0.12	0.10	64.6	211.9	215.2	230.3	45	64.8	1.79			D-F	39.33
CS05-2	0.12	0.10	64.6	211.9	215.2	230.3	45	63.1	19.34			D-F	37.98
CS05-3	0.12	0.10	64.6	211.9	215.2	230.3	45	63.7	5.46			D-F	39.32
CS06-1	0.30	0.04	65.3	198.5	203.4	225.5	28	66.1	6.63	L	29.00	F-T	43.24
CS06-2	0.30	0.04	65.3	198.5	203.4	225.5	28	62.2	6.66	L	26.60	F-T	40.51
CS06-3	0.30	0.04	65.3	198.5	203.4	225.5	28	59.6	11.98	L	26.38	F-T	38.66
CS06-4	0.30	0.04	65.3	198.5	203.4	225.5	28	59.7	7.06	FT	25.66	L	28.24
CS07-1	0.06	0.01	66.0	194.4	200.4	226.9	23	66.4	5.03			F	35.10
CS07-2	0.06	0.01	66.0	194.4	200.4	226.9	23	60.8	28.12	D	34.45	F	36.38
CS08-1	0.20	0.31	65.7	204.4	207.4	233.4	47	60.2	18.20			L	94.74
CS08-2	0.20	0.31	65.7	204.4	207.4	233.4	47	60.1	16.74			L	93.36
CS08-3	0.20	0.31	65.7	204.4	207.4	233.4	47	63.3	3.51			L	95.96
CS09-1	0.08	0.01	70.0		230.0		30	78.5	1.87	L	47.41	L	76.55
CS09-2	0.08	0.01	70.0		230.0		30	91.8	8.53	L	51.69	L	77.86
CS09-3	0.08	0.01	70.0		230.0		30	80.1	3.04	L	48.20	L	79.54
CS10-1	0.08	0.11	68.7	215.4	219.7	237.4	35	66.5	8.86	L	43.41	F	58.92
CS10-2	0.08	0.11	68.7	215.4	219.7	237.4	35	68.1	5.15	L	44.53	F	59.31
CS10-3	0.08	0.11	68.7	215.4	219.7	237.4	35	68.8	9.43	L	46.97	F	55.58
CS10-4	0.08	0.11	68.7	215.4	219.7	237.4	35	66.4	26.17	L	44.71	F	58.04
CS11-1	0.29	0.02	64.7	208.5	214.2	235.0	26	64.2	2.67	T	6.67	L	10.37
CS11-2	0.29	0.02	64.7	208.5	214.2	235.0	26	64.2	1.87	T	5.79	L	10.30
CS11-3	0.29	0.02	64.7	208.5	214.2	235.0	26	64.3	0.14	T	5.95	L	9.62
CS11-4	0.29	0.02	64.7	208.5	214.2	235.0	26	63.9	3.82	T	5.75	L	8.76
CS12-1	0.08	0.11	63.8	184.9	188.4	214.8	36	62.3	19.51	L	13.11	D	30.20
CS12-2	0.08	0.11	63.8	184.9	188.4	214.8	36	48.9	25.16	L	10.87	D	29.60
CS12-3	0.08	0.11	63.8	184.9	188.4	214.8	36	62.9	10.97	L	12.24	D	28.74
CS12-4	0.08	0.11	63.8	184.9	188.4	214.8	36	64.0	19.02	L	12.36	D	27.77

S - Squashing / L - Local / D - Distortional / F - Flexural / T - Torsional

B.4 Numerical results

RHS - Eindhoven													
Test	FE					Exp					FE / Exp		
	E_c kN/mm ²	Mode	N_{cr} kN	Mode	N_u kN	E_c kN/mm ²	$\Delta\sigma$ N/mm ²	Mode	N_{cr} kN	Mode	N_u kN	Bif.	Fail.
RHS01						69.9	29.0			S	130.05		
RHS02						68.6	8.1			S	129.67		
RHS04						67.1	12.3			S	125.08		
RHS05	65.3	L	600.32	S	121.48	67.9	12.0			S	128.52		0.95
RHS06	66.4	L	92.479	L	86.946	70.8	6.8			L	83.80		1.04
RHS07	66.4	L	89.64	L	84.92	70.6	19.9			L	82.21	1.09	1.03
RHS08	67.1	L	87.025	L	83.123	69.5	14.5			L	86.51	1.01	0.96
RHS09	66.3	L	82.972	L/F	82.972	70.0	5.8			L/F	84.23	0.99	0.99
RHS10	66.4	L	216.1	L	172.43	68.0	8.8			L	173.28		1.00
RHS11	66.5	L	210.56	L	164.62	67.7	23.4			L	159.76		1.03
RHS12	67.5	L	190.21	L/F	163.77	69.4	0.6			L/F	167.19		0.98
RHS13	67.5	F	163.62	F	141.38	74.2	15.8			L/F	173.30	0.94	0.82
RHS14	64.1	L	78.669	L/F	131.69	65.1	3.3	L	87.12	F	117.64	0.90	1.12
RHS15						70.1	3.4			F	85.22		
RHS16						71.0	8.0			L/F	80.88		
RHS17						68.8	5.9			S	218.70		
RHS19						67.7	3.4			F	223.90		

S - Squashing / L - Local / D - Distortional / F - Flexural / T - Torsional

US - Eindhoven													
Test	FE					Exp					FE / Exp		
	E_c kN/mm ²	Mode	N_{cr} kN	Mode	N_u kN	E_c kN/mm ²	$\Delta\sigma$ N/mm ²	Mode	N_{cr} kN	Mode	N_u kN	Bif.	Fail.
US01	69.3	L	78.38	F	29.359	68.8	2.5			L + T	30.96		0.95
US02	62.4	L	23.55	L	40.008	72.3	9.3	L	23.85	F	40.62	0.99	0.98
US04	63.2	L	24.41	L	40.313	67.6	5.5	L	24.89	L	40.84	0.98	0.99
US05	69.1	L	52.51	L	35.059	68.4	3.7			L + F	38.42		0.91
US06	69.2	L	28.70	L	38.051	68.7	14.5	L	27.06	L	39.03	1.06	0.98
US08	68.9	L	26.39	L	36.381	71.1	4.2	L	28.57	L	38.84	0.92	0.94
US10	69.3	L	43.03	L	38.792	67.2	5.9			L + F	43.07	1.00	0.90
US11	69.5	F	37.05	F	33.54	65.3	1.4			F	33.92	1.09	0.99
US13	66.6	F	211.98	F	51.184	67.6	4.0			F	52.36		0.98
US14	66.7	L	166.77	L/T	108.16	70.0	4.0			D + T	110.58		0.98
US17	66.7	T	285.87	T	66.982	65.5	11.5			D + T	71.11		0.94
US18	66.7	L	210.53	L	95.71	67.6	8.1			D + T	99.25		0.96
US20	66.8	L	204.96	L/T	96.157	69.8	9.8			D + T	98.55		0.98
US21	51.0	F	103.17	F	65.722	63.4	37.5			F	66.03		1.00
US22	66.9	L	300.98	L/F	89.357	62.8	6.4			F	92.36		0.97
US25	66.0	L	147.19	L/T	56.167	68.4	22.3			D + T	59.84		0.94
US26	65.2	L	58.52	L	72.803	68.8	14.8	L	59.30	L	74.11	0.99	0.98
US29	66.1	L	106.02	L	64.361	69.7	29.5			L	67.72		0.95
US30	66.1	L	67.16	L	69.652	65.2	30.5	L	61.59	L	71.52	1.09	0.97
US33	66.3	L/F	90.77	L/F	67.097	62.9	7.5			F	73.64		0.91
US34	65.8	L	92.15	L/F	75.489	61.9	10.5			L+F	77.29		0.98

S - Squashing / L - Local / D - Distortional / F - Flexural / T - Torsional

CS - Eindhoven

Test	FE						Exp				FE / Exp		
	Mode	N_{cr} kN	Mode	N_U kN	N_t kN	E_c kN/mm ²	$\Delta\sigma$ N/mm ²	Mode	N_{cr} kN	Mode	N_U kN	Bif.	Fail.
AL01-1	L	22.68	FT	32.89		63.6	2.2	L	22.67	F-T	33.82	1.00	0.97
AL01-2	L	22.68	FT	32.89		64.1	4.9	L	23.62	F-T	36.46	0.96	0.90
AL02-1	L	75.97	L	67.90		63.6	0.8			F	65.61		1.03
AL02-2	L	75.97	L	67.90		63.2	3.1			L	65.42		1.04
AL02-3	L	75.63	L	66.74		64.7	3.0			F	64.77		1.03
AL02-4	L	75.63	L	66.74		63.1	1.0			F	64.48		1.03
AL03-1	L	32.79	L	73.45		60.4	7.0	L	32.23	L	68.38	1.02	1.07
AL03-2	L	32.79	L	73.45		66.5	7.0	L	29.69	L	68.65	1.10	1.07
AL03-3	L	32.45	L	71.98		62.3	2.7	L	31.23	L	66.60	1.04	1.08
AL04-1	L	30.89	L	39.06		59.7	25.5			F-T	36.07	0.86	1.08
AL04-2	L	30.89	L	35.69		61.9	11.5			F-T	34.92	0.88	1.02
AL04-3	FT	29.83	FT	28.10		65.2	4.9			L	29.83	1.00	0.94
AL04-4	FT	20.11	FT	23.63	21.69	70.7	19.6	L/T	18.58	L	21.84	1.08	0.99
AL05-1	D	45.86	D	38.38		64.8	1.8			D-F	39.33		0.98
AL05-2	D	45.86	D	38.38		63.1	19.3			D-F	37.98		1.01
AL05-3	D	43.11	D	37.24		63.7	5.5			D-F	39.32	1.10	0.95
AL06-1	L	29.93	L	44.45		66.1	6.6	L	29.00	F-T	43.24	1.03	1.03
AL06-2	L	29.76	L	43.50		62.2	6.7	L	26.60	F-T	40.51	1.12	1.07
AL06-3	L	29.61	L	40.92		59.6	12.0	L	26.38	F-T	38.66	1.12	1.06
AL06-4	FT	28.84	FT	32.12	28.83	59.7	7.1	FT	25.66	L	28.24	1.12	1.02
AL07-1	D	42.03	F	37.48		66.4	5.0			F	35.10		1.07
AL07-2	D	42.03	F	37.48		60.8	28.1	D	34.45	F	36.38	1.22	1.03
AL08-1	L	95.38	L	95.62		60.2	18.2			L	94.74	1.01	1.01
AL08-2	L	95.38	L	95.62		60.1	16.7			L	93.36	1.02	1.02
AL08-3	L	94.65	L	95.52		63.3	3.5			L	95.96	0.99	1.00
AL09-1						78.5	1.9	L	47.41	L	76.55		
AL09-2						91.8	8.5	L	51.69	L	77.86		
AL09-3						80.1	3.0	L	48.20	L	79.54		
AL10-1	L	44.18	L	61.39		66.5	8.9	L	43.41	F	58.92	1.02	1.04
AL10-2	L	44.18	L	61.39		68.1	5.1	L	44.53	F	59.31	0.99	1.04
AL10-3	L	43.83	L	59.81		68.8	9.4	L	46.97	F	55.58	0.93	1.08
AL10-4	L	43.76	L	58.13		66.4	26.2	L	44.71	F	58.04	0.98	1.00
AL11-1	T	6.71	T	10.66		64.2	2.7	T	6.67	L	10.37	1.01	1.03
AL11-2	T	6.12	T	10.29	10.28	64.2	1.9	T	5.79	L	10.30	1.06	1.00
AL11-3	T	5.92	T	9.61	9.54	64.3	0.1	T	5.95	L	9.62	1.00	0.99
AL11-4	T	5.72	T	8.63	8.43	63.9	3.8	T	5.75	L	8.76	0.99	0.96
AL12-1	L	13.69	D	29.17	28.53	62.3	19.5	L	13.11	D	30.20	1.04	0.94
AL12-2	L	14.79	L	35.03	33.47	48.9	25.2	L	10.87	D	29.60	1.36	1.13
AL12-3	L	13.57	D	28.76		62.9	11.0	L	12.24	D	28.74	1.11	1.00
AL12-4	L	13.50	D	28.24		64.0	19.0	L	12.36	D	27.77	1.09	1.02

S - Squashing / L - Local / D - Distortional / F - Flexural / T - Torsional

B.5 Results prediction model

RHS - Eindhoven													
Test	Material			Input					Results		pm / exp		
	E kN/mm ²	$f_{0.2}$ N/mm ²	n -	A_1 mm ²	A_2 mm ²	σ_{cr} N/mm ²	Mode	$\sigma_{cr,2}$ N/mm ²	Mode	N_{cr} kN	N_u kN	N_{cr} -	N_u -
RHS01	70.0	230.0	30	274.6	283.7	995.8		1016		121.8	121.8	0.94	0.94
RHS02	70.0	230.0	30	274.4	282.1	992.3		1017		121.4	121.4	0.94	0.94
RHS04	70.0	230.0	30	290.5	296.1	1115.3		1117		128.7	128.7	1.03	1.03
RHS05	65.4	198.5	28	289.6	297.1	1025.1	L	1159	S	111.4	111.4	0.87	
RHS06	70.0	230.0	30	297.5	155.9	204.0	L	872	L	87.4	87.4	1.04	1.04
RHS07	70.0	230.0	30	297.6	157.9	205.2	L	898	L	87.9	87.9	1.07	1.07
RHS08	66.5	231.5	32	302.0	149.1	192.9	L	860	L	86.9	86.9	1.00	1.00
RHS09	66.5	231.5	32	295.8	148.3	186.5	L	768	L/F	82.8	82.8	0.98	0.98
RHS10	66.6	230.5	34	549.6	265.9	265.0	L	1091	L	162.2	162.2	0.94	0.94
RHS11	66.6	230.5	34	544.0	269.0	260.5	L	1120	L	161.4	161.4	1.01	1.01
RHS12	67.6	233.1	30	686.1	172.6	221.5	L	5356	L/F	169.1	169.1	1.01	1.01
RHS13	67.6	233.1	30	690.7	167.5	220.1	F	5175	F	168.9	168.9	0.97	0.97
RHS14	70.0	230.0	30	765.5	184.7	82.8	L	1835	L/F	78.7	111.7	0.95	0.95
RHS15	66.4	191.0	39	428.2	78.0	182.0		10768		81.7	81.7	0.96	0.96
RHS16	66.4	191.0	39	427.8	85.1	189.2		11022		83.2	83.2	1.03	1.03
RHS19	70.0	230.0	30	738.0	283.4	549.2		4858		215.4	215.4	0.96	0.96

S - Squashing / L - Local / D - Distortional / F - Flexural / T - Torsional

US - Eindhoven													
Test	Material			Input					Results		pm / exp		
	E kN/mm ²	$f_{0.2}$ N/mm ²	n -	A_1 mm ²	A_2 mm ²	σ_{cr} N/mm ²	Mode	$\sigma_{cr,2}$ N/mm ²	Mode	N_{cr} kN	N_u kN	N_{cr} -	N_u -
US01	69.2	206.2	35	77.20	71.75	526.2	L	1248.3	F	28.3	28.3		0.91
US02	69.2	206.2	35	231.34	76.50	76.5	L	1076.9	L	23.5	36.4	0.99	0.90
US04	69.2	206.2	35	234.38	76.04	78.6	L	1123.4	L	24.4	37.0		0.91
US05	69.2	206.2	35	77.98	112.70	275.4	L	1272.3	L	34.4	34.4		0.90
US06	69.2	206.2	35	192.42	76.40	106.7	L	1146.7	L	28.7	35.2	1.06	0.90
US08	69.2	206.2	35	187.09	73.76	101.2	L	1069.3	L	26.4	33.6	0.92	0.86
US10	69.2	206.2	35	152.35	92.28	175.9	L	272.9	L	42.1	42.1		0.98
US11	69.2	206.2	35	156.16	54.76	175.6	F	287.4	F	36.3	36.3		1.07
US13	66.6	195.0	40	144.92	132.05	765.4	F	5238.0	F	51.0	51.0		0.97
US14	66.6	195.0	40	440.32	142.28	286.2	L	4553.3	L/T	100.3	100.3		0.91
US17	66.6	195.0	40	144.08	212.92	800.8	T	5194.7	T	65.9	65.9		0.93
US18	66.6	195.0	40	372.71	141.84	409.2	L	4857.2	L	91.2	91.2		0.92
US20	66.6	195.0	40	372.55	140.48	399.5	L	4710.5	L/T	90.8	90.8		0.92
US21	66.6	195.0	40	296.05	95.24	263.7	F	1111.9	F	66.9	66.9		1.01
US22	66.6	195.0	40	301.04	173.52	634.2	L	1143.0	L/F	86.5	86.5		0.94
US25	65.9	195.4	32	137.74	156.22	500.7	L	1597.7	L/T	52.9	52.9		0.88
US26	65.9	195.4	32	387.25	138.36	111.3	L	1448.2	L	58.5	66.9	0.99	0.90
US29	65.9	195.4	32	138.39	214.46	300.5	L	1570.6	L	61.1	61.1		0.90
US30	65.9	195.4	32	330.39	137.29	143.6	L	1411.1	L	67.2	67.2	1.09	0.94
US33	65.9	195.4	32	284.77	102.11	234.6	L/F	378.9	L/F	65.5	65.5		0.89
US34	65.9	195.4	32	261.79	161.45	217.7	L	323.3	L/F	71.1	71.1		0.92

S - Squashing / L - Local / D - Distortional / F - Flexural / T - Torsional

CS - Eindhoven															
Test	Material			Input						Results				pm / exp	
	E	$f_{0.2}$	n	A_1	A_2	σ_{cr}	Mode	$\sigma_{cr,2}$	Mode	N_{cr}	N_u	N_{cr}	N_u	-	-
	kN/mm ²	N/mm ²	-	mm ²	mm ²	N/mm ²		N/mm ²		kN	kN	-	-		
CS01-1	64.8	221.9	22	82.5	186.7	84.3	L	188.3	FT	22.7	38.8	1.00	1.15		
CS01-2	64.8	221.9	22	82.5	186.7	84.3	L	188.3	FT	22.7	38.8	0.96	1.06		
CS02-1	65.5	223.7	24	144.3	224.3	206.2	L	512.1	L	65.2	65.2	0.00	0.99		
CS02-2	65.5	223.7	24	144.3	224.3	206.2	L	512.1	L	65.2	65.2	0.00	1.00		
CS02-3	65.5	223.7	24	144.3	224.3	205.2	L	512.1	L	65.1	65.1	0.00	1.01		
CS02-4	65.5	223.7	24	144.3	224.3	205.2	L	512.1	L	65.1	65.1	0.00	1.01		
CS03-1	64.4	204.7	50	35.8	298.6	98.1	L	158.9	L	32.8	47.1	1.02	0.69		
CS03-2	64.4	204.7	50	35.8	298.6	98.1	L	158.9	L	32.8	47.1	1.10	0.69		
CS03-3	64.4	204.7	50	35.8	298.6	97.0	L	158.9	L	32.5	47.1	1.04	0.71		
CS04-1	65.2	239.0	31	185.4	0.0	220.0	L	320.7	L	37.3	37.3	0.00	1.03		
CS04-2	65.2	239.0	31	43.1	161.7	150.9	L	320.7	L	30.9	33.9	0.00	0.97		
CS04-3	65.2	239.0	31	204.8	0.0	145.7	FT	-	FT	29.8	32.0	0.00	1.00		
CS04-4	65.2	239.0	31	204.8	0.0	98.2	FT	-	FT	20.1	27.1	1.08	0.92		
CS05-1	64.6	215.2	45	259.3	0.0	176.9	D	-	D	45.9	45.9	0.00	1.17		
CS05-2	64.6	215.2	45	259.3	0.0	176.9	D	-	D	45.9	45.9	0.00	1.21		
CS05-3	64.6	215.2	45	259.3	0.0	166.3	D	-	D	43.1	43.1	0.00	1.10		
CS06-1	65.3	203.4	28	56.5	251.6	97.1	L	-	L	29.9	42.6	1.03	0.98		
CS06-2	65.3	203.4	28	56.5	251.6	96.6	L	-	L	29.8	42.6	1.12	1.05		
CS06-3	65.3	203.4	28	56.5	251.6	96.1	L	-	L	29.6	42.6	1.12	1.10		
CS06-4	65.3	203.4	28	308.1	0.0	93.6	FT	-	FT	28.8	43.9	1.12	1.02		
CS07-1	66.0	200.4	23	109.3	255.2	115.3	D	-	F	42.0	49.3	0.00	1.20		
CS07-2	66.0	200.4	23	109.3	255.2	115.3	D	-	F	42.0	49.3	1.22	1.16		
CS08-1	65.7	207.4	47	134.5	230.1	141.3	L	119.2	L	95.4	96.7	0.00	1.02		
CS08-2	65.7	207.4	47	134.5	230.1	138.7	L	119.2	L	95.4	97.6	0.00	1.05		
CS08-3	65.7	207.4	47	134.5	230.1	140.2	L	119.2	L	94.7	96.3	0.00	1.00		
CS10-1	68.7	219.7	35	249.5	83.5	115.3	L	354.8	L	44.2	52.5	1.02	0.89		
CS10-2	68.7	219.7	35	249.5	83.5	115.3	L	354.8	L	44.2	52.5	0.99	0.89		
CS10-3	68.7	219.7	35	249.5	83.5	114.3	L	354.8	L	43.8	52.3	0.93	0.94		
CS10-4	68.7	219.7	35	249.5	83.5	114.2	L	354.8	L	43.8	52.3	0.98	0.90		
CS11-1	64.7	214.2	26	34.0	47.1	82.3	T	115.0	T	6.7	10.2	1.01	0.99		
CS11-2	64.7	214.2	26	34.0	47.1	75.1	T	108.2	T	6.1	9.9	1.06	0.96		
CS11-3	64.7	214.2	26	34.0	47.1	72.6	T	107.0	T	5.9	9.9	1.00	1.02		
CS11-4	64.7	214.2	26	34.0	47.1	70.2	T	106.6	T	5.7	9.8	0.99	1.12		
CS12-1	63.8	188.4	36	285.3	0.0	48.0	L	-	D	13.7	25.2	1.04	0.84		
CS12-2	63.8	188.4	36	285.3	0.0	51.8	L	150.1	L	14.8	31.8	1.36	1.08		
CS12-3	63.8	188.4	36	285.3	0.0	47.5	L	-	D	13.6	25.2	1.11	0.88		
CS12-4	63.8	188.4	36	285.3	0.0	47.3	L	-	D	13.5	25.1	1.09	0.91		

S - Squashing / L - Local / D - Distortional / F - Flexural / T - Torsional

Appendix C - Comparison of experimental, numerical and predicted results

This appendix presents the results of the experiments, finite element analyses, as well as those of the prediction model by in diagram form. These diagrams show the influence of the type of buckling (as explained in the main text) as well as the influence of material characteristic.

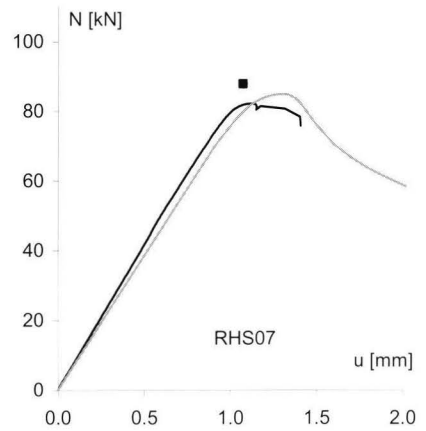
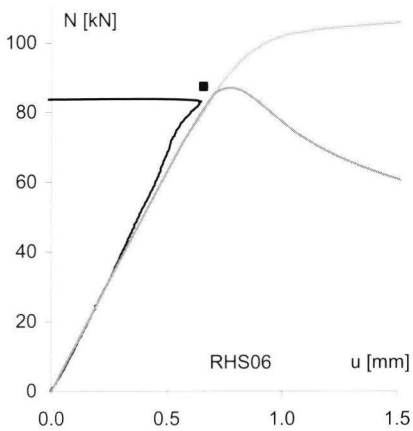
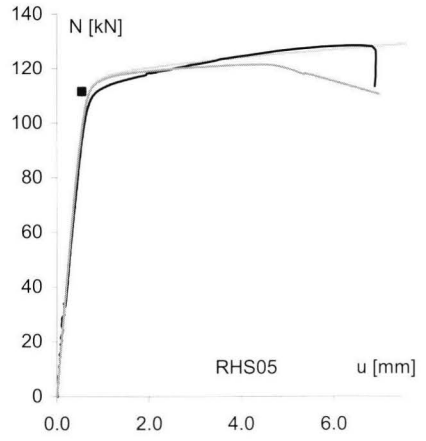
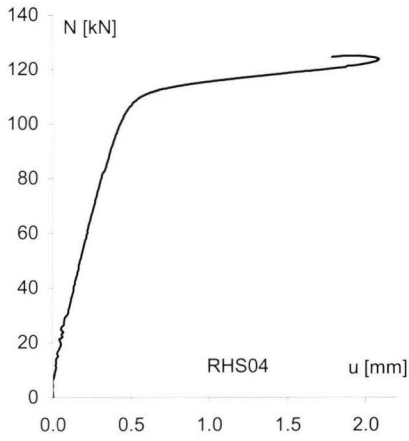
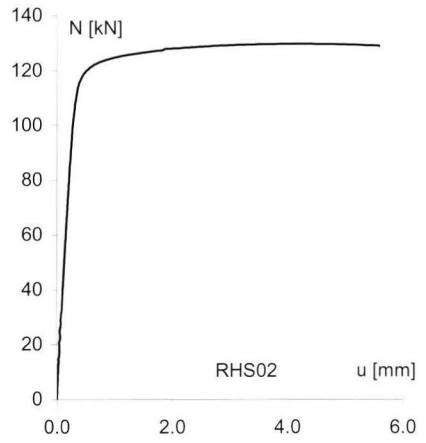
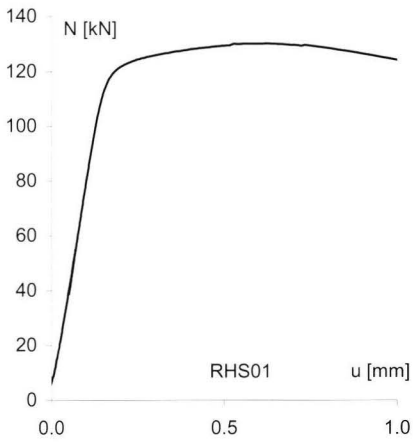
Each of the diagrams presents the results of each test specimens (RHS, US, and CS) of the Eindhoven program. The diagrams relate the axial resistance N (kN) to the axial shortening u (mm). The diagrams consist of the following components:

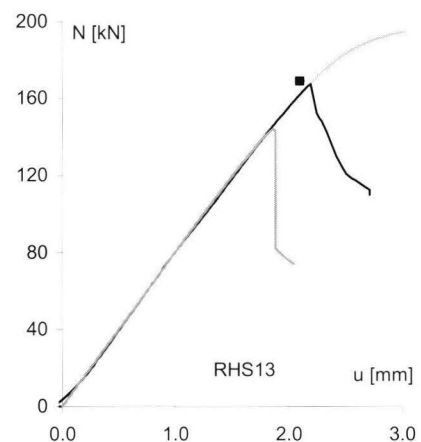
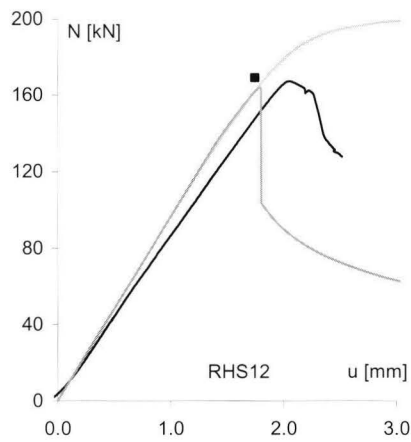
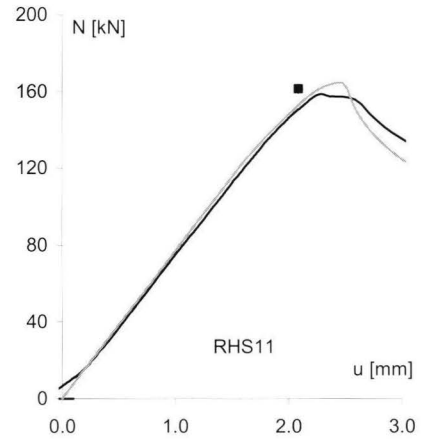
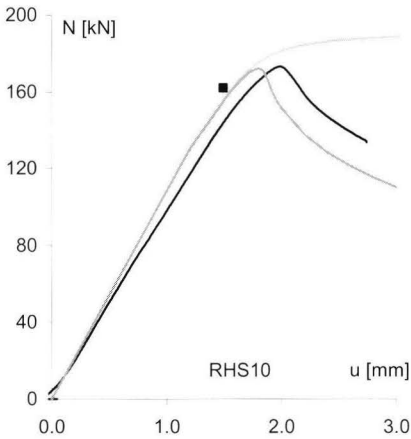
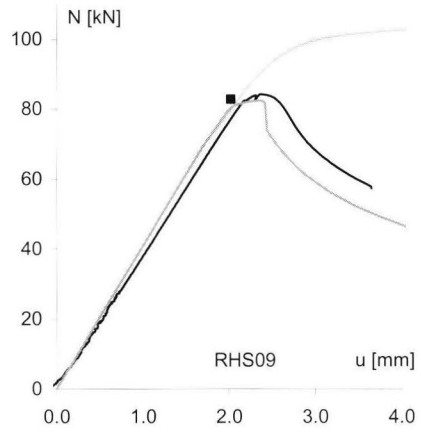
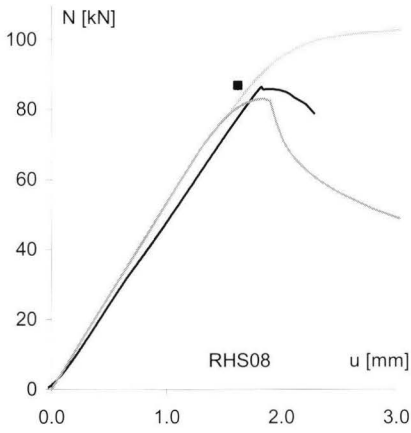
- The stress-strain results of the tensile tests (in light grey) have been scaled to a load-displacement curve by means of the measured cross-sectional area and axial length ($N = A \cdot \sigma$ and $u = L \cdot \varepsilon$)
- The experimentally measured load-displacement curves are presented in black.
- The results of the FE-analyses are presented in dark grey.
- The predicted value of initial buckling: $N_{cr;T} = A \cdot \sigma_{cr;T}$ and $u_{cr;T} = L \cdot \sigma_{cr} / E$, is presented by a block.
- The predicted axial resistance at the proportional limit: $N_{pm}(\varepsilon)$ and $u_p = L \cdot \varepsilon_p$, is presented by a diamond.

Notes:

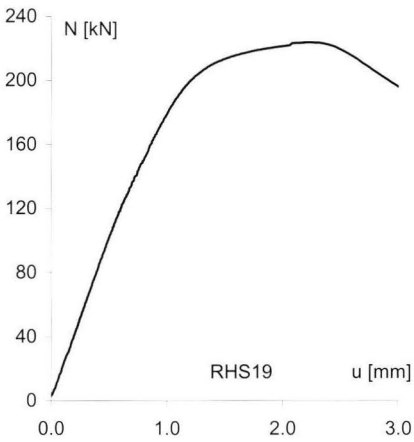
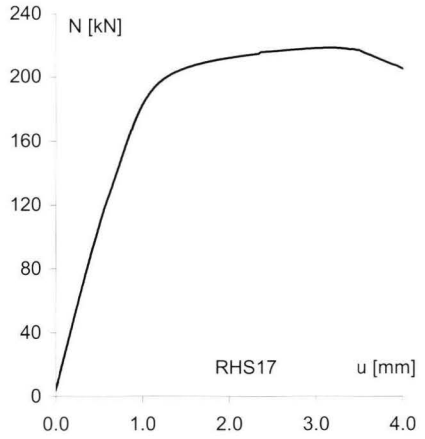
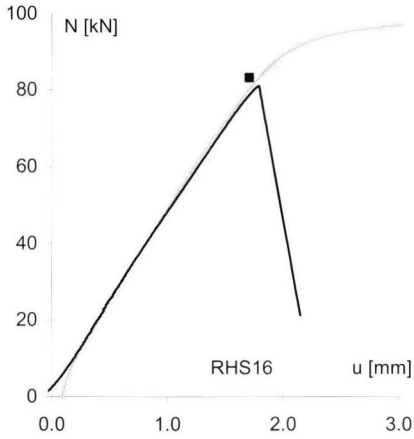
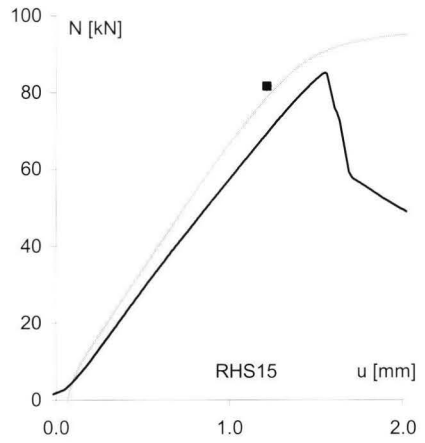
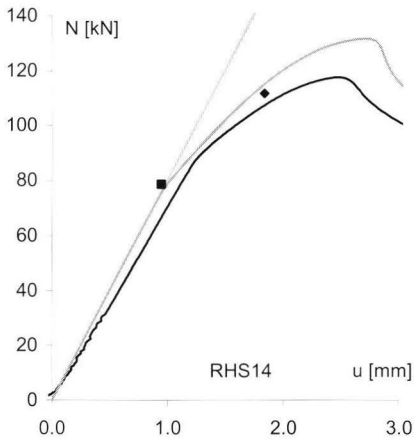
In case of inaccurate tensile tests, neither the results of the material nor those of the prediction model are presented.

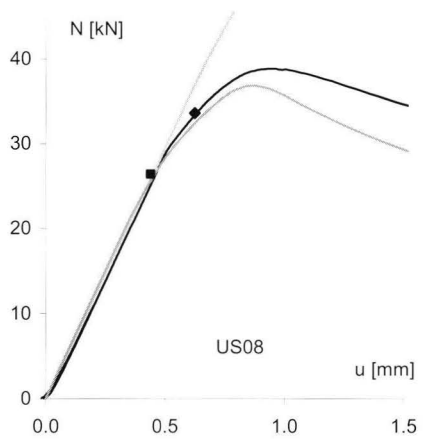
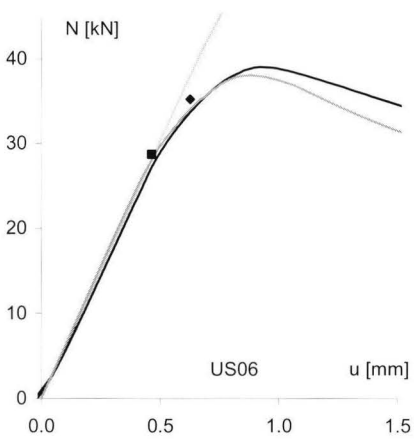
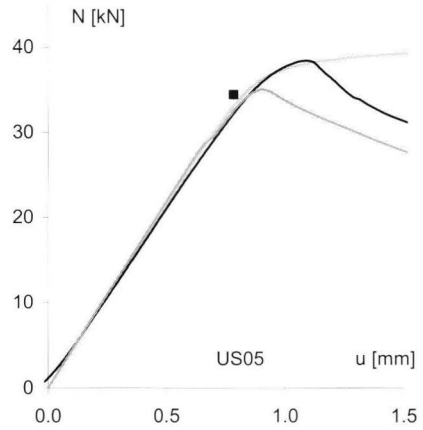
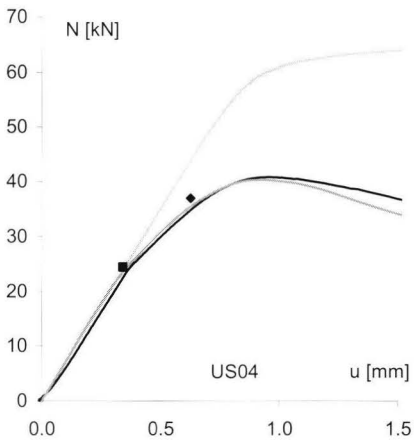
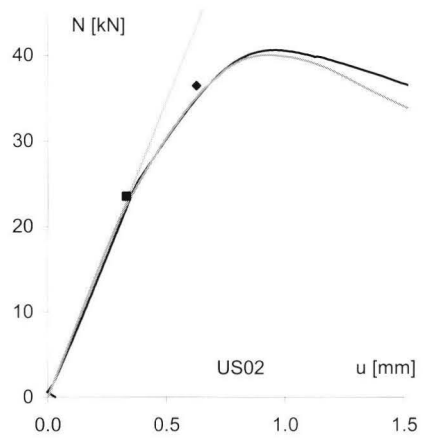
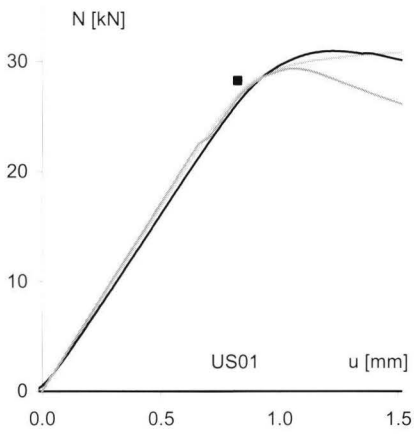
Comparison of experimental, numerical and predicted results



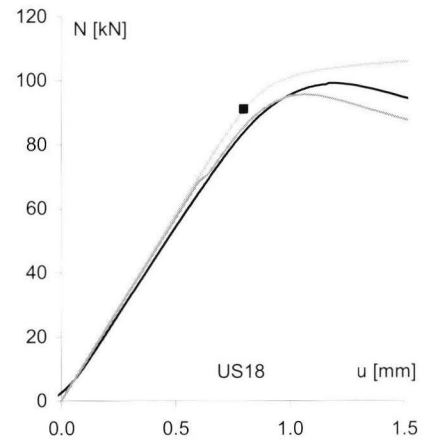
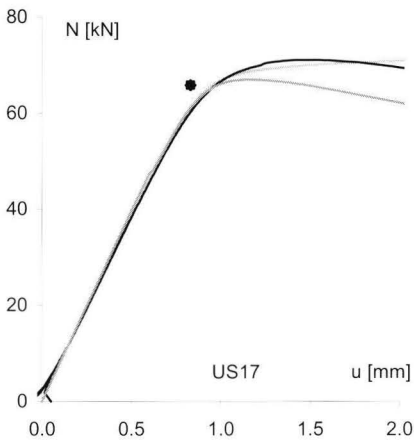
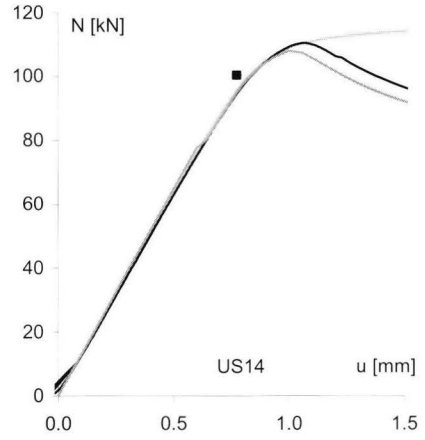
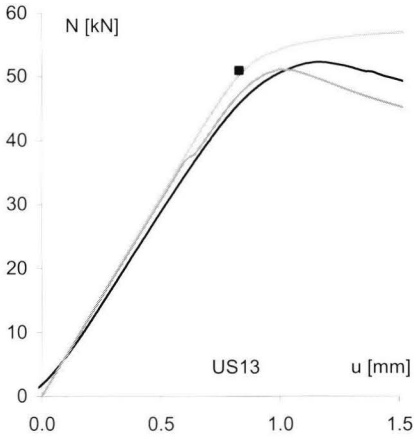
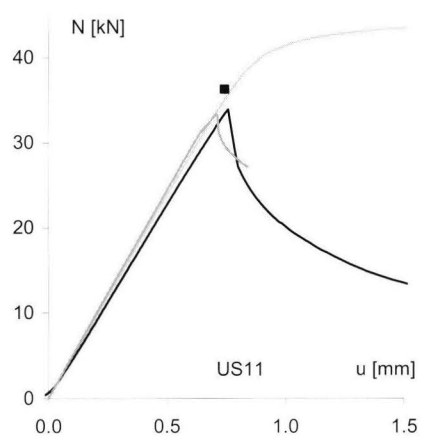
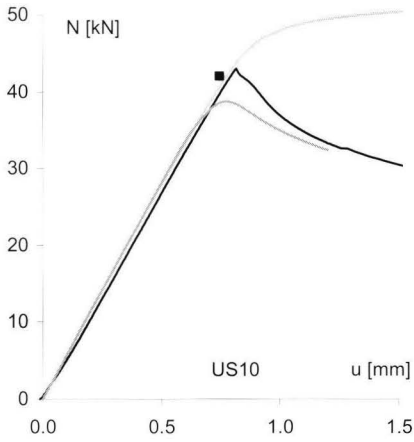


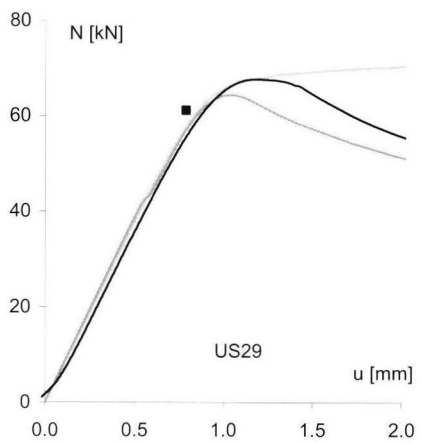
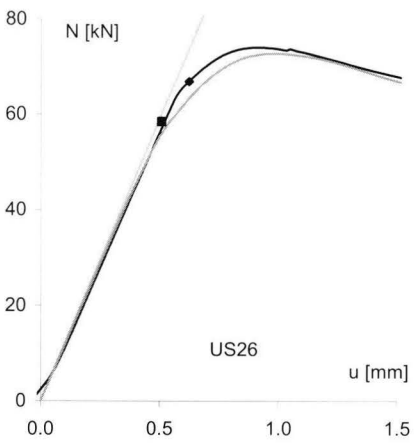
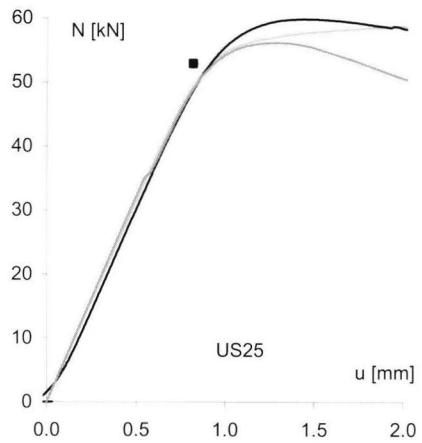
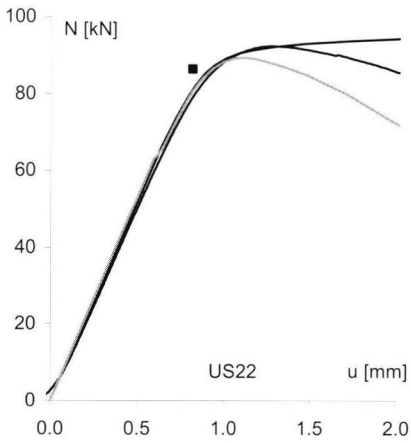
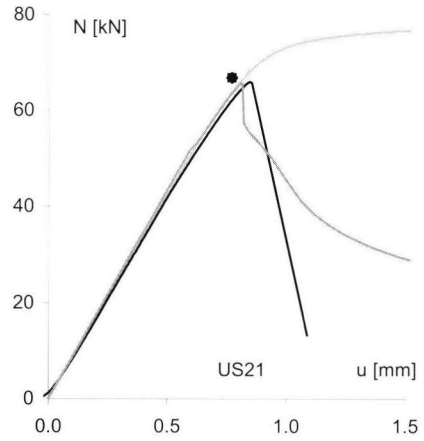
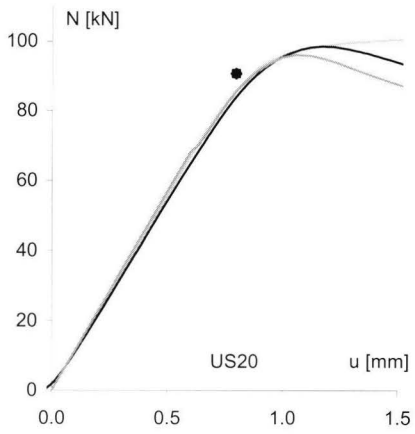
Comparison of experimental, numerical and predicted results



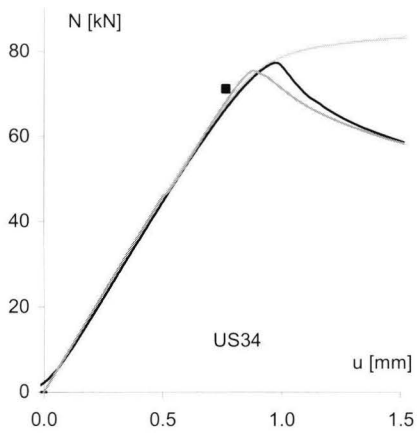
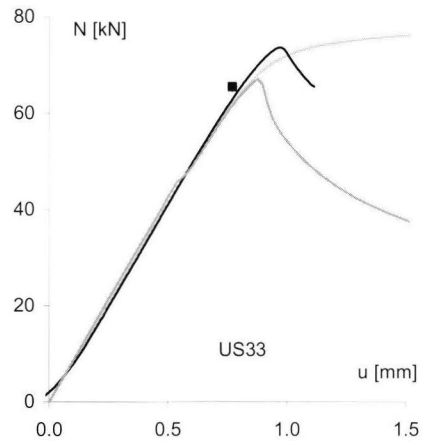
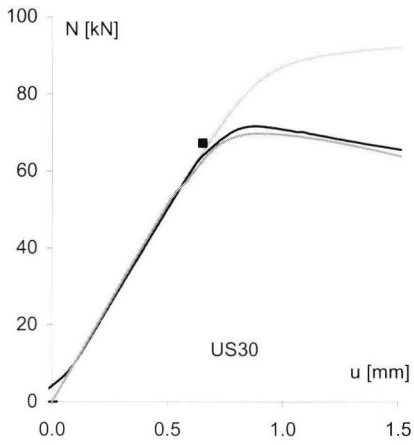


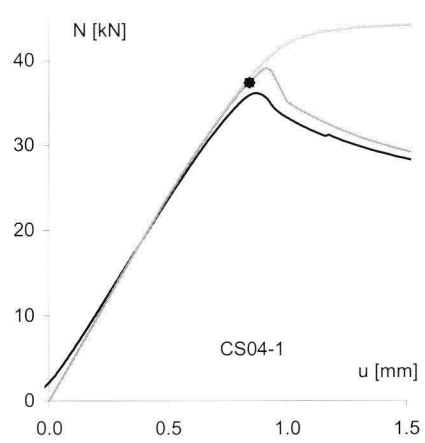
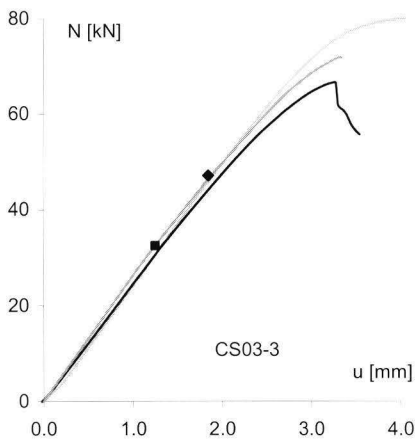
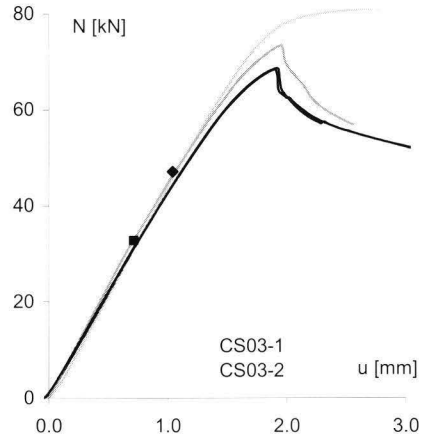
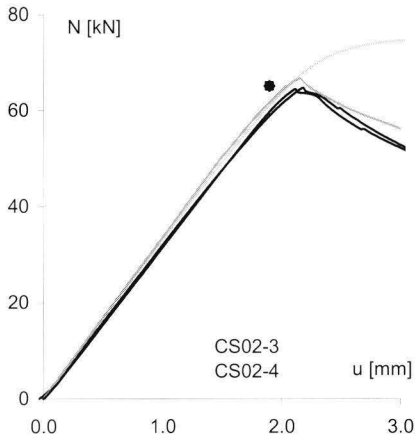
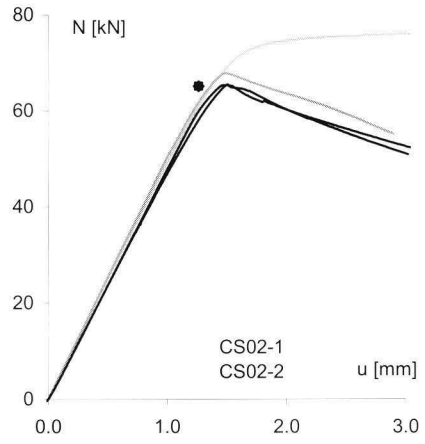
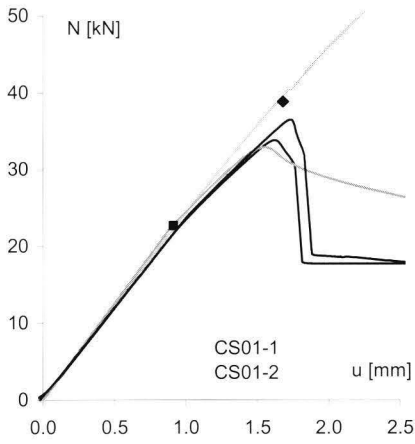
Comparison of experimental, numerical and predicted results



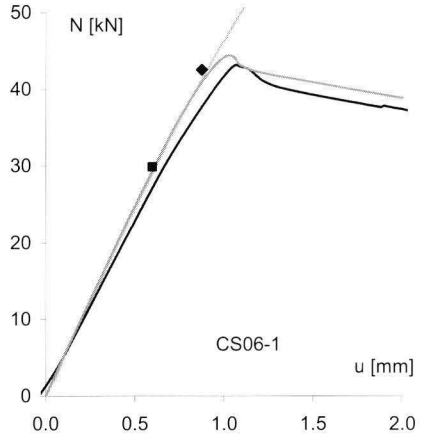
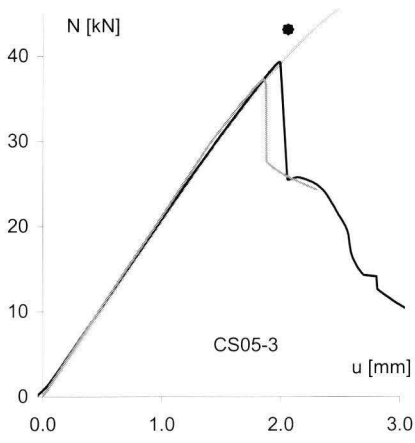
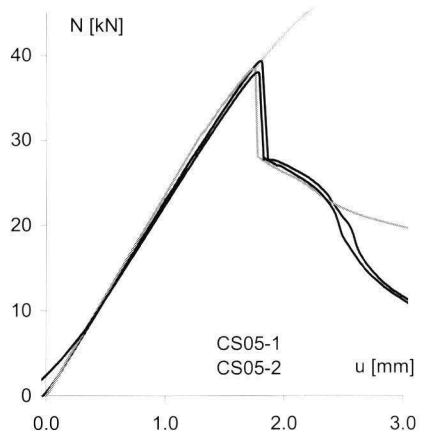
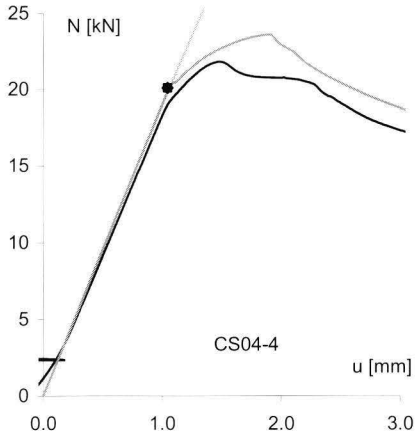
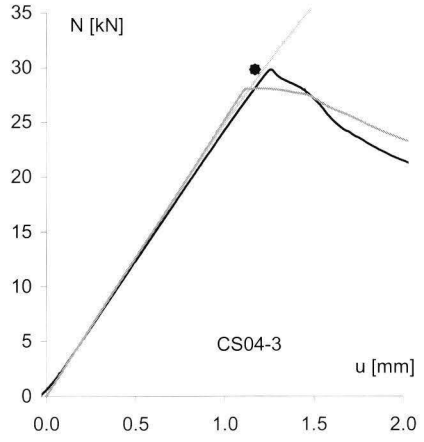
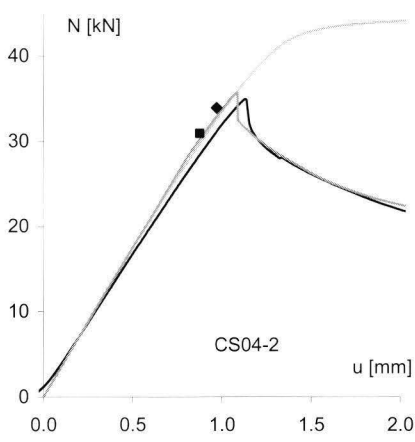


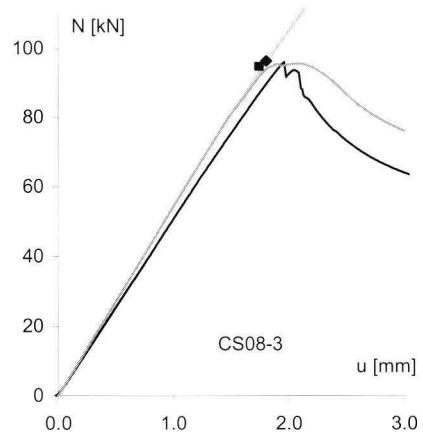
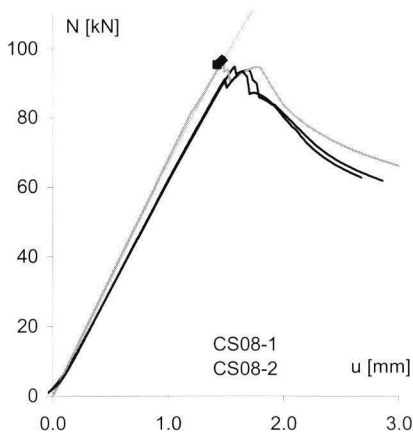
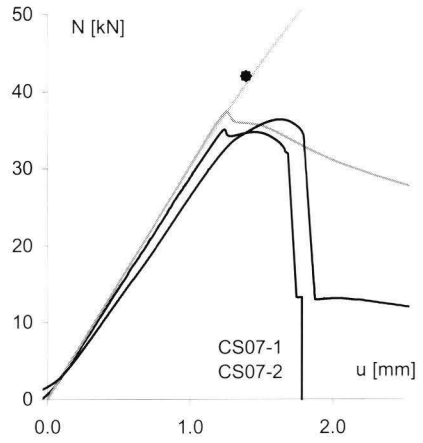
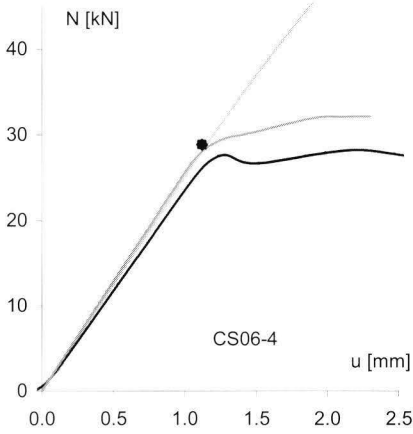
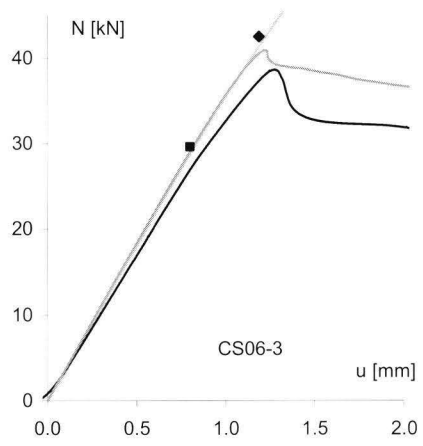
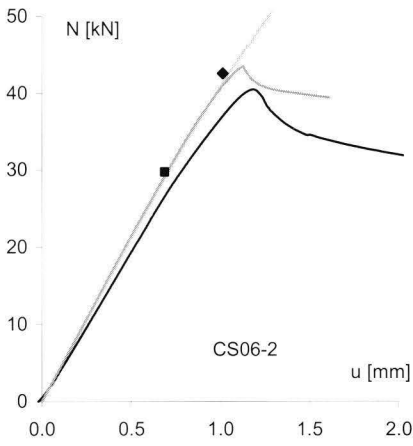
Comparison of experimental, numerical and predicted results



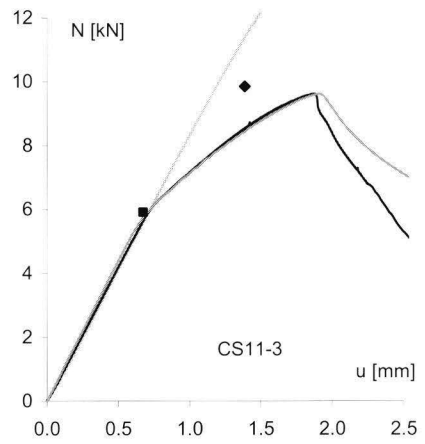
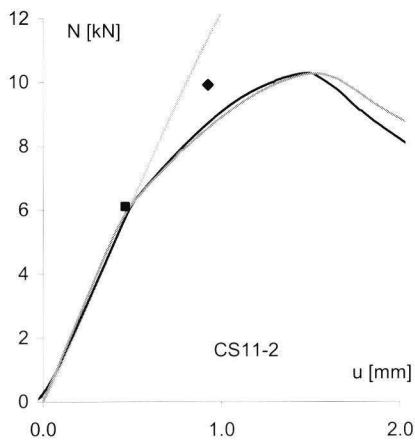
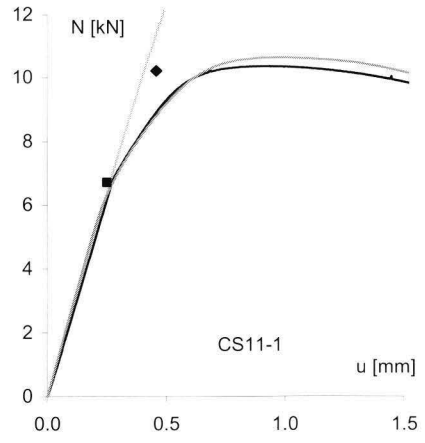
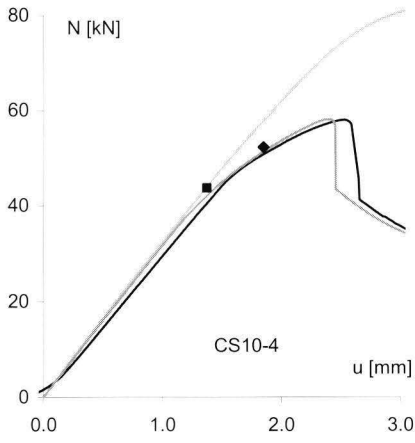
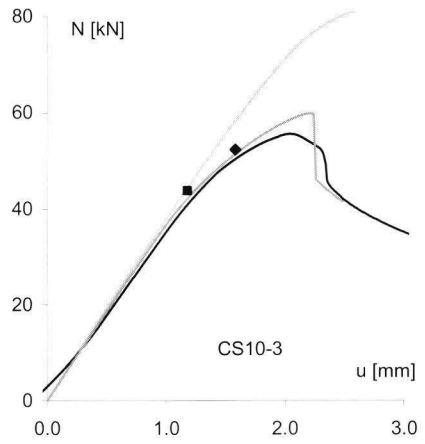
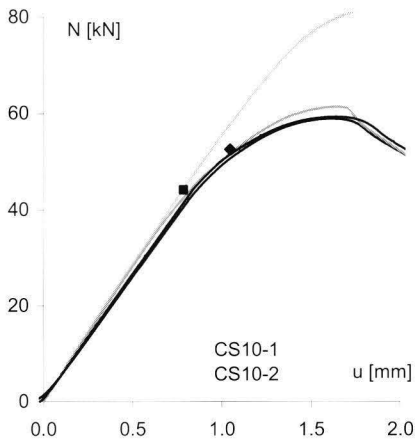


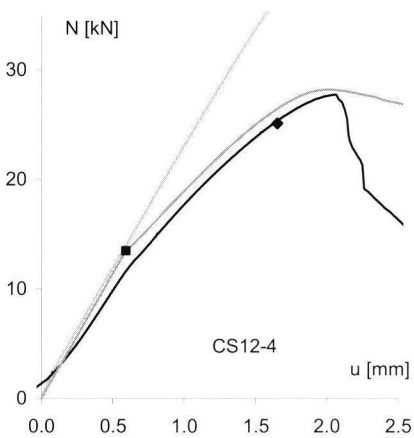
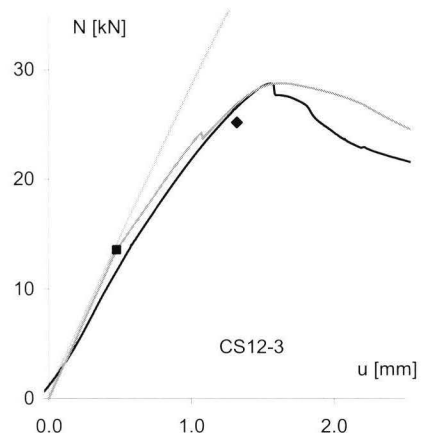
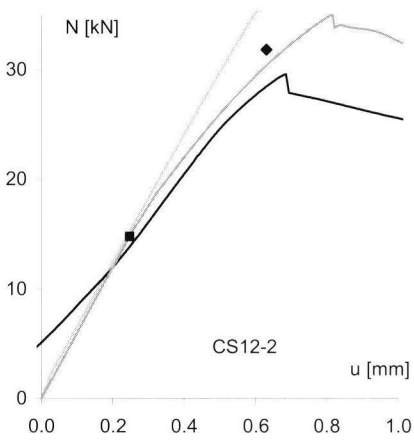
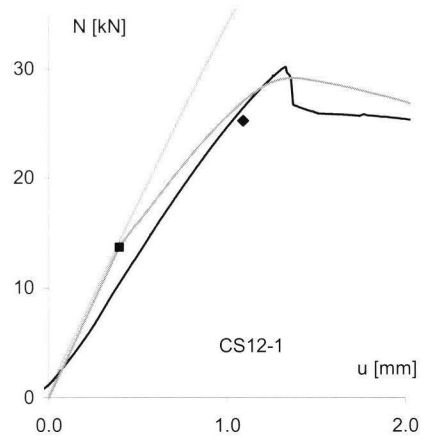
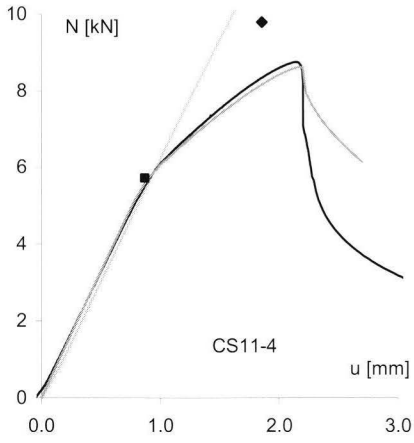
Comparison of experimental, numerical and predicted results





Comparison of experimental, numerical and predicted results





Samenvatting

Constructief toegepaste aluminium extrusieprofielen zijn vaak dunwandig en complex van vorm. Hierbij is de vorm van de doorsneden gebaseerd op een groot aantal vaak niet-constructieve eisen. Dit heeft tot gevolg dat instabiliteit kan optreden door verschillende knikvormen, plooi, distortional buckling, alsook diverse interactievormen. Bestaand onderzoek naar knik is meestal gericht op het gedrag van simpele symmetrische profielen. Plooi en distortional buckling worden beschouwd door de doorsnede op te knippen in losse plaatdelen. Aangezien plaatinteractie bepalend is, is het zeer de vraag of de resulterende rekenregels een nauwkeurige voorspelling geven van het daadwerkelijke gedrag van willekeurige (complexe) doorsneden. Daar komt bij dat het voorspelde bezwijkfenomeen niet overeen hoeft te komen met het daadwerkelijke. Hierdoor is het mogelijk dat de huidige rekenregels voor complexe doorsneden overmatig conservatief zijn, of tot onveilige resultaten leiden.

Om een beter inzicht te verkrijgen in het daadwerkelijke stabiliteitsgedrag van complexe aluminium profielen is een uitgebreid experimenteel onderzoek uitgevoerd op de Technische Universiteit Eindhoven. Dit onderzoek bestaat uit axiale drukproeven op rechthoekige buizen, U-profielen en complexe doorsneden. Hierbij is specifiek gekeken naar de invloed van de proefopstelling, initiële imperfecties en de materiaalkarakteristiek. Dit heeft geresulteerd in een omvangrijke set experimentele data van profielen bezwaken door plooi, distortional buckling, knik, torsieknik, alsook interactievormen.

Een groot aantal eindige-elementenberekeningen is uitgevoerd ter ondersteuning van deze experimenten, waarbij de daadwerkelijke proef zo nauwkeurig mogelijk is gemodelleerd. Vergelijking van de numerieke en experimentele resultaten laat zien dat de berekeningen tot een nauwkeurige voorspelling leiden. Op basis van deze gevalideerde berekeningen is het mogelijk een nauwkeurige analyse te geven van de verschillende aspecten zoals de kritische last, de bezwijklast, de invloed van imperfecties, de proefopstelling en stabiliteitsinteractie.

De numerieke en experimentele resultaten hebben geresulteerd in een nieuw en algemeen toepasbaar voorspellingsmodel. Dit model geeft een nauwkeurige beschrijving van het daadwerkelijke gedrag van axiaal belaste profielen en is toepasbaar voor doorsneden bestaand uit willekeurige combinaties van vlakke plaatdelen. Daarmee is het breed toepasbaar voor commercieel toegepaste aluminium extrusieprofielen. Nog op te stellen rekenregels kunnen daarmee leiden tot een economischer ontwerp van profielen. Daarnaast is het model uit te breiden met distortional buckling en stabiliteitsinteractie.

Geconcludeerd kan worden dat de gepresenteerde combinatie van experimenteel, numeriek, en analytisch onderzoek resulteert in een nauwkeurige beschrijving van het daadwerkelijke (plooi)gedrag van aluminium extrusieprofielen met arbitraire complexe doorsnedevormen.

Curriculum Vitae



Name Jeroen Mennink
Date of birth June 7th, 1973
Place of birth Sumve, Tanzania

Education

1985-1991 Koninklijke Scholengemeenschap Apeldoorn, Atheneum

1991-1996 Delft University of Technology,
Faculty of Civil Engineering
September 1996, master's degree with honours in both the
Structural Mechanics and Building Engineering group. Graduation
subject: *Bends in steel pipelines, a new analytical model to calculate
stresses, strains, and deformations.*

PhD-research

1996-2002 Eindhoven University of Technology,
Faculty of Building, Architecture, and Planning
Department of Structural Design

Daily practice

1996- TNO Building and Construction Research,
Department of Building Structures
Various research activities with respect to the structural application
of aluminium and steel structures, focusing on design issues, finite
element analyses, and stability analysis.

May 10th, 2002 Married to Barbara Renier